Magnetic properties of selected 3d- and 4f- systems on α-Al_2O_3 substrates

Dissertation
zur Erlangung des Grades
Doktor der Naturwissenschaften (Dr. rer. nat.)
am Fachbereich Physik
der Johannes Gutenberg-Universität Mainz

von
Jens Oster
geb. in Bendorf/Rh.

Mainz, 2003

D77

Tag der mündlichen Prüfung: 17.01.2005

Contents

List of Figures

List of Tables

Introduction

The search for applications of various kinds of magnetic materials has been of large interest since centuries. Nowadays, with the increasing necessity to miniaturization, new magnetic materials and preparation methods are in great demand for an emerging field of high technology industry. In microelectronics and integrated functional units, for example, the design of sensors, transducers, and actuators on a small scale has become of fundamental interest. The versatile properties of thin magnetic films may enable the generation of intelligent systems operating at low magnetic fields. In digital storage technology, for example, the domain size of the underlying magnetic materials is decreasing rapidly, yielding a rise in the storage density of 60% per year. For next generation magnetic recording media, new and preferably simple preparation technologies for creating particles with domain sizes in the nanometer scale have to be developed. Furthermore, the magnetic properties of the nanostructures have to be investigated.

The technological realization of devices of nanoscopic scale can be performed in two different ways. The first method is the standard top-to-bottom approach of e-beam or UV lithography. In UV lithography light sources with a wavelength of $\lambda \sim 250$ nm are applied. The main advantage of exploiting this technology for nanopatterning is their widespread use in CMOS technology, where sizes of 45 nm are expected to be the final limit due diffraction effects. However, this and new technologies using smaller wavelengths are very expansive and especially not affordable for fundamental research at a university. In e-beam lithography, on the other hand, very small structures can be produced. However, this process is very time intensive and therefore only practicable for small areas of the system.

In the second method, the bottom-up approach, nanoscaled structures are created by employing self organization properties of matter. This method is more suited for fundamental university research for most pre-treatments like annealing or etching are relatively inexpensive. The controllability and variability of the obtained objects, on the other hand, is often rather low. Mostly, self organization creates periodic structures, rendering the realization of complex systems like transistors without further nanopatterning techniques difficult. In other applications, like high-resolution magnetic field sensors, magnetic random access memories or high density magnetic storage devices, periodically arranged nanoparticles could gain a broad technological relevance. In basic research studies of the different processes of self-organization and the understanding of the respective driving forces are of tremendous interest.

One example for self organization of matter is the high temperature faceting of the $(10\bar{1}0)$ α-Al_2O_3 surface [1, 2]. Due to an increased surface free energy of these sapphire m-plane substrates the formation of a zigzag like structure arises after one-day annealing in air [3]. The almost macroscopic size of the occurring facets surpasses the atomic steps in vicinal cut substrates by far. Aim of this work was to test wether the ferromagnetic and superconducting properties of 3d- and 4f- systems, relevant for fundamental research and technical application, could be combined with the three dimensional morphology of these faceted substrates. Hereby, the growth properties and new deposition techniques for these metals had to be investigated.

Magnetostrictive materials are investigated for application relevance in integrated microsystems, thus augmenting established techniques based on piezoelectric and shape memory materials. Magnetostriction is the change of shape of a ferromagnetic material in an external magnetic field due to the magneto-elastic coupling of magnetization and crystal lattice. Magnetic bulk materials with large magnetostriction are employed as actuators or motors, when large forces at high efficiencies and high power levels are necessary. Furthermore, they are employed in sonar and ultrasonic technique and as sensors, when electrical energy has to be converted in mechanical motion and vice versa [4]. Prepared as thin films, magnetostrictive materials could operate as micro-actuators – umbrella term microelectromechanical systems (MEMS) –, nano-sensors, and surface acoustic wave (SAW) delay lines [5, 6, 7].

Taking the rare earth (R) metals terbium and dysprosium, the cubic C15 RFe_2 Laves phases show the highest magnetostrictive response at room temperature known to date [8, 9]. Crystalline $TbFe_2$, for example, has a saturation magnetostriction of $\lambda=\frac{\Delta l}{l}=2.5\cdot10^{-3}$ along $\{111\}$. Furthermore, it has a large magnetic anisotropy with the easy axis of magnetization along $\{111\}$. In the alloy $Tb_{0.27}Dy_{0.73}Fe_2$, known as Terfenol-D, the magnetic anisotropy is strongly reduced, still remaining high magnetostriction values. Prepared as bulk, Terfenol-D has already got a wide use of applications.

The epitaxial growth of thin RFe_2 films by molecular beam epitaxy (MBE) can be achieved by using high quality templates of niobium or molybdenum [10, 11, 12]. For the epitaxial growth of these 3d-metal templates, however, sapphire substrates can be employed. Hereby, a unique three dimensional epitaxial relationship of Mo and especially Nb with sapphire is observed [13, 14, 15].

Connecting the above described properties, the three dimensional epitaxy of Nb and Mo on α-Al_2O_3, the usability of Nb and Mo as buffer layer and template for the epitaxial RFe_2 growth, and the faceting of sapphire m-plane, the experimental evaluation of the growth properties of Mo, Nb, and RFe_2 on facetted and non-faceted sapphire m-plane is obvious. The wide application possibilities of the RFe_2 compounds render different epitaxial growth orientations of the C15 Laves phases very attractive. Furthermore, a periodic modulation of the template is expected to excite new effects in the guiding of surface acoustic waves in thereupon prepared films.

In addition to the creation of undulated films, the (semi-)periodic hill-and-valley morphology of the faceted sapphire substrates can furthermore be tested for the preparation of low dimensional structures: Taking the advantage of the hitchless propagation of the molecular beam in ultrahigh vacuum and the self shadowing of the facets, the preparation of one dimensional wires or zero dimensional dots in the nanometer scale could be possible [16, 17]. Due to the reduced scales and dimensions effects different to those in macroscopic samples can be expected. In a type II superconductor, for example, the interaction of the vortices with each other and the morphology of the material can lead to matching and guiding effects. In a ferromagnet, for example, the weight of the energy contributions influencing the magnetic structure is altered compared to macroscopic structures. This leads to different domain structures and magnetization reversal processes in nanopatterned samples. The feasibility of preparing nanostructures of as well the superconductor Nb as the ferromagnet Fe is therefore interesting for both, fundamental research and potential applications.

In this thesis the experimental results of the preparation and magnetic properties of selected magnetic 3d- and 4f- systems on different α-Al_2O_3 substrates are discussed. In the first chapter an overview to the materials and methods applied in this work is given. Here, the preparation of faceted α-Al_2O_3 is described, the theory of magneto-elasticity and the employed RFe_2 compounds are introduced, the employed MBE chamber and the MBE preparation process are presented, and the applied methods of crystallographic characterization are illustrated. In the second chapter the properties of 3d transition metals on faceted and non-faceted α-Al_2O_3 m-plane are analyzed. In the beginning the growth of Mo, Nb and Fe on α-Al_2O_3 m-plane is discussed. Afterwards, first applications of faceted Nb films are presented. Finally, the preparation and first measurements of Nb nano-wires will be introduced. In the third chapter X-ray measurements revealing the crystallographic properties of differently oriented RFe_2 films on α-Al_2O_3 substrates are discussed. With (211)-oriented crystals a new epitaxial growth direction of the cubic C15 Laves phases will be introduced. In the fourth chapter the measurements of the magnetic and magneto-elastic properties of crystalline RFe_2 films are discussed. The different epitaxial growth orientations will be compared with amorphous and polycrystalline RFe films for application relevance. In the last chapter, a preparation method of Fe nano-structures is introduced. Measurements of the magnetic and electric properties give rise to the discussion of the magnetization reversal processes in these systems by micromagnetic modeling.

Chapter 1

Preparatory operations

In this work, the properties with regard to applications of thin ferromagnetic films on α-Al_2O_3 (corundum, sapphire[1]) substrates were studied. Before the results are presented in the following chapters, an introduction to the relevant theoretical background and preparatory operations is given here.

The employed sapphire substrates represent a versatile material: Cut to the sapphire $(11\bar{2}0)$-plane (a-plane) they are known to serve for the epitaxial growth of several metallic layered systems. The high temperature faceting of sapphire $(10\bar{1}0)$ (m-plane), on the other hand, is an interesting example for the self organization of matter. The applicability of the mesoscopic hill-and-valley morphology of faceted sapphire to epitaxial film growth, in particular the growth of metallic nanostructures, was a main subject of this work. Prior to deposition attempts, however, the optimized preparation parameters for the creation of faceted structures had to be found. An introduction to the properties of sapphire in general and of faceted sapphire in special is given in the first section of this chapter.

Another main subject of this work was the research on highly magnetostrictive films of the cubic C15 Laves phases of the rare-earth iron compounds. Therefore, an introduction to the theory of magnetoelasticity, to the material properties of the RFe_2 ($R = Dy$, Tb, $Tb_{0.7}Dy_{0.3}$) compounds, and the self designed magnetoelasticity measurement setup is given in the second section of this chapter.

In the scope of this work a recently installed molecular beam epitaxy (MBE)

---

[1] The crystallographic correct denotation for α-Al_2O_3 is corundum. In the literature of solid state physics α-Al_2O_3 is often called sapphire. In sapphire, strictly speaking, the corundum lattice is contaminated with Ti ions dyeing the crystal in a blue color. Sapphires are found chiefly in Thailand, India (Kashmir), Sri Lanka, Myanmar/Burma, Australia and in the United States of America (Montana). In this work sapphire denotes the pure corundum lattice.

preparation system was employed. The MBE preparation process, which was in principle the same for all metallic systems analyzed here, will be introduced in the third section.

One very important property of the investigated thin film systems was their crystalline orientation and quality. These characterizations were performed by X-ray diffraction in two different setups. Therefore, an overview over the employed characterization methods is given in the last section of this chapter.

1.1 Properties of sapphire

1.1.1 Crystallography of sapphire

Sapphire is rhombohedral with space group R$\bar{3}$c, but it is usually indexed with a hexagonal structural unit cell (a = 4.7589 Å, c = 12.991 Å) containing 18 O^{2-} and 12 Al^{3+} ions [18]. In the hexagonal unit cell, the Al^{3+} cations occupy 2/3 of the octahedral interstices within the h.c.p. lattice of the O^{2-} ions. The ideal octahedral arrangement is altered by a displacement of the Al^{3+} cations in a direction parallel to the c-axis of the hexagonal unit cell and towards the unoccupied Al lattice sites in the layer above or below. Due to this, the O^{2-}-ions are also displaced in the plane of the individual layers. Within the crystal structure, two Al sublattices can be distinguished. One Al sublattice consists of lattice sites that are displaced in the same direction from the ideal octahedral interstices.

Sapphire crystals are grown by several methods, like for instance the standard Czochralski method. sapphire substrates are commercially available in the following orientations: a-plane (11$\bar{2}$0), c-plane (0001), m-plane (10$\bar{1}$0), and r-plane (1$\bar{1}$02). The a-, c-, and r-plane surfaces are thermally stable and can be smoothed by high temperature annealing in air [19]. Even the mosaicity of a sapphire a-plane substrate can be reduced by high temperature annealing in air or vacuum [20].

Sapphire a-plane substrates are known to serve for the epitaxial growth of several - also exotic - metallic systems, like for instance the low carrier density Kondo system CeSb and the bcc transition metals Mo, Nb, Ta, or W [21, 22, 23, 24].

Especially the growth of Nb on sapphire is frequently used as a template for the epitaxial growth of further metallic and ceramic films. This application, first presented by Schuller [25], has subsequently been adopted as a standard method for the growth of metallic single-crystal multilayers and thin films by molecular beam epitaxy [14, 26, 27]. The epitaxial orientation of Nb (and Mo) on sapphire proceeds in a unique three-dimensional growth mode [13, 14, 15]. The growth of Nb on faceted sapphire m-plane, represents an hitherto unknown epitaxial system and the epitaxy is elucidated in this work.

1.1.2 Faceting of sapphire $(10\bar{1}0)$

Faceting is a process by which a given planar surface evolves into two or more tilted planar surfaces. The type of surface structure that develops from faceting depends on the material and the orientation of the surface. In a vicinal cut surface, the faceting results in a terrace-step morphology. As the angle between the original surface normal and that found in the equilibrium form grows, faceting gives rise to a hill-and-valley morphology.

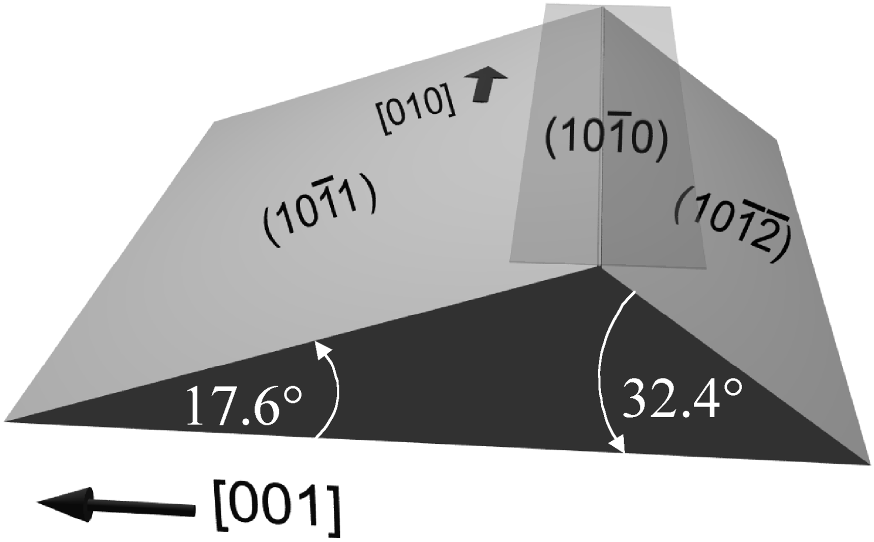

Figure 1.1: Schematic of a sapphire facet. The driving force of the faceting process of sapphire $(10\bar{1}0)$ is the lower surface free energy of the $(10\bar{1}\bar{2})$ and $(10\bar{1}1)$ surfaces.

$(10\bar{1}0)$-cut sapphire (m-plane) is known to develop a semi periodic faceted surface when annealed at high temperatures in air [1, 2]. In the literature the faceting is reported to occur into the more stable $(10\bar{1}\bar{2})$ plane, with the second plane being slightly curved but approximately parallel to the $(10\bar{1}1)$ surface [3, 28]. The angle of the facet planes with respect to the original $(10\bar{1}0)$ surface are given by $\alpha = 32.4°$ for the $(10\bar{1}\bar{2})$ surface and $\beta = 17.6°$ for the $(10\bar{1}1)$ surface, respectively (see Figure 1.1).

A survey of the faceting process is given in [29]. For a thermodynamically unstable surface the first explanation for the driving force of the faceting process was developed by Herring [30] and states, that surfaces other than those found on the equilibrium crystal shape (ECS) will decompose into a hill-and-valley structure in order to reduce the overall surface free energy. Accordingly, the faceting of sapphire m-plane is driven by the large surface free energy of the $(10\bar{1}0)$ surface. Within an ionic point charge model, with corrections for the Born repulsion energies, the stabilized $(10\bar{1}1)$ and $(10\bar{1}\bar{2})$ facets have specific surface energies of 4796 and 2552 erg/cm^2 [31]. A spontaneous formation of a facet structure is initiated by the destabilization of the given surface due to its large specific surface free energy $\gamma(\phi)$, where ϕ is the angle of the facet with respect to the non-faceted surface [30, 32]. Nevertheless, this process will not favor a specific period D, unless additional free energy contributions from the intrinsic surface stress τ_{ij} are taken into account. They comprise an edge contribution F_{edge} to $\gamma(\phi)$, as a consequence of the discontinuous change of τ_{ij} at the facet ridges, and a long-range elastic strain leading to $\Delta E_{elastic}$ [33]. The theory of periodically faceted surfaces was developed by Andreev and Marchenko [34, 35, 36]. The free energy of the faceted surface per unit projected area is [33]:

$$F(D) = \frac{\gamma(\phi)}{\cos(\phi)} + \frac{\eta(\phi)}{D} - \frac{C(\phi)\tau^2}{YD} \quad \ln\left|\frac{D}{a}\right| \tag{1.1}$$

where η is the averaged short-range energy of the convex and concave edges per unit length, C is a geometric factor accounting for the symmetry of the averaged stress tensor τ, Y is Young's modulus, and a is the lattice parameter. Two important aspects are readily observable: Firstly, there exists an optimal periodicity D_{min} for which F takes on its minimal value

$$D_{min} = a \exp\left(\frac{\eta(\phi)Y}{C(\phi)\tau^2} + 1\right) \tag{1.2}$$

Secondly, the stability of this optimal periodicity (as determined by the local curvature of F at $D = D_{min}$) decreases with increasing D_{min}. The instability of a single-period faceting for larger D_{min} is a consequence of the reduced influence of the edge and elastic energy contributions. This also implies that for small period facet lengths, approaching the lattice constant a, almost perfect facet structures can be expected within this continuum theory. This has been observed for a large selection of vicinal-cut or low-index singular surfaces of semiconductors and metals [37].

Heffelfinger et al. [3, 28] have pointed out five stages of surface faceting for $(10\bar{1}0)$ surfaces of sapphire:

1.) **Surface smoothing**

In AFM measurements the RMS roughness value was found to decrease from 2.1 nm to 0.2 nm after 1 h of annealing at 1400°C.

2.) **Individual facet formation**

The faceting of the sapphire surface starts with the nucleation and growth of individual (surface) facets. Individual facets as well as facet domains were observed on the $(10\bar{1}0)$ surface after annealing the sample for 2 h at 1400°C. The individual facets consist of a ridge which separates a simple and complex surface. The simple surface is that of the low surface energy facet, the $(10\bar{1}\bar{2})$ sapphire surface, and the complex surface is a curved surface that corresponds to no particular crystal orientation but is approximately the $(10\bar{1}1)$ orientation. The facet propagates along the [010] direction and is perpendicular to the [001] direction.

3.) **Forming of facet domains**

After the formation of individual facets, the formation of second, smaller facets on the wake of the larger facets is observed. As the individual facet grows, surface distortions on either side of the facet grow in size. These distortions act as sides for the nucleation of adjacent facets. Due to the distortions the surface is altered such that the orientation of the distorted surface is closer to the energy-reduced surface than the orientation of the original surface is. Facets were found to predominately nucleate on the simple surface side of the facet, where surface distortions tend to be larger in size. Consequently, facet domains are built, which are found to have a semi-elliptical shape with one major axis of the ellipse running parallel to the axis of the facets, the [010]. The rate of facet nucleation was found to be inversely related to the angle separating the simple surface and the non-faceted surface. The size of the individual facet becomes limited by the formation of facets on either side of the original facet. Thus, the width of the individual facet is limited until coarsening occurs. Individual facets as well as adjacent facets are able to grow in length up to the point where they impinge on other individual facets or groups of facets.

4.) **Facet coalescence**

As domains coalesce, regions with a high density of facet junctions are formed at the perimeter. Facet junctions are points were two facets merge to form one facet. These regions of facet junctions result from the misalignment of facet corners between different domains.

5.) **Facet coarsening**

Facet coarsening is the process by which the completely faceted surface increases its average facet size with increased annealing time. After 4 h of annealing at 1400°C, Heffelfinger et al. found the $(10\bar{1}0)$ surface to be completely faceted into a hill-and-valley structure. As a function of annealing time the density of facet junctions decreases while the average width of the facets increases, both approaching constant values for long annealing times. This implies the movement of two facet junctions in opposite directions along the facet axis and their merging, leading to the elimination of one facet and to the increase of the other one. The motion of facet junctions provides an immediate and simple way for this surface to reduce its free energy.

1.1.3 Preparation of faceted sapphire

Though the faceting of sapphire m-plane was already investigated [3, 28], the preparation parameters allowing an adjustment of the facets height and periodicity is not given in literature. The non-faceted sapphire m-plane substrates were received by Crystec Kristallechnology (Berlin) and were cleaned as described in the subchapter of the MBE preparation process. After cleaning, the substrates were put in a DEGUSSIT Al23 alumina Friatec boat liner. This liner was put in the center of an alumina tube oven[2] . The samples were transferred at room temperature. To decrease the thermal gradient of the oven, the ends of the tubes were closed by firebricks. When the oven was heated to 1650°C, the temperature in the tube oven's center varied by up to 4°C at a distance of ± 6cm. The thermal gradient for the alumina liner therefore amounted to 0.2%.

An annealing series was performed with temperatures from 1400°C to 1700°C. The characterization of the facets was performed by AFM measurements[3]. The characteristic parameters facet width, facet height, and the facet angles α and β were determined by evaluating and averaging the line profiles of several scans.

---

[2] The oven was provided by AK Tremel at the university of Mainz

[3] Courtesy by A. Dion

$\mathbf{T}_{anneal}$ [°C]	α [°]	β [°]	<**width**> [*nm*]	<**height**> [*nm*]
1400	10	7	115	9
1500	20	14	100	15
1600	24	18	255	50
1650	21	15	250	45

Table 1.1: Mean characteristic values of faceted sapphire m-plane annealed at different temperatures.

The width of the facet was defined by the distance of two minima. The height was determined by the distance of the facet peak to the basal plane between two minima. The angles α and β were then given by trigonometry. However, due to the finite size of the AFM tip and a height difference of the minima the determination of the characteristic facet values is not exact.

The annealing series shows that the characteristic parameters, especially the height and width of the facets, depend on the annealing temperature. This is in contrast to the statements of Heffelfinger et al. [3, 28]. For substrates annealed at 1400°C, the average width and height of the facets amount to 115 nm and 10 nm, respectively, as shown in Figure 1.2.

By increasing the annealing temperature to 1500°C, the height of the facets increases to 15 nm, as can be seen in Figure 1.3. Compared to substrates annealed at 1400°C the average width of the facets seems reduced to 100 nm.

A further increase of the annealing temperature to 1600°C also increases the height and width of the facets to 50 nm and 255 nm, respectively, as shown in Figure 1.4. At this annealing temperature the crests of the facets are still sharp.

At an annealing temperature of 1650°C the height and width of the facets stagnate at 45 nm and 250 nm, respectively, as shown in Figure 1.5. Compared to substrates annealed at 1600°C, the crests of the facets tend to show a slight rounding.

A further increase of the annealing temperature above 1650°C also leads to broad facets. However, compared to the other samples, the facets do not posses sharp crests any more. The rounding of the peaks is pronounced, leading to broad plateaus of presumably a new surface on the top of the facets, as shown in Figure 1.6. This phenomenon is known as rounding transition.

The characteristic values for the facet annealing series are listed in Table 1.1.

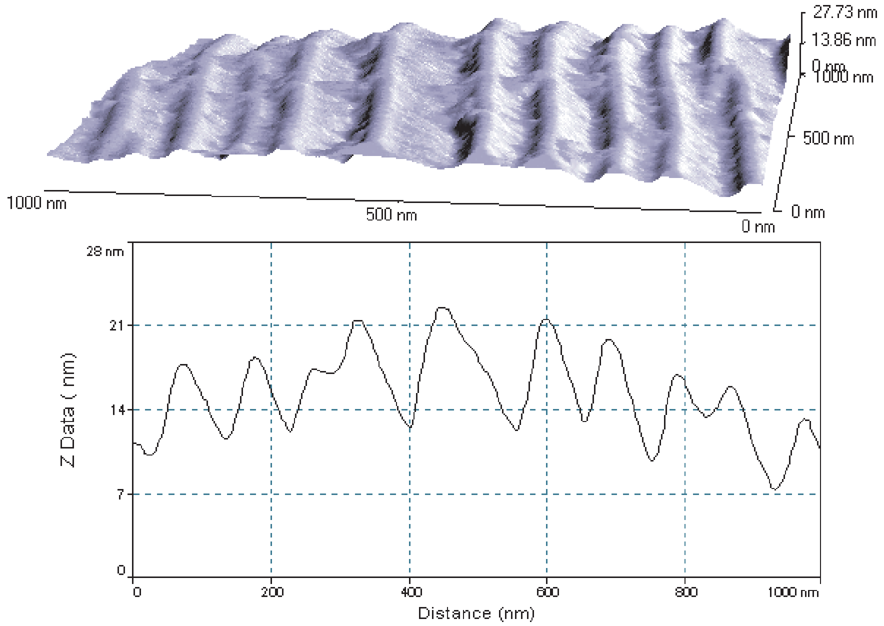

Figure 1.2: AFM image and linescan of a faceted sapphire m-plane substrate annealed at 1400°C.

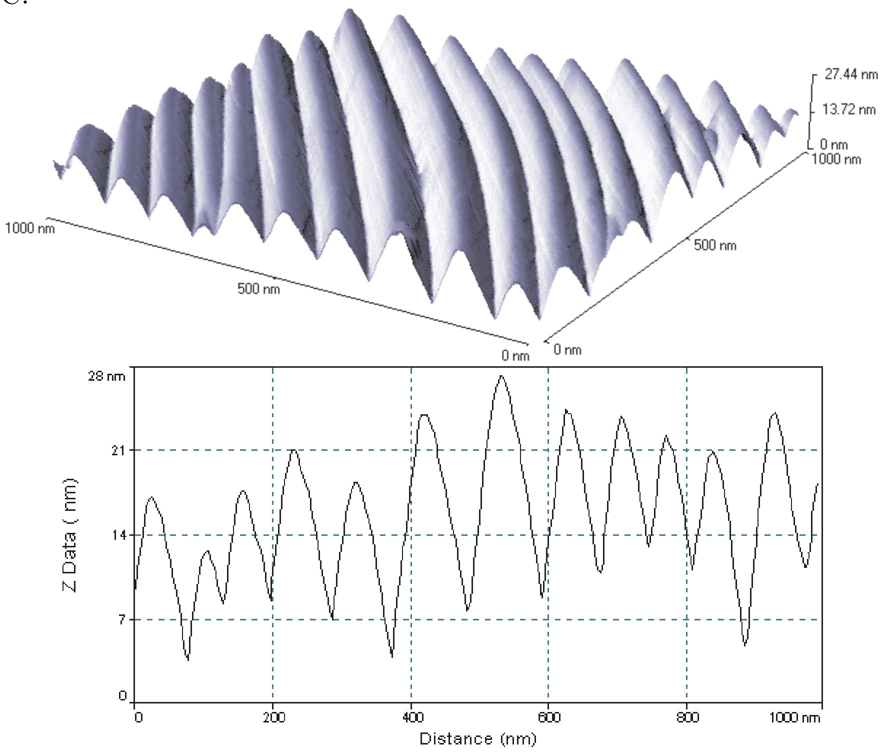

Figure 1.3: AFM image and linescan of a faceted sapphire substrate annealed at 1500°C.

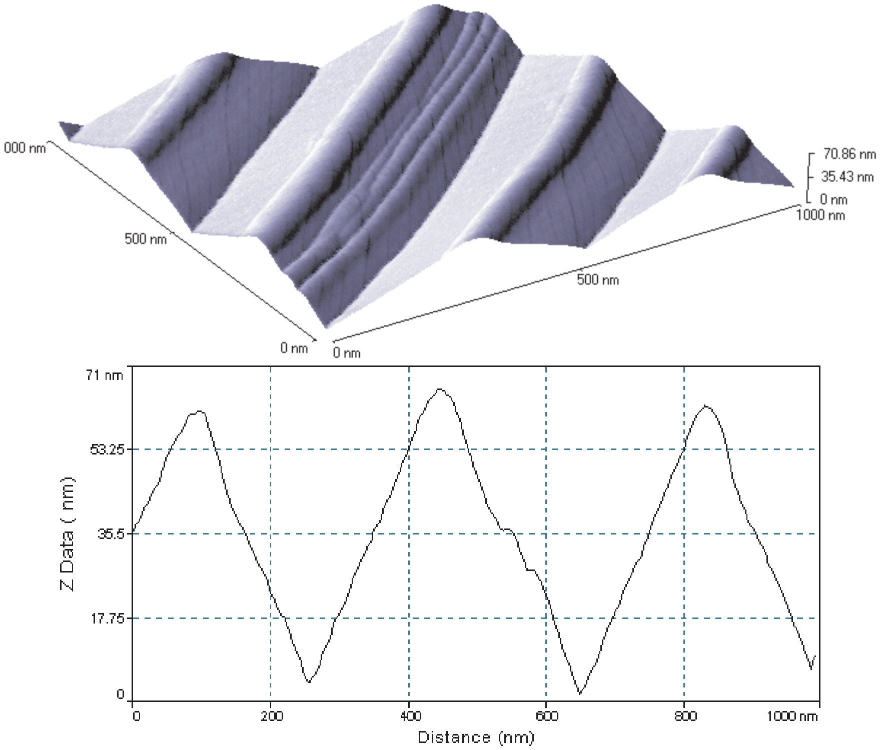

Figure 1.4: AFM image and linescan of a faceted sapphire m-plane substrate annealed at 1600°C.

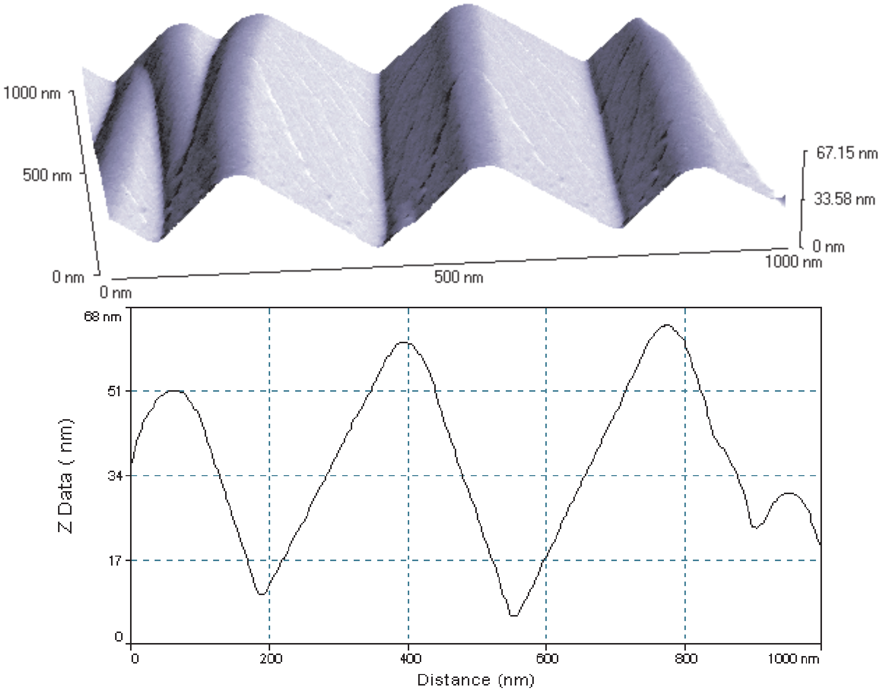

Figure 1.5: AFM image and linescan of a faceted sapphire m-plane substrate annealed at 1650°C.

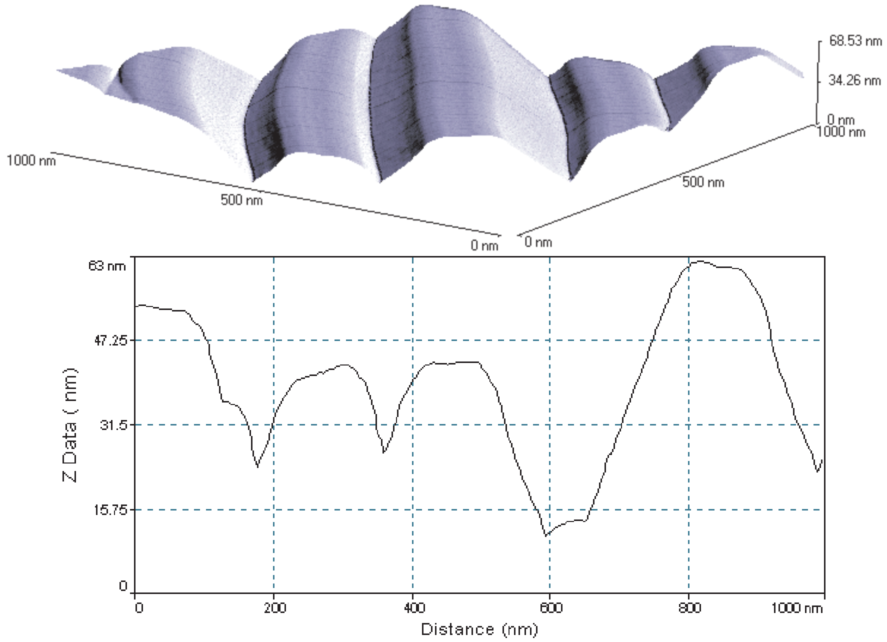

Figure 1.6: AFM image and linescan of faceted sapphire m-plane substrate annealed at 1700°C.

Literature values of the sapphire lattice predict an angle of $\alpha = 32.4^\circ$ for the expected $(10\bar{1}\bar{2})$ plane. This value deviates strongly from the observed values. As will be shown in the transmission electron microscopy (TEM) measurement in the next chapter, the formation of the $(10\bar{1}\bar{2})$ plane is not exactly smooth. The surface consists mainly of $(10\bar{1}\bar{2})$ terraces but atomic steps occur, which round the macroscopic surface and reduce the angle. The angle of the second facet plane is more close to the real $\beta = 17.6^\circ$ of the Al_2O_3 $(10\bar{1}1)$ plane. This is also observable in the TEM measurements, where the $(10\bar{1}1)$ plane is completely smooth and straight. These results are in contradiction to the observations and calculations given in the literature: Heffelfinger et al. report the $(10\bar{1}\bar{2})$ surface to be the simple plane of the faceting process and the $(10\bar{1}1)$ surface to be slightly curved [3, 28]. Calculations performed by Hartman predict the surface free energy of the sapphire $(10\bar{1}\bar{2})$ surface to be notedly smaller than the surface free energy of the $(10\bar{1}1)$ surface. A further discussion of this problem will be given in chapter 2, when the TEM measurements are presented.

In order to determine the periodicity of the facet structure, various line scans of a faceted substrate annealed at 1600°C were analyzed by Fourier transformation [29]. This was compared with the Fourier spectrum of a perfectly periodic

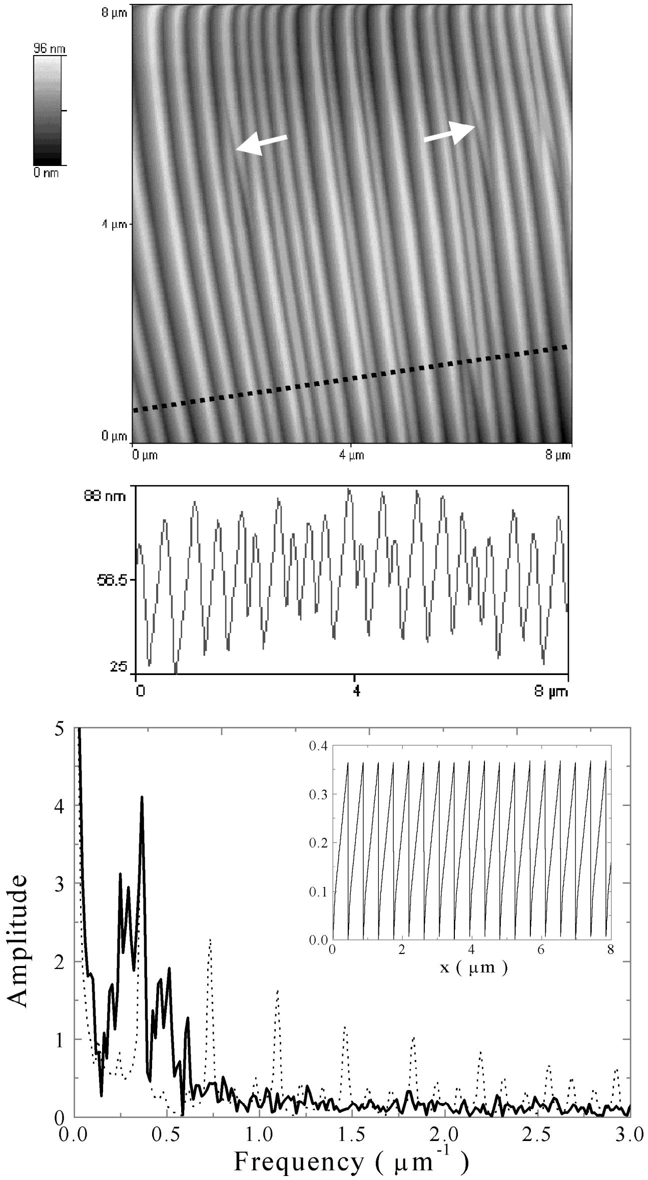

Figure 1.7: AFM image (top), linescan (middle) of a faceted sapphire substrate. In the image at the bottom a Fourier spectrum of the linescan is compared with one of a periodic zigzag [29].

faceted (zigzag) surface of comparable facet width. The actual faceted surface shows a dominant, but somewhat broadened, spectral component at the periodic length of the system. Higher harmonics were suppressed, mainly due to the non-perfect periodicity of the facet ridges.

Further annealing series to tune the facet periodicity can be proposed. When the substrate is covered before annealing, for example with SiO_2 [2], the interface energy between the cover layer and the substrate will change the short-range energy η and the elastic properties of the surface. For time reasons these experiments were not performed in the scope of this work.

1.2 Theory of magnetoelasticity

1.2.1 Magnetoelasticity in bulk materials

In 1842 J. P. Joule observed the change of length in a ferromagnetic rod when magnetized. This so called magnetostrictive effect, qualified with the magnetostriction coefficient λ, is related to the relative change in length [8, 38]

$$\frac{\Delta l(M)}{l} = \frac{l(M) - l(0)}{l(0)} = \lambda \tag{1.3}$$

In a single crystalline material the magnetostriction $\lambda_{\alpha,\beta}$ is generally depending on the direction α of the magnetic field and on the direction β in which the change of length is measured with respect to the crystal axes. In some alloys the volume of the unit cell is changed due to magnetostriction while the outer shape of the body is conserved. This is called shape invariant magnetostriction. In most of the magnetostrictive materials the volume is conserved, but a change of the shape of the body occurs. Accordingly, this is called volume invariant shape magnetostriction. As a consequence of magnetostriction the crystal becomes strained when cooled below the Curie temperature. To be more specific, every Weiss region becomes strained. In the demagnetized state all spontaneous strains are statistically distributed. In an applied magnetic field the strains are getting aligned which leads to an macroscopic change of the system's shape.

The origin of magnetostriction is the strain dependence of the magnetic anisotropy energy. The crystal deforms in order to minimize its total energy. The total energy of a ferromagnetic material is given by [8]:

$$E = E_0 + E_a + E_{me} + E_{el} \tag{1.4}$$

Here E_0 denotes the part of the magnetic energy which is independent of the magnetization direction.

The magnetocrystalline anisotropy energy E_a describes the direction dependence of the work $\int HdM$, which is required to magnetize a crystal in an external magnetic field H. This direction dependence has its origin in the spin-orbit coupling of the valence electrons of the sample. In irreducible representation, the anisotropy energy can be described by the material dependent anisotropy constants $\{K^{\alpha,l}\}$ and the symmetry polynomials $\{S^{\alpha,l}\}$ of the lattice:

$$E_a = \sum_l K^{\alpha,l} S^{\alpha,l} \tag{1.5}$$

For a cubic lattice, in lowest order in the direction cosines α_i, the magnetocrystalline anisotropy energy in given by:

$$E_a^{cubic} = K^{\alpha,4}(\alpha_x^4 + \alpha_y^4 + \alpha_z^4 - \tfrac{3}{5}) \tag{1.6}$$

In addition to this directional dependence of the magnetic anisotropy, the magnetic properties depend on the orbital overlap which leads to a strain-dependence of the magnetic anisotropy. Therefore, a sample can lower its energy by changing its length l in the magnetization process until elastic forces balance the magnetostrictive strain. In the cubic system the symmetry strain components can be classified into three irreducible representations $\{\epsilon_i^\mu\}$, designated by $\mu = \alpha, \gamma, \epsilon$. The subscript denotes the components belonging to the same irreducible representation. Taking the direct products of the symmetry strains and the direction cosine polynomials, the magnetoelastic energy E_{me} is described by the magnetoelastic coupling coefficients $\{\mathrm{B}^{\mu,l}\}$ in the following way:

$$E_{me}^{cubic} = \sum_l \left[B^{\alpha,l} \epsilon^\alpha S^{\alpha,l} + B^{\gamma,l} \sum_i \epsilon_i^\gamma S_i^{\gamma,l} + B^{\epsilon,l} \sum_i \epsilon_i^\epsilon S_i^{\epsilon,l} \right] \tag{1.7}$$

Hereby, the magnetoelastic coupling coefficients $\{\mathrm{B}^{\alpha,l}\}$ describe the volume magnetostriction. The coefficients $\{\mathrm{B}^{\gamma,l}\}$ and $\{\mathrm{B}^{\epsilon,l}\}$ describe the first order shape (Joule) magnetostriction. The expression for the magnetoelastic energy E_{me} in Equation (1.7) is a function of the strains $\{\epsilon_i^\mu\}$. The most important consequence of the strain dependence of E_{me} is that magnetoelastic stresses are inherently connected with the concept of magnetoelastic coupling. The observation of magnetostriction in bulk samples is a consequence of the magnetoelastic stress that acts to strain the sample until it is balanced by the restoring elastic forces. The driving force for this magnetostrictive strain is the minimization of the total energy of the sample in the magnetization process. A lowering of the sum of elastic and magnetoelastic energy by a non-zero strain is always possible, as the magnetoelastic energy contribution depends linearly on the strains in the approximation given above.

The elastic energy E_{el} of a cubic system can be described by the elastic constants of the cubic symmetry $\{c^{\mu}\}$:

$$E_{el}^{cubic} = \tfrac{1}{2}c^{\alpha}\left(\epsilon^{\alpha}\right)^2 + \tfrac{1}{2}c^{\gamma}\left(\left(\epsilon_1^{\gamma}\right)^2 + \left(\epsilon_2^{\gamma}\right)^2\right) + \tfrac{1}{2}c^{\epsilon}\left(\left(\epsilon_1^{\epsilon}\right)^2 + \left(\epsilon_2^{\epsilon}\right)^2 + \left(\epsilon_3^{\epsilon}\right)^2\right) \tag{1.8}$$

which reads in cartesian coordinates:

$$\begin{aligned} E_{el}^{cubic,cartesian} &= \tfrac{1}{2}c_{11}\left(\epsilon_{xx}^2 + \epsilon_{yy}^2 + \epsilon_{zz}^2\right) + c_{12}\left(\epsilon_{yy}\epsilon_{zz} + \epsilon_{zz}\epsilon_{xx} + \epsilon_{xx}\epsilon_{yy}\right) \\ &\quad + \tfrac{1}{2}c_{44}\left(\epsilon_{xy}^2 + \epsilon_{yz}^2 + \epsilon_{zx}^2\right) \end{aligned} \tag{1.9}$$

Minimizing the energy term (1.4) with respect to the strains $\{\epsilon_i^{\mu}\}$ leads to the cubic symmetry equilibrium strains

$$\begin{aligned} \epsilon^{\alpha} &= \sum_{l=4,6,\ldots} \lambda^{\alpha,l} S^{\alpha,l}(\alpha_K) \\ \epsilon_i^{\gamma} &= \sum_{l=2,4,6,\ldots} \lambda^{\gamma,l} S^{\gamma,l}(\alpha_K) \\ \epsilon_i^{\epsilon} &= \sum_{l=2,4,6,\ldots} \lambda^{\epsilon,l} S^{\epsilon,l}(\alpha_K) \end{aligned} \tag{1.10}$$

,with α_K the direction cosines of the magnetic field with respect to the lattice. Equation (1.10) defines the magnetostriction constants $\{\lambda^{\mu,l}\}$. The linear elongation due to the Joule magnetostriction measured along a given direction ($\beta_K = \beta_1,\ \beta_2,\ \beta_3$) is given by the general expression:

$$\lambda^{[\beta]} = \sum_{\mu,i} S_i^{\mu,2}(\beta_K)\epsilon_i^{\mu} = \sum_{\mu,i,l} \lambda^{\mu,l} S_i^{\mu,l}(\alpha_K) S_i^{\mu,2}(\beta_K) \tag{1.11}$$

The $\lambda^{\alpha,4}$ and $\lambda^{\alpha,6}$ coefficients describe strains which are isotropic with respect to the measuring direction. The $\lambda^{\gamma,2}$ and $\lambda^{\epsilon,2}$ are the main magnetostriction coefficients. They describe the first order magnetoelastic properties of the cubic crystal. They are roughly proportional to the commonly used constants λ_{100} and λ_{111}. Here, λ_{100} and λ_{111} denote the change in length along the [100] and [111] direction, respectively, when the magnetization is also aligned in this direction.

$$\begin{aligned}\lambda_{100} &= \frac{2}{3}\left\{\lambda^{\gamma,2} + \frac{1}{2}\lambda^{\gamma,4} + \frac{1}{11}\lambda^{\gamma,6}\right\} + \frac{2}{15}\lambda^{\alpha,4} + \frac{2}{231}\lambda^{\alpha,6} \\ &\approx \frac{2}{3}\lambda^{\gamma,2} \qquad (1.12)\end{aligned}$$

$$\begin{aligned}\lambda_{111} &= \frac{2}{3}\left\{\lambda^{\epsilon,2} + \frac{4}{21}\lambda^{\epsilon,4} - \frac{4}{99}\lambda^{\epsilon,6} - \frac{1}{18}\lambda^{\epsilon,6'}\right\} - \frac{4}{45}\lambda^{\alpha,4} + \frac{32}{2079}\lambda^{\alpha,6} \\ &\approx \frac{2}{3}\lambda^{\epsilon,2} \qquad (1.13)\end{aligned}$$

Using the coefficients λ_{100}, λ_{111} the magnetostriction reduces to:

$$\begin{aligned}\frac{\Delta l}{l} &= \tfrac{3}{2}\lambda_{100}(\alpha_x^2\beta_x^2 + \alpha_y^2\beta_y^2 + \alpha_z^2\beta_z^2 - \tfrac{1}{3}) \\ &\quad +3\lambda_{111}(\alpha_x\alpha_y\beta_x\beta_y + \alpha_y\alpha_z\beta_y\beta_z + \alpha_z\alpha_x\beta_z\beta_x) \qquad (1.14)\end{aligned}$$

In polycrystalline and amorphous samples the Joule magnetostriction is isotropic giving $\lambda^{\gamma,2} = \lambda^{\epsilon,2} = \lambda$, and all other coefficients being null. With the angle θ between the magnetization and the measuring direction the magnetostrictive response can be written as:

$$\lambda_\theta = \lambda^{\gamma,2} \sum_{\mu(=\gamma,\epsilon),i} S_i^{\mu,2}(\beta_K) = \lambda^{\gamma,2}(cos^2\theta - \frac{1}{3}) = \frac{3}{2}\lambda_s(cos^2\theta - \frac{1}{3}) \qquad (1.15)$$

The saturation magnetostriction λ_s is the relative change in length of the sample in measurement direction between the magnetically saturated and demagnetized state. However, the shape and the amplitude of the magnetostrictive hysteresis loop depends strongly on the magnetic history of the material. This problem can be circumvented by firstly measuring the magnetostriction $\lambda_\parallel$ of the sample with the magnetic field parallel to the measuring direction after the sample was previously magnetized in perpendicular orientation. Secondly, the magnetostriction $\lambda_\perp$ of the sample, with the magnetic field perpendicular to the measurement orientation, is determined. The saturation magnetostriction is then given by:

$$\lambda_s = \frac{2}{3}(\lambda_\parallel - \lambda_\perp) \tag{1.16}$$

The magnetostriction and the magnetoelastic coupling in bulk samples can be determined by various techniques. One has to distinguish between direct and indirect methods [38, 39].

Direct techniques

In the strain gauge-technique the relative change of length measured along various directions, with the magnetization aligned along other directions, is determined, from which all magnetostriction coefficients of the crystal can be determined.

In a capacitive set-up the bulk sample is part of a plate capacitor, and magnetostrictive changes of the sample's length can be measured with high sensitivity by monitoring the resulting change in capacity.

Fibre-optic techniques can also be used to determine the magnetostrictive strain of bulk samples: Here, the sample is used as a shutter in a fibre-optic light path. Thus, a periodic magnetostrictive strain modulates the light intensity.

In a scanning tunnelling microscope the dependence of a tunnel current between the tunnelling tip and a magnetostrictive sample can be used to measure magnetostriction.

Finally, for bulk samples in the form of ribbons and wires, the Wiedemann effect[4] is used to determine the saturation magnetostriction of elastically and magnetically isotropic samples very accurately.

Indirect techniques

In the indirect methods the samples are exposed to an externally applied stress by pressing, stretching or bending the samples. The main idea of these methods is to exploit the contribution of the magnetoelastic coupling to the magnetic anisotropy. The magnetoelastic coupling coefficients are then derived by changes in the initial susceptibility, the shape of the magnetization curve, or the ferromagnetic resonance.

---

[4] An electric current sent through a ferromagnetic wire will produce a circular magnetic field in a plane perpendicular to the wire. Therefore, the magnetic moments will tend to align in the circumferential direction. If furthermore an axial magnetic field is applied, some of the moments align in a helical fashion creating a helical magnetic field. The resulting twist observed in the wire is called the Wiedemann effect. The inverse Wiedemann effect, known as the Matteuci effect, is the change in axial magnetization of a current carrying wire when it is twisted.

1.2.2 Strain in thin ferromagnetic films

As was discussed before, the magnetic properties of ferromagnetic materials are influenced by the strain of the crystal due to magnetoelastic coupling [40]. Due to a lattice mismatch with respect to the substrate and due to other effects, like different thermal expansion coefficients of film and substrate, thin films mostly show strains in the film plane and, consequently, also in perpendicular direction. Therefore, thin ferromagnetic films are inclined to show different magnetoelastic properties than their correspondent bulk samples. For example, epitaxial film strain was found to change the sign and magnitude of the magnetoelastic coupling coefficients in ultrathin epitaxial films [41, 42]. In thin $DyFe_2$ films the temperature dependence of the easy magnetization axis differs strongly from those of bulk samples [43, 44, 45]. Therefore, the magnitude of the in-plane strains ϵ_{xx} and ϵ_{yy}, or in the isotropic case $\epsilon_{\|}$, and the perpendicular strain $\epsilon_{zz} = \epsilon_{\perp}$ is important for the discussion of the magnetoelastic contribution to the magnetic anisotropy.

The total film strain in a given crystal direction, induced due to lattice mismatch and further stress effects like different thermal expansion during the cooling process after film preparation, is given by

$$\epsilon = \frac{a_{film} - a_{bulk}}{2a_{bulk}} \tag{1.17}$$

Here, a_{film} is the experimentally determined film lattice constant and a_{bulk} is the bulk value of the crystal lattice.

The elastic energy of the cubic lattice in cartesian coordinates is given by equation (1.9). For a film growth orientation which is different from (100), the easiest way to calculate the in-plane strain of the film is to transform the film's strain tensor into the cartesian system of a (100)-oriented film. The transformation matrix is derived by expressing the new film strains ϵ'_{ij} as a function of the crystal directions. Finally, the crystal strains are expressed as a function of the film strains, and equation (1.9) can be used with the strains ϵ_{ij} replaced with the appropriate expressions in terms of the ϵ'_{ij}.

1.2.3 Magnetoelastic coupling in thin films

In the discussion of magnetoelastic coupling in bulk samples, the magnetoelastic coupling coefficient b (or B) and the magnetostriction coefficient λ are often used synonymously. In ferromagnetic thin films, on the other hand, the thermodynamical potential is strongly modified as compared to bulk materials due to the interaction with the substrate. Here, the in-plane strains are fixed due to the strong film-substrate interaction and can not freely adjust to minimize the energy of the system. Instead, magnetostrictive strains are induced. When a film is magnetized, its magnetoelastic coupling energy competes with the elastic energy of the substrate, not of the film. Therefore, for ferromagnetic films the equivalence between the magnetoelastic coupling and the magnetostrictive strain is not given [46]. In the assessment of the measurements of this work, the use of magnetoelastic coupling coefficients b, which give the magnetostrictive strain, is preferred. Nevertheless, for comparison with other publications, the magnetostriction coefficient λ of the films will also be calculated.

Various techniques have been developed for studying the magnetoelastic coupling of thin films. One of them consists in measuring the deflection of a cantilever under the application of a magnetic field. The corresponding deflection-striction formula proposed in 1976 by Klokholm [47] has been criticized and recently corrected [46, 48, 49, 50, 51].

In the experiment a cantilever is prepared with the long axis being several times larger than the short axis. This cantilever is fixed at the short axis to a nonmagnetic holder. Rotating the magnetization of the film by means of an outer magnetic field, the magnetoelastic stress in the film causes a bending of the substrate-film bimorph along the long and the short axis. This field-dependent deflection corresponds to the Joule magnetostriction and may exhibit features very different from those conventionally observed in bulk materials. Due to the clamping and the appreciably larger length of the long axis compared to the short axis, the dominantly effect is the bending along the long axis of the cantilever. To eliminate a bias in the signal due to a previous magnetization of the sample, the curvature of the cantilever is determined with the magnetic field aligned parallel ($R_{\parallel}$) and perpendicular ($R_{\perp}$) to the long axis. Provided surface effects are negligible (film thickness $\gg$ 100 atomic layers), the magnetoelastic coefficient is given by [39]:

$$b = \frac{Y_S t_S^2}{6(1+\nu_S^2)t_F}\left(\left(\frac{1}{R_{\parallel}}\right) - \left(\frac{1}{R_{\perp}}\right)\right) \tag{1.18}$$

Here, Y_S denotes the Young's modulus of the substrate, t_S the thickness of the substrate, ν_S the poisson ratio of the substrate, and t_F the thickness of the film. For comparison with other publications, the "magnetostriction coefficient λ" of the film is described by the magnetostriction coefficient $\lambda^{\mu,2} = (3/2)(\lambda_s)$, which is given by the equation ($\lambda^{\mu,2}$) = -($b^{\mu,2}$)/(c^{μ}). The elastic film constants c^{μ} can be expressed by Young's modulus Y_F and the poisson ratio ν_F and accordingly to [48, 52]:

$$\frac{2}{3}\lambda^{\mu,2} = \lambda_s = -\frac{(1+\nu_F)}{Y_F}\frac{Y_S t_S^2}{6(1-\nu_S^2)t_F}\left(\left(\frac{1}{R_\parallel}\right) - \left(\frac{1}{R_\perp}\right)\right) \tag{1.19}$$

1.2.4 The ΔE - effect

Due to the magnetoelastic coupling, the elastic properties of the ferromagnetic material are field dependent. This change in the Young modulus, called the ΔE-effect, was first observed in 1846 by Guillemin. This means that the magnetostriction does not only influence the magneto-crystalline anisotropy, but it also influences the elastic properties of the material.

If a tension is applied to any non-magnetic sample, e.g. a rod, its length increases along the direction of application of the stress τ, according to Hook's law:

$$\left(\frac{\delta l}{l}\right)_\parallel = \frac{\tau}{Y_0} \tag{1.20}$$

Here, Y_0 is Young's modulus, which is determined by the elastic constants c^{α} and c^{γ}. In general, when a stress is applied along the direction [γ_1, γ_2, γ_3] the elongation measured along [β_1, β_2, β_3] is given by:

$$\left(\frac{\delta l}{l}\right)_{[\beta]} = \frac{\tau^{\alpha}P^{\alpha}}{c^{\alpha}} + \sum_i \frac{\tau_i^{\gamma}P^{\gamma}(\beta_i)}{c^{\gamma}} \tag{1.21}$$

where $\{P_i^{\mu}\}$ are the polynomials for a spheric symmetry.

Using the orthonormalization relation of the $\{P_i^{\gamma}\}$ polynomials, equation (1.21) leads to:

$$\left(\frac{\delta l}{l}\right)_{\zeta} = \tau\left[\frac{1}{3c^{\alpha}} + \frac{1}{c^{\gamma}}(cos^2\zeta - 1/3)\right] \tag{1.22}$$

,where $cos\zeta = \sum_i \beta_i\gamma_i$, and ζ is the angle between the direction of the measurement of the elongation and the direction of the application of stress.

For a ferromagnetic material the strain is not simply proportional to the stress but is also influenced by the magnetoelastic coupling contribution:

$$\epsilon^{\alpha} = \frac{\tau^{\alpha} - B^{\alpha,0} P^{\alpha,0}}{c^{\alpha}}, \quad \epsilon_i^{\mu} = \frac{\tau_i^{\mu} - B^{\mu,2} P_i^{\mu,2}(\alpha_i)}{c^{\mu}} \tag{1.23}$$

This means, when applying an external stress τ one observes:

1.) The strain predicted by Hook's law

2.) An additional strain caused by the change in $P_i^{\gamma,2}(\alpha_K)$ induced by τ.

Therefore the apparent Young modulus Y differs from Y_0:

$$\frac{\Delta Y}{Y} = \frac{Y_0 - Y}{Y} \tag{1.24}$$

Due to the magnetoelastic coupling an additional strain occurs, which reduces the apparent Young modulus.

1.2.5 Magnetoelasticity of RFe_2 alloys

For the ferromagnetic metals Fe, Ni and Co the room temperature magnetostrictive strain $\Delta l/l$ is of order of 10^{-5}. But magnetostriction is not necessarily small. Terbium and dysprosium show a large magnetostriction of the order 10^{-2} at low temperatures [53, 54]. To achieve highly magnetostrictive materials operating at room temperature, alloys of rare-earth (R) with transition metals, TM = Fe, Ni, and Co were investigated in the early 1970's. All the Ni-compounds possess Curie temperatures below 200 K. The Curie temperatures of Co compounds span a large range from 1200 K (Tb_2Co_{17}) to near 0 K (Er_3Co). The Fe compounds show a low Curie temperature for the Fe rich alloys (RFe_{17}) and the highest Curie temperatures for the least iron-rich representatives (RFe_2). Amorphous thin film R-TM alloys also posses a wide range of ordering temperatures. Most Co containing alloys films have a higher ordering temperature, the Fe alloys films have a lower Curie temperature than their bulk compounds [8].

The RFe_2 alloys crystallize in the cubic C15 Laves phase of $MgCu_2$ type (space group Fd3m) with 24 atoms in the unit cell [55, 56]. The rare-earth atoms are ordered in hexagonal double planes and the Fe atoms are building tetrahedrons with the larger R atoms being situated between the tetrahedrons. A schematic of the RFe_2 crystal structure is shown in Figure 1.8

First measurements on $TbFe_2$ were performed in 1972 by Clark and Belson [57]. This compound possesses the largest room temperature magnetostriction known to date and shows a rhombohedral deformation $\lambda_{\parallel} - \lambda_{\perp} > 2000 \cdot 10^{-6}$. Contrary to expectations, $DyFe_2$ possesses with $\lambda_{\parallel} - \lambda_{\perp} \approx 600 \cdot 10^{-6}$ a much

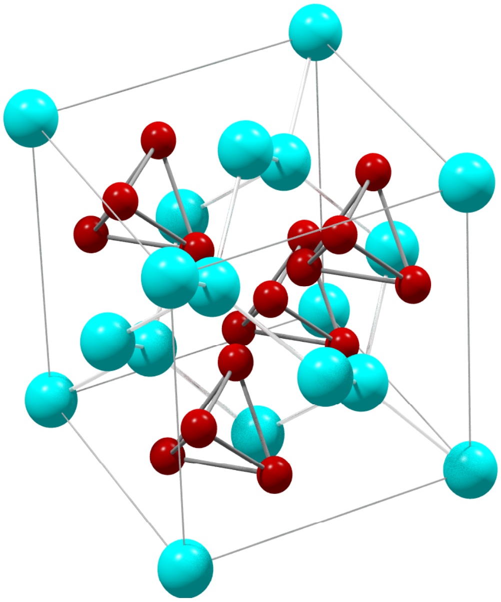

Figure 1.8: RFe_2 crystal structure. Bright: rare-earth metal, dark: iron.

smaller magnetostriction than $TbFe_2$ [8]. The coupling between the iron and the rare-earth moments in $TbFe_2$ and $DyFe_2$ is ferrimagnetic, but no compensation temperature exists. This is due to a relatively strong R-Fe coupling of 300 T, which is not negligible with respect to the dominating Fe-Fe interaction [58, 59]. In $TbFe_2$ the easy axis of magnetization directs along <111>, while for $DyFe_2$ the easy axes of magnetization are <100> [60]. In both systems the $\lambda^{\epsilon,2}$ component ($\approx \lambda_{111}$) exceeds the $\lambda^{\gamma,2}$ component ($\approx \lambda_{100}$) by two orders of magnitude [8]. For bulk samples $TbFe_2$ and $DyFe_2$ the easy magnetization direction does not depend on temperature. The magneto-crystalline anisotropy is with 10^7 ergs/cm^3 rather large in both systems, in spite of the ($\bar{4}3m$) point symmetry at the lanthanide site [9].

The temperature dependence of the λ_{111} magnetostriction coefficient of $TbFe_2$ can be described by a single-ion model. A monotonous decrease from $\lambda_{111}^{TbFe_2}(4.2\text{ K}) = 4.4{\cdot}10^{-3}$ to $\lambda_{111}^{TbFe_2}(300\text{ K}) = 2.46{\cdot}10^{-3}$ can be observed. On the other hand, λ_{100}(T) is small for $DyFe_2$ and cannot be fit by a simple single-ion function. Having a negative value of -74.5$\cdot 10^{-6}$ at 4.2 K, it shows a minimum at about 100 K and a zero-crossing at 280 K.

Due to the opposite signs of the magneto-crystalline anisotropy constant K_1 in $TbFe_2$ and $DyFe_2$ it is possible to reduce the large magnetocrystalline

measurement	**DyFe$_2$**	**TbFe$_2$**	**Tb$_{0.3}$Dy$_{0.7}$Fe$_2$**
λ_s amorphous	38 $\cdot 10^{-6}$	308 $\cdot 10^{-6}$	xx
λ_s polycrystalline	433 $\cdot 10^{-6}$	1753 $\cdot 10^{-6}$	1068
$\lambda_\parallel$ - $\lambda_\perp$ single crystal	610 $\cdot 10^{-6}$	2600 $\cdot 10^{-6}$	1600 $\cdot 10^{-6}$
λ_{111} (s.c)	1260 $\cdot 10^{-6}$	2460 $\cdot 10^{-6}$	1600 $\cdot 10^{-6}$
K$_1$	-7.6 $\cdot 10^{-6}$ J/m^3	2.1 $\cdot 10^{-6}$ J/m^3	-0.06 $\cdot 10^{-6}$ J/m^3
M (300K)	810 emu/cm^3	800 emu/cm^3	800 emu/cm^3
T$_C$	635K	697K	650K
a	7.325Å	7.347Å	7.331Å

Table 1.2: Material constants of DyFe$_2$, TbFe$_2$, and Tb$_{0.3}$Dy$_{0.7}$Fe$_2$ bulks. Data taken from [8, 9, 63, 64, 65].

anisotropy of the RFe$_2$ compounds by still maintaining their large magnetostriction values. In the substitution series Tb$_x$Dy$_{1-x}$Fe$_2$ the pseudo-ternary compound Tb$_{0.27}$Dy$_{0.73}$Fe$_2$ shows the largest magnetostriction of $\lambda_{111} \approx 1600 \cdot 10^{-6}$ with an anisotropy compensation at 300 K [61]. In contrast to the binary compounds the magnetic temperature dependence of Tb$_x$Dy$_{1-x}$Fe$_2$ compound is much more complicated due to spin reorientation processes.

An atomistic model for the magnetostriction of C15 Laves phase compounds was proposed by Cullen and Clark [62]. In this model, potentially large values of λ_{100}, arising from the asymmetry of the rare earth 4f electron shell, are effectively shorted out because of the tetrahedral ($\bar{4}$3m) symmetry at the rare earth sites. On the other hand, a large λ_{111} coefficient is allowed because two inequivalent tetrahedral sides exist in the C15 structure which permit internal distortions along <111>. This internal distortion lowers the symmetry and drives an rhombohedral distortion.

The material constants of DyFe$_2$, TbFe$_2$, and Tb$_{0.3}$Dy$_{0.7}$Fe$_2$ bulk materials are listed in Table 1.2.

Single crystals of TbFe$_2$ and DyFe$_2$ can be prepared by Bridgman, Czochralski and zone melting methods [8, 66]. Most applied material is the ternary compound Tb$_{0.27}$Dy$_{0.73}$Fe$_2$ (called Terfenol-D for: TERbium, FE, NOL for Naval Ordinance Labs, and D for Dy) with vanishing magneto-crystalline anisotropy at room temperature. Here, even at low fields of 100kA/m, large changes in the magnetostriction dλ/dH occur (burst-effect) [67]. Up to now, Terfenol-D has been applied to many devices when large forces at high efficiencies and high power levels are necessary. In particular, it is very favorable if electrical energy has to be converted into mechanical motion, and vice versa. Terfenol-D is commercially available and has an appreciable amount of applications: Sonar, active vibration control [4, 68], actuators, sensors, motors, ultrasonic applications [69], fuel injection systems, fluid and valve control, powerful oscillators and sound receiver [70, 71]. Bulk actuators designed with the Terfenol-D alloy consist usually of rods, a few centimeters long, submitted to a bias magnetic field and a driving field created by a solenoid [72].

Most of the work on nanocrystalline bulk TbDyFe materials deals with rapidly quenched ribbons [73]. Some authors prepared amorphous TbDyFe ribbons with additional 5-8% B. The best results were obtained with a coercive field of $\mu_0 H_S$=20 mT and a magnetostriction $\lambda \approx 400 \cdot 10^{-6}$ at an applied field of $\mu_0 H_{ext}$=1.0 T using the composition $(Tb_{0.3}Dy_{0.7})_{0.3}Fe_{0.62}B_{0.08}$ [74].

Now, there is a growing trend towards the development of smaller active systems. There is a need for powerful transducer materials in thin film form to provide the active actuator elements in micro-systems such as miniature switches, micro-pumps and valves. Thin Terfenol-D films are therefore discussed as possible compounds for applications such as nano-actuators - umbrella term microelectromechanical systems (MEMS) -, nano-sensors or surface acoustic wave (SAW) delay lines [5, 6, 7].

Different methods have been employed to prepare thin giant magnetostrictive RFe_2 films (here R = Tb, Dy, and $Tb_{0.3}Dy_{0.7}$):

1.) Sputtering of amorphous films [75, 76, 77, 78, 79, 80, 81, 82, 83, 84, 85, 86, 87]

2.) Sputtering and annealing with addition of further metals [88, 89, 90]

3.) Sputtering and annealing of multilayers with addition of further metals, evaporation of amorphous films [91, 92]

4.) Flash-evaporation [93]

5.) Pulsed Laser Deposition (PLD): amorphous films [94], epitaxial (111)-oriented films [95, 96]

6.) Molecular Beam Epitaxy (MBE)

By means of MBE different crystalline orientations were prepared:

- epitaxial (110)-oriented films [10, 43, 45, 97, 98, 99]
- epitaxial (111)-oriented films [12, 98]

The main aim of preparing amorphous films is the reduction of the magneto-crystalline anisotropy. The hope is to obtain still large magnetoelastic responses of the systems at low magnetic fields and vanishing coercive fields. Until now, amorphous films did not show large magnetoelastic values comparable to bulk magnetostrictions. Figure 1.9 shows the magnetostrictive response of a composition series of amorphous $\mathrm{Tb}_x\mathrm{Fe}_{1-x}$ films. The largest values of $\lambda \approx 400{\cdot}10^{-6}$ with fields up to 1 T are obtained for the composition $\mathrm{Tb}_{0.42}\mathrm{Fe}_{0.58}$.

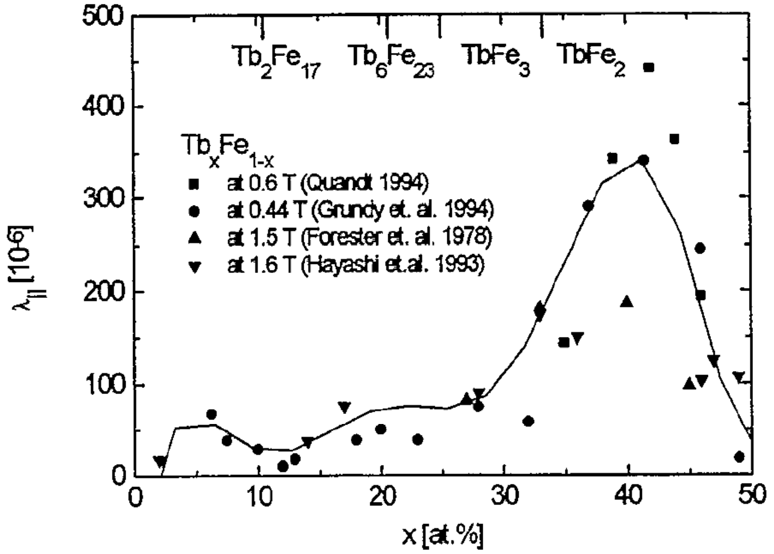

Figure 1.9: Magnetostriction as a function of composition of amorphous $\mathrm{Tb}_x\mathrm{Fe}_{1-x}$. Data taken from [75, 91, 83, 77]. Published in [84].

In sputtered $\mathrm{Tb}_x\mathrm{Fe}_{1-x}$ films the easy axis of magnetization depends on the Tb-Fe ratio: For x < 0.1 the easy direction is in-plane and the films are partially crystalline. Between 0.12 < x < 0.40 the films are amorphous and exhibit the well known magnetization compensation effect with room temperature compensation (RTC) at about x = 0.22. The low value of magnetization and the presence of a strong, induced perpendicular anisotropy results in an easy magnetization normal to the film plane. For x > 0.35 the easy direction varies for different films. Above x = 0.48 T_C sinks below 25 K. Thin sputtered $\mathrm{Dy}_x\mathrm{Fe}_{1-x}$ film series show a similar behavior with the Dy to Fe ratio [79].

One main disadvantage of amorphous and polycrystalline RFe_2 films is the comparably low Curie temperature of $T_C \leq 400$ K. The main advantage of amorphous films is their reduced magnetic anisotropy [100]. One successful optimization approach for applying magnetostrictive thin films is to increase the total rare-earth content and to alloy different rare earths to compensate the anisotropy

[83, 85]. The sign and the magnitude of the film's strrain can be controlled by the preparation conditions, the thermal expansion coefficient of the substrate, or by stress annealing [82, 101].

First applications of RFe_2 films were published by Honda et al and by Quandt [76, 84]. Honda et al coated both sides of a thin polymide substrate with amorphous $TbFe_2$ and $SmFe_2$, respectively. Having two materials with opposite sign of the magnetoelastic response, they observed a 300 μm bending of the 3 mm long bimorph at fields of 300 Oe. With the same preparation method they were able to build a travelling machine operating in an alternating magnetic field [76]. With $TbFe_2$ and $SmFe_2$ coated substrates Quandt was able to build magnetostrictive membrane pumps and a magnetostrictive linear ultrasonic motor [84].

1.3 Assembly of magnetoelasticity measurement setup

Within the scope of this thesis a magnetoelasticity measurement setup was designed and built. As already explained before, the magnetoelastic strains of a ferromagnetic film in an external magnetic field can be determined by the bending of a clamped film-substrate bimorph. In the literature, mainly two different measurement setups are described: In a capacitive setup, the film is used as one capacitor plate and the bending of the film is determined by the change of the capacitance of the system [47, 102, 103]. Using a highly sensitive capacitance technique combined with lock-in-assisted signal detection, substrate deflections of a few nanometers can be detected [50]. The advantage of this setup is its applicability in a ^{4}He cryostat for low temperature measurements in high magnetic fields. In the optical setup, on the other hand, a laser beam is reflected at the end of the cantilever and is detected in a position sensitive photodiode [104, 105]. Depending on the curvature of the cantilever, the position of the laser spot on the photodiode changes. By this method the bending due to monolayer stresses during the film growth can also be detected [106]. The main advantage of an optical deflection setup is that it is a sensitive and simple technique. Furthermore, an optical setup to determine the magnetoelastic properties of a sample can easily be adapted to other optical measurement methods like magneto-optical Kerr rotation (MOKE).

Therefore, an optical deflection measurement setup was designed in this work.

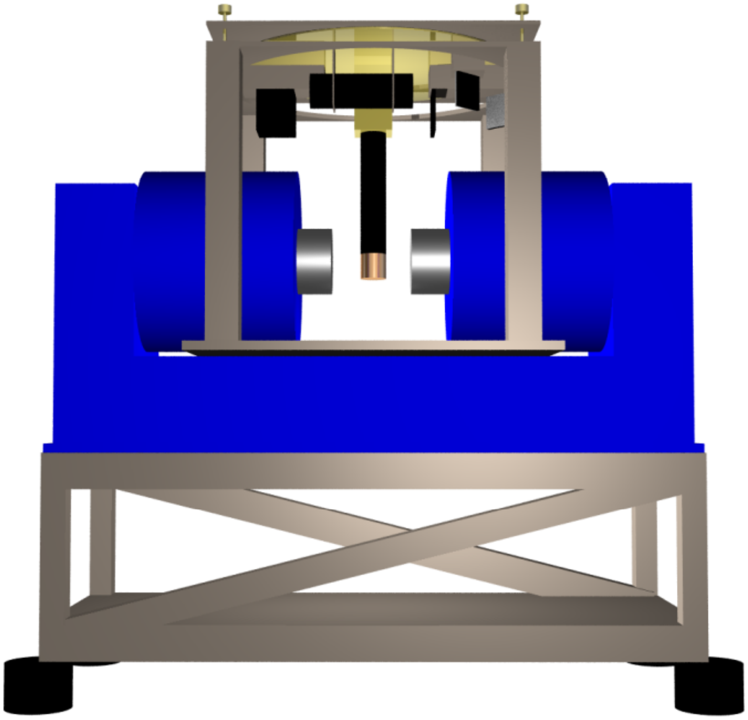

Figure 1.10: Schematic drawing of the magnetoelasticity measurement assembly.

A schematic drawing of the complete assembly is shown in Figure 1.10. The magnetic field was generated by an electromagnet with a maximum field of 1.07 T. To avoid a spurious response of the setup due to magnetic stray fields, the complete assembly was designed of aluminum, brass and oxygen free high purity copper (OFHC). For noise reduction the setup was mounted on the heavy electro magnet which was furthermore damped by air cushions. An aluminum frame was fixed to the magnet, carrying the 480 x 480 mm^2 aluminum base plate of the optical setup. On top of the base plate a square of the same size was mounted, allowing to level the optical setup. On this plate a 45 cm diameter disk was attached, containing a mesh of screw holes to arrange the optical components. The disk was rotatable with a scaling.

Figure 1.11 shows a photograph and a schematic of the optical setup. As light source a 630 nm diode laser was used. The laser beam was guided by two mirrors onto the optical path and focussed by a lens with a focal length of 1000 mm, yielding the focuss in the split photodiode. A mirror tilted by 45° to the normal plane reflected the beam onto the cantilever. This mirror, and the second 45° mirror guiding the reflected beam onto the photodiode, were relocatable and tilt-

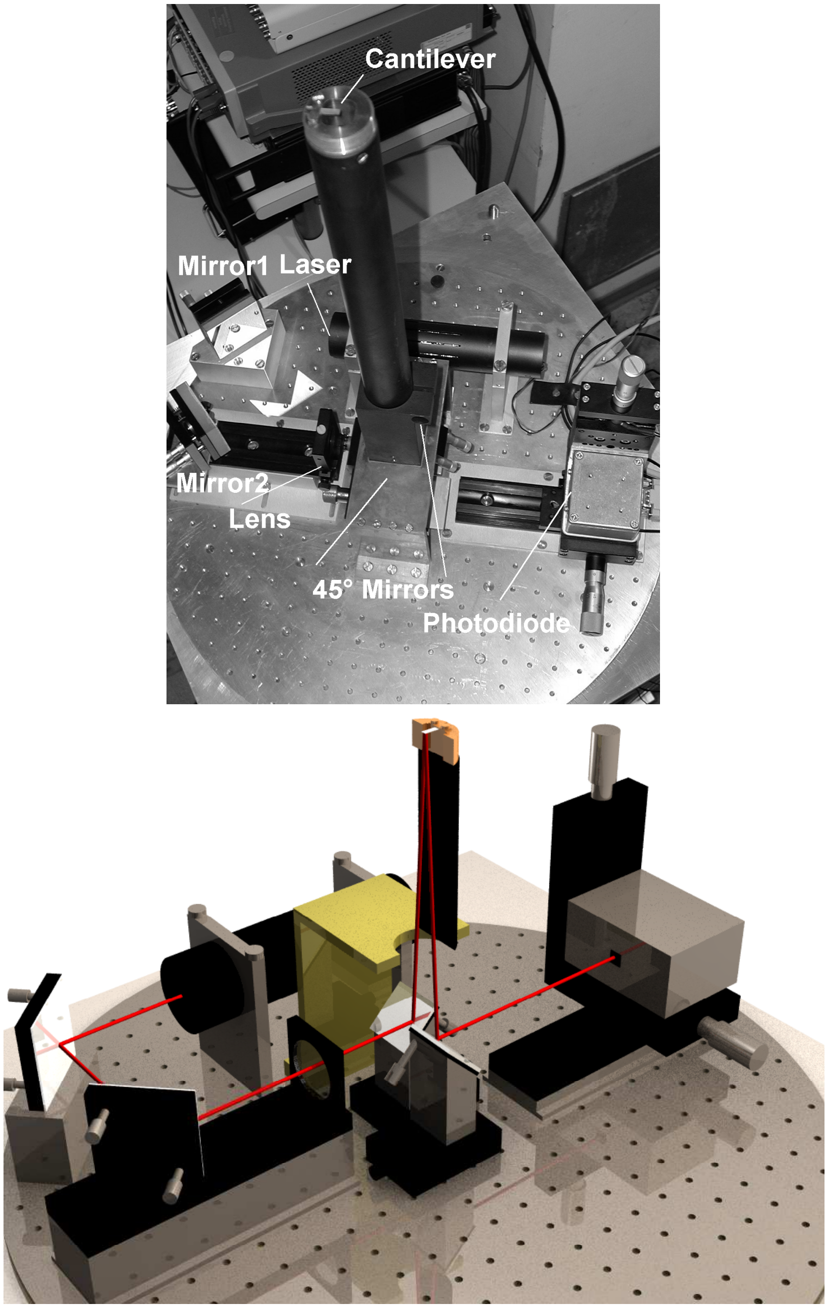

Figure 1.11: Photograph and schematic of the magnetoelasticity measurement setup.

ing to adjust the beam path. Being reflected by the first 45° mirror, the beam was guided through a 325 mm long 33 mm diameter anodized brass tube. On top of the tube the measuring head was fixed. The tube and the measuring head were designed for multiple applications like magnetoelasticity measurements in- and out of the sample plane, magneto-optical Kerr measurements in different orientations, and furthermore subsequent extensions of these optical measurements to low sample temperatures. To reduce any magnetostrictive response of the setup, the measuring head for the magnetostriction measurements was made of non-magnetic OFHC copper. The cantilever was fixed along its short side at a distance of 0.5 mm by a copper sheet plate in a milled guiding. The complete measuring platform was light-and-sound insulated by a screwed cap. Further sound insulation was performed by an aluminum box, which was covered inside with sound-damping foam and was put over the complete setup.

The photodiode was a four-times-split Si diode in a plastic case with a total active area of 1.5 x 2 mm^2 and a horizontal & vertical gap of 15 μm each (Hamamatsu S6242). A first amplification of the single element signals was performed close to the photodiode. The signals were then passed via a screened cable to the main amplifier. The main amplifier did not only handoff the individual diode signals, but also provided the sum of all adjacent elements and their total sum. The amplified signals were fed into an analogue-digital converter (ADC) (BMC Messsysteme PC20TR) attached to the computer. Here, the signals were processed by a self designed C++[5] respectively HP-Vee program.

To fine-adjust the beam position and to calibrate the signal, the photodiode box was mounted on an xy-relocatable system. This consisted of two optical tables which could be moved by either piezoelectric transducers or more coarsely by micrometer screws. By means of a digital-analogue conversion supplied by the ADC/DAC-card, the piezoelectric transducers were able to move the photodiode in a 25 x 25 μm^2 square, yielding a calibration of the position sensitivity of the photodiode. During a magnetostriction measurement the position of the photodiode stayed fixed, and the signal of the photodiode was recorded in dependence of the magnetic field.

The deflection angle γ of the cantilever is given by the displacement Δx of the Laser beam on the photodiode and the length S of the optical path from the cantilever to the photodiode:

---

[5] Courtesy by M. Huth

$$\gamma = \frac{1}{2} arcsin \left(\frac{\Delta x}{S} \right) \tag{1.25}$$

In the setup described above, the optical path amounted to 550 mm.

A magnetoelastic measurement was performed in the following way: First, the cantilever was fixed with the short end at the measurement head. Then, the laser beam was adjusted on the cantilever. One main problem during the performance of the experiment was the exact determination of the laser spot position on the cantilever. Due to stray effects on the edge, the spot could not be set to the end of the cantilever. With a laser spot diameter of 1 mm, a positioning uncertainty of 1 mm has to be assumed. This leads to an error of 6% in the determination of the magnetoelastic coefficient. After the alignment of the laser, a calibration of the photodiode signal was performed by moving the piezoelectric tables in a pre-defined square and recording the position signal of the laser spot. The magnetoelastic response depended strongly on the magnetic history of the sample, which was already discussed before. One possibility to circumvent this problem was to measure the bending of the bimorph parallel and perpendicular to the cantilever's long axis with a previous magnetization of the sample along the short axis orientation.

To calculate the magnetoelastic coupling factor b (or B) and the magnetostriction coefficient λ from the bending of the cantilever according to Equations (4.1) and (1.19) the following parameters were choosen:

- effective substrate Young's module $Y_S^{eff} = Y_S/(1+\nu_S)$ for sapphire [107]:
  - Y^{eff} = 388 GPa for the direction parallel to the c-axis.
  - Y^{eff} = 370 GPa for the direction perpendicular to the c-axis.
- effective length of the cantilever, laser beam position on the cantilever: L = 8 mm
- substrate thickness: t_S = 0.5 mm
- for the effective thin film Young's module $Y_F^{eff} = Y_F/(1+\nu_F)$ of RFe_2 the elastic values of bulk Terfenol-D can be calculated to [8]: Y^{eff} = 64 GPa

The magnetoelasticity measurement setup was calibrated by a nickel film and a platinum film, both deposited by means of magnetron sputtering in argon on sapphire a-plane substrates. For thin Ni films a magnetostriction of $\lambda = -37 \cdot 10^{-6}$

was observed which is in good agreement with the bulk values. The non-magnetic platinum film was used to detect a possible magnetostrictive response of the measurement setup. The response of the setup was about ten times smaller than that for the nickel films. For the magneto-elastic numbers of the RFe_2 films measured in this work this effect is negligible.

1.4 Preparation method: Molecular Beam Epitaxy

1.4.1 The MBE preparation chamber

In the scope of this thesis a previously installed MBE system was employed. The MBE system is a custom-designed multi-chamber system manufactured by Omicron Vacuum Physics. The system consists of four connected UHV chambers, separated by gate valves. These four chambers are the load-lock chamber, the central distribution (R2P2) chamber, the analysis chamber and the MBE chamber. Three of these chambers have a heating stage. These stages share a common construction principle: The samples can either be heated by direct heating of a special sample holder or by radiation heating of the standard molybdenum or stainless steel sample holder. By radiation heating, which was solely used in this work, a pyrolytic graphite plate, isolated by a BN coating, is heated by electric currents of up to 2.2 A. This allowed maximum sample temperatures of 850°C. The temperature calibration was performed by means of an optical pyrometer.

The load-lock chamber contains a carousel for six sample holders. It is pumped by a roughing pump and a turbo molecular pump. Its base pressure is $\cdot 10^{-9}$ mbar. To anneal samples and to remove the solvent of the conducting silver which was used to attach the substrates to the sample plates, a heating stage was attached. To change the position of the heater an additional xyz manipulator was designed[6]. In the central distribution R2P2 chamber the sample holders can be transferred in up to eight different chambers. In stationary state it is pumped by an ion getter pump and a titanium sublimation pump. This leads to a base pressure of $5 \cdot 10^{-11}$ mbar. The analysis chamber mainly consists of the variable temperature scanning tunneling microscope (STM) manufactured by Omicron. It is pumped by a roughing pump, a turbo molecular pump, an ion getter pump and a titanium

---

[6] Courtesy by M. Huth

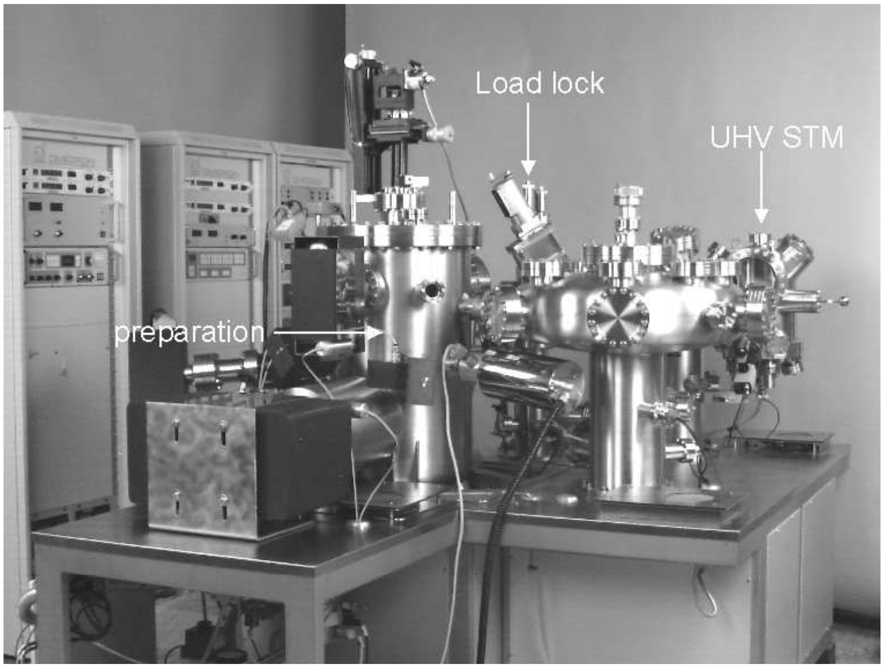

Figure 1.12: Photo of the preparation system.

sublimation pump. The base pressure of the analysis chamber is $5{\cdot}10^{-12}$ mbar. To pick up the transferred sample holder and to anneal the samples, a heating stage is attached. The STM is vibration-damped by springs and a magnetic eddy current system. The exchange of the tunneling tips can be performed in situ via tip carriers which can be loaded and transferred like usual sample holders. The STM can optionally be operated with the direct heating platform, heating the samples up to 400°C.

The main chamber of the system is the MBE preparation chamber. It is pumped by a roughing pump, a turbo molecular pump, two ion getter pumps and a titanium sublimation pump. This lead to a base pressure of $5{\cdot}10^{-11}$ mbar. During the preparation processes reported here, the pressure did not exceed 10^{-8} mbar. In addition to the conventional pumping system, a copper cooling shroud is suspended inside the chamber. This shroud serves two proposes: On the one hand, it operates as a cryo-shield for residual gas pumping. On the other hand, it devides the MBE chamber into an analysis part and a preparation part. The analysis part contains a LEED and Auger system. The preparation part is equipped with a four-crucible electron beam evaporator and up to 8 effusion cells. Three effusion cells were used in this work. The sample manipulator has five degrees of freedom: linear up and down, x-y position, polar 0° to 360°

and inclination up to 90° from the horizontal position. The sample platform can be protected from the evaporation sources by an automatic shutter. An other automatic shutter is attached to separate the preparation part from the analysis part of the chamber. During the deposition the crystal growth of the films can be monitored by a RHEED system (Staib-Instrumente NEK-2035-R). To control the rate of the evaporated materials, a Hiden (HAL/3F 301) cross beam quadrupole mass spectromter operated up to 300 amu. The quadrupol spectromter was used to steer the rate controller of the electron beam evaporator. Up to eight different masses, expressed in partial pressures, in individual pressure ranges can be monitored simultaneously. Via leakage function it can also be used for leakage detection.

1.4.2 The MBE preparation process

The source materials were purchased from Alfa Aesa company. The purity of the 3d transition metals amounted to 99.95% while the rare earth metals had an impurity of 99.9%. The sapphire substrates were purchased from Crystec Kristalltechnologie (Berlin). They were delivered as an crystallographic oriented wafer with the substrates already cut to 10mm×10mm pieces. The miscut was determined by X-ray diffraction in the four-circle X-ray diffractomter for one reference substrate. It amounted typically to less than 0.5°. Most of these substrates were cut again with a diamond-coated wire saw to 5mm×3mm and 10mm×3mm pieces, respectively. This was done, firstly, for economical reasons, secondly, because the crystallographic orientation of the substrate and film could be determined more easily during the characterizations, and thirdly to obtain samples of appropriate size for magnetoelastic measurements. Before deposition, the substrates were cleaned in an ultrasonic bath by several steps: Firstly, the protective polymeric film from the manufacturer and the glue used for the sawing was dissolved by acetone and isopropanol. Then the substrates were cleaned in a soap sud, and afterwards cleaned from the soap sud with distilled water. Finally, the substrates were again cleaned by acetone an isopropanol. The substrates were attached with silver paint on the Omicron sample holder. After installation, the sample holders were heated in the load lock chamber to 600°C in order to remove the solvent of the silver paint.

The evaporation of the rare earth metals was done from effusion cells. The temperature ramps for heating and cooling the cells were driven by a home made

PC based HP-Vee program which controlled and monitored via RS232 interfaces Eurotherm temperature controllers. Dysprosium was evaporated out of a Varian standard effusion cell with an alumina liner. To enable the preparation of a buffer layer during heated effusion cell, a separate shutter for the Dy cell was designed. During preparation, the Dy cell temperature was kept at 1130°C for pure $DyFe_2$ films, leading to a Dy deposition rate of 0.21Å/s. For the preparation of $Tb_{0.3}Dy_{0.7}Fe_2$ films the Dy cell temperature was kept at 1107°C, leading to a Dy rate of 0.15Å/s. Terbium was evaporated out of a high-temperature effusion cell with a tantalum liner. Two different high-temperature cells for Tb evaporation were used in this work. A MBE-Komponenten HTEZ-40 cell was used first. Tb was evaporated mainly out of a VTS-Createc cell. During the preparation of $TbFe_2$ films the temperature of the VTS Createc cell was kept at 1450°C, resulting in a Tb deposition rate of 0.21Å/s. For $Tb_{0.3}Dy_{0.7}Fe_2$ films the Tb cell temperature was set to 1390°C, giving a Tb deposition rate of 0.06Å/s. The deposition rates of the rare earth materials were determined by approximately 50 calibration films. Hereby, a pure element film was deposited onto a flat sapphire substrate held at a temperature of 100°C. Subsequently the film thickness was determined by small angle X-ray diffraction. Due to the high stability, the rare earth rate was accurately fixed by the cell's temperature.

Iron, molybdenum and niobium were evaporated out of a Caburn-MDC EV-FMP-10RUHV electron beam evaporator. The electron beam evaporator consists of four copper crucible pockets which can be rotated into evaporation position, so only one element can be evaporated at any one time. For Nb a Cu liner and for Mo a Mo liner was used. Fe was evaporated liner-free. Again, the deposition rate for the metals evaporated by the electron beam evaporator were determined by calibration films. Hereby, the deposition rate was correlated with the evaporator's emission current and the partial pressure measured by the quadrupole mass spectrometer. During the preparation process the deposition rate of the 3d elements was controlled by the quadrupole mass spectrometer. This was connected to a Eurotherm control, which displayed the first value of the quadrupole's table list. In a remote control option the Eurotherm controlled the current source of the electron beam evaporator to stabilize to the given quadrupole value. The acceleration voltage of the electron beam was held fixed at -9 kV. Prior to each preparation the evaporant was pre-melted for obtaining a well-defined surface. For the buffer layer preparation, Nb and Mo were deposited with a rate of 0.3Å/s. The emission current for this rate amounted to approximately 190 mA for Mo and 200 mA for Nb, respectively. Due to the high evaporation temperatures of Mo and Nb, the brightness of the material during the preparation process prevented RHEED studies during growth. Fe was deposited at rates of 0.13Å/s, both for RFe_2 films and for Fe nanostructures. The emission current for such a rate amounted to 14 mA. To enable RHEED observations during the preparation process, which were performed at an acceleration voltage of 15 kV, the evaporator's magnetically-induced spacial oscillation of the emitted electron beam was deactivated.

1.5 Crystallographic characterization by X-ray diffraction

The crystallographic properties of the films were determined by X-ray diffraction. With a two-circle diffractometer and a four-circle diffractometer, two different setups for different applications were used. The two-circle diffractometer was used for the standard characterization of the films. The four-circle diffractomter was used for the detailed studies of the epitaxy of selected films. The measurement procedures used in these two setups are described in the following.

In the Phillips (X'Pert-MPD) two-circle X-ray diffractometer the samples are measured in Bragg-Brentano geometry employing Cu-K_α radiation. In this geometry, only reciprocal lattice points along the substrates normal are observed. In an $(\omega/2\theta)$-scan the incident angle ω and detector angle 2θ are varied simultaneously. Reflections occur according to Bragg's law

$$\sin\alpha = \frac{n \cdot \lambda}{2 \cdot d} \tag{1.26}$$

at an angle α given by the wavelength λ of the radiation, and the distance d between successive lattice planes. The occurrence and intensity of the peaks provides information of the growth orientation and quality of the films. In an ω-scan, the detector is fixed at the angle 2θ of the observed reflection, while the incident angle is about the position ω=$2\theta/2$. Hence, a tilt spectrum of the perpendicular oriented planes with inter-lattice spacing d is taken. The width (FWHM) of the so-called rocking curve gives a measure for the quality of the film growth. The film thickness can be determined by performing an $(\omega/2\theta)$-scan at low 2θ angles of about 0.3° to 10°. Hereby, the influence of a small deviance δ

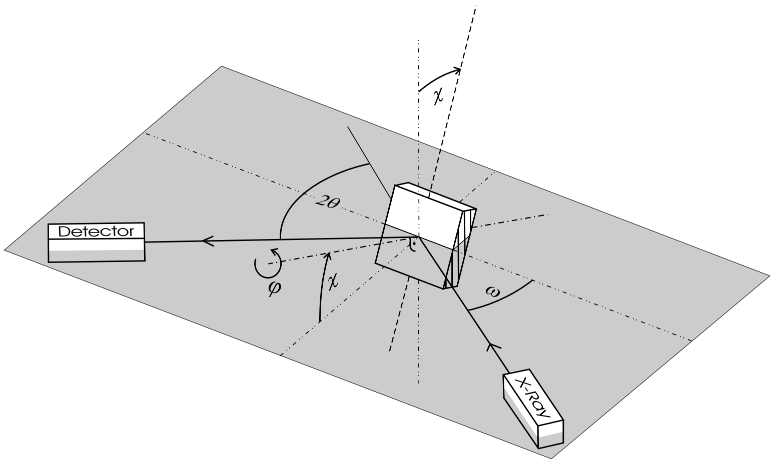

Figure 1.13: Schematic of the operating angles of a four-circle diffractometer.

($\mathrm{Re}(\delta)\propto 10^{-6}$) of the film's diffraction index with regard to air and the substrate causes a modification of the Bragg equation 1.26 to

$$\sin\alpha = \left(\frac{n\cdot\lambda}{2\cdot\Lambda}\right)^2 + 2\delta \tag{1.27}$$

where Λ is the layer thickness. Plotting the detected intensity against 2θ, a steep function with oscillating flank results. From the periodicity and numbers of the oscillations the film thickness and roughness can be deduced.

For an acquisition of film reflections with in-plane components the utilization of a four-circle geometry is necessary. The employed four-circle diffractometer has a rotating Cu anode manufactured by Nonius and a goniometer from Stoe in Eulerian cradle configuration. The four independent angles are ω, θ, χ and φ, see Figure 1.13. A beam focussing osmic setup was used which limited the goniometer's maximum ω position to $\pm 40°$. Hence, the range of detectable film reflections was strongly limited. In particular, the bcc transition metals Fe, Mo and Nb the observable range was limited to the $\{110\}$, $\{200\}$ and $\{211\}$ reflections.

The four-circle diffractometer was used to determine the in-plane lattice parameters of the deposited films. The position of two independent reflections with respect to the goniometer's coordinate system had to be determined in order to calculate the orientation matrix of the crystal. This was done by the software Stadi 4. By using the 3×3 orientation matrix, the position of all other reflections and the lattice parameters of the crystal were calculated. The orientation matrix was refined by centering on various other calculated reflections.

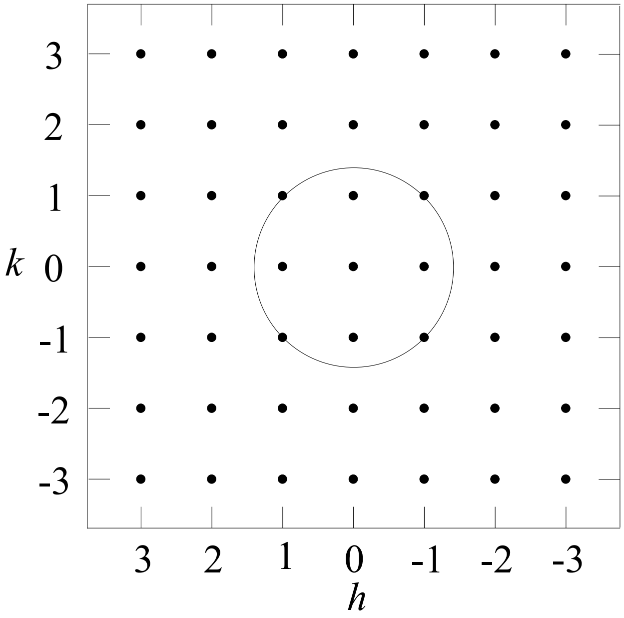

Figure 1.14: Schematic of a φ-scan in a cubic lattice. Sector of a plane with constant Miller index l. Rotating the sample around the substrate normal with fixed momentum transfer $|\vec{q}|$, the intersections of this circle with the reciprocal lattice points create a reflection.

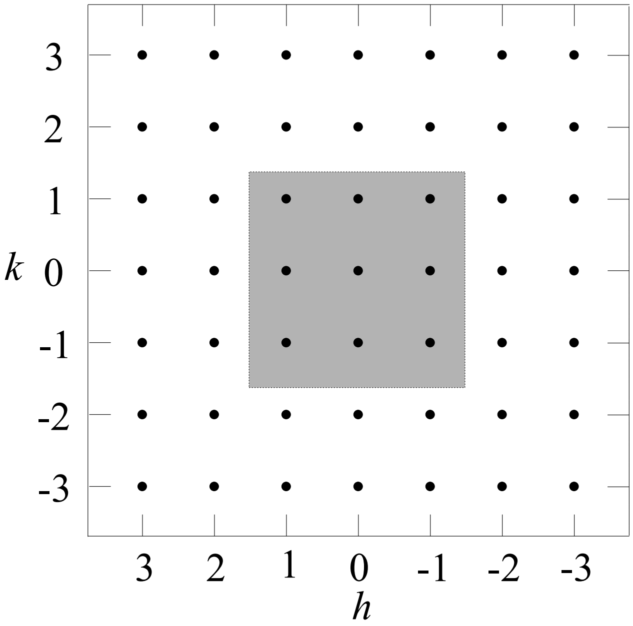

Figure 1.15: Schematic of a Q-scan in a cubic lattice. Sector of a plane with constant Miller index l. In this example all points in the plane segment are scanned.

Furthermore, the in-plane orientation of the films with respect to the substrate or buffer layer was determined via X-ray diffraction in the four-circle diffractomter. In a φ-scan the sample is rotated around the substrate normal at constant momentum transfer $|\vec{q}|$ with $\vec{q}$ describes a circle in reciprocal space. The intersections of this circle with the points of the reciprocal lattice causes reflection peaks to occur at the according φ angles, see Figure 1.14.

In a Q-scan a planar sector of reciprocal space is scanned. Hereby, $\vec{q}$ is varied and all points of the reciprocal lattice lying in this reciprocal space segment occur as reflections, see Figure 1.15.

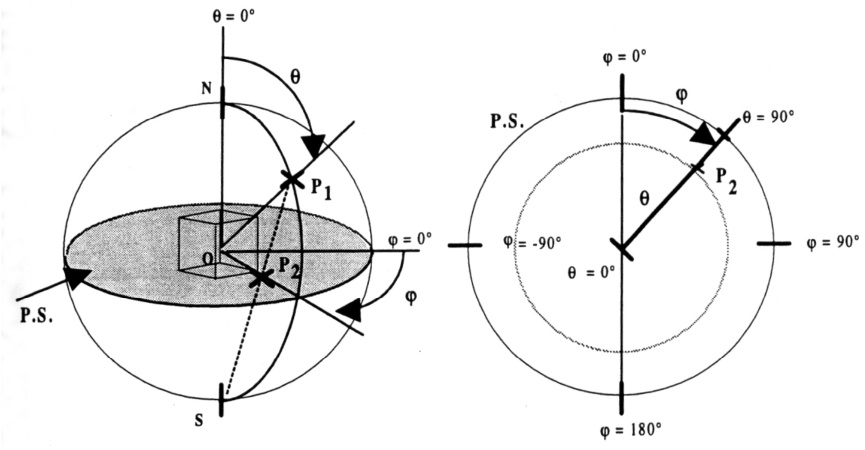

Figure 1.16: Method of stereographic projection. Explanation see text.

The position and order of reflections of a crystal of given orientation can be visualized by a stereographic projection, see Figure 1.16. The construction goes as following: A sphere is constructed around the crystal's representation in reciprocal space, with the crystal being in the center of the sphere. The orientation of the crystal is such, that the axis of the orientation direction is pointing to the north pole of the sphere. To each reflection of order (hkl) a pole P(χ, φ) can be determined. This is given by the intersection of the reflection direction with the sphere. The projection of this pole P to the equatorial plane is given by the intersection of the line $\bar{P}S$ from the pole to the south pole S. The polar and radial position of the points on this equatorial plane therefore represent the φ and χ values of the individual reflection directions in the oriented crystal. The χ and φ values correspond directly to the χ and φ angles of the four-circle diffractometer.

Chapter 2

Thin transition metal films on sapphire m-plane

Body centered cubic transition metals show a wide range of properties and applications. Due to their high melting point and low reactivity, the refractory metals Nb and Mo are suited as templates for the growth of other systems, like for instance the highly magnetostrictive C15 laves phases of the rare earth iron compounds, discussed in chapter 3. Additionally, Nb reveals an unique three dimensional epitaxial relationship with sapphire, as already mentioned in chapter 1. Furthermore, thin Nb films are type II superconductors with a critical temperature T_C of 9 K. The ferromagnetic properties of Fe, on the other hand, are widely utilized in applications and fundamental research.

Therefore, the growth of the bcc metals Fe, Mo, and Nb on faceted and non-faceted sapphire m-plane substrates was studied. For characterization, a first in-situ analysis of the films was performed by RHEED. The morphological properties of the films were explored by UHV scanning tunnelling microscopy (STM), atomic force microscopy (AFM) and scanning electron microscopy (SEM). The crystallographic studies were mainly performed by X-ray analysis in the four-circle diffractometer. A transmission electron microscopy (TEM) measurement of a Mo film deposited on faceted sapphire m-plane augments the analysis. In addition to the characterization of the crystal properties, electric and magnetic measurements were performed at the faceted and non-faceted films.

Following the idea of K. A. Ritley[1], the feasibility of preparing metallic nanowires by utilizing the self shadowing effect of sapphire facets was explored. There-

---

[1] private communication

fore, Nb was deposited under shallow incidence onto faceted m-plane sapphire substrates. SEM, AFM and optical methods were used to characterize the morphological properties of these samples.

In this chapter, the preparation and the properties of thin films of Fe, Nb, and Mo deposited on faceted and non-faceted sapphire m-plane are described. Firstly, thin films of Nb and Mo are discussed. Secondly, the crystallographic properties of Fe films on sapphire m-plane are introduced. Subsequently, first applications of faceted Nb films are introduced. In the last part of this chapter, the preparation and first measurements on Nb nano-wires will be discussed.

2.1 Morphology of Nb and Mo on faceted sapphire

Nb and Mo were deposited under normal incidence on faceted Al_2O_3 m-plane substrates held at elevated temperatures of 850°C. The metals were evaporated out of the electron beam evaporator, and their deposition rate of 0.3Å/sec was controlled by the quadrupole mass spectrometer. Prior to deposition, RHEED images of the faceted sapphire m-plane substrate were taken, shown in Figure 2.1.

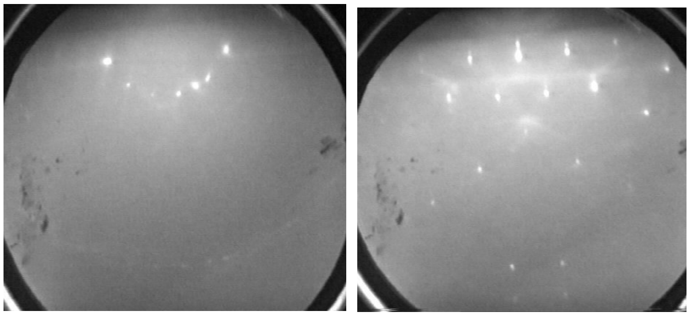

Figure 2.1: RHEED images of faceted sapphire m-plane substrates. Left: Beam $\parallel [010]_{Al_2O_3}$. Right: Beam $\parallel [001]_{Al_2O_3}$.

Due to the high evaporation temperatures, the glow of the transition metal melt outshone the diffraction pattern on the RHEED screen. Accordingly, a first RHEED impression of the crystal quality of the films could only be gained after deposition. The RHEED patterns of Nb and Mo thin films on faceted sapphire m-plane, shown in Figure 2.2, indicate crystalline growth. Due to the low incident angle, the electron beam of a RHEED analysis is solely sensitive to the crystal quality of the upper atomic layers. Thus, the diffraction pattern is strongly depending on the morphology of the surface. Reflected from a smooth two-dimensional crystal surface, the RHEED pattern consists of stripes. For a rough crystal surface the RHEED pattern consists of points as a consequence of the bulk diffraction in transmission. For the growth of Nb and Mo on faceted sapphire, the patterns reach from bulk-like to tilted stripes, depending on the azimuthal angle of the incident beam. When the electron beam was directed along $[010]_{Al_2O_3}$ and therefore parallel to the facet ridges two tilted rows of RHEED stripes were observed (see left image in Figure 2.2). The tilting angle of the rows is approximately -15° and 23°, respectively, with respect to the direction of the electron beam. These angles correspond well to the sapphire facet angles obtained from the AFM analysis discussed in chapter 1. Slight deviations of the beam from this high-symmetry direction cause one set of reflections to disappear due to partial penetration of the electron beam. The stripe pattern indicate two-dimensional crystal growth on both facet surfaces. When the electron beam is directed along $[001]_{Al_2O_3}$ and therefore perpendicular to the facet ridges, a regular pattern of points was observed, as shown in the right part of Figure 2.2. This is caused by the electron beam penetrating the three-dimensional structure of the undulated crystal films. Similar RHEED pattern were also reported by Sugawara and Mae for NaCl (110) faceted into (100) and (010) surfaces [108].

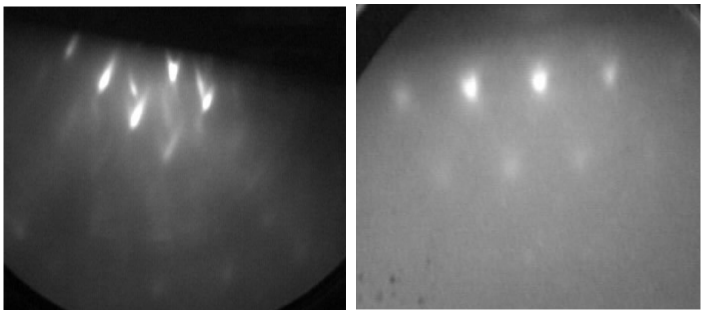

Figure 2.2: RHEED images of Nb and Mo on faceted sapphire m-plane substrates. Left: Faceted Nb, beam $\parallel$ $[010]_{Al_2O_3}$. Right: Faceted Mo, beam $\parallel$ $[001]_{Al_2O_3}$.

STM measurements of faceted Nb films were performed in the UHV STM in constant current mode. The annealing temperature of the substrate, prior to deposition, was 1500°C. Figure 2.3 indicates that the sapphire facets are directly replicated in the 40 nm thick niobium film.

In figure 2.4 a line scan of a faceted Nb film is presented. The shape of the

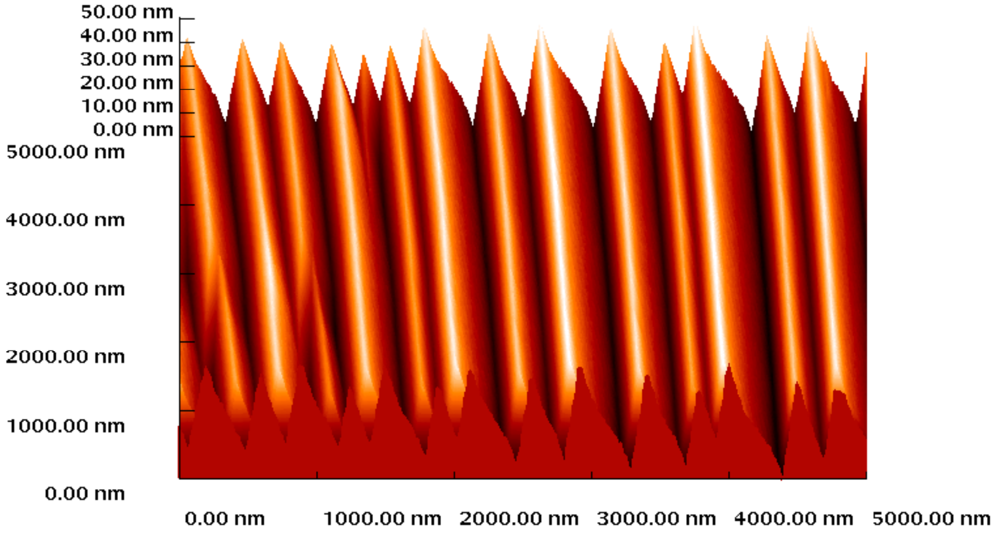

Figure 2.3: STM image of Nb on faceted sapphire. The facets are replicated by the 40 nm thick film.

facets is reproduced from the substrate. Furthermore, the Nb appears to grow rather smooth on the steep facet side (the sapphire $(10\bar{1}\bar{2})$ surface) while a wave like growth can be observed on the flat facet side (the sapphire $(10\bar{1}1)$ surface). The origin of this is not understood yet.

In SEM images the formation of facets can be observed, see left image of Figure 2.5. The contrast between the two facet surfaces is caused by the different emission angles of the secondary electrons on either facet with respect to the detector. The 2d projection of the facet surfaces can be estimated to a length ratio of 2:3. The image also reveals some facet junctions. Next to the fact that the periodicity of faceted structures decreases with increasing facet size D, as discussed in chapter 1, the variation of the width can partly be explained by the junctions: The wider facets occur at regions where the density of junctions is lower, approving the explanations of Heffelfinger et al. that the movement of the junctions is the origin for the coarsening and broadening of the facets [3]. Furthermore, the junctions occur cumulative in some regions, indicating the domain like origin of the facet growth. An analysis of Figure 2.5 gives the average length of the individual facets to be approximately 100μm.

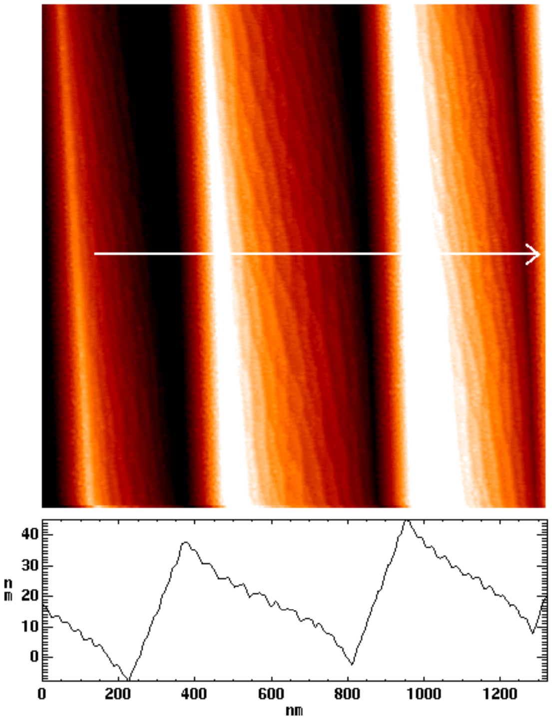

Figure 2.4: STM image and linescan of Nb on faceted sapphire. Nb shows a homogenous overgrowth over the facets and a modulation on the sapphire $(10\bar{1}1)$ facet.

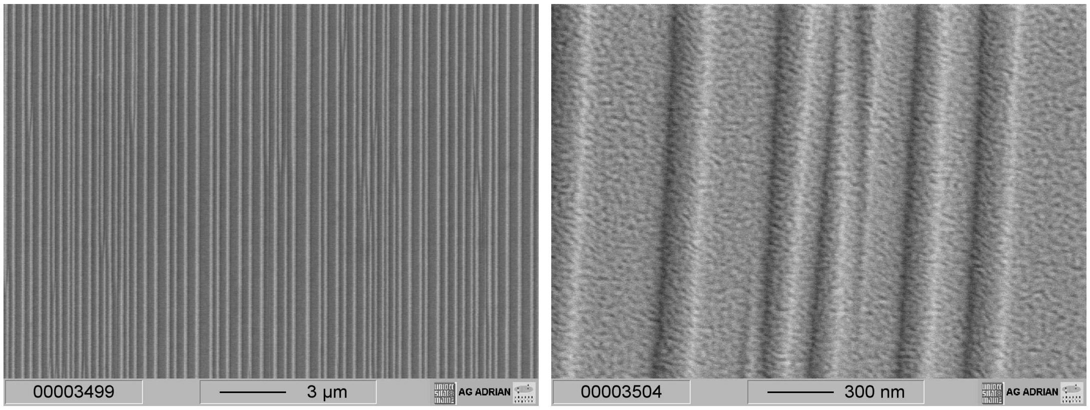

Figure 2.5: SEM image of Nb on faceted sapphire. The contrast occurs due to different emission angles of the secondary electrons. The average facet length can be estimated to 100 μm.

High resolution SEM and STM images show the structure of the Nb crystals on the facets, see right image in Figure 2.5 and Figure 2.6. Nb grows in small grains of 10 nm diameter. The STM image also reveal the wave like growth on the sapphire $(10\bar{1}1)$ surface.

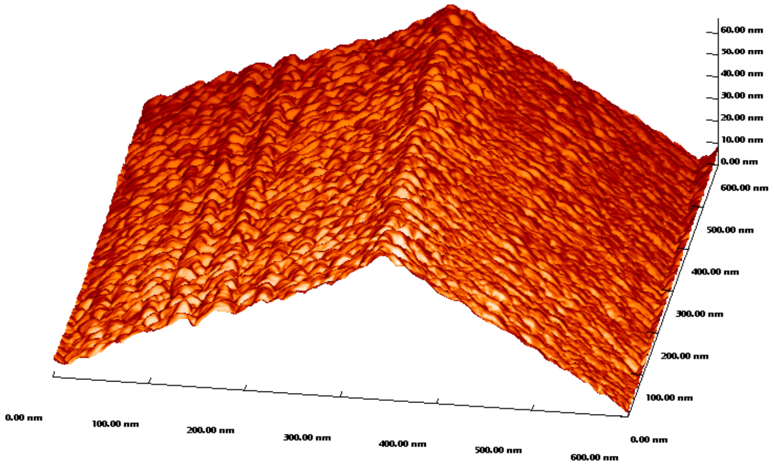

Figure 2.6: STM image of Nb on faceted sapphire. The facet is reproduced by the 40 nm Nb film. Nb shows a 3d growth mode, which overgrow the facet ridges.

2.2 Crystallography of Nb and Mo on sapphire m-plane

2.2.1 Four-circle-diffractometry

The crystallographic studies of the samples were performed by X-ray analysis in the four circle diffractometer. The determination of the crystal orientation was performed by a systematic scan of reciprocal space: keeping the ω and 2θ angle fixed at the calculated Bragg angles of the film reflections, χ-scans with fixed φ angle, with the reflection plane aligned parallel and perpendicular to the in-plane sapphire [010] direction, were performed. Due to it's technical restrictions, the four-circle diffractometer only allows ω angles up to 40° limiting the detectable bcc reflections to $\{110\}$, $\{200\}$ and $\{211\}$, respectively. The positions of the observed reflections were plotted in a stereographic projection. This projection was compared to corresponding stereograms calculated for several crystal orientations. For the (211) orientation all experimental peak positions could be identified. Further reflection positions were calculated by means of the orientation matrix, followed by a systematic scan of the corresponding reflections.

Performing this procedure for both bcc metals Nb and Mo, a (211)-oriented growth on sapphire m-plane can be identified. It has to be emphasized, that the growth on faceted sapphire m-plane shows the same crystalline quality as on non-faceted sapphire m-plane. Therefore, a homogenous overgrowth of Mo and Nb over the facets is probable. Though faceted substrates prepared at different annealing temperatures and therefore different sizes of the facets were used, no difference in the crystalline properties of the deposited films were observed. In-plane, the Nb and Mo $[01\bar{1}]$ axis is parallel to the sapphire [010] axis and therefore parallel to the facets. Perpendicular to the facets and therefore parallel to sapphire [001] lies bcc $[\bar{1}11]$.

A further elucidation of the epitaxial relationship was gained by φ-scan. In Figure 2.7 φ-scans of selected Mo and sapphire reflections as well as stereographic projections of a (211) oriented cubic crystal and sapphire m-plane are compiled. The upper part of Figure 2.7 shows φ-scans of the Mo $\{110\}$ and $\{200\}$ reflections and the sapphire $\{110\}$ and $\{104\}$ reflections, respectively. Comparing each reflection position with the stereographic plot, the correspondence of the Mo $\{110\}$ and sapphire $\{110\}$ reflections is evident. This indicates bcc $[01\bar{1}]$ to be parallel or antiparallel to the sapphire b-axis. In addition to this, the 180° shift of the Mo (200) reflection with regard to the sapphire c-axis, shown in the lower part of Figure 2.7, establishes the epitaxial relationship to be

$$\begin{aligned}
&(10\bar{1}0)_{Al_2O_3}||(211)_{Nb/Mo}\\
&[010]_{Al_2O_3}||[01\bar{1}]_{Nb/Mo}\\
&[001]_{Al_2O_3}||[\bar{1}11]_{Nb/Mo}
\end{aligned} \tag{2.1}$$

In chapter 3 similar measurements for Nb on faceted and non-faceted sapphire m-plane are presented. Furthermore, this orientation is also valid for the epitaxial growth of the highly magnetostrictive rare earth iron compounds RFe_2 on Nb (211) on sapphire m-plane.

Crystalline films with this epitaxial quality were also used to measure an angle dependency of the guided vortex motion in the type II superconductor Nb, as will be presented below.

Due to the anticipated epitaxial overgrowth over the sapphire facets and the observed in-plane relationship, the growth orientation of Nb and Mo on the facet

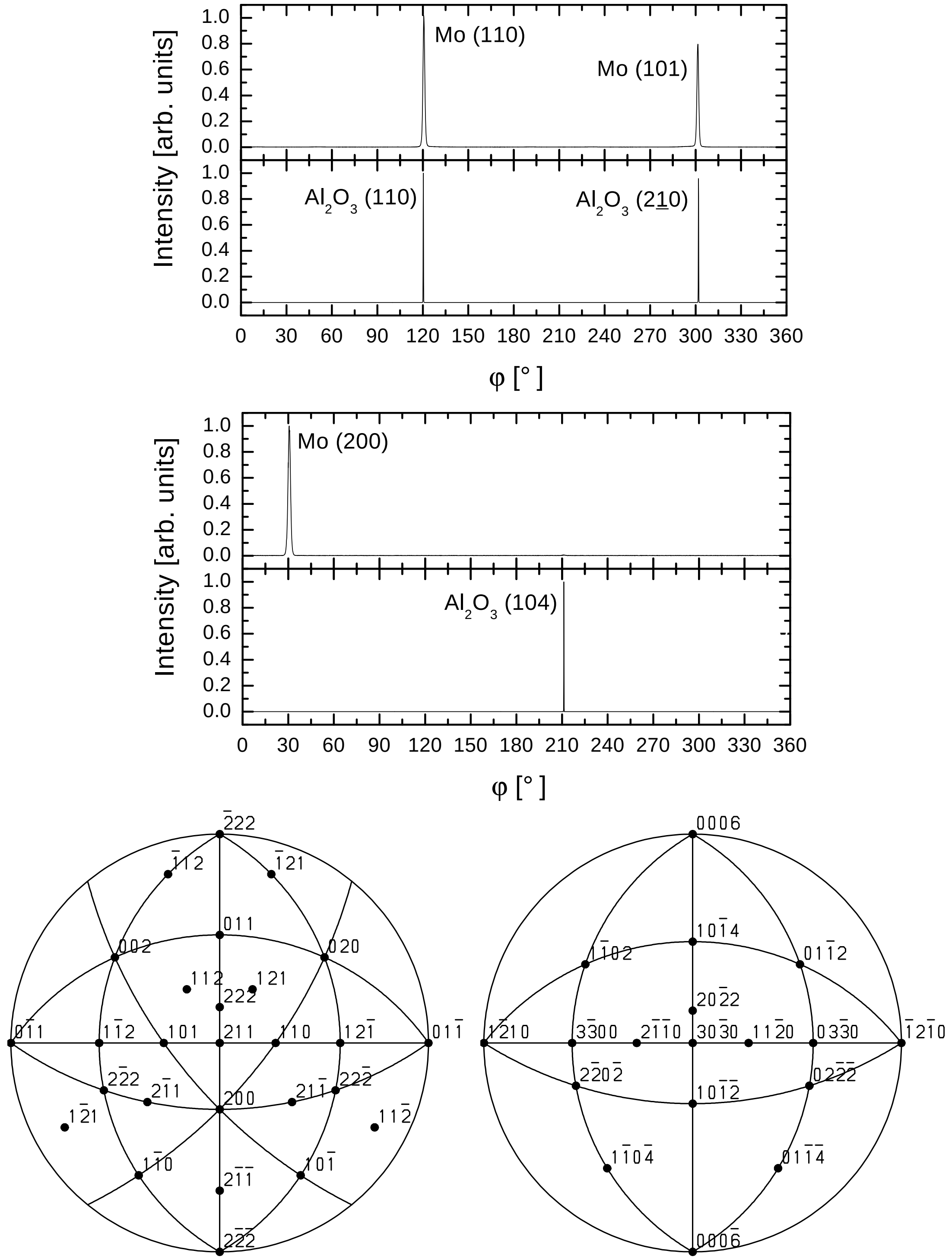

Figure 2.7: φ-scans of Mo {110} (top) and Mo (200) (middle) compared with sapphire in-plane reflections. The relationship of the reflection positions exhibits the in-plane orientation of the (211) oriented bcc metals. Bottom: Stereographic projection of a (211)-oriented bcc crystal (left) and sapphire m-plane (right).

surfaces can be determined. By comparing the stereographic projections of a (211)-oriented bcc crystal and of sapphire $(10\bar{1}0)$, see lower part of Figure 2.7, one finds the Nb/Mo (222) plane is nearly parallel to the sapphire $(20\bar{2}2)$ $(=(10\bar{1}1))$ surface. Furthermore, the Nb/Mo (200) plane is nearly parallel to the sapphire $(10\bar{1}\bar{2})$ surface. But the stereographic projections also reveal the appearance of a tilted growth of these layers, for the planes do not coincide exactly. The same conclusion can be drawn from geometrical considerations: For a cubic crystal the angle between the (211) and the (222) plane normals is 19.5°, while the angle between the (211) and (200) plane normals is 35.3°. Assuming a non-tilted relationship between the cubic (211)-plane and the original sapphire $(10\bar{1}0)$ plane, this leads to a small tilting in the bcc growth on the facet surfaces which have a theoretical value of 17.6° and 32.4° to the substrate normal, respectively. Then, the absolute value of tilting has to be approximately 2° for the growth on sapphire $(10\bar{1}1)$ and 3° for the growth on sapphire $(10\bar{1}\bar{2})$, respectively, with opposing signs to fulfill the requirement. Such a tilted growth is found frequently, since it also allows to relieve a part of misfit strain, as was e.g. reported by Du and Flynn for the growth of hexagonal $(10\bar{1}2)$-oriented rare earth crystals on (211)-oriented bcc crystals [109]. Furthermore, a slight misorientation of approximately 3° was also observed in the (001)-oriented growth of Nb on sapphire $(1\bar{1}02)$ [15], which can also be directly proposed by comparison with the stereographic projections, and which is important to fulfill the three dimensional epitaxial relationship between some bcc metals and sapphire, as will be discussed later.

2.2.2 TEM measurement of an undulated Mo film

The crystallographic properties of the Mo and Nb films deposited on sapphire m-plane were mainly studied by X-ray analysis in the four circle diffractometer. However, some questions could not be answered by this method. Firstly, though the X-ray diffraction indicated the twin-free growth of Nb and Mo, the existence of grain boundaries at the ridges and valleys of the facets could not be excluded. Additionally, if no grain boundaries could be detected, a tilting of the bcc planes with respect to the sapphire planes should occur. Secondly, the angular deviation of the facets as prepared in this work (17° and 23°) from the theoretical values of an sapphire crystal (17.6° and 32.4°), as independently measured by AFM and RHEED, was still an unresolved issue. Thirdly, the conclusion of homogenous overgrowth over the facet ridges and valleys, even for different facet angles and sizes, seemed cryptical. Therefore, a cross section high resolution TEM measurement of a Mo film prepared on faceted sapphire m-plane was made by L. Wiehl, using a TECNAI F30 electron microscope.

In Figure 2.8 a cross section of sapphire facets covered with Mo and partially oxidized $TbFe_2$ is shown. In this case, the electron beam was directed along the sapphire $[0\bar{1}0]$ direction. The long facet sides appear smooth and show no curvature. These planes correspond to the sapphire $(10\bar{1}1)$ plane, as could be shown by fast Fourier transformation of high resolution images. The more steep facet sides, which are attributed to the sapphire $(10\bar{1}\bar{2})$ planes, show a change of slope at a few nm below the facet ridges and above the valleys, and a curved shape on the main part of the facet. This is presented in Figure 2.9, where a high resolution image of a $(10\bar{1}\bar{2})$ surface is shown. According to simulations of electron microscopy imaging, the sapphire $(10\bar{1}\bar{2})$ planes are given by the prominent rows, parallel to the black lines drawn in the image. The surface of the facet, however, is not flat but formed by stacked $(10\bar{1}\bar{2})$ planes. The amount of stacking planes increases in direction of the facet valleys. Therefore, a diffusion limitation for the formation of the $(10\bar{1}\bar{2})$ facet has to be assumed. Figure 2.8 reveals an angle of the $(10\bar{1}1)$ plane with respect to the $(10\bar{1}0)$ plane of 18°, which is in good agreement with the AFM and RHEED measurements and the theoretical angle of 17.6° in sapphire. The $(10\bar{1}\bar{2})$ plane, on the other hand, reveals estimated angles between 22° and 24° with respect to the $(10\bar{1}0)$ plane. This again is in good agreement with the values obtained from the other experiments and deviates by more than 8° from the theoretical value of 32.4°.

The angle of the facet ridges and valleys amounts to 130° and is independent of the size of the facets and the angle of the $(10\bar{1}\bar{2})$ plane. This value fits exactly to the theoretical value of 130° for sapphire. Therefore it can be concluded that the $(10\bar{1}1)$ facet is always formed, independently of the annealing temperature and the resulting facet sizes. The second low energy surface to be formed is the sapphire $(10\bar{1}\bar{2})$ surface, but obviously the facet formation is kinetically limited due to slow diffusion on this surface.

Figure 2.8 also reveals the morphology of the deposited Mo film. Compared to the STM measurements of Nb films presented above, the Mo film is much thicker (100 nm) but still the undulating shape of the faceted sapphire template is reproduced. The topmost $TbFe_2$ film, on the other hand, is not reproducing the morphology of it's template, and will be discussed more extensively in chapter 3.

Figure 2.10 shows the cross section of an sapphire $(10\bar{1}1)$ surface. The surface

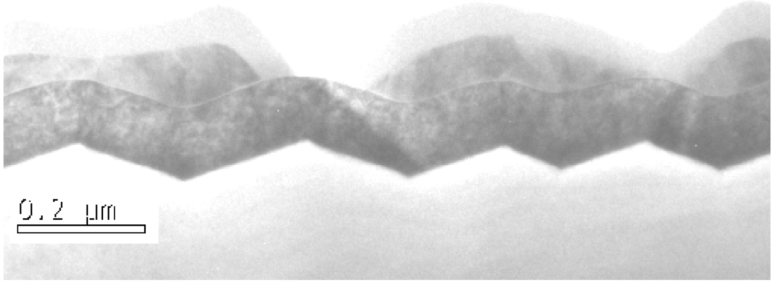

Figure 2.8: TEM image of $TbFe_2$ on Mo (211) on faceted sapphire. While the $(10\bar{1}1)$ surface is fully formed, the $(10\bar{1}\bar{2})$ surface shows a curvature. However, the angles of the facet ridges and valleys reveal the expected value of 130° (see text for details). The 100 nm thick Mo film reproduces the undulating morphology of the template.

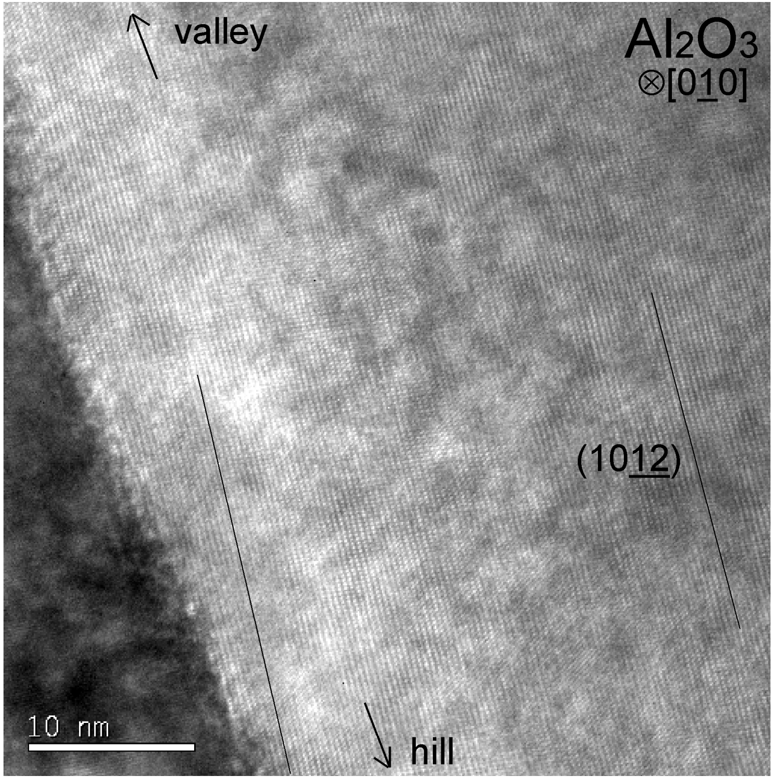

Figure 2.9: TEM image of a sapphire $(10\bar{1}\bar{2})$ facet. The surface is curved with a higher amount of material at the valley side. This can be due to diffusion limitation on the energy reduced surface. The curvature is a consequence of atomic step bunching.

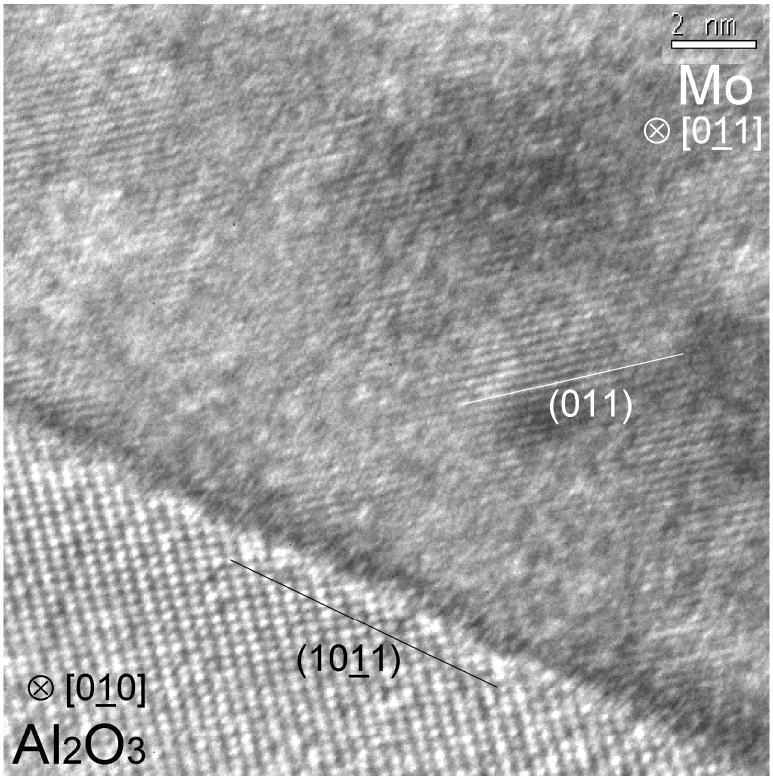

Figure 2.10: TEM image of Mo (111) on a sapphire $(10\bar{1}1)$ facet.

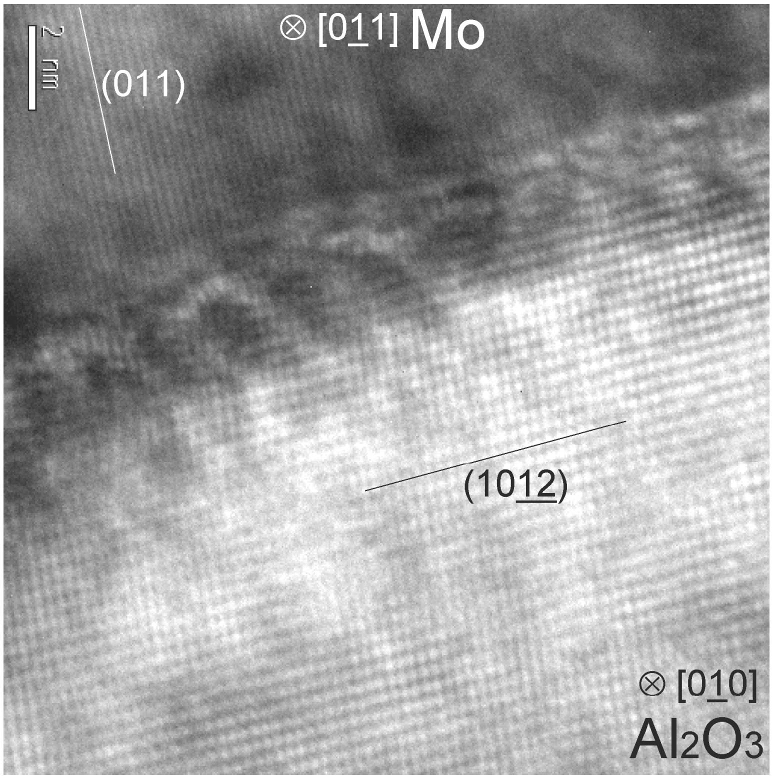

Figure 2.11: TEM image of Mo (100) on a sapphire $(10\bar{1}\bar{2})$ facet.

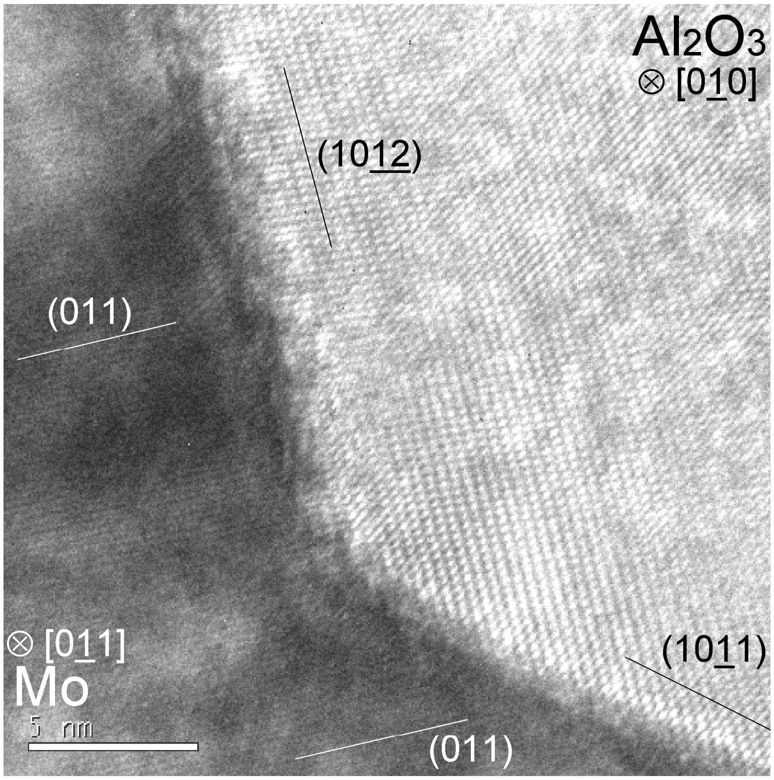

Figure 2.12: TEM image of Mo on faceted sapphire. Image of facet ridge.

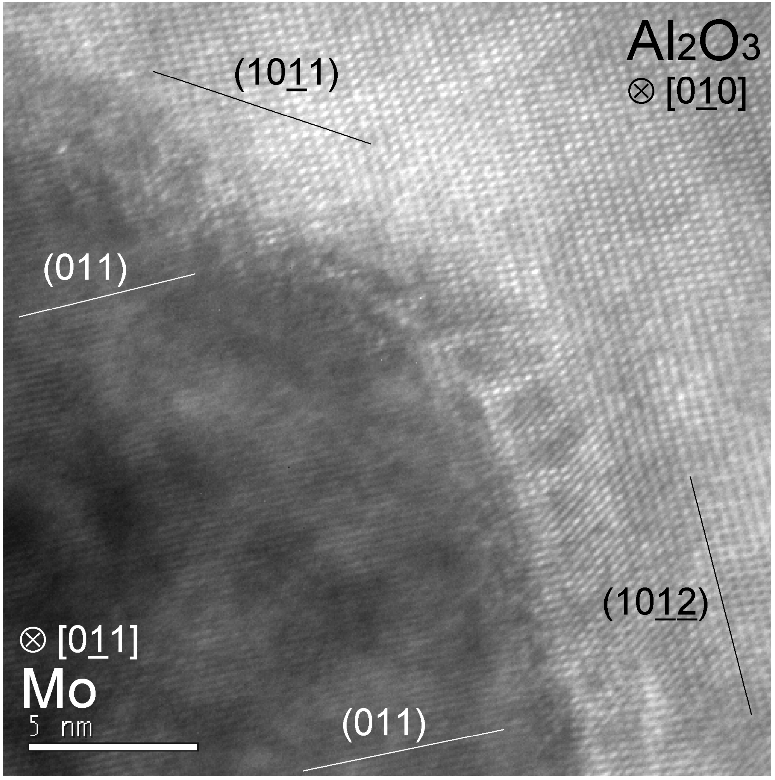

Figure 2.13: TEM image of Mo on faceted sapphire. Image of a facet valley. No grain boundary of Mo is observed in the region of the ridge or the valley.

of the facet is flat on the atomic scale. Only slight distortions and one atomic step can be seen. On top of this surface Mo grows crystalline with a diffuse zone smaller 5 Å. The prominent Mo lattice rows reveal an atomic distance which fits to the distance of the Mo {110} planes. The electron beam is aligned in the Mo $[0\bar{1}1]$ direction. From fast Fourier transformation analysis and because of the epitaxial relationships obtained from the X-ray measurements, these planes have to be attributed to the (011) planes of the Mo crystal. The growth orientation of the bcc metal on the $(10\bar{1}1)$ surface is therefore (111). The angle of the (011) planes with respect to the sapphire $(10\bar{1}1)$ surface is 37°. The planes of the (111) growth orientation are therefore also tilted by approximately 2° with respect to the facet plane.

Figure 2.11 shows an sapphire $(10\bar{1}\bar{2})$ surface. Like in Figure 2.9 it is corrugated and consists of steps of $(10\bar{1}\bar{2})$ planes. Nevertheless, Mo again grows crystalline on this surface. The prominent rows, which run nearly perpendicular to the sapphire $(10\bar{1}\bar{2})$ surface, again have the lattice distance of Mo {110} planes and fast Fourier transformations show them to be Mo (011) planes. The (011) planes show a small tilting angle of approximately -3° with respect to the substrate normal. For the Mo (100) growth orientation, which is perpendicular to the (011) planes, this tilting angle is therefore also valid with respect to the underlying sapphire $(10\bar{1}\bar{2})$ planes.

In Figure 2.12 a TEM image of a facet ridge and the Mo film is shown. On both sides of the ridge the characteristic stripes of the (011) planes are visible. No grain boundary can be observed in the region of the ridge. The same behavior is also observed in the TEM image of Figure 2.13. Mo overgrows the valley of the facets homogenously without grain boundary. Therefore, the conclusions taken from the X-ray data for the overgrowth of the bcc metals Nb and Mo are are fully confirmed by the TEM measurements.

2.2.3 Discussion: Growth of Nb and Mo on sapphire

The TEM measurement resolved the remaining questions on the growth of Mo (and Nb) on faceted sapphire.

Firstly, the expected growth orientations of Mo (and Nb) on the facet surfaces were confirmed. Additionally, no grain boundaries of Mo could be found either on the facet planes, nor on the ridges nor in the facet valleys. Furthermore, the expected tilting angles of 2° and -3° were observed. Therefore, a twin-free homogenous overgrowth of Mo (and Nb) over the sapphire facets can be stated.

Secondly, the deviation of the experimentally observed facet angles from the theoretical sapphire angles is explained. While the sapphire $(10\bar{1}1)$ surface is fully formed the $(10\bar{1}\bar{2})$ surface is curved, leading to lower angles on the coarse scale of an AFM measurement.

Thirdly, the somewhat unexpected independence of the crystal growth of the two bcc metals from the facet size of the sapphire template can be explained. It originates from the shape of the facets, in particular of the sapphire $(10\bar{1}\bar{2})$ facet. Firstly, the angle of the facet ridges and valleys does not depend on the facet size but always amounts to 130°. This is caused by the fact, that the $(10\bar{1}1)$ surface is always formed. Therefore, the facet edges are automatically produced in the aforementioned angle, even if the second sapphire $(10\bar{1}\bar{2})$ plane is not formed on the macroscopic scale. Secondly, the curved shape of the second facet is given by $(10\bar{1}\bar{2})$ steps or step bunches. On the local scale this allows the growth of Mo/Nb on the $(10\bar{1}\bar{2})$ surface, independent of the macroscopic curvature or angle of the facet.

The above discussed properties of faceted sapphire seem to be consistent and solve the questions of the growth of Nb/Mo on these structures. However, they contradict the calculations and observations reported in literature. Here, the $(10\bar{1}\bar{2})$ surface is proposed to be favored in the faceting process compared to the $(10\bar{1}1)$ plane. As already mentioned in chapter 1, Hartman has calculated the specific surface energies of various sapphire planes in an ionic point charge model with corrections for the Born repulsion energies [31]. According to this, the $(10\bar{1}\bar{2})$ facet has with 2552 erg/cm^2 a strongly reduced specific surface energy compared to the 4796 erg/cm^2 of the $(10\bar{1}1)$ plane. Further Hartman-Perdok-Theory (HPT) calculations on sapphire were performed by Dekkers et al [110]. Again the $(10\bar{1}\bar{2})$ surface has with 1785 mJ/m^2 a reduced surface energy compared to the 2802 mJ/m^2 of the $(10\bar{1}1)$ surface. In an experimental work Heffelfinger et al. scrutinized the facet formation of sapphire m-plane during high temperature annealing [3, 28]. The substrates were annealed in air at 1400°C in a high-purity alumina crucible. The only difference of the preparation parameters with respect to the here presented samples was that Heffelfinger et al. transferred the substrates at the elevated temperatures and that they used different solvents for cleaning the substrates. In AFM and TEM measurements Heffelfinger et al. report the formation of a "simple" flat and a "complex" curved surface. The simple surface is attributed to the $(10\bar{1}\bar{2})$ plane. With increasing annealing time the complex surface is reported to become a flat $(10\bar{1}1)$ plane.

The origin for this discrepancy is not clear until now. However, the surface energy calculations are performed for the surface formation in thermodynamical equilibrium. This is not the case in the facet formation process. Here, the material has to diffuse out of the valleys to the ridges and is not necessarily available in the proportions needed for the equilibrium facet formation. Furthermore, the diffusion of Al_2O_3 on the $(10\bar{1}\bar{2})$ surface could be too slow on the low energy surface. The discrepancy to the observations of Heffelfinger et al. however, cannot be solved.

The growth of bcc transition metals and especially of Nb on sapphire is studied since more than 20 years. The epitaxial orientation of Nb (and Mo) on sapphire was found to be unique and three dimensional [15, 14, 13, 23, 24, 111]. In X-ray and TEM analysis the following epitaxial relationships were found:

$$\begin{aligned}
&(11\bar{2}0)_{Al_2O_3}\|(110)_{Nb} \quad \text{and} \quad [001]_{Al_2O_3}\|[\bar{1}11]_{Nb}\\
&(0001)_{Al_2O_3}\|(\bar{1}11)_{Nb} \quad \text{and} \quad [2\bar{1}0]_{Al_2O_3}\|[101]_{Nb}\\
&(10\bar{1}0)_{Al_2O_3}\|(211)_{Nb} \quad \text{and} \quad [001]_{Al_2O_3}\|[\bar{1}11]_{Nb}\\
&(1\bar{1}02)_{Al_2O_3}\|(001)_{Nb} \quad \text{and} \quad [001]_{Al_2O_3}\|[\bar{1}11]_{Nb} \qquad (2.2)
\end{aligned}$$

These results agree with the observations done in this work: As will be shown in chapter 3, thin Nb and Mo films have been used as template for the epitaxial growth of the highly magnetostrictive C15 Laves phases of the RFe_2 compounds on sapphire a-plane. Here, the two bcc metals grow twin-free (110)-oriented, with the in-plane relationship of $[001]_{Al_2O_3} \parallel [\bar{1}11]_{Nb/Mo}$ and $[\bar{1}10]_{Al_2O_3}\|[\bar{1}1\bar{2}]_{Nb/Mo}$. As shown above, Nb and Mo grow epitaxially, twin-free (211)-oriented on non-faceted and faceted sapphire $(10\bar{1}0)$ with an in-plane relationship of $[001]_{Al_2O_3} \parallel [\bar{1}11]_{Nb/Mo}$ and $[010]_{Al_2O_3} \parallel [01\bar{1}]_{Nb/Mo}$.

As one result of this work, the observations for the growth of the two bcc metals on faceted sapphire complete this three dimensional epitaxial relationship. Both, the X-ray data and the TEM measurements, reveal the (111)-oriented growth of Mo (and Nb) on sapphire $(10\bar{1}1)$ with a tilting angle of 2° of the bcc metal with respect to the template. On the other facet side, the sapphire $(10\bar{1}\bar{2})$ surface, Mo (and Nb) grows (100)-oriented with a observed tilting angle of -3°. Furthermore, the notation of the bcc planes is already fitting to the notation chosen in Equation (2.2). This can be deduced by comparing the stereographic projection of an sapphire $(10\bar{1}0)$ and a (211)-oriented cubic crystal. Therefore, the relationships (2.2) can be extended to

$$\begin{aligned} (10\bar{1}1)_{Al_2O_3} &\| (111)_{Nb/Mo} \\ (10\bar{1}\bar{2})_{Al_2O_3} &\| (100)_{Nb/Mo} \end{aligned} \tag{2.3}$$

The origin for this unique three dimensional epitaxial relationship of the bcc metals Nb and Mo and sapphire can be explained by the crystal structure of the materials. Besides the hexagonal description, sapphire also can be described by a morphological unit cell, which can be constructed by connecting the empty octahedral interstices or the lattice sites of one Al sublattice [15, 18]. The morphological unit cell is rhombohedral with an angle of 85.7° and a lattice parameter a of 3.5 Å. Then, the $\{001\}^{Rhomb}$ planes are identical with the $\{1\bar{1}02\}^{Hex}$ planes of the hexagonal unit cell, and the $(111)^{Rhomb}$ plane is parallel to the $(0001)^{Hex}$ plane. The lattice constants of the bcc metals Nb and Mo are 3.3 Å and 3.147 Å, respectively, and therefore close to the lattice constant of the rhombohedral sapphire cell. For Fe, on the other hand, which has a lattice constant of $a = 2.87$ Å, the misfit is too large to reveal this three-dimensional relationship. Therefore, the Fe growth on sapphire m-plane is much more complicated than for Nb and Mo, as will be discussed next.

2.3 Crystallography of Fe on sapphire m-plane

To determine the crystallographic properties of Fe on sapphire m-plane, Fe was deposited under normal incidence on faceted and non-faceted substrates heated to 450°C. The Fe rate was 0.13Å/sec. In analogy to Nb and Mo films on sapphire m-plane, χ-scans of the accessible Fe reflections were performed parallel and perpendicular to the facets. Expecting a (211)-oriented growth, also φ-scans with fixed χ values of the (211)-oriented cubic lattice were performed, as shown in Figure 2.14 for Fe deposited on a facetted substrate. In contrast to the (211)-oriented twin-free growth of Mo and Nb on faceted and non-faceted sapphire m-plane, the growth of Fe on this substrates is much more complicated. A comparison of the occurring reflections with the stereographic projection of a (211)-oriented cubic crystal leads to at least four different epitaxial domains. Furthermore, the orientation of the domains is different for Fe on non-faceted than on faceted sapphire m-plane.

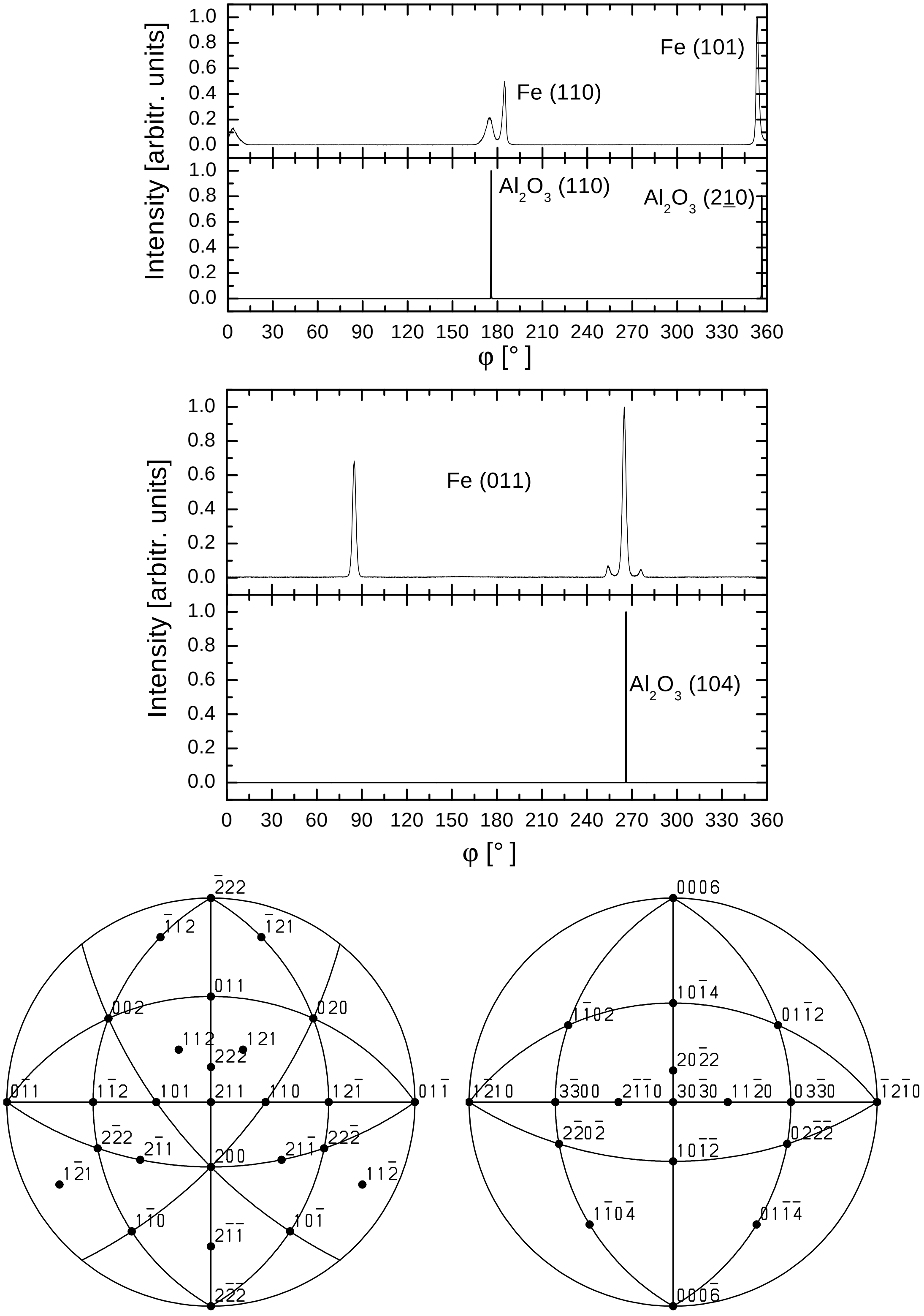

Figure 2.14: φ-scans of Fe {110} (top) and Fe (011) (middle) compared with sapphire in-plane reflections. The splitting of the reflections indicates the occurrence of several domains. Bottom: Stereographic projection of a (211)-oriented bcc crystal (left) and sapphire m-plane (right).

Domain	$\angle(\mathbf{[211]}_{Fe},\mathbf{[210]}_{Al_2O_3})$	$\angle(\mathbf{[\bar{1}11]}_{Fe},\mathbf{[001]}_{Al_2O_3})$	$\angle(\mathbf{[01\bar{1}]}_{Fe},\mathbf{[010]}_{Al_2O_3})$
1 ☆	3°	0°	3°
2 ★	-3°	0°	-3°
3 ◇	3°	180°	3°
4 ✦	-3°	180°	-3°

Table 2.1: Orientation of the Fe axes with respect to non-faceted sapphire m-plane. The symbols correspond to Figure 2.15

Domain	$\angle(\mathbf{[211]}_{Fe},\mathbf{[210]}_{Al_2O_3})$	$\angle(\mathbf{[\bar{1}11]}_{Fe},\mathbf{[001]}_{Al_2O_3})$	$\angle(\mathbf{[01\bar{1}]}_{Fe},\mathbf{[010]}_{Al_2O_3})$
1 ☆	3.3°	1.4°	3.6°
2 ★	-3.3°	1.4°	-3.6°
3 ◇	4.6°	177.1°	4.6°
4 ✦	-4.6°	177.1°	-4.6°

Table 2.2: Orientation of the Fe axes with respect to faceted sapphire m-plane. The symbols correspond to Figure 2.16

For all four domains the [211] axis is close to the substrate normal. The four domains can be classified into two pairs of domains. The two pairs are associated by a twin law with a $(\bar{1}11)$ twin plane. For each pair, the two domains differ from each other by a tilting of the [211] axis by an angle of roughly ± 3° with regard to the substrate normal.

Therefore, the growth of Fe on non-faceted sapphire m-plane shows the following domains, as deduced from the data shown in Figure 2.15 and schematically displayed in Figure 2.17: Two of the four domains are oriented similarly to the Nb or Mo domains on sapphire m-plane. They have a common $[\bar{1}11]$ axis aligned parallel to the sapphire [001] axis. The two domains differ from each other by a rotation around the Fe $[\bar{1}11]$ axis by an angle of +3° and -3°. Therefore, their [211] axis is not parallel to sapphire [210] but tilted by about ± 3° in the sapphire [210]-[010] plane. Therefore, their $[01\bar{1}]$ axis is not parallel to the sapphire [010] axis but tilted about ± 3° in the same plane. The other two domains reveal the same ± 3° rotation around Fe $[\bar{1}11]$ and therefore the ± 3° tilting of the [211] axis with regard to the sapphire [100] axis occurs. Due to the mirroring, the common $[\bar{1}11]$ axis shows anti-parallel to sapphire [001]. Accordingly, the $[01\bar{1}]$ axis is, neglecting the ± 3° tilting, anti-parallel to the sapphire $[0\bar{1}0]$ axis. Table 2.1 compiles the angles of the three Fe axes with respect to the substrate orientations.

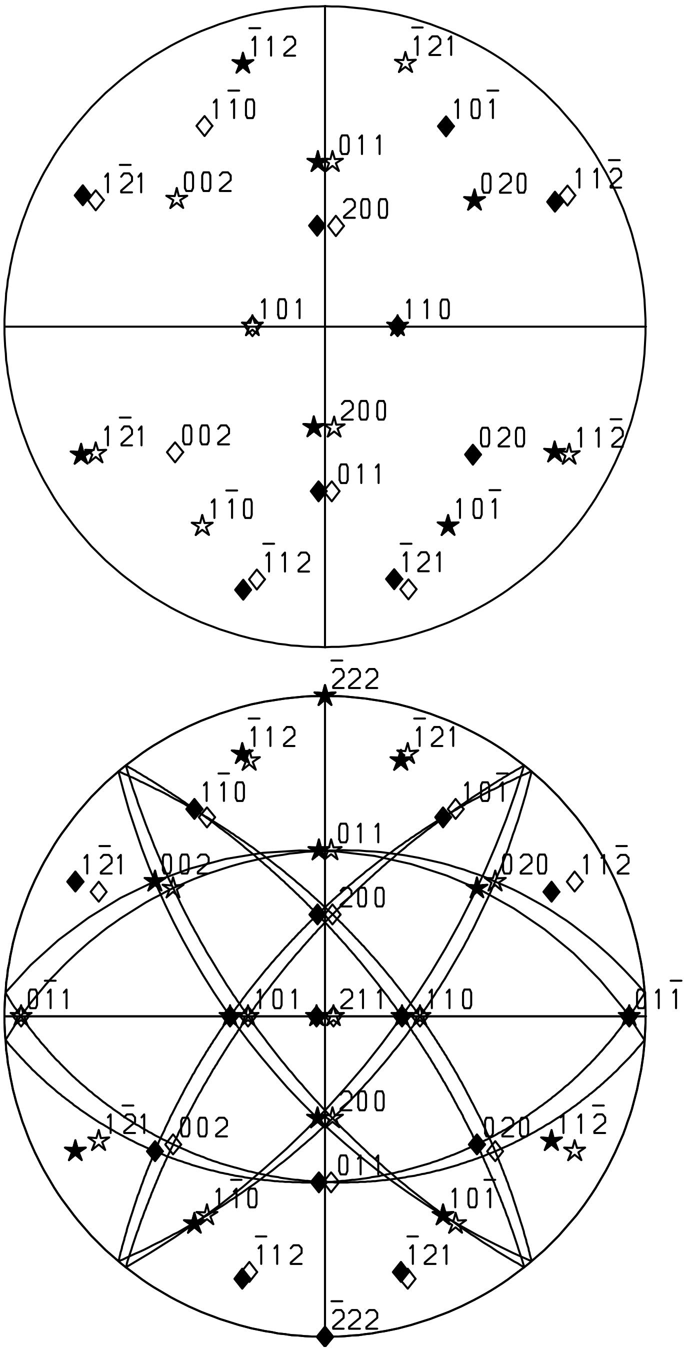

Figure 2.15: Top: Stereographic plot of the observed Fe reflections deposited on non-faceted sapphire m-plane. Bottom: Stereographic plot of Fe reflections calculated for four close to (211)-oriented crystals with domain orientations given by the values of Table 2.1.

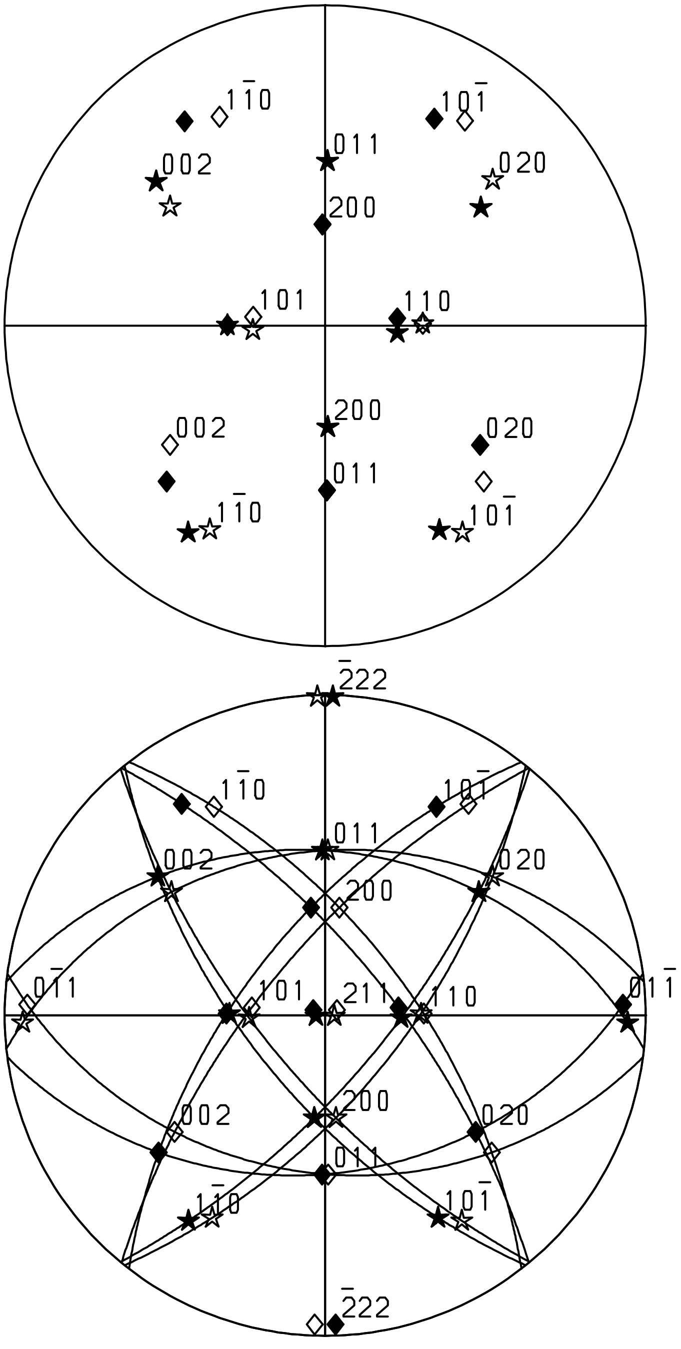

Figure 2.16: Top: Stereographic plot of the observed Fe reflections deposited on faceted sapphire m-plane. Bottom: Stereographic plot of Fe reflections calculated for four close to (211)-oriented crystals with domain orientations given by the values of Table 2.2.

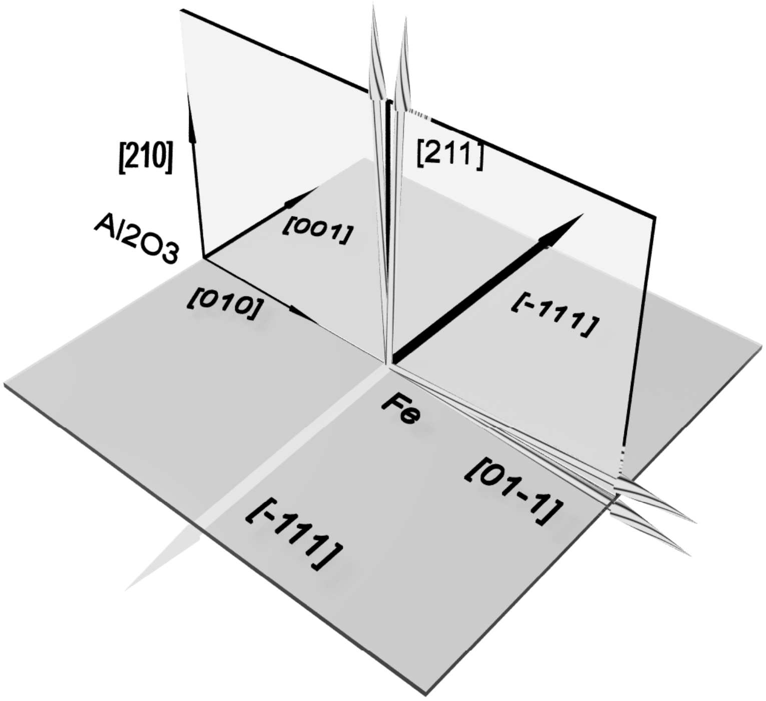

Figure 2.17: Schematic representation of the four-domain growth of Fe on non-faceted sapphire m-plane. The monochrome arrows represent the directions of one crystal pair while the striped arrows represent crystal directions shared by both twins.

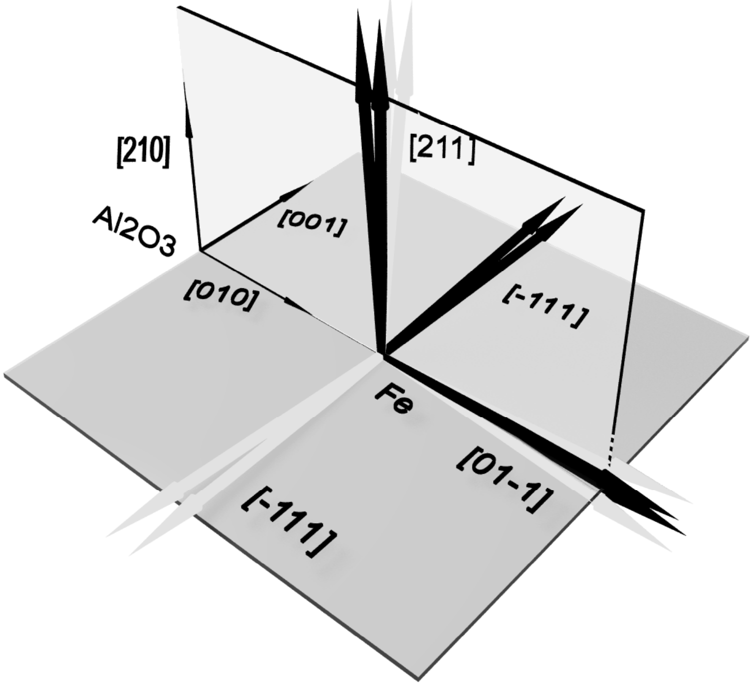

Figure 2.18: Schematic representation of the four-domain growth of Fe on faceted sapphire m-plane.

For Fe deposited on faceted sapphire m-plane, presented in the stereographic plots of Figure 2.16, the orientation of the domains with respect to the ideal (211)-oriented growth must be described by three rotations. In addition to a more than ±3° rotation around the $[\bar{1}11]$ axis as was observed for Fe grown on non-faceted m-plane sapphire, a rotation around the substrate normal occurs. Furthermore, the faceted surface leads to a rotation of the crystals around the sapphire b-axis. Due to the different angles of the two facet surfaces the rotation angle is not equal for the two pairs. Therefore, strictly speaking, the $(\bar{1}11)$ plane is no mirror plane any more. This is again summarized in tabular form in Table 2.2 and schematically sketched in Figure 2.18.

2.4 Electric measurements on undulated Nb films

A first application of the epitaxial twin-free bcc films on faceted sapphire was the study of the influence of the periodic surface faceting on the electrical properties of the superconductor Nb. Although very pure Nb single crystals are type I superconductors, even nearly perfect epitaxial thin films are of type II. In a type II superconductor, the magnetic field H versus temperature T phase diagram contains a so-called mixed state in which magnetic flux enters the superconductor in quantized form, the flux vortices. The amount of vortices entering the superconductor is proportional to the magnetic field. If an electric transport current is applied to the superconductor, a Lorentz force acts on these vortices, moving the vortices perpendicular to the current direction. This motion of the magnetic vortices, on the other hand, induces an electric field parallel to the current, and accordingly energy dissipation occurs. The motion of the vortices can be damped due to pinning in regions of the superconductor, where the order parameter is reduced. In equilibrium, the Lorentz force is balanced against this pinning force. With increasing transport current, the vortex movement changes its character from a thermally activated motion to that of a viscous flux flow. This crossover point defines the critical current density j_C that the superconductor can sustain in an applied magnetic field without appreciable ohmic dissipation [112]. Due to their repulsive interaction, the vortices form a regular two dimensional lattice of hexagonal or quadratic symmetry.

A periodic modulation of the pinning force density has interesting implications on the movement of the vortex lattice [113, 114, 115]: If the vortex lattice reveals a commensurate matching of its lattice constant with the underlying pinning structures, the effective pinning force will be enhanced. This is again a consequence of the repulsive inter-vortex interaction, since the pinning of the whole vortex lattice is then more effective than the pinning of isolated vortices. Such an enhanced pinning is indicated by a correspondingly enhanced critical current density.

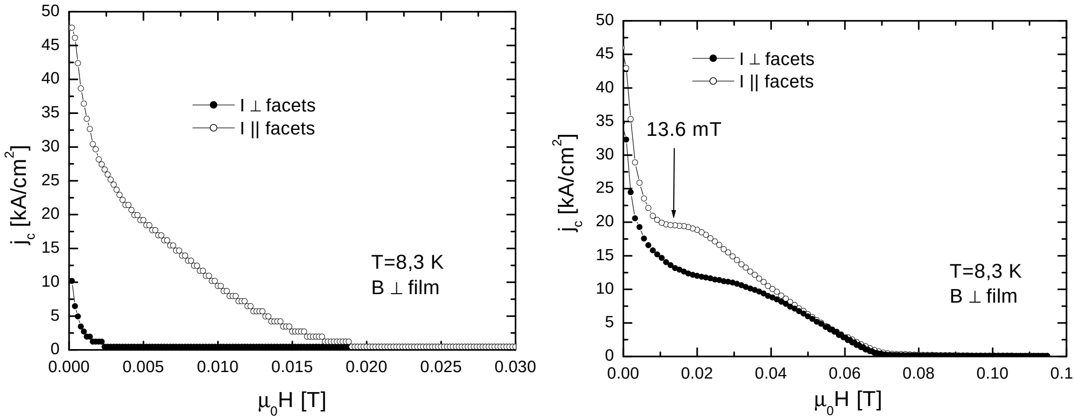

Figure 2.19: Critical current density j_C vs. magnetic field for an epitaxial Nb (211) film on faceted sapphire. With the current flow parallel to the facet ridges (open symbols), j_C is increased compared to currents perpendicular to the facets (full symbols). Left image: Film thickness 25 nm; Right image: Film thickness 40 nm.

For electrical measurements, undulated epitaxial Nb films of different thicknesses were prepared on faceted sapphire as described above. M. Huth and O. K. Soroka patterned the films in a micro-bridge structure and performed the measurements in ^{3}He and ^{4}He cryostates [29, 116, 117]. Figure 2.19 shows the dependence of the critical current density of epitaxial Nb films for two different orientations of the transport current with respect to the facet ridges. The magnetic field was applied parallel to the averaged surface normal of the films. In the left image of Figure 2.19, the nominal film thickness was 25 nm, while the nominal thickness of the right film was 40 nm. In both images a strong direction dependence of the critical current density $j_C(B = \mu_0 H)$ with respect to the sapphire facets can be identified: For the thinner film j_C(B $\rightarrow$ 0) was enhanced by a factor of 4.75 when the current was applied parallel to the ridges, while for the thicker film this factor is still 1.9. This effect can be explained by an enhanced pinning of the system when the vortices have to move perpendicular to the facet ridges. The right graph of Figure 2.19 shows a second feature: Only when the current is aligned parallel to the facet ridges, j_C(B) shows a pronounced plateau.

The center of the plateau corresponds to a magnetic induction of $B_P = 13.6$ mT. The vortex lattice parameter of an assumed hexagonal lattice is given by [112]:

$$a = \left(\frac{4}{3}\right)^{1/4} \left(\frac{\Phi_0}{B}\right)^{1/2} \tag{2.4}$$

Here, Φ_0 is the magnetic flux quantum, $\Phi_0 = \frac{hc}{2e}$, and B is the magnetic field. Therefore, the field B_P corresponds to a vortex lattice parameter of $a_L = 421$ nm. The best matching of the vortex lattice with the underlying ridge structure would then be expected for a ridge period length of $a_L \cdot \sqrt{3}/2 = 365$ nm. This corresponds to the average period length of the faceted surface for substrates annealed at temperatures of 1650°C. However, this plateau is not observed in the thinner film. A final explanation for this is not given yet, but an increased isotropic pinning due to a higher defect density in the thinner film could be assumed.

Further measurements of angular dependencies of the longitudinal and transversal (Hall) voltages of undulated Nb films were performed by O. K. Soroka. They reveal a guided vortex motion in these systems and will be detailed in his Phd-thesis.

2.5 Preparation of Nb nanowires

The mesoscopic height of the facets, which can amount to more than 70 nm for individual facets, can also be employed for nano-scale patterning. K. A. Ritley[2] suggested the possibility of preparing nanowire structures by employing self-shadowing effects of faceted sapphire. The idea was the following: Due to the hitchless propagation of the atomic/molecular beams in the MBE technique, the deposited atoms should solely cover the ridges of the facets if the deposition angle with respect to the substrate is sufficiently low. Similar experiments had already been performed on other undulated surfaces: Teichert et al. for example, exploited the elastic stress relief mechanisms of thin films on crystal substrates, leading to the formation of periodic surface and interface patterns, for the preparation of Co patches [118]. Sugawara et al. utilized the elevated temperature faceting of NaCl (110) to prepare semi periodic Fe nanowires [17].

In a feasibility study, Nb was evaporated out of the electron beam evaporator with a deposition rate of 0.3 Å, calibrated to normal incidence. To prepare

---

[2] Hewlett Packard, Stuttgart

nanostructures, the deposition occurred under a glancing incidence angle of 9° with regard to the substrate surface. The substrate temperature was 850°C.

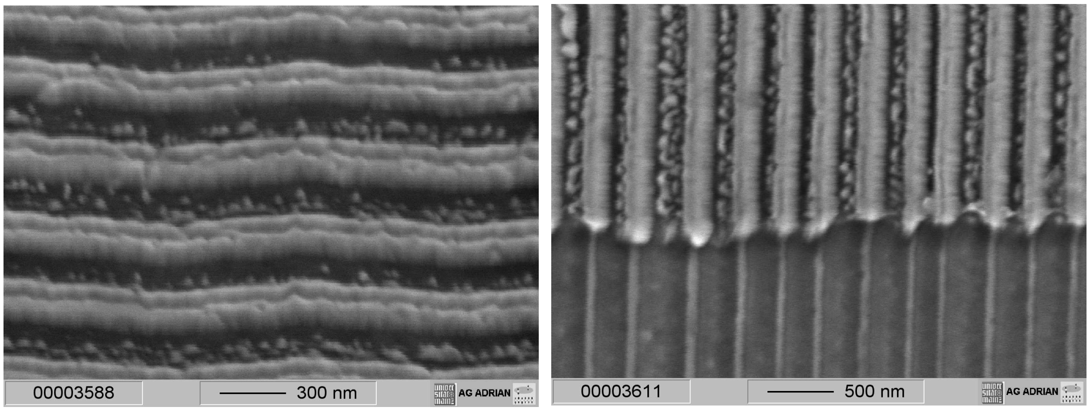

Figure 2.20: SEM image of Nb nanowires on faceted sapphire substrate. The stripes form due to a shallow incidence of the atomic beam in addition with a de-wetting from the facet sides. In the right image the film was partly etched, revealing the faceted substrate.

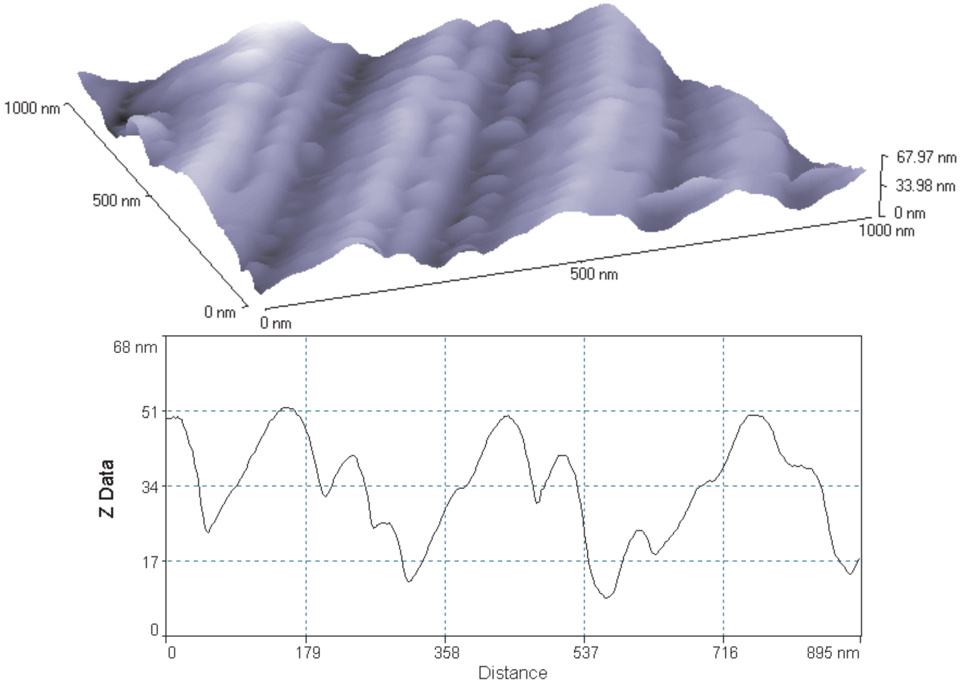

Figure 2.21: AFM image and linescan of Nb nanowires on faceted sapphire. Compared to the SEM images, the nanowire morphology is hard to detect. A determination of the wire thickness is not possible.

SEM measurements, shown in the left image of Figure 2.20, reveal the formation of isolated Nb wires covering the faceted substrate in stripes, about 100 nm wide, on the convex ridges. At the ridge position, a line-like discontinuity of the secondary electron emissivity indicated an additional step-like structure. In between the ridges, largely separated island-like structures were observed on the facets. These are most likely due to Nb that de-wets the respective surfaces. The assumption, that the Nb wires form on the convex ridges, stems from comparison with the re-exposed sapphire surface after ion-beam etching parts of the Nb surface, see right image of Figure 2.20. The high intensity line-like structure can be attributed to the convex ridges of the re-exposed sapphire surface, and the locations of the Nb wires clearly coincide with these ridges. Due to charging effects, the image contrast is reduced. Nevertheless, the mentioned discontinuous change in the secondary electron emissivity could be located at the exact ridge positions. Furthermore, the Nb stripe coverage shows a left-to-right asymmetry with regard to the ridges. This asymmetry roughly amounts to 1/2, which is compatible to the width ratio of the projected facets of the underlying sapphire surface.

Figure 2.21 shows an AFM image and a linescan of the Nb nanowires of Figure 2.20. Compared to the SEM measurements, the AFM measurements do not reveal the nano-wire topology of the sample. Drop like accumulations of Nb can be observed in the valleys of the facets in analogy to the SEM image. A second, accumulation of Nb occurs on the facet ridges. However, no uncovered sapphire surface can be observed on the facets. Due to this difficulties in interpreting the AFM images of nanostructures, and especially of the Fe nanostructures discussed in chapter 5, the thickness of these structured could only be estimated indirectly.

The formation of the above discussed nanostructures is not completely explained by self-shadowing effects of the facets. In Figure 2.22 measurements performed for Nb deposited on faceted sapphire under an incident angle of 9° are shown. Here, the only difference in the preparation parameters compared to the films presented in Figure 2.20 was a reduced substrate temperature of 350°C. The left image of Figure 2.22 shows a SEM measurement. Compared to Figure 2.20, no wire formation can be detected. The Nb seems to coat the complete faceted structure. This impression is underlined in the AFM measurement of the same film, presented in the right image of Figure 2.22. Both facet sides are coated with Nb islands. To explain this, the emitted atomic beam profile of an electron beam evaporator has to be considered. Here, the source can be described by a sphere, which leads to a large penumbra effects. Therefore, the whole faceted

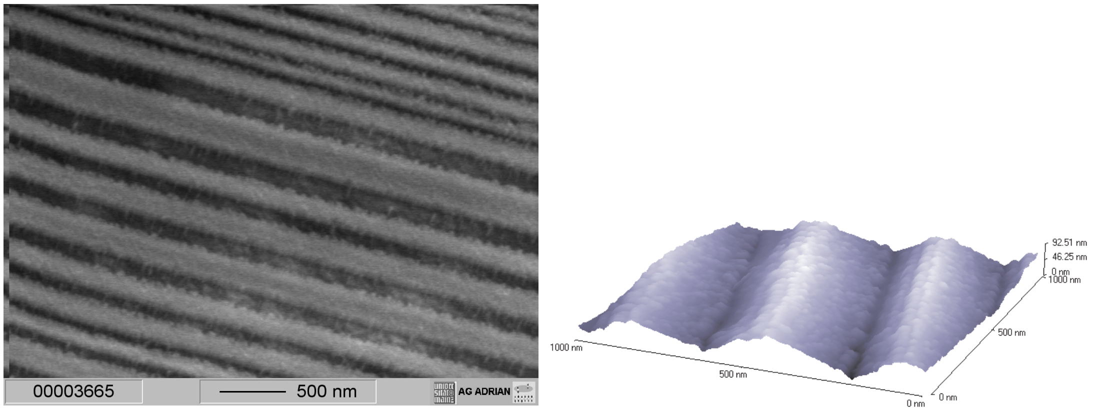

Figure 2.22: Left: SEM, right: AFM image of Nb on faceted sapphire deposited at an incident angle of 9° but lower substrate temperature. Compared to samples prepared at high deposition temperatures, these samples do not reveal the formation of nanowires.

surface area is exposed to the Nb beam, even at this small deposition angle of 9°. The difference in the morphology of the samples prepared at high substrate temperatures compared to low substrate temperatures implies, that the high substrate temperature and therefore the enhanced mobility of the ad-atoms plays an important role in the formation of nanowires.

Therefore, de-wetting effects of the Nb-sapphire system have to be considered to explain the formation of metallic nanostructures on faceted sapphire in addition to the self-shadowing effects of the facets [29]. Wire formation in normal incidence for faceted surfaces is known to be possible for facet formation on the atomic scale [37]. A precondition is, that the layer material de-wets the facets. In this case, the ad-atoms predominately diffuse to the concave regions. This is due to the closer proximity to neighboring surface atoms on the upward sloping facets, a mechanism that is more effective for steep facet angles. In contrast, if the layer material wets the substrate, a layer of homogenous thickness will grow. With increasing deposition time, the formation of a closed film will also occur in the de-wetting case. This limits the wire thickness for perpendicular preparations to a few monolayers.

In the present investigation, however, the situation is considerably different. Firstly, the faceting is on the 100 nm scale, which renders geometrical differences in the interfacial energies at the concave and convex edges irrelevant. Secondly, the thickness of the stripes can be several tens of nanometers. Thirdly, the stripes form on the ridges, not in the valleys.

In the deposition process under shallow incidence, a laterally modulated rate for the Nb atoms occurs. The largest deposition rate appears on the ridges and falls off towards the valley regions of the surface. At 850°C, the Nb ad-atoms can not diffuse across the ridge-to-valley distance. The upper limit for the average diffusion length can be estimated to $\sqrt{\langle r^2 \rangle} \approx 12$ nm [29]. Consequently, the lateral rate modulation causes a lateral thickness modulation, with the thickest Nb layer on the facet ridges. The observed islanding on the facets indicates a de-wetting process. The specific surface energies of Nb (100) and (111) amount to 2500 ± 250 erg/cm^2 [119, 120]. They are the same for both orientations, because the number of nearest neighbor surface atoms is four in both cases. The specific surface energies of the two sapphire facets amount to 4800 erg/cm^2 and 2550 erg/cm^2 for the $(10\bar{1}1)$ and $(10\bar{1}\bar{2})$ surfaces, respectively. TEM studies of the Nb/sapphire interface do not reveal chemical reaction or interdiffusion for the most prominent epitaxial orientations [15, 13]. It is thus save to assume that the interface energies are in the range of 1000 to 2500 erg/cm^2, as observed for metals layers grown on insulating substrates. Therefore, a nucleation of the Nb is solely expected at the steps of the facet ridges and valleys. Similar de-wetting is also observed for Fe deposited on heated faceted sapphire substrates, as will be discussed in chapter 5.

The de-wetting behavior of metals on sapphire is also reported in the literature: Silver builds strung nanodrops in the valleys of faceted sapphire when deposited in normal incidence on heated substrates [121]. Further de-wetting effects of Nb on sapphire were also observed by Wölfing et al. [20]. They scrutinized the growth of Nb on annealed and non-annealed sapphire a-plane. When deposited at 900°C on a non-annealed substrate, the formation of Nb islands of 20 - 40 nm diameter and 2 nm thickness without preferred orientation is observed. The islands are believed to nucleate at defects of the substrate due to a miscut or polishing induced defects. On annealed substrates, on the other hand, the occurrence of Nb islands only at the step edges of the substrate is observed. It is therefore believed, that the annealed surface is too smooth and defect-free to offer Nb atoms a nucleation center and that the elevated temperatures induce a desorption of the non-nucleated atoms.

2.5.1 First measurements on Nb nanowires

After characterizing the Nb nanowire systems, some further measurements were performed on these samples. The superconducting properties of the wires were measured in a Oxford vibrating sample magnetometer (VSM). Due to a low magnetic response of the temperature-dependent remanence signal, temperature dependent magnetic hysteresis loops were measured, shown in Figure 2.23. At temperatures below 7 K an opening of the hysteresis loops occurs. Due to the penetration of the vortices and their pinning in the structures the loops are hysteretic. Furthermore, small dips in the magnetization curve are observed. Their occurrence is symmetrical in the magnetization reversal curves. Their position depends on temperature. For a temperature of 2 K they occur at 70 mT while at 5 K they are at 40 mT. The origin of these dips could be vortex lattice matching effects. Due to the one dimensional periodic structure of the Nb nano-wires low dimensional vortex lattice structures could be expected, which would show different features than in standard thin films. By means of the annealing temperature, the periodicity of the faceted sapphire and accordingly of the Nb nano-wires is adjustable. Further magnetization measurements with different wire periodicity are therefore possible.

In electrical measurements on a film of Nb nanowires performed with a multimeter the resistance parallel to the wires was found to be in the Ohm regime. Perpendicular to the wires, on the other hand, the resistance was infinite. This again proofs that the nanowires are electrically insulated against each other.

Therefore, further electrical measurements can be suggested. For instance, conductivity quantization or superconductivity in single wires could be analyzed in an appropriate setup. An example for such a setup is given in chapter 5, where the electrical properties of a low number of Fe nano-wires were analyzed.

With the preparation of Nb nanowires the feasibility of preparing crystalline metallic nanostructures, with relative ease, was proofed. There is no doubt, that the same preparation technique can be applied for further systems, like for instance ferromagnets. By using properly arranged multiple evaporation sources, even alloys could be prepared as nano-structures. Further examination of the growth process of the sapphire facets, on the other hand, could help to find ways to tune the periodicity of the facets and lead to a more regular array of wires. By sticking together two faceted substrates with perpendicular rows of nano-wires, for example, point contacts or even tunneling elements of a nano-wired network

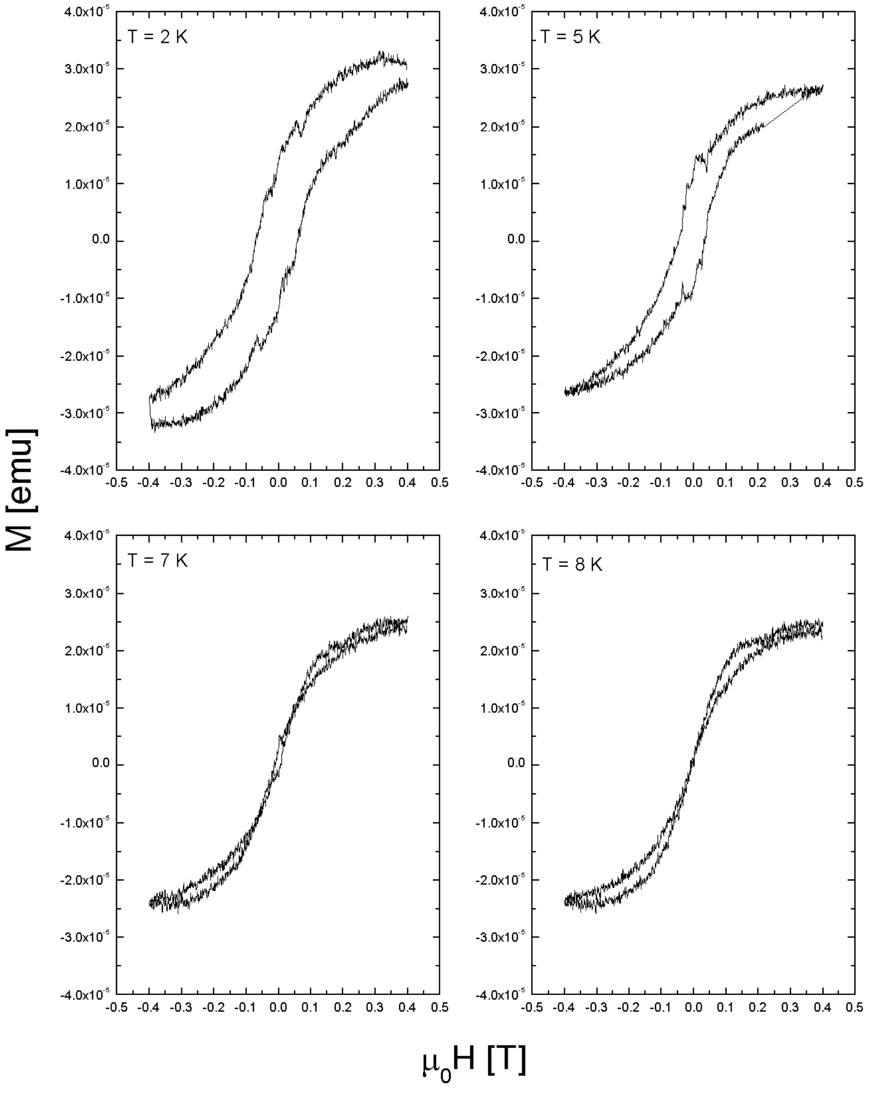

Figure 2.23: Temperature dependence of the magnetization of Nb nanowires measured in a VSM. The hysteresis loops close above 7 K. For low temperatures symmetric dips occur in the hysteresis loops. The position of the dips depends on the temperature.

can be suggested. The application relevance of the above described preparation technique seems only limited by the human imagination.

Chapter 3

Growth of RFe_2 on α-Al_2O_3

The highly magnetostrictive C15 Laves phases of the RFe_2 compounds show a large magnetocrystalline anisotropy. For $TbFe_2$, $DyFe_2$ and $Tb_{0.3}Dy_{0.7}Fe_2$ the magnetostriction coefficient $\lambda^{\epsilon,2}{\approx}\lambda_{111}$ is several times larger than $\lambda^{\gamma,2}{\approx}\lambda_{100}$ [8]. As most applications are restricted to in-plane driving field directions in order to avoid large demagnetization losses an in-plane magnetic easy axes is often required for magnetostrictive thin film materials.

Therefore, thin films with a [111] axis aligning in the film plane are interesting for large magnetoelastic responses, when the magnetic field is aligned in the film plane. (110)-oriented RFe_2 films posses an in-plane $[\bar{1}11]$-axis. (111)-oriented RFe_2 films, on the other hand, should exhibit a large magnetoelastic response when high fields are aligned out of the film plane. In the scope of this work, a new growth orientation of epitaxial RFe_2 films has been observed: The (211)-orientation which has an out-of plane direction fitted by 19° with regard to a [111] axis and furthermore an in-plane $[\bar{1}11]$ axis. With the possibility of depositing the same compound with these desired crystalline orientations and the same crystalline quality also on macroscopically faceted templates, a range of new opportunities for the applicability of RFe_2 systems is opened.

Due to the magnetoelastic coupling, the direction of the magnetic easy axis is directly related to the strain of the film. The minimum of the magnetoelastic energy for an isotropic ferromagnet is given by $E_{me} = -\frac{3}{2}\sigma\lambda_s cos^2\alpha$, where α is the angle between the directions of the magnetization and of the application of the stress, and λ_s is the saturation magnetostriction [38]. Therefore, the direction of the magnetic easy axis depends on the direction of the film stress σ. This implies an in-plane magnetic easy axis for a positive product $\sigma \cdot \lambda_s$, while a negative product leads to perpendicular anisotropy. $TbFe_2$, $DyFe_2$, and $Tb_{0.3}Dy_{0.7}Fe_2$ possess a positive magnetostriction. Mougin et al. have shown that the strains induced in RFe_2 films (here R = Y, Sm, Gd, Tb, $Tb_{0.3}Dy_{0.7}$, Dy, Er, and Lu) do not depend on the bulk lattice parameter of the compound, rendering the misfit with the buffer irrelevant [44]. Therefore, a substrate had to be chosen which allows the epitaxial RFe_2 film growth and induces an in-plane tensile stress to the considered RFe_2 films. Huth and Flynn have shown that $LiNbO_3$ substrates induce a compressive strain in the RFe_2 film plane, yielding an easy out-of-plane magnetization, while sapphire substrates induce an in-plane tensile stress, leading to an easy in-plane magnetization [12]. Therefore, sapphire substrates had been chosen as templates for the RFe_2 growth.

To obtain high quality samples for magnetic and magnetoelastic measurements, the preparation parameters of thin epitaxial RFe_2 films on sapphire substrates had to be optimized for the employed MBE chamber. At the beginning of this work, the growth results of Oderno et al. and Huth and Flynn [10, 11] for (110)- and (111)-oriented films on sapphire a-plane had to be reproduced. With the knowledge of the appropriate parameters, the new (211) growth orientation of RFe_2 on sapphire m-plane could be prepared and explored. The crystal quality of the films and their strain state was determined by two-circle and four-circle X-ray diffraction.

In the first section of this chapter, the sequences and parameters for the preparation of epitaxial RFe_2 films on sapphire substrates are described. Afterwards, all different growth orientations employed in this work are presented in different sections.

3.1 Preparation sequence of RFe_2 films

Within the scope of this work approximately 250 RFe_2 films with different crystal orientations have been prepared on sapphire substrates. The substrates were cleaned by organic solvents and water as described in chapter 2. Sapphire a-plane and non-faceted sapphire m-plane substrates were employed as purchased without pre-annealing. Faceted sapphire m-plane substrates were prepared by pre-annealing at different temperatures, resulting in different facet sizes as detailed in chapter 2. In analogy to the growth of Nb and Mo on faceted sapphire, no dependence of the growth properties of RFe_2 films on the facet size could be observed.

The RFe_2 compound melt peritectically and do not have a volatile component. Therefore the rate of the evaporated materials has to be controlled precisely to assure a phase-pure formation of the Laves phase.

For the preparation of epitaxial RFe_2 films on sapphire a buffer layer is needed. Of all the elements in the periodic table only the group VB and VIB elements (V, Nb, Ta, Cr, Mo, and W) react very little with the rare earth elements [122]. Thin Nb films, for example, are extensively used as buffer layers for the epitaxial growth of other metals and have proven to be useful for the preparation of epitaxial rare earth superlattices to avoid substrate-induced oxidation [123, 124, 125, 126]. The above mentioned bcc metals grow epitaxially (110)-oriented on sapphire a-plane [13, 23, 24, 127, 128]. For the RFe_2 compounds, these orientation is suitable for a (110)- or (111)-oriented growth [10, 11, 95, 98]. Huth and Flynn have shown that RFe_2 compounds do not interdiffuse into these materials when deposited at temperatures up to 550°C [11]. Due to their reduced melting points and evaporation temperatures compared to other possible transition metals employed for the buffer layer growth of RFe_2 like Ta and W, Nb and Mo buffer layer have been chosen in this work. In the beginning, approximately 30 calibration films of Nb and Mo were prepared on sapphire a-plane to determine the deposition rate and to optimize the buffer layer growth. Later, the Nb (110)-oriented films were used as a buffer layer for RFe_2 (110)-oriented films, while (110)-oriented Mo is known to be a good buffer layer for the (111)-oriented RFe_2 growth [10, 11]. As one result of this work it could be shown, that Nb and Mo grow twin-free (211)-oriented on non-faceted and faceted sapphire m-plane, as was already discussed in chapter 2. Films with such an excellent epitaxial quality were obvious candidates as a buffer layer for the epitaxial growth of non-faceted an faceted RFe_2 films on sapphire m-plane.

The thin RFe_2 film preparation sequence was started with a 500 Å thick film of Nb or Mo, deposited by means of electron beam evaporation. The rate of the transition metals was 0.3 Å/s and was controlled by the quadrupole mass spectrometer. The sapphire substrates were held at elevated temperatures of 850°C. The optimal temperature for the epitaxial growth of (110)-oriented Nb single crystals on sapphire $(11\bar{2}0)$ is known to be 900°C ± 50°C [124]. During the evaporation of the refractory metals the RHEED pattern were outshone by the electron beam evaporator, as already explained in chapter 2. Accordingly, a first RHEED characterization of the crystal quality of the buffer layer could only be gained after the deposition. The energy of the electron beam in the RHEED observations was set to 15 kV.

After the preparation of the buffer layer, the films were cooled down to 530°C within 10 minutes. At 530°C a Fe seed layer of approximately 20 Å thickness was deposited out of the electron beam evaporator at a rate of 0.13 Å/s. Again, the Fe deposition rate was controlled by the quadrupole mass spectrometer. This Fe seed layer is mandatory for the (110)-oriented growth of the RFe$_2$ alloys on Nb (110). For the (111)-oriented growth on Mo (110) it is not obligatory but helpful. For the crystalline RFe$_2$ growth on (211)-oriented Nb or Mo it is essential. Dy and Tb were evaporated out of effusion cells. The RFe$_2$ compound was co-deposited with a rare earth rate of 0.21 Å/sec and a Fe rate of 0.13 Å/s. This gives a RFe$_2$ growth rate of 0.25Å/s. The Fe rate again was controlled by the quadrupol mass spectrometer while the constant temperatures of the effusion cells ensured constant rare earth rates. In addition to the preparation of pure DyFe$_2$ and TbFe$_2$ compounds, films of the (pseudo-ternary composition) Tb$_{0.3}$Dy$_{0.7}$Fe$_2$ were generated. During RFe$_2$ growth the substrate temperature was kept at 530°C. The crystal quality of the RFe$_2$ films was observed with in-situ RHEED during the growth.

For crystallographic characterization the films were investigated by X-ray diffraction. The newly observed crystal orientation of the transition metals and RFe$_2$ films prepared on faceted and non-faceted sapphire m-plane was evaluated by the systematic scans described in chapter 2. Knowing the principle in-plane orientation and after determining the orientation matrix of the films, φ- and Q-scans were performed to determine the epitaxial quality.

The determination of the lattice parameters and the strain of the films was performed by several refinement steps of the orientation matrix. The bulk lattice parameters of DyFe$_2$ and TbFe$_2$ are a=7.325 Å and a=7.347 Å, respectively [129]. Mougin et al., Oderno et al., and Huth and Flynn have shown that the RFe$_2$ exhibit a strain relaxation of the lattice mismatch between film and buffer during the growth [10, 11, 44]. The different thermal expansion coefficients of the sapphire substrate and the RFe$_2$ films are thought to induce a stress in the films during the cooling process after preparation, and to be the reason for the observed strains in the films at room temperature. Therefore, the strain ϵ_{xy} in the film plane is assumed to be isotropic, and can be determined by:

$$\epsilon_{xy} = \frac{a_\perp - a_\parallel}{2a} \tag{3.1}$$

Here, $a_\perp$ and $a_\parallel$ are the lattice constants perpendicular and parallel to the film plane, respectively.

3.2 Epitaxial RFe$_2$ (110) films

Epitaxial (110)-oriented RFe$_2$ film growth can be achieved by using a Fe seed layer on a Nb (110) buffer layer on sapphire a-plane [10, 97, 99]. The in-plane orientation of the Nb buffer layer is $[001]_{Al_2O_3}||[\bar{1}11]_{Nb}$ and $[\bar{1}20]_{Al_2O_3}||[\bar{1}1\bar{2}]_{Nb}$. Mougin et al. report the formation of a NbFe-φ phase when the Fe seed layer is deposited [44, 99]. From the analysis of the RHEED pattern they observe a rectangular mesh with lattice parameters $a_{r.m.}$=7.0±0.1 Å and $b_{r.m.}$=4.8±0.1 Å. The epitaxial relationship of this NbFe-φ phase with regard to Nb is: $[001]_{Nb}||a_{r.m.}$ and $[\bar{1}10]_{Nb}||b_{r.m.}$. The RFe$_2$ cubic lattice follows the Nb orientation with $a_{r.m.}||[001]_{RFe_2}$ and $b_{r.m.}||[\bar{1}10]_{RFe_2}$. The epitaxy is favored by the decrease of mismatch between the parameters of the Laves phase compound and the buffer, especially along the [001] direction. The complete epitaxial relationship of the system can be recapitulated to

$$\begin{aligned}&(11\bar{2}0)_{Al_2O_3}||(110)_{Nb}||(110)_{RFe_2}\\&[001]_{Al_2O_3}||[\bar{1}11]_{Nb}||[\bar{1}11]_{RFe_2}\\&[\bar{1}20]_{Al_2O_3}||[\bar{1}1\bar{2}]_{Nb}||[\bar{1}1\bar{2}]_{RFe_2}\end{aligned} \tag{3.2}$$

The epitaxial orientation of RFe$_2$ (110) on Nb (110) on sapphire a-plane is shown in Figure 3.1.

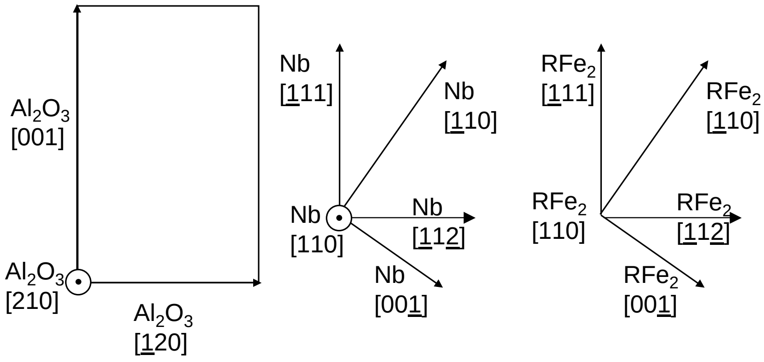

Figure 3.1: Schematic of the lateral orientations of RFe$_2$ on Nb on sapphire a-plane.

For the preparation route as described above, RHEED reveals a 2d growth of Nb on sapphire a-plane, shown in Figure 3.2. The Fe seed layer also reveals 2d growth with a rectangular symmetry, as shown in Figure 3.3. By starting the RFe$_2$ deposition, the RHEED image almost immediately becomes diffuse. With a deposition rate of 0.25 Å/s, the first RHEED reflections of (110)-oriented RFe$_2$ can be observed after 30 seconds deposition time. In the beginning the reflections are spot-like, indicating a 3d growth mode, see Figure 3.4. After 15 minutes stripes tend to become visible between the spots, pointing towards a smoothing of the surface, but the growth mode stays mainly 3d during the complete deposition time. A similar growth behavior of RFe$_2$ is described in the literature [10, 44, 97]. This behavior implies the formation of islands at the beginning of the growth, as also reported in the literature. The formation of three dimensional islands is driven by the large film to buffer misfit [44].

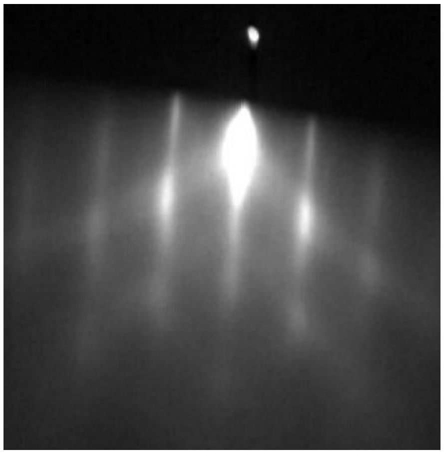

Figure 3.2: RHEED image of a 500Å thick Nb (110)-oriented buffer layer. Beam $\|$ $[\bar{1}11]$.

Two-circle X-ray diffraction reveals a good crystal quality of the (110)-oriented Nb films. The Nb rocking curve displayed in the left image of Figure 3.5 consists of a broad background component with a width (FWHM) of 0.5° and a pronounced narrow component with a width of 0.05°.

The $(\omega/2\theta)$-scan shown in Figure 3.5 reveals the (110)-oriented growth of RFe$_2$ on Nb (110). The width of the rocking curves of the $(ll0)$-reflections amounts to 0.9°.

In-plane the RFe$_2$ films epitaxially ordered as can be seen in the Q-scan shown in Figure 3.6. Next to the in-plane peaks slight stripes occur, which indicate a polycrystalline component in the film. To further check the lateral orientation, a

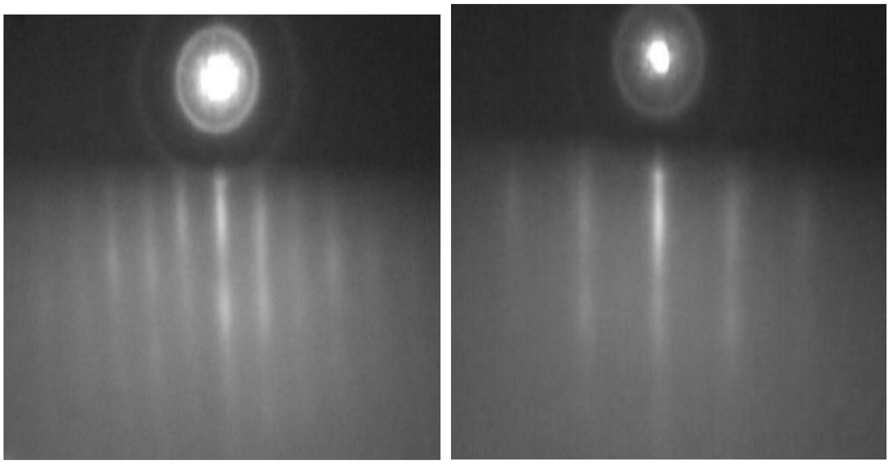

Figure 3.3: RHEED image of a Fe seed layer on Nb (110) after 3 minutes deposition time. Left: Beam $\parallel$ a$_{r.m.}$. Right: Beam $\parallel$ b$_{r.m.}$.

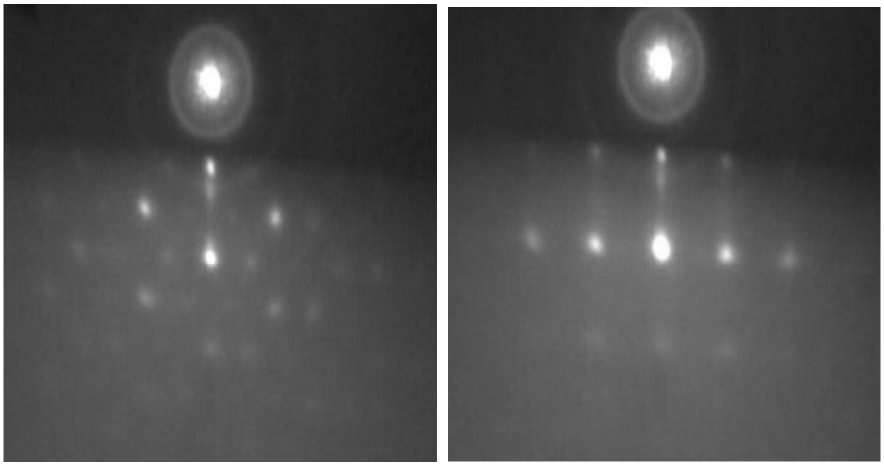

Figure 3.4: RHEED image of (110)-oriented DyFe$_2$. Left: Beam $\parallel$ $[\bar{1}11]$, deposition time 5 minutes. Right: Beam $\parallel$ $[\bar{1}10]$, deposition time 15 minutes.

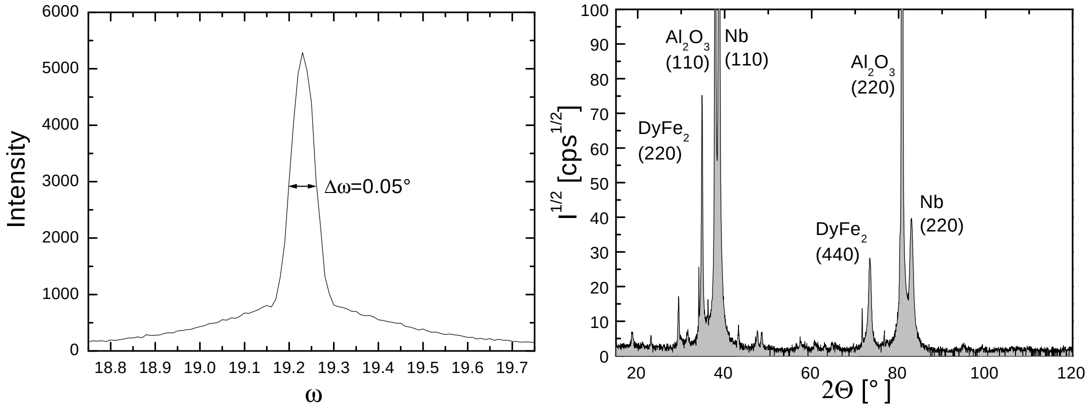

Figure 3.5: Left: Rocking curve of Nb (110) deposited on sapphire a-plane. Right: Bragg scan of RFe$_2$ on Nb (110) on sapphire a-plane.

φ-scan of the DyFe$_2$ {202} peaks was performed. The peak positions coincidence with the peak positions of a corresponding φ-scan of the Nb {101} reflections. Furthermore, the sapphire {030} peaks occur at the expected angles, see Figure 3.6. The width $\Delta\varphi$ of the DyFe$_2$ peaks is 2.2°. The width of the Nb peaks is 0.6°. The width of the sapphire peaks is limited by the resolution of the diffractometer and amounts to 0.2°. In addition to the four expected DyFe$_2$ {202} peaks, four further weak DyFe$_2$ peaks can be observed. They can be described by (110)-oriented crystals rotated in plane by ±65° with regard to the main orientation. The origin of these are stacking faults during the growth.

From the orientation matrix the lattice constants of the DyFe$_2$ films are found to be: a = 7.310Å; b = 7.298Å; c = 7.395Å. $\alpha = 89.5°$, $\beta = 90.3°$, $\gamma = 91.0^{c}irc$. The fit amounts to 0.0015.

The lattice constants $a_\perp$ and $a_\parallel$ are therefore:

$$\begin{aligned} a_\perp &= \sqrt{2} \cdot \frac{a_{[220]}}{2} = \frac{\sqrt{a^2+b^2}}{\sqrt{2}} = 7.304\text{Å} \\ a_\parallel &= a_{[00\bar{1}]} = 7.395\text{Å} \end{aligned} \tag{3.3}$$

This leads to ϵ_{xy} = -0.6%. This strain agrees with the values obtained by Oderno et al. [130] and is slightly higher than the one calculated by Mougin et al. [45]. A similar lattice constant of $a_{[220]}$ = 7.310 Å can also be determined by two-circle measurements.

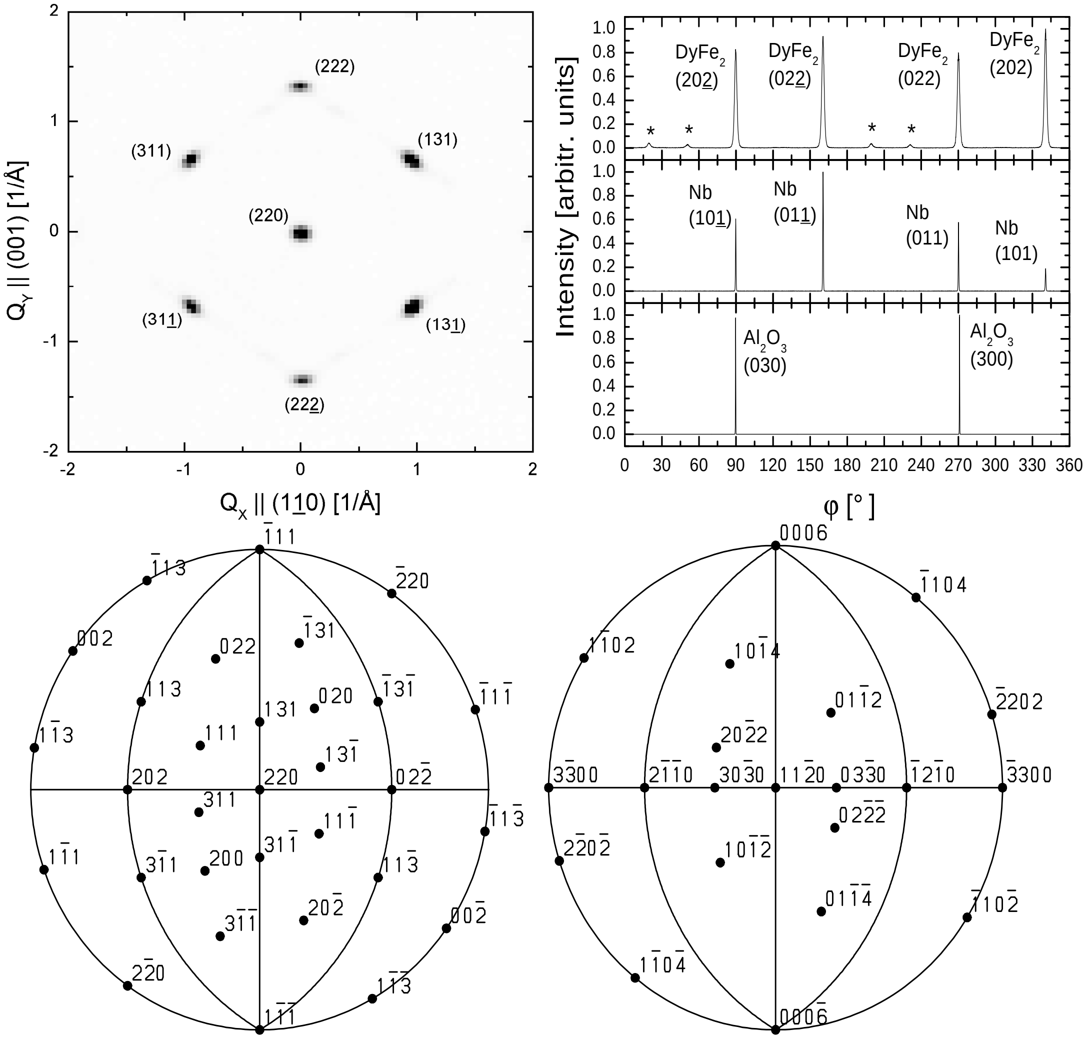

Figure 3.6: Up left: Q-Scan of the DyFe$_2$ (220) plane (asterisks: ± 65° rotated domains). Up right: φ-scan of the DyFe$_2$ {202} peaks (top), the Nb {101} peaks (middle) and the sapphire {030} peak (bottom). A comparison with the stereographic projections of fcc(110) (bottom left) and sapphire a-plane (bottom right) proves that the alignment of the peaks at the same φ-angles give the in-plane epitaxial relationship.

3.3 Epitaxial RFe$_2$ (111) films

The (111)-oriented epitaxial RFe$_2$ film growth can be achieved by using a Mo (110) buffer layer on sapphire a-plane [11]. The in plane orientation of the Mo buffer layer is $[\bar{1}11]_{Mo} \| [001]_{Al_2O_3}$ and $[\bar{1}1\bar{2}]_{Mo} \| [\bar{1}20]_{Al_2O_3}$. Contrary to the (110)-oriented RFe$_2$ growth on Nb (110), the (111)-oriented growth on Mo (110) does not require a Fe seed layer. In-plane the RFe$_2$ cubic lattice has the following orientation with regard to the Mo lattice: $[\bar{1}10]_{RFe_2} \| [\bar{1}10]_{Mo}$ and $[11\bar{2}]_{RFe_2} \| [00\bar{1}]_{Mo}$. The same relationship between RFe$_2$ film and the transition metal buffer layer is also reported by Jaren et al. for the (111)-oriented growth of TbFe$_2$ on W (110) [95]. The lateral orientation of these films is shown in Figure 3.7.

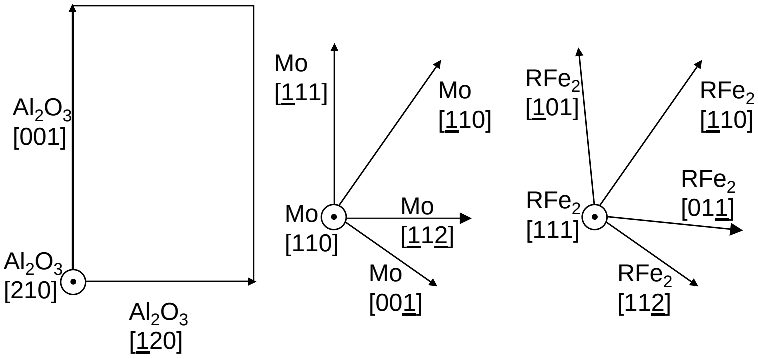

Figure 3.7: Schematic of the lateral orientations of RFe$_2$ on Mo on sapphire a-plane.

RHEED reveals a 2d growth of Mo on sapphire a-plane, as is shown in Figure 3.8. The growth mode of RFe$_2$ (111) does not deviate strongly from the (110)-oriented RFe$_2$ growth behavior: With a deposition rate of 0.25 Å/s the first RHEED reflections of (111)-oriented RFe$_2$ can be observed 20 seconds after the start of the deposition. At the beginning the growth is 2d, see Figure 3.9. After 2 minutes the growth is 3d with spot-like reflections occurring. After about 20 minutes the peaks are connected by stripes again. This rough 2d growth mode is for the rest of the deposition time. A similar growth behavior is also observed by Huth and Flynn [11].

X-ray analysis reveals (110)-oriented Mo films of good quality with a width of the rocking curve of 0.02°, as is shown in the left part of Figure 3.10. Reflectrometry measurements, shown in the right part of Figure 3.10, reveal the (111)-oriented growth of RFe$_2$ on Mo (110) with a good crystalline quality and a width of the rocking curves of 0.9°.

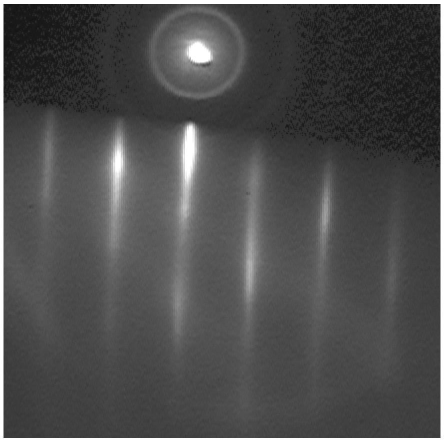

Figure 3.8: RHEED image of a 500Å thick Mo (110)-oriented buffer layer. Beam $\parallel$ $[1\bar{1}1]$.

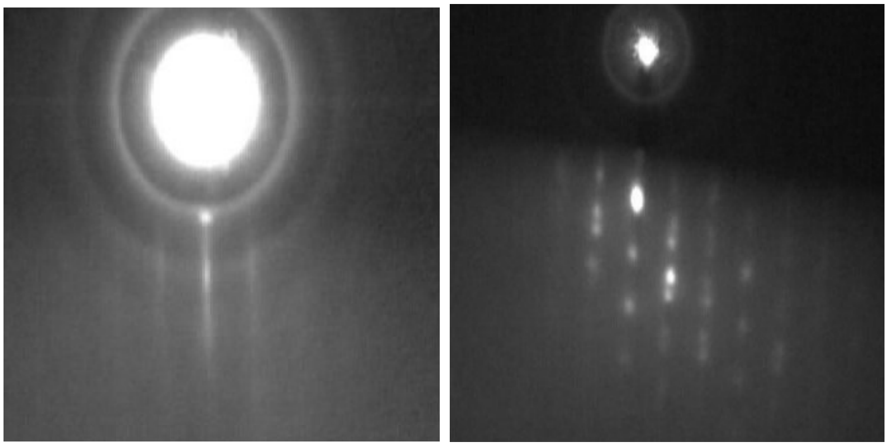

Figure 3.9: RHEED image of a (111)-oriented DyFe$_2$ film. Left: Beam $\parallel$ $[1\bar{1}1]$, t$_{dep.}$ = 60 sec. Right: Beam $\parallel$ $[1\bar{1}1]$, t$_{dep.}$ = 5 min.

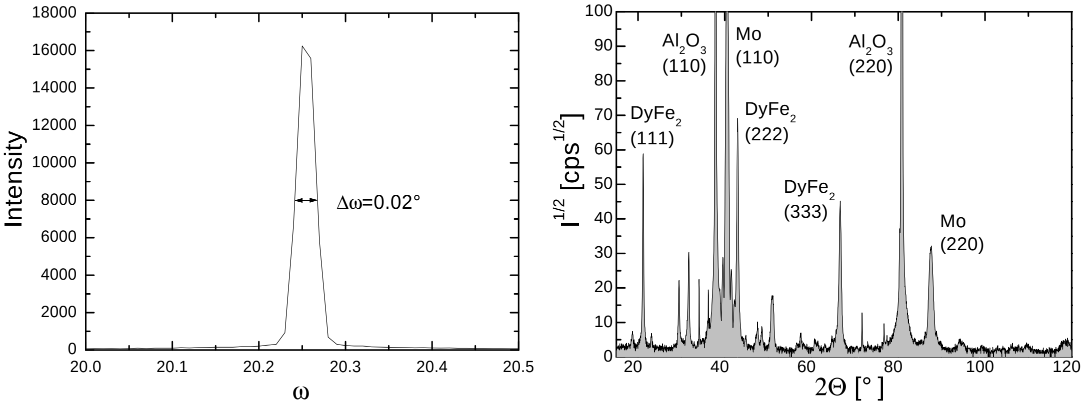

Figure 3.10: Left: Rocking curve of Mo (110) deposited on sapphire a-plane. Right: Bragg scan of DyFe$_2$ on Mo (110) on sapphire a-plane.

In-plane the films are epitaxially ordered as demonstrated in the Q-scan given in Figure 3.11. The epitaxial relationship as indicated in Figure 3.7 is proven by a ϕ-scan of RFe$_2$ (220) shown in the upper right part of Figure 3.11.

From the orientation matrix the lattice parameters of DyFe$_2$ thin films are determined to be: a = 7.345Å; b = 7.350Å; c = 7.349Å. $\alpha = 90.3°$, $\beta = 90.4°$, $\gamma = 90.4°$. The fit amounts to 0.001

The lattice constants a$_\perp$ and a$_\parallel$ are therefore:

$$\begin{aligned} a_\perp &= \frac{d_{[111]}}{\sqrt{3}} = \frac{\sqrt{a^2+b^2+c^2}}{\sqrt{3}} = 7.348\text{Å} \\ a_\parallel &= \frac{d_{[11\bar{2}]}}{\sqrt{6}} = \frac{\sqrt{a^2+b^2+(2c)^2}}{\sqrt{6}} = 7.349\text{Å} \end{aligned} \tag{3.4}$$

This leads to a negligible strain ϵ_{xy}. Measurements in the two-circle diffractometer, on the other hand, reveal a lattice constant of 7.310Å. With this value and assuming a conservation of the lattice volume the in-plane strain is of the same size of -0.6% like for (110)-oriented films. The error of the lattice determination in the four circle diffractrometer can occur due to a mounting misalignment of the sample with regard to the incident beam. Négre et al. report for (111)-oriented TbFe$_2$ films prepared by PLD an out-of-plane strain of $\epsilon_\perp$ = -0.15%. In-plane they observe a strain of $\epsilon_\parallel$ = 0.7% [96]. This gives a total strain of ϵ_{xy} = -0.42%. Similar in-plane strains of -0.5% are also reported by Huth and Flynn for (111)-oriented TbFe$_2$ films prepared by MBE [11].

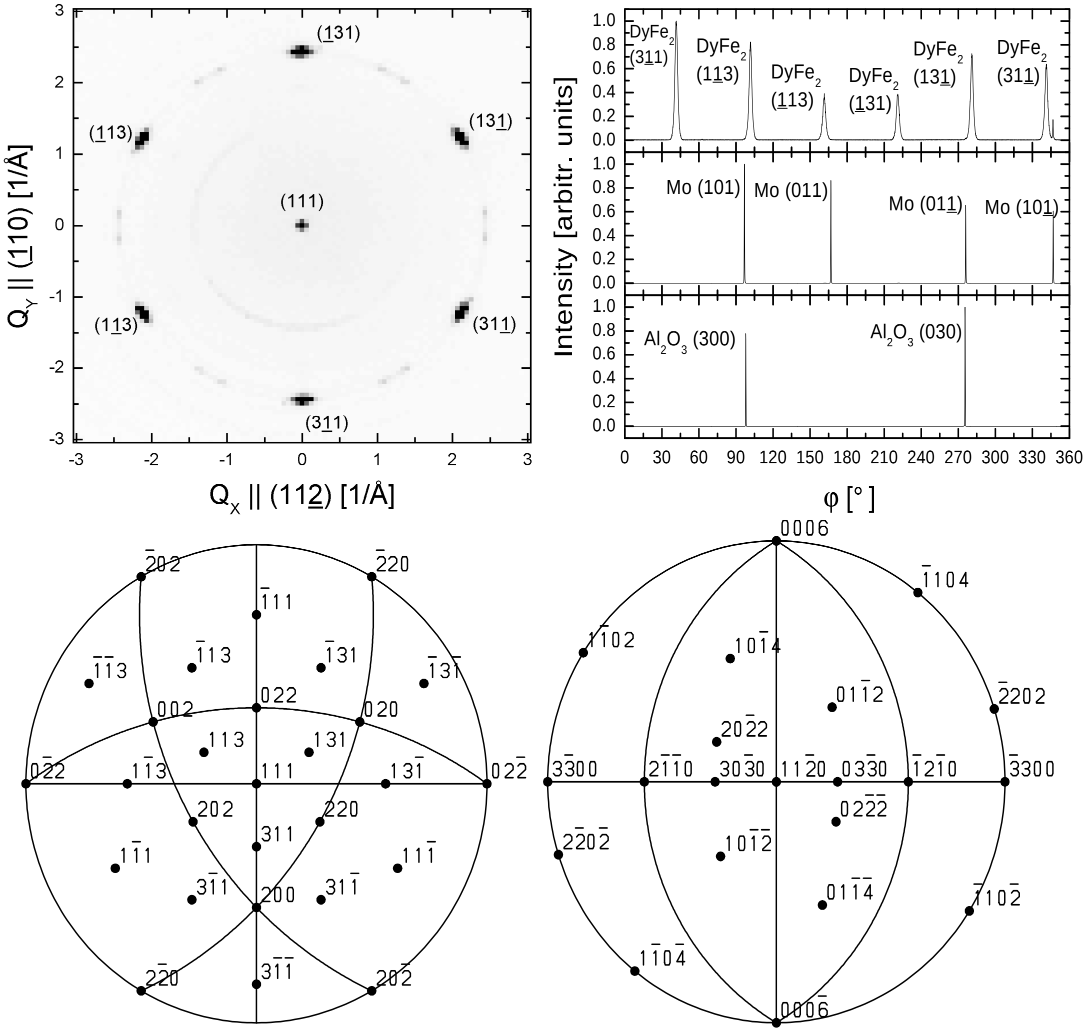

Figure 3.11: Up left: Q-Scan of the TbFe$_2$ (111) plane. Up right: φ-Scan of the DyFe$_2$ (220) reflections (top), the Mo (110) reflections (middle) and the sapphire (300) reflections (bottom). Bottom: Stereographic projections of fcc (110) and sapphire a-plane.

3.4 Crystalline RFe$_2$ on Mo (211)

The growth of Mo on faceted and non-faceted Al$_2$O$_2$ m-plane was already discussed in chapter 2. Four-circle X-ray analysis and TEM measurements reveal a twin-free (211)-oriented growth of Mo on both, faceted and non-faceted surfaces. Because of the excellent buffer layer properties of (110)-oriented Mo films, the growth of RFe$_2$ on (211)-oriented Mo layers was analyzed. By means of RHEED observation during the RFe$_2$ growth the necessity of employing a 20 Å Fe seed layer on top of the Mo buffer was obvious after a few preparation attempts.

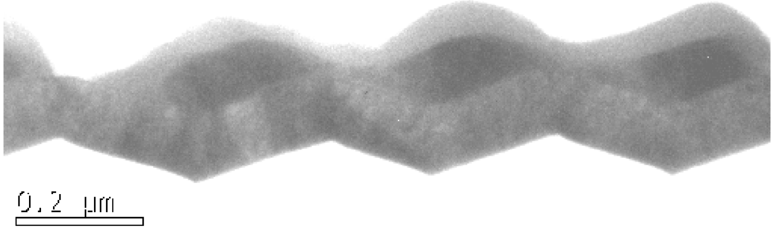

Figure 3.12: TEM image of TbFe$_2$ on Mo (211) on faceted sapphire m-plane. The Mo layer reproduces the facets rather exactly. The TbFe$_2$ (dark regions) is already partly oxidized. TbFe$_2$ grows preferentially on the Mo (111) plane (long facet plane).

However, in contradistinction to films on sapphire a-plane, no twin-free epitaxial growth of RFe$_2$ occurs on Mo (211). Instead, the appearance of multiple crystallographic orientations was observed by four-circle X-ray analysis. Out of these, one is (211)-oriented. The others are given by spinel twin laws. The exact crystallographic orientations were not analyzed in the scope of this work. A preferred (211)-oriented growth behavior with the occurrence of twins is also observed for the growth of RFe$_2$ bulk material [66]. From the TEM measurement, shown in Figure 3.12, it can be seen that TbFe$_2$ grows preferential on the (111)-oriented Mo facet.

For further magnetic and magnetoelastic measurements the RFe$_2$ films on Mo on sapphire m-plane are regarded as modulated or non-modulated polycrystalline films.

3.5 Epitaxial RFe$_2$ (211) films

In analogy to Mo, Nb also grows (211)-oriented on faceted and non-faceted sapphire m-plane, as already demonstrated in chapter 2. Furthermore, Nb (110) provides the (110)-oriented growth of RFe$_2$ with a cube to cube relationship of the lattice directions. This property, which is different for growth on Mo, was expected to allow the preferential (211) growth orientations. Therefore, the (211)-oriented Nb buffers were even more promising candidates as template for the epitaxial RFe$_2$ growth. The preparation of RFe$_2$ on Nb (211) with a 20 Å Fe seed layer was performed in the way described above.

In order to get an overview of the epitaxial relationship of the layers, the main result of the characterization is listed first and will be proved in the following: Four-circle X-ray analysis reveals a twin-free (211)-oriented growth of the rare earth compounds without evidence of any other growth domains. The lateral relationship of the Nb and RFe$_2$ crystals is again cube to cube like in the (110)-oriented case. Like in the case of Nb grown on sapphire m-plane, it has to be emphasized that the crystalline orientations and properties are the same for RFe$_2$ films prepared on faceted as well as on non-faceted templates. Again, this implies a homogenous overgrowth of the rare earth iron compounds over the facet ridges and valleys. Neglecting the Fe seed layer, the following relationships of the cubic axes are obtained:

$$\begin{aligned}
&[310]_{Al_2O_3}\|[211]_{Nb}\|[211]_{RFe_2}\\
&[010]_{Al_2O_3}\|[01\bar{1}]_{Nb}\|[01\bar{1}]_{RFe_2}\\
&[001]_{Al_2O_3}\|[\bar{1}11]_{Nb}\|[\bar{1}11]_{RFe_2}
\end{aligned} \tag{3.5}$$

The in-plane orientations are sketched in Figure 3.13.

For the growth of RFe$_2$ on faceted Nb (211) buffer layers, the RHEED images of the RFe$_2$ films were similar to the ones obtained for the faceted bcc metals: Aligning the beam in the [010]-direction of the substrate, two tilted rows of stripes occur. This indicates a crystalline growth of the RFe$_2$ on the faceted surface, but gives no further information of the growth mode of the film. Further information of the growth mode of RFe$_2$ can be deduced from the deposition on non-faceted (211) Nb.

Compared to the RHEED images of the Fe seed layer on Nb (110) the intensity of the Fe seed reflections on Nb (211) are rather weak. Parallel stripes are

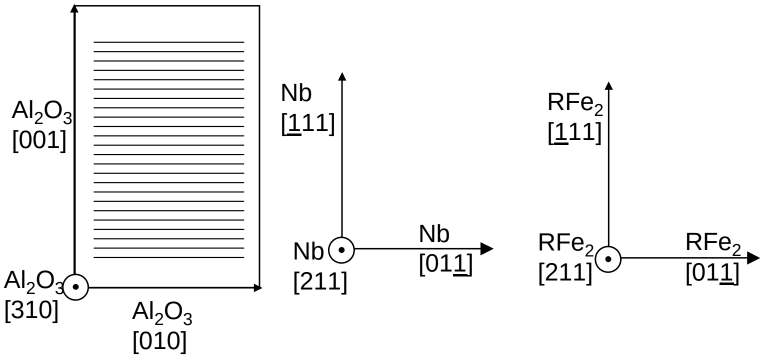

Figure 3.13: Schematic of the lateral orientation of RFe$_2$ on Nb on sapphire m-plane.

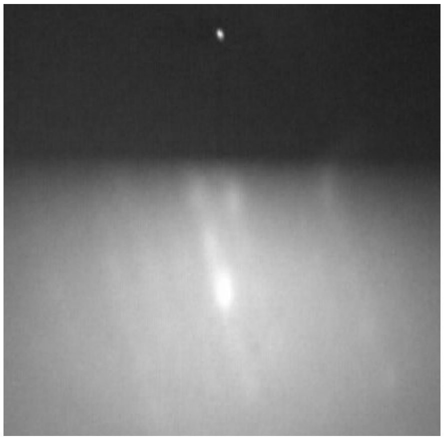

Figure 3.14: RHEED image of Fe seed on non-undulated Nb (211) after 3 minutes preparation time. Beam $\parallel$ a$_{r.m.}$.

observed, but they are tilted by an angle of 12° to the beam normal as shown in Figure 3.14.

The initial growth mode of RFe$_2$ is 3d: After the first 20 seconds of deposition single reflection peaks occur. After about 20 minutes of preparation these points get more and more connected by stripes, indicating a transition to a 2d growth mode. However, the brightness of the RHEED patterns decreases with increasing preparation time, which indicates a surface roughening during the growth. Figure 3.15 shows RHEED patterns of a DyFe$_2$ film deposited on non-faceted sapphire m-plane with the electron beam aligned in two different directions, taken after 10 minutes deposition time.

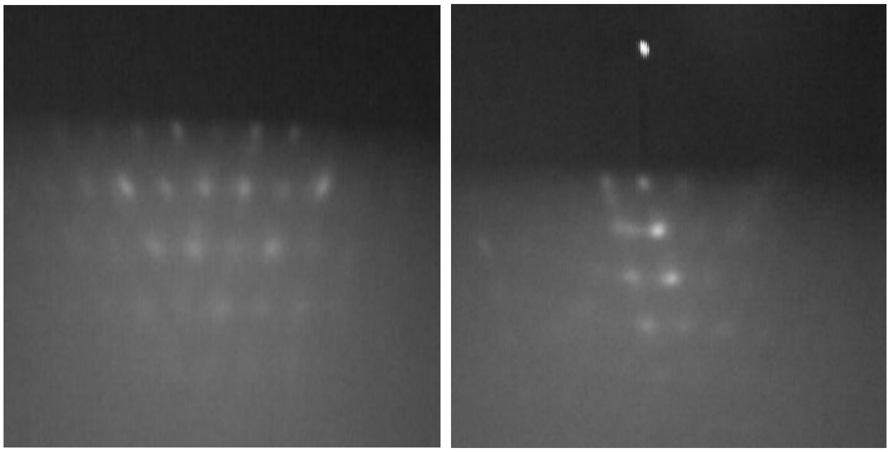

Figure 3.15: RHEED image of DyFe$_2$ (211) on Nb (211) on non faceted sapphire m-plane. Left: Beam $\perp$ $[\bar{1}11]_{DyFe_2}$. Right: Beam $\parallel$ $[01\bar{1}]_{DyFe_2}$.

The in-plane relationship and the comparable quality of faceted and non-faceted films is indicated by φ-scans of the RFe$_2$ (022) and RFe$_2$ (220) reflection, as shown in Figure 3.16.

The Q-scan of a faceted RFe$_2$ film displayed in Figure 3.17 shows the first layer of the [211]-zone, that is the plane spanned by the reciprocal lattice vectors $[01\bar{1}]$ and $[\bar{1}11]$ at a distance $d_{(211)}$ from the origin. It reveals no other reflections than the expected DyFe$_2$ {202} and {311}. The reflexes intensities varies from 103000 to 195000 counts/sec while the background is always below 200 counts/sec. The width of the reflexes is 2°. This again underlines the high epitaxial quality of the RFe$_2$ films even on the faceted template.

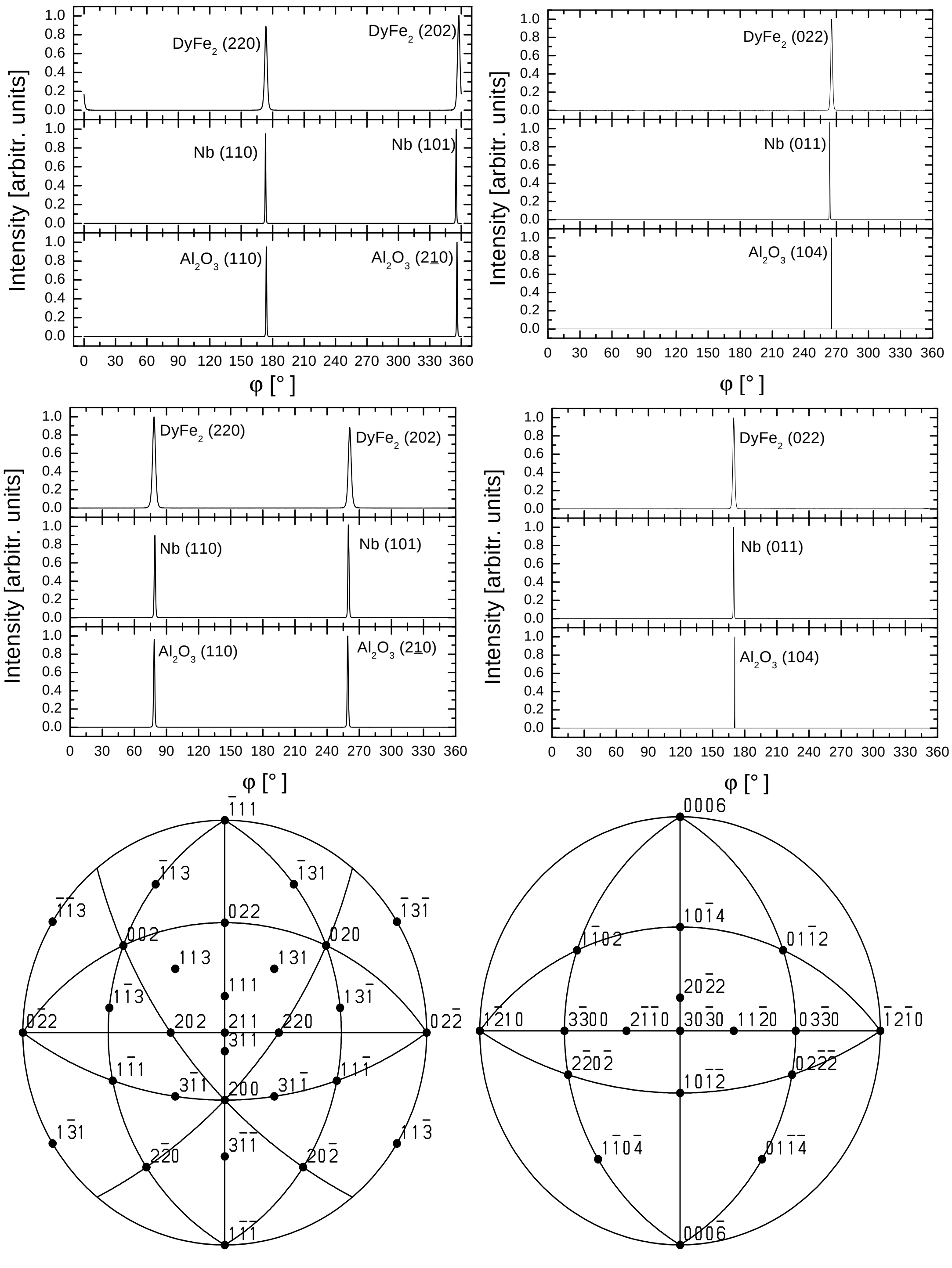

Figure 3.16: In-plane orientation of RFe$_2$ on Nb on non-faceted (top) and faceted (middle) sapphire m-plane: φ-scan of the DyFe$_2$ (022) (left) and (220) peak (right). Bottom: Stereographic projections of fcc (211) and sapphire m-plane.

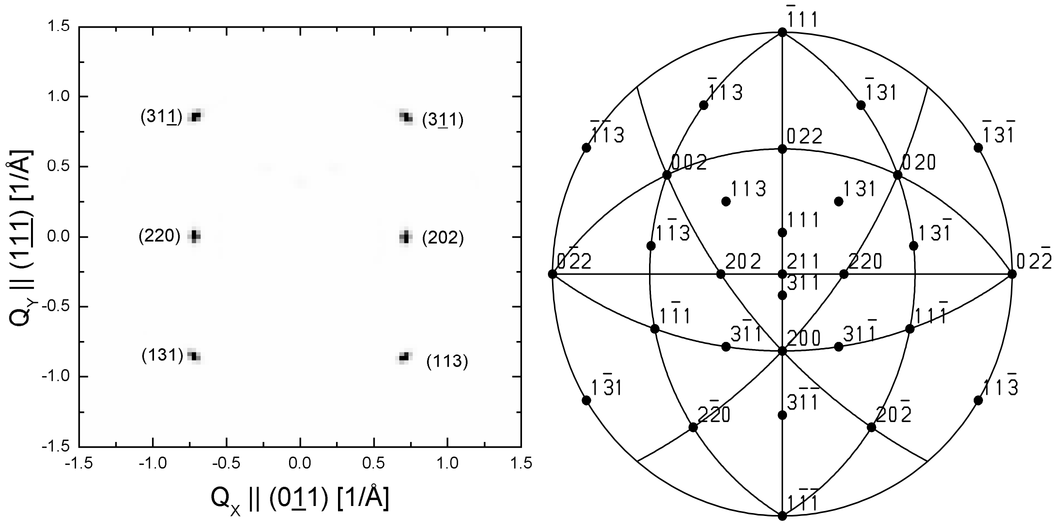

Figure 3.17: Left: Q-scan of the DyFe$_2$ (211) plane. Right: Stereographic projection of fcc (211).

From the orientation matrix of non-faceted DyFe$_2$ the following lattice constants are obtained: a = 7.319Å; b = 7.364Å; c = 7.355Å. $\alpha = 90.2°$; $\beta = 90.5°$; $\gamma = 90.5°$. The fit amounts to 0.003

The lattice constants $a_\perp$ and $a_\parallel$ are:

$$\begin{aligned} a_\perp &= \frac{d_{[211]}}{\sqrt{6}} = \frac{\sqrt{(2a)^2 + b^2 + c^2}}{\sqrt{6}} = 7.333\text{Å} \\ a_\parallel &= \frac{d_{[01\bar{1}]}}{\sqrt{2}} = \frac{\sqrt{b^2 + c^2}}{\sqrt{2}} = 7.360\text{Å} \end{aligned} \tag{3.6}$$

This leads to a strain of $\epsilon_{xy} = -0.2\%$.

Analogously, for faceted DyFe$_2$ thin films one obtains: a = 7.310Å; b = 7.359Å; c = 7.354Å. $\alpha = 90°$; $\beta = 90.5°$; $\gamma = 90.5°$. The fit amounts to 0.005

The lattice constants $a_\perp$ and $a_\parallel$ in this case are:

$$\begin{aligned} a_\perp &= \frac{d_{[211]}}{\sqrt{6}} = \frac{\sqrt{(2a)^2 + b^2 + c^2}}{\sqrt{6}} = 7.326\text{Å} \\ a_\parallel &= \frac{d_{[01\bar{1}]}}{\sqrt{2}} = \frac{\sqrt{b^2 + c^2}}{\sqrt{2}} = 7.357\text{Å} \end{aligned} \tag{3.7}$$

This leads to a strain of $\epsilon_{xy} = -0.2\%$.

Based on the lattice parameters as obtained by X-ray analysis in the four-circle diffraction, the strain of the (211)-oriented films is clearly reduced as compared to (110)- or (111)-oriented films. Still, due to possible mounting offsets in the four-circle and missing two-circle comparisons, the results have to be taken with a grain of salt.

Chapter 4

Magnetic properties of of RFe_2 films

One main task of this work was to characterize thin epitaxial RFe_2 films with regard to their applicability as magnetoelastic sensors or actuators. The crystallographic characterization of the prepared samples, as discussed in chapter 3, revealed a high crystal quality comparable to differently oriented films discussed in the literature. The magnetoelastic response of the epitaxial samples and magnetization curves of samples oriented in various crystalline directions were measured. The magnetic behavior of the films was measured in a vibrating sample magnetometer (VSM). The magnetoelastic properties of the samples were evaluated in the self designed magnetoelastic measurement setup explained in chapter 1.

In the first section of this chapter details of the performed measurements are presented. In the following sections the magnetic and magnetoelastic properties of RFe_2 films of different crystalline orientations are presented. In the last section the results are discussed.

4.1 Measurement procedures

The determination of the magnetoelastic coefficient b from the observed bending of a clamped bimorph is discussed in chapter 1. The corresponding equation [39]

$$b = \frac{Y_S t_S^2}{6(1+\nu_S^2)t_F}\left(\left(\frac{1}{R_\parallel}\right) - \left(\frac{1}{R_\perp}\right)\right) \tag{4.1}$$

is relying on the assumption that the length-to-width ratio of the clamped cantilever is larger than three. Therefore, the 10 mm × 10 mm substrates were cut to 10 mm × 3 mm stripes. The thickness of the substrates was unaltered and amounted to 0.5 mm. The edges of the cantilever were cut parallel and perpendicular to the sapphire [001] edges. Therefore, for one crystallographic growth orientation of the film, two different lateral crystalline orientations of the cantilever with the long axis parallel or perpendicular to sapphire [001] were prepared and measured. No significant dependence of the magnetoelastic response on the orientation of the substrate could be observed. Therefore, mainly results on samples with the long cantilever axis lying parallel to the sapphire c-axis are presented.

Cutting sapphire m-plane substrates in the above described way leads to edges parallel to the sapphire [001] and [010] axis, respectively. For the sapphire a-plane substrates the corresponding axes are the [001] and the [$\bar{1}$20] direction. Therefore, especially for the (110)- and (111)-oriented films, not all investigated magnetization directions were parallel to low indexed RFe$_2$ crystallographic axes. As discussed in chapter 3, the [$\bar{1}$11] direction of (110)-oriented films lies parallel to sapphire [001]. Parallel to sapphire [$\bar{1}$20] lies the RFe$_2$ [$\bar{1}1\bar{2}$] direction. Here, the next lower indexed in-plane direction is the RFe$_2$ [00$\bar{1}$] axis, which is rotated by and angle of 35°. In (111)-oriented RFe$_2$ films the situation is more difficult: Neither parallel nor perpendicular to sapphire [001] lies a low indexed RFe$_2$ axis. In both cases the next axes are of {110} form. They are rotated in the plane by approximately 5° with respect to the substrate edges. In (211)-oriented RFe$_2$ the sapphire [001] axis is parallel to RFe$_2$ [$\bar{1}$11] and the sapphire [010] axis is parallel to RFe$_2$ [01$\bar{1}$]. For generality, the magnetoelastic results and the according magnetization measurements are therefore discussed with respect to the axes of the substrate, wether the magnetization was aligned parallel or perpendicular to sapphire [001] in the corresponding system.

The magnetoelastic measurements were performed at room temperature in the self-designed setup explained in chapter 1. As already said, the magnetoelastic response depends strongly on the magnetic history of the sample. One possibility to circumvent this problem is to successively measure the magnetoelastic coefficient parallel ($b_{\parallel}$) and perpendicular ($\mathrm{b}_{\perp}$) to the cantilever's long axis. In the RFe$_2$ C15 Laves phases the resulting difference ($b_{\parallel}$ - $b_{\perp}$) is mainly equivalent to the magnetoelastic coefficient $b^{\epsilon,2}$.

To correlate the magnetoelastic signal with the magnetic state of the sample, magnetization measurements were performed in an Oxford ^{4}He vibrating sample magnetometer (VSM) at 300 K up to fields of 1.2 T. As already discussed in chapter 1, the magnetic anisotropy of a ferromagnet is influenced by the magnetoelastic coupling. Due to the tensile strain in the film plane of RFe$_2$ films deposited on sapphire substrates, as demonstrated in chapter 3, a preferred in-plane magnetization is expected. Differences in the magnetic anisotropy can therefore give information about the magnetoelastic coupling of the systems in consideration of the crystallographic orientation.

4.2 Epitaxial RFe$_2$ (110) films

(110)-oriented RFe$_2$ samples reveal an in-plane tensile strain of ϵ_{xy} = -0.6%. Due to the magnetoelastic coupling a pronounced anisotropy with a preferred in-plane magnetization should be induced. This anisotropy was observed for all (110)-oriented RFe$_2$ samples of the discussed systems. Figures 4.1, 4.3, and 4.5 show magnetization measurements of (110)-oriented DyFe$_2$, TbFe$_2$ and Tb$_{0.3}$Dy$_{0.7}$Fe$_2$ films, respectively. For magnetic fields up to 1.0 T no magnetic saturation of the [110] out-of-plane direction can be observed. The shape anisotropy is least pronounced in DyFe$_2$, while Tb$_{0.3}$Dy$_{0.7}$Fe$_2$ reveals a rather hard axis magnetization in the [110] direction. This can be concluded from the magnetization values at 1 T, which are close to the in-plane values in DyFe$_2$ [110], and by the opening of the hysteresis, which is much more distinct in DyFe$_2$ than in the two other systems.

In the film plane the hysteresis loops of (110)-oriented DyFe$_2$ and Tb$_{0.3}$Dy$_{0.7}$Fe$_2$ films reveal a similar behavior: The easier direction lies parallel to sapphire [$\bar{1}$20], and therefore parallel to the RFe$_2$ [$\bar{1}1\bar{2}$] axis. The loops are more squared than in the direction parallel to the sapphire c-axis, which is parallel to the RFe$_2$ [$\bar{1}$11] axis. In comparison, this squareness is more pronounced in DyFe$_2$ films, which also leads to a smaller coercive field of $B_C = 0.22$ T and a closing of the hysteresis at $B_S = 0.24$ T. In the ternary compound B_C is 0.27 T and the hysteresis closes at $B_S = 0.34$ T. The closing of the magnetization loops is not identical with the saturation of the system, as can be seen by the increase of the magnetization with increasing field above B_S. The magnetization is not completely saturated at 1 T[1] In the direction parallel to the sapphire c-axis the loops are more rounded,

---

[1] However, some publications define this closing of the loop as the saturation of the system.

leading to $B_C = 0.35$ T and $B_S = 0.4$ T for DyFe$_2$, and to $B_C = 0.3$ T and $B_S = 0.4$ T for Tb$_{0.3}$Dy$_{0.7}$Fe$_2$. In the plane the magnetization at 1 T is with 605 kA/m and 735 kA/m in DyFe$_2$ smaller than the 700 kA/m and 800 kA/m in the pseudo-ternary compound and smaller than the values of a bulk single crystal [8].

The non-accomplished saturation at 1 T was also observed in Terfenol-D bulk samples: For (110)-oriented single crystal disks Clark et al. showed that the non-saturated state results from the formation of an immobile domain structure. This consists of 109° domain walls between domains oriented along the easy $\langle 111 \rangle$ axes, inclined to the surface of the disk [131].

In TbFe$_2$ (110) the in-plane magnetic anisotropy is reduced compared to the two other systems: Both observed directions show nearly the same squared hysteresis shape. The direction parallel to TbFe$_2$ $[\bar{1}1\bar{2}]$ reveals a slightly larger magnetization at 1 T (805 kA/m) compared to the direction parallel to sapphire $[\bar{1}10]$ (725 kA/m). This result is surprising, because parallel to sapphire [001] lies the easy TbFe$_2$ $[\bar{1}11]$ axis, which should show a dominant behavior. The coercive field of TbFe$_2$ is increased when compared to the two other systems and amounts to $B_C = 0.6$ T. The closing of the loop occurs at 1 T.

All three systems show the characteristic step in the magnetization at magnetization reversal fields of ≈ 0 T. This step was observed in all of the RFe$_2$ films analyzed in this work and its possible origins will be discussed more detailed in the discussion part of this chapter. In (110)-oriented DyFe$_2$ and Terfenol-D the step is more pronounced in the easier magnetization direction.

The magnetoelastic response of a (110)-oriented DyFe$_2$ film is shown in Figure 4.2. The shape of the loop is of the butterfly-type as expected. The coercive field of the loop is 0.3 T, which is similar to the coercive field of the magnetization measurements. The absolute change of the magnetoelastic coefficient $\Delta b \approx \Delta b^{\epsilon,2}$ is -36.5 MPa for a maximum magnetic field of 1.1 T. The calculated change in the magnetostriction is $\Delta\lambda \approx \Delta\lambda^{\epsilon,2} = 573 \cdot 10^{-6}$, which is 90% of the value of single crystalline DyFe$_2$ bulk samples [8]. Obviously, the orthorhombic distortion is not saturated at the maximum applied field of 1.1 T. The fact, that the magnetoelastic response of epitaxial RFe$_2$ films does not saturate according to the magnetic signal is also discussed in the literature. Ciria et al. [97] observed no saturation of the magnetoelastic signal of (110)-oriented TbFe$_2$ films even at applied fields of 12 T. They proposed that a strained clamping to the underlying template could account for this fact. Also, some contribution of forced magnetoelastic distortion could

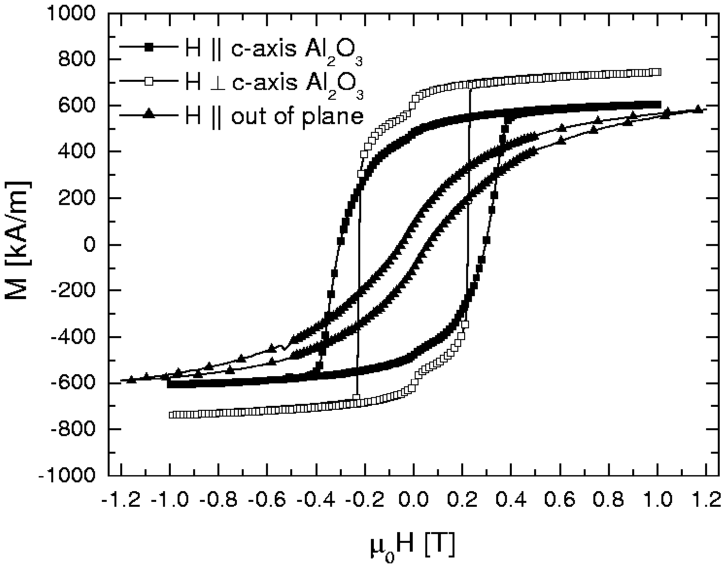

Figure 4.1: Magnetization vs. field of a (110)-oriented DyFe$_2$ film.

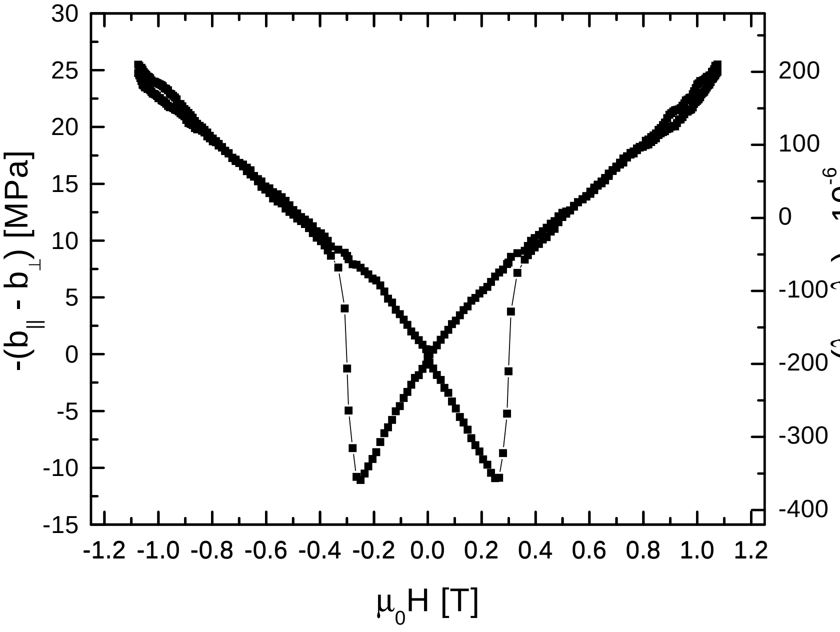

Figure 4.2: Magnetoelastic response of a (110)-oriented DyFe$_2$ film.

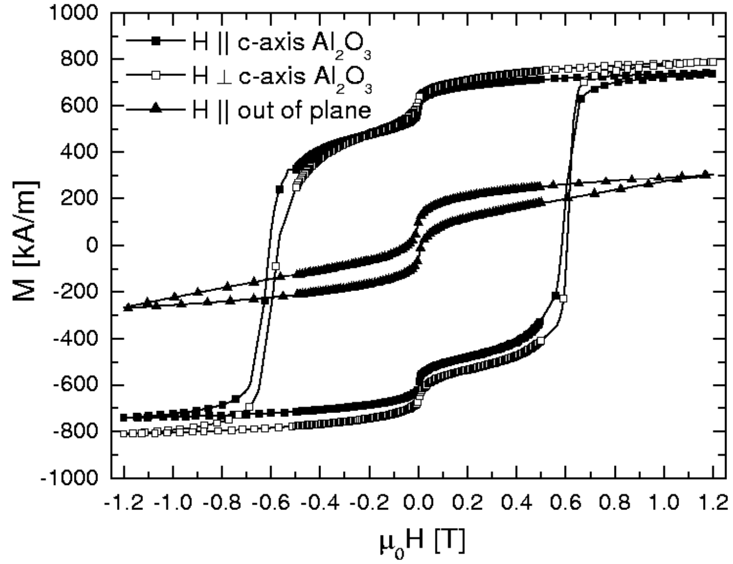

Figure 4.3: Magnetization vs. field of a (110)-oriented TbFe$_2$ film.

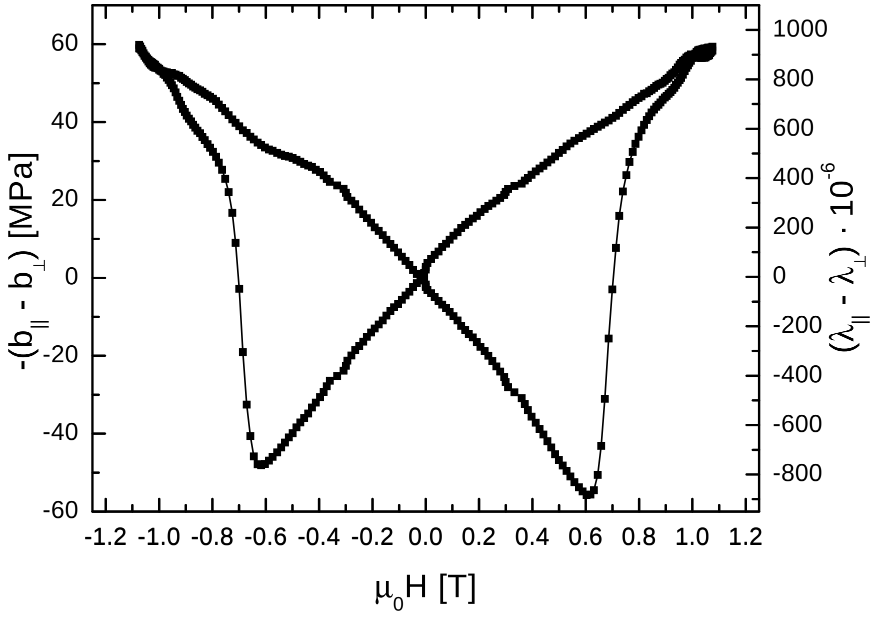

Figure 4.4: Magnetoelastic response of a (110)-oriented TbFe$_2$ film.

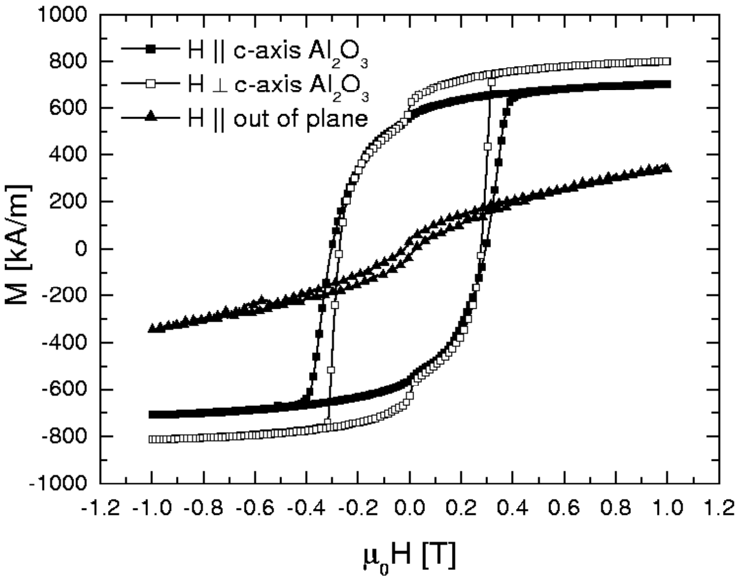

Figure 4.5: Magnetization vs. field of a 110)-oriented Dy$_{0.7}$Tb$_{0.3}$Fe$_2$ (film.

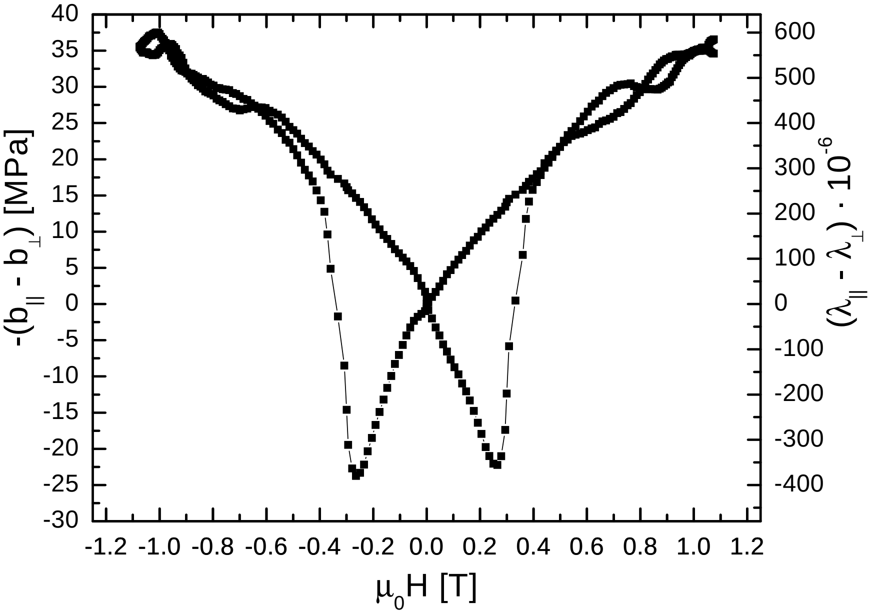

Figure 4.6: Magnetoelastic response of a (110)-oriented Dy$_{0.7}$Tb$_{0.3}$Fe$_2$ film.

be responsible for the slow approach to saturation observed.

Much higher magnetoelastic responses than those of DyFe$_2$ are shown by (110)-oriented TbFe$_2$ films, as shown in Figure 4.4. At a maximum achievable field of 1.1 T the signal is definitely not saturated. The absolute change of the magnetoelastic coefficient $\Delta b^{\epsilon,2}$ amounts to -108 MPa. The coercive field is 0.7 T. Taking the shear modulus of TbFe$_2$ the magnetostriction $\Delta\lambda^{\epsilon,2}$ can be estimated to $1695 \cdot 10^{-6}$. These values are about 75% of the values of a single crystalline TbFe$_2$ bulk at 1 T [8]. The results are similar to magnetoelastic stress measurements of (110)-oriented TbFe$_2$ films reported in the literature [97, 132].

Figure 4.6 shows the magnetoelastic response of a (110)-oriented Tb$_{0.3}$Dy$_{0.7}$Fe$_2$ film. Similar to the DyFe$_2$ samples, and analogous to the magnetization measurement, the coercivity of the pseudo-ternary film is not reduced but reveals a value of 0.3 T. With a magnetic field loop of up to 1.1 T the absolute change of the magnetoelastic coefficient $\Delta b^{\epsilon,2}$ amounts to -60 MPa. This gives a magnetostriction $\Delta\lambda^{\epsilon,2}$ of $942 \cdot 10^{-6}$. This value is only 60% of the value of bulk Terfenol-D. Again, the magnetoelastic response is not saturated at 1.1 T which agrees with measurements of Arnaudas et al. who observe a saturation of the signal only at 4 T [133].

4.3 Epitaxial DyFe$_2$ (111) films

(111)-oriented RFe$_2$ films also possess an in-plane tensile strain of -0.6%. Compared to (110)-oriented DyFe$_2$ films, (111)-oriented DyFe$_2$ films show a more pronounced magnetic anisotropy with the easy axis lying in the film plane, see Figure 4.7. In the plane, an anisotropy between the film directions aligned parallel and perpendicular to the c-axis of the sapphire a-plane substrate are observed. Again, the direction perpendicular to the sapphire c-axis shows the highest magnetization of 850 kA/m at 1 T. Here, the coercive field B_C is reduced to 0.1 T and the hysteresis loop closes at 0.4 T. Parallel to the sapphire c-axis the DyFe$_2$ film reaches a magnetization of 740 kA/m, with a coercive field of 0.1 T and a closing of the hysteresis loop at 0.5 T. The step at 0 T is again more pronounced in the more dominant direction, like in DyFe$_2$ (110).

The magnetoelastic measurement of a (111)-oriented DyFe$_2$ film is shown in Figure 4.8. The magnetoelastic coefficient performs an absolute change of -36.5 MPa for 1.1 T loops. Taking the shear modulus of DyFe$_2$ this leads to a magnetostriction of $573 \cdot 10^{-6}$. The change of the magnetostriction signal occurs

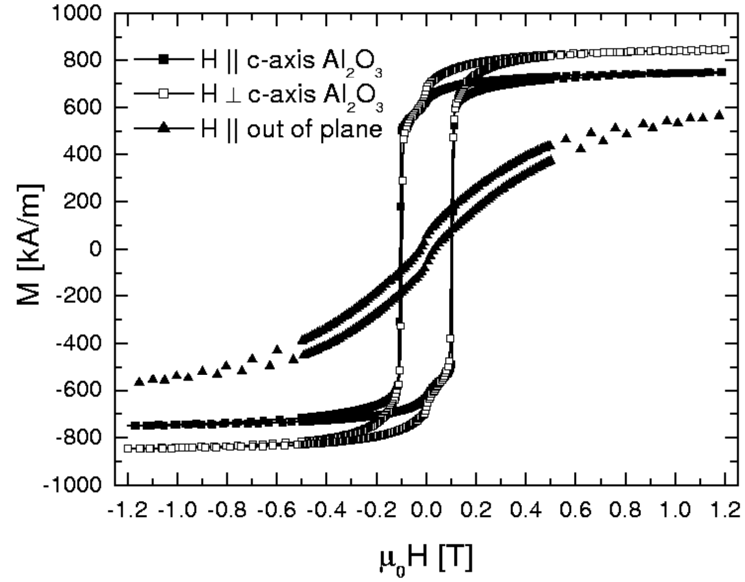

Figure 4.7: Magnetization vs. field of a (111)-oriented DyFe$_2$ film.

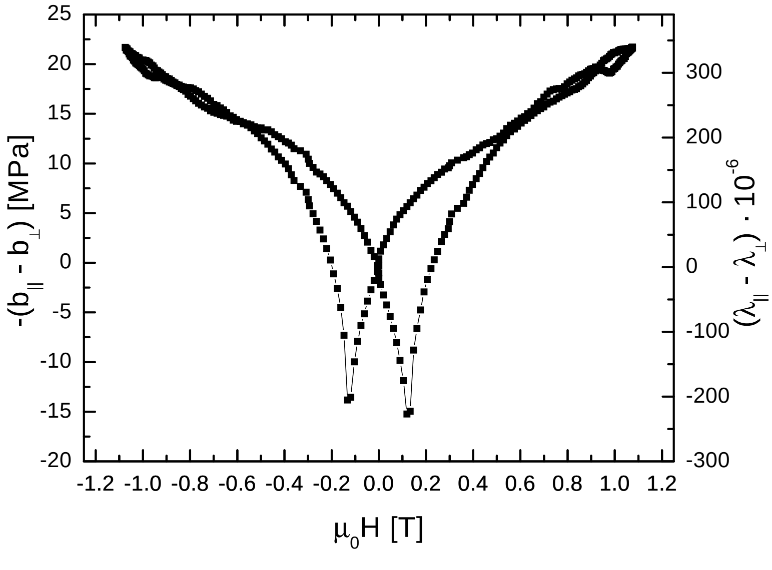

Figure 4.8: Magnetoelastic response of a (111)-oriented DyFe$_2$ film.

at magnetization reversal fields of 0.13 T. The magnetoelastic response is the same as for DyFe$_2$ (110), but in the (111)-oriented system the coercive field is halved. Again, the signal is not saturated at 1.1 T.

4.4 RFe$_2$ on Mo on sapphire m-plane

As already discussed in chapter 3, RFe$_2$ films prepared on (211)-oriented Mo on sapphire m-plane do not consist of one single epitaxial orientation but possess at least four twins given by spinel-twin laws. Though this crystals fulfill epitaxial relationships with the template, magnetically these films can be regarded as polycrystalline.

The magnetization measurements of DyFe$_2$ films prepared on Mo (211) on non-faceted sapphire m-plane and on faceted sapphire are shown in the Figures 4.11 and 4.13. The magnetization of the quasi-polycrystalline DyFe$_2$ films is comparable to the epitaxial (110)- and (111)-oriented films. They also reveal a magnetic anisotropy with a preferred in-plane magnetization. For films prepared on faceted templates the out-of-plane magnetization reveals a pronounced hard axis behavior with no loop opening. However, for films prepared on non-faceted templates this direction contains more easy axis contributions, expressed by an opening of the hysteresis loop and a higher magnetization value at 1 T. In the film plane, both systems do not reveal a pronounced anisotropy, as expected. The two loops mainly differ in the intensity of the magnetization reversal step, which is higher for the direction parallel to the sapphire c-axis and which is also more pronounced for the faceted films. Compared to the films prepared on sapphire a-plane, the films prepared on Mo (211) show a strongly reduced coercive field of $B_C < 0.1$ T. The loops close at 0.4 T.

Compared to the DyFe$_2$ films prepared on sapphire a-plane, the magnetoelastic response of DyFe$_2$ films prepared on Mo (211) on sapphire m-plane is reduced, as shown in Figures 4.12 and 4.14. The magnetoelastic coefficient for loops of 1.1 T is -33.5 MPa for a non-faceted film and -34 MPa for a faceted film. The magnetostriction $\Delta\lambda^{\epsilon,2}$ can therefore be calculated to $525 \cdot 10^{-6}$ and $534 \cdot 10^{-6}$, respectively. This deviation between the undulated and the flat film is definitely in the range of the measurement error. The reversal of the magnetoelastic signal occurs at 0.13 T.

For Tb$_{0.3}$Dy$_{0.7}$Fe$_2$ films prepared on Mo (211) on non-faceted sapphire m-plane, the magnetic anisotropy is strongly reduced compared to all former RFe$_2$

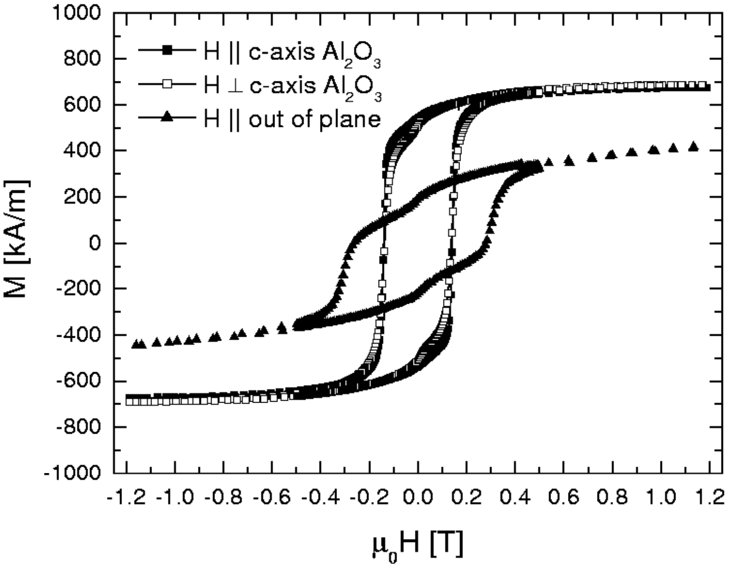

Figure 4.9: Magnetization vs. field of a $Tb_{0.3}Dy_{0.7}Fe_2$ film on Mo (211) on non-faceted sapphire m-plane.

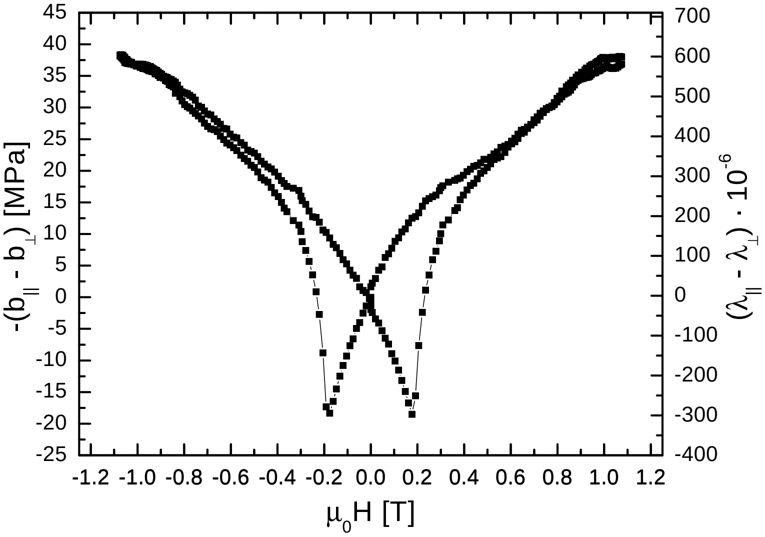

Figure 4.10: Magnetoelastic response of a $Tb_{0.3}Dy_{0.7}Fe_2$ film on Mo (211) on non-faceted sapphire m-plane.

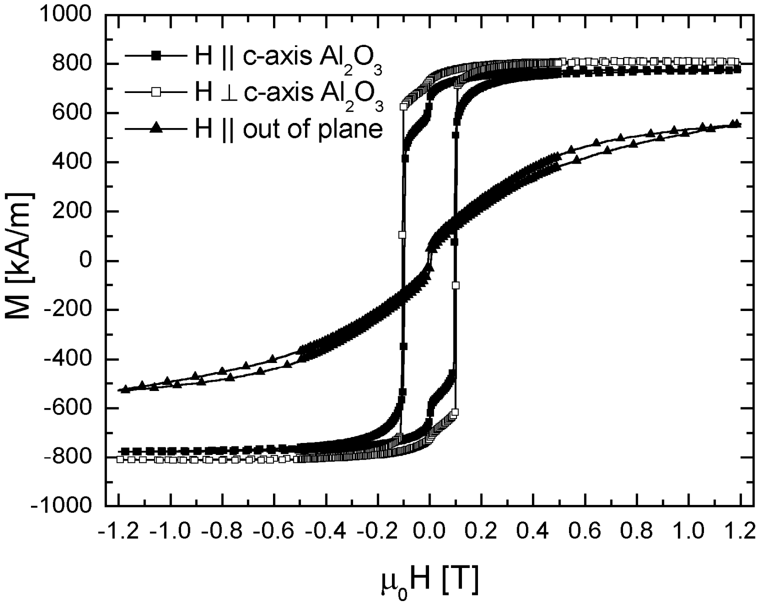

Figure 4.11: Magnetization vs. field of a DyFe$_2$ film on Mo (211) on non-faceted sapphire m-plane.

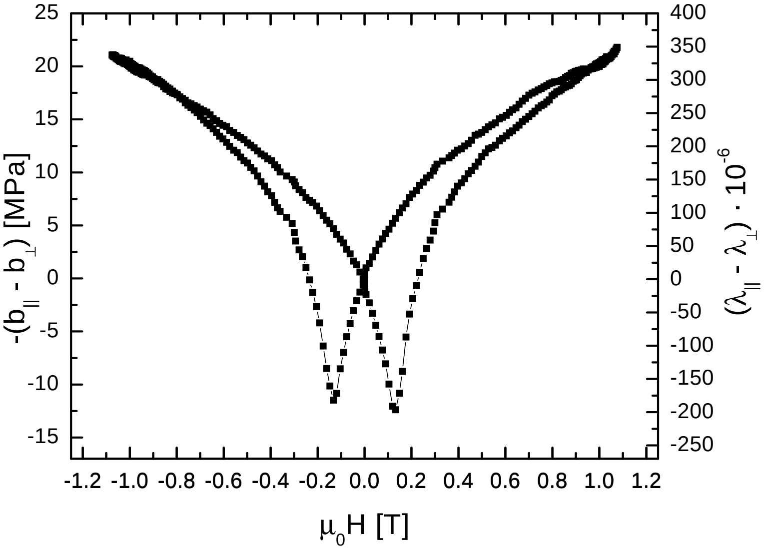

Figure 4.12: Magnetoelastic response of a DyFe$_2$ film on Mo (211) on non-faceted sapphire m-plane.

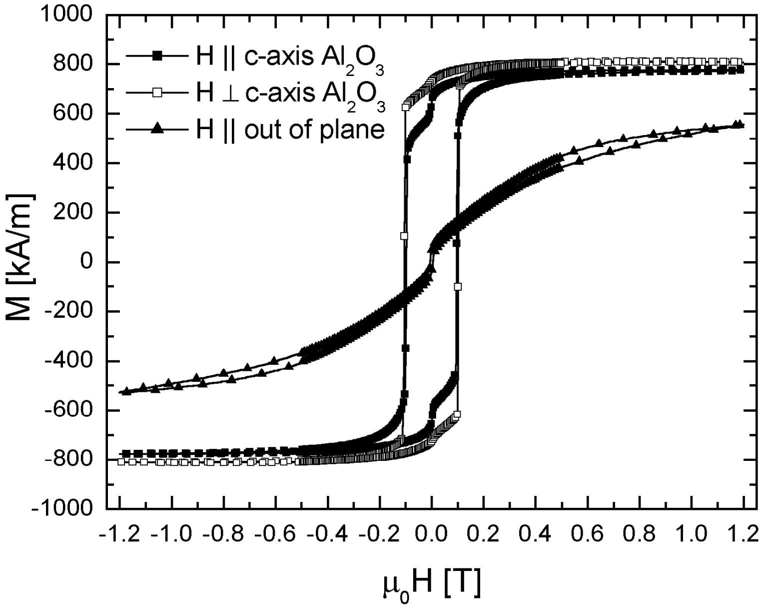

Figure 4.13: Magnetization vs. field of a DyFe$_2$ film on Mo (211) on faceted sapphire m-plane.

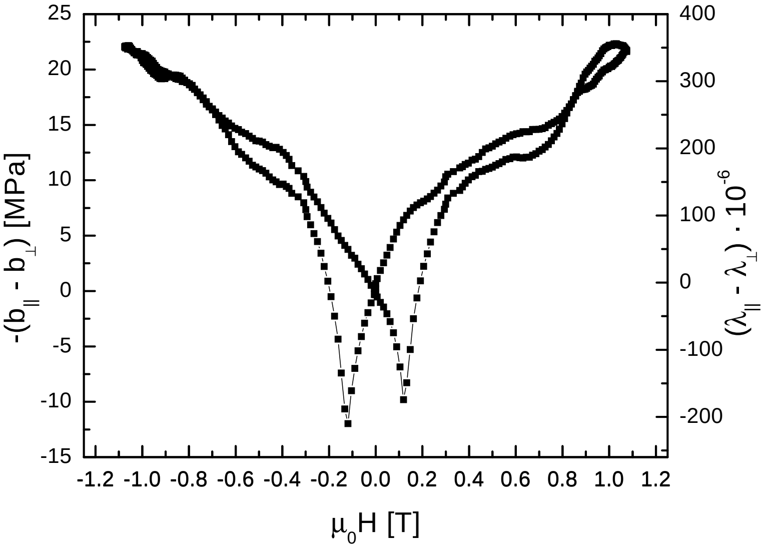

Figure 4.14: Magnetoelastic response of a DyFe$_2$ film on Mo (211) on faceted sapphire m-plane.

films, see Figure 4.9. The out-of-plane hysteresis has a larger coercive field of 0.25 T and a magnetization of 420 kA/m at 1 T. In the film plane no anisotropy can be observed. In both directions, parallel and perpendicular to the sapphire c-axis, the magnetization at 1.2 T is 685 kA/m. The coercive field is 0.14 T, and therefore larger than for the DyFe$_2$ films prepared on the same template. The loops close at 0.4 T.

Figure 4.10 shows the magnetoelastic response of a Tb$_{0.3}$Dy$_{0.7}$Fe$_2$ film deposited on Mo (211) on non-faceted sapphire m-plane. The magnetoelastic coefficient change is -58 MPa leading to a magnetostriction of $910 \cdot 10^{-6}$ at 1.1 T. These values are slightly smaller as compared to (110)-oriented Tb$_{0.3}$Dy$_{0.7}$Fe$_2$ films. The reversal of the magnetoelastic signal occurs at 0.18 T.

4.5 Epitaxial (211)-oriented RFe$_2$ films

The magnetic and magnetoelastic properties of (211)-oriented RFe$_2$ films have not been reported in the literature up to now. With the in-plane $[01\bar{1}]$ and $[\bar{1}11]$ axis, two main magnetic axes are lying parallel to the edges of the substrates. Furthermore, the reduced strain of the films, deduced from X-ray analysis, should lead to changes in the shape anisotropy of these systems compared to the other two twin-free epitaxial orientations. Again, a special interest was put on possible difference in the magnetic and magnetoelastic properties of faceted and non-faceted films.

Magnetization measurements of DyFe$_2$ films deposited on Nb (211) on non-faceted and faceted sapphire m-plane are displayed in the Figures 4.15 and 4.17. Like all films prepared on sapphire substrates, these two systems show a magnetic anisotropy with the easy axis lying close to the in-plane directions. But compared to the films on sapphire a-plane, the [211] out-of-plane direction is not of an extremely hard-axis type. In both cases an opening of the hysteresis loop occurs, and the magnetization at 1 T is close to the magnetization value in the plane. The two systems differ in the shape of the out-of-plane loop: While this shows a larger opening in non-faceted films, it is more rectangular in faceted films and closes before 0.9 T. In the film plane the magnetization at 1 T is about 760 kA/m. Only a slight magnetic anisotropy can be observed. This anisotropy is larger for non-faceted films than for faceted films. The coercive fields are 0.13 T and the loops close at 0.4 T.

Compared to the twin-free films on sapphire a-plane, the step in the magnetization reversal at 0 T is only slightly visible for epitaxial DyFe$_2$ (211) films.

A reduced coercive field of the (211)-oriented samples is also observed in single crystal bulk samples: Lord et al. have shown that (112) oriented single crystal Terfenol-D disks reveal a strongly enhanced change in the domain configuration when the field was applied along the in-plane [111] direction compared to other orientations [134].

The magnetoelastic coefficients of non-faceted and faceted (211)-oriented DyFe$_2$ films are shown in Figures 4.16 and 4.18. The absolute change of the magnetoelastic coefficient $\Delta b^{\epsilon,2}$ is -37 MPa and -36.5 MPa for non-faceted and faceted films, respectively. Therefore the magnetostriction can be calculated to $580 \cdot 10^{-6}$ and $573 \cdot 10^{-6}$. Compared to other DyFe$_2$ films these values are rather high. The change in the magnetoelastic signal occurs at a coercive field of 0.17 T.

A much more pronounced shape anisotropy compared to epitaxial DyFe$_2$ (211) films is observed in epitaxial TbFe$_2$ (211) films on non-faceted and faceted sapphire m-plane, as displayed in Figures 4.19 and 4.21. Here, the non-faceted films show the more pronounced hard-axis behavior for the out-of-plane direction. In-plane, both systems show a pronounced anisotropy with an easy axis parallel to the sapphire c-axis, which is parallel to the TbFe$_2$ $[\bar{1}11]$ axis. The magnetization at 1 T amounts to 820 kA/m. The two systems show distinct differences in the shape of the in-plane loops: In both cases, the $[\bar{1}11]$ axis loop is rectangular and has a coercive field of 0.4 T, but the step at magnetization reversal of 0 T is much more pronounced for the faceted film. The non-faceted-film, on the other hand, shows the same rounded shape of the TbFe$_2$ $[01\bar{1}]$ axis (parallel to sapphire [010]) and a coercive field of 0.35 T, but here the loop reveals a much more pronounced kink at 0 T than in the faceted film.

Figures 4.20 and 4.22 show the magnetoelastic behavior of epitaxial (211)-oriented TbFe$_2$ films on non-faceted and faceted sapphire m-plane. In a magnetic field loop of 1.1 T the magnetoelastic coefficient change $\Delta b^{\epsilon,2}$ amounts to -107 MPa in both cases. This gives a magnetostriction $\Delta\lambda^{\epsilon,2}$ of $1680 \cdot 10^{-6}$. The coercivity of the magnetoelastic response amounts to 0.5 T.

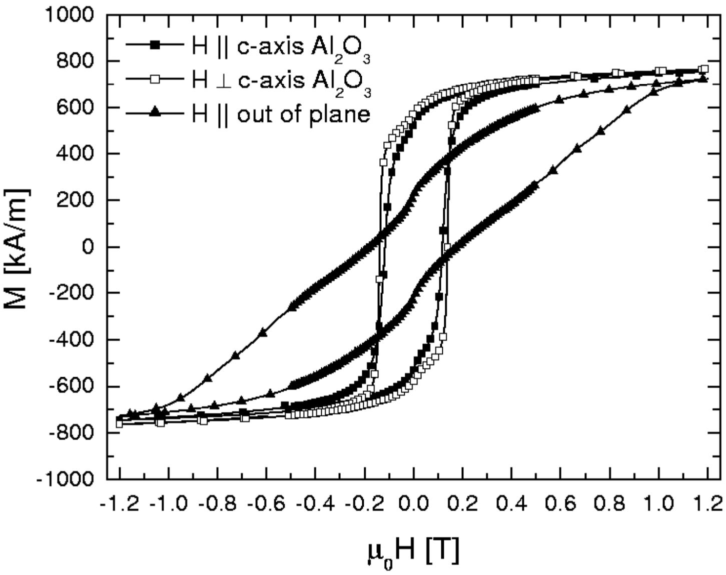

Figure 4.15: Magnetization vs. field of a plane (211)-oriented DyFe$_2$ film.

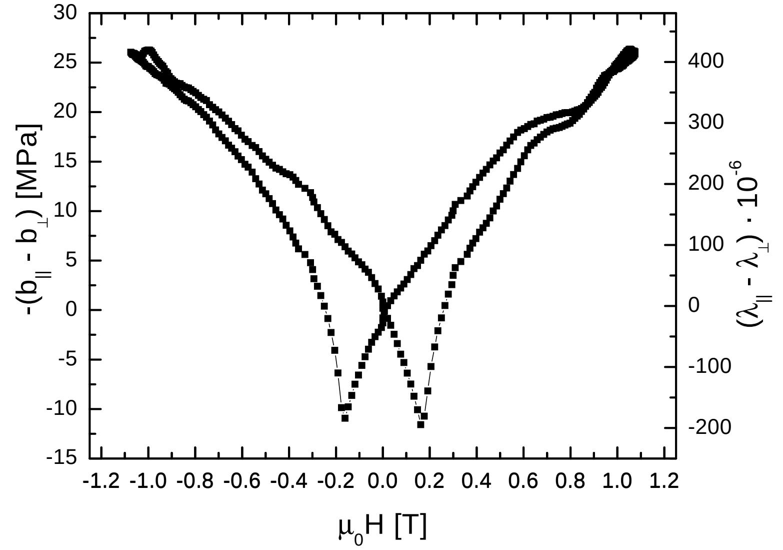

Figure 4.16: Magnetoelastic response of a plane (211)-oriented DyFe$_2$ film.

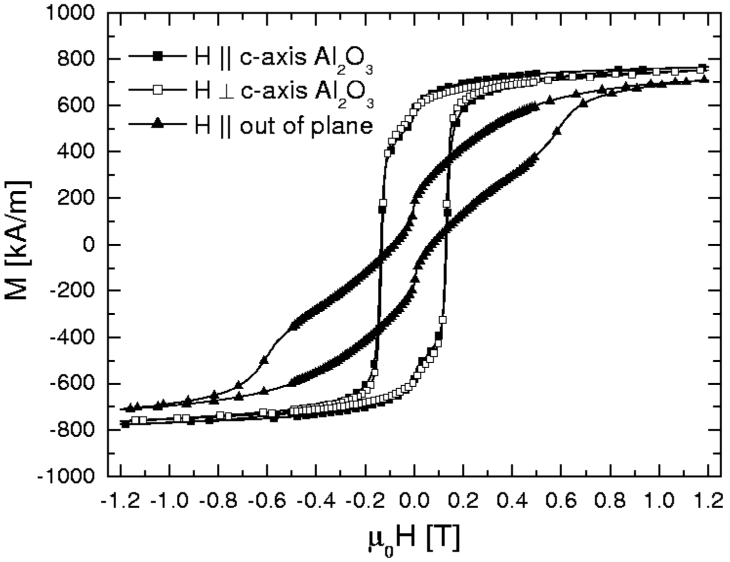

Figure 4.17: Magnetization vs. field of an undulated (211)-oriented DyFe$_2$ film.

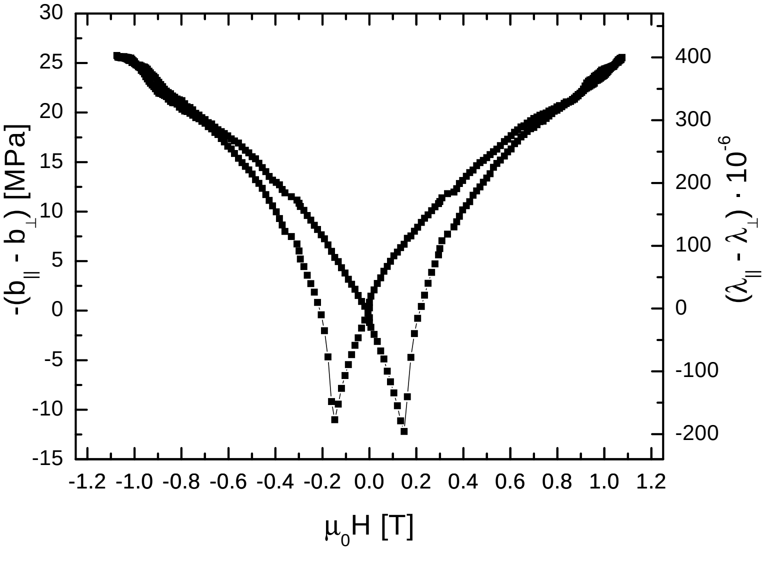

Figure 4.18: Magnetoelastic response of an undulated (211)-oriented DyFe$_2$ film.

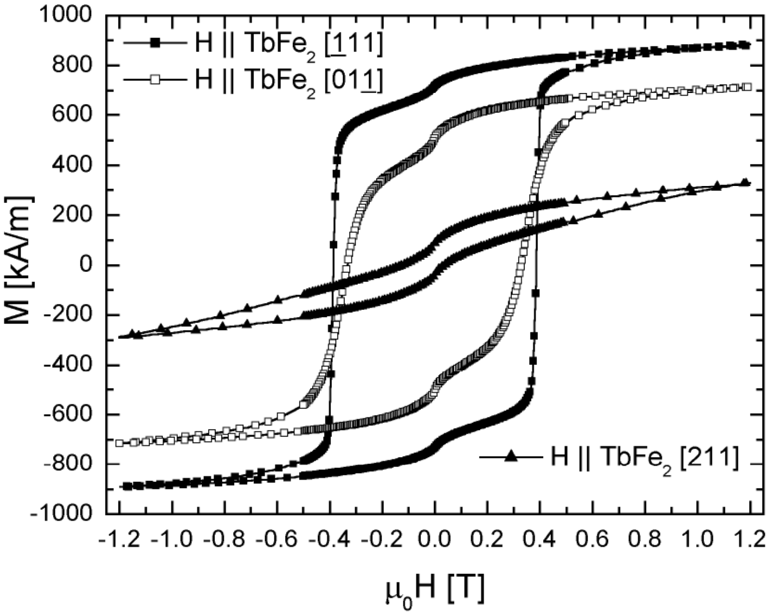

Figure 4.19: Magnetization vs. field of a plane (211)-oriented TbFe$_2$ film.

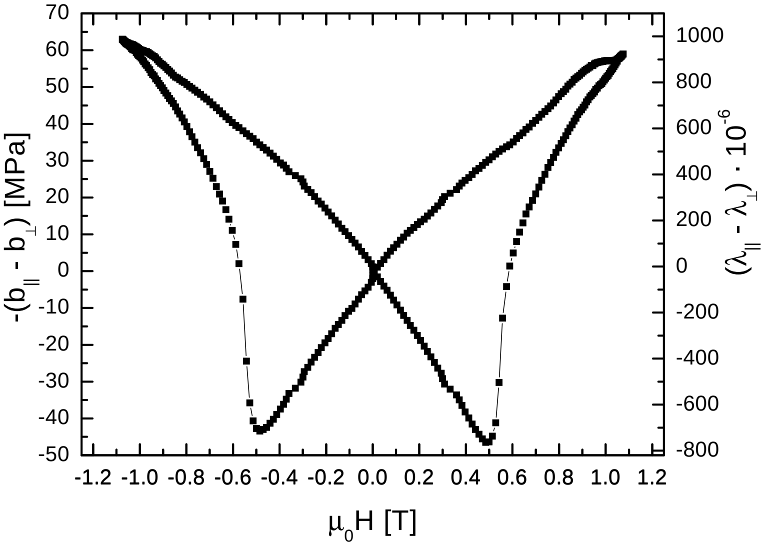

Figure 4.20: Magnetoelastic response of a plane (211)-oriented TbFe$_2$ film.

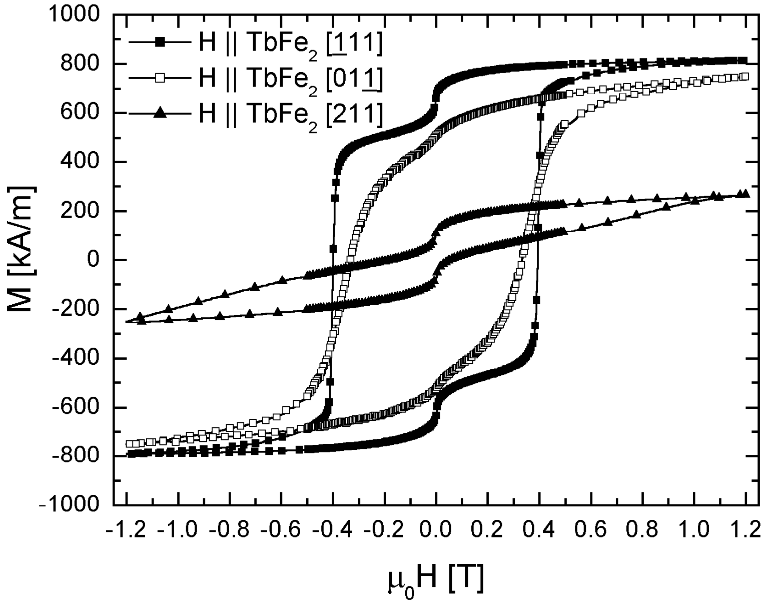

Figure 4.21: Magnetization vs. field of an undulated (211)-oriented TbFe$_2$ film.

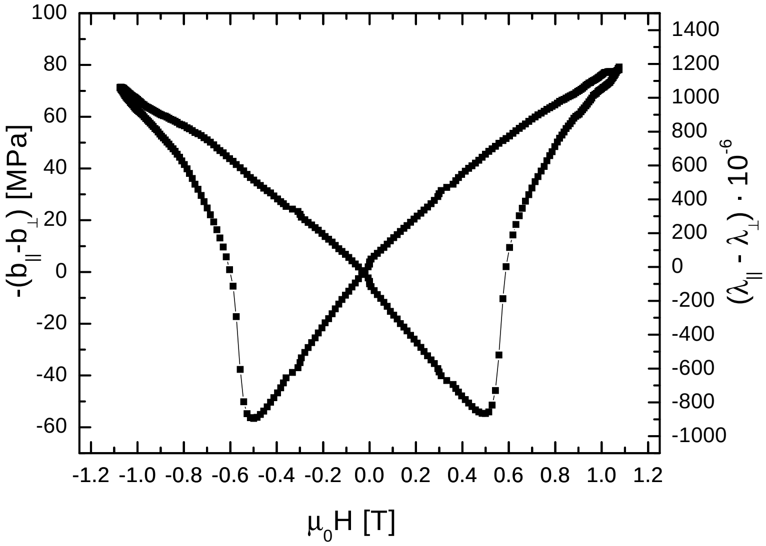

Figure 4.22: Magnetoelastic response of an undulated (211)-oriented TbFe$_2$ film.

4.6 Discussion

Most of the RFe$_2$ films presented here show a pronounced step in the magnetization signal during the magnetization reversal at 0 T. The intensity of this step depends on the field direction with regard to the crystallographic directions. This step is not only a property of RFe$_2$ films but also of other thin films of rare earth transition metals systems, like, for instance, Sm-Co films [135].

However, the step is not evident in all publications of RFe$_2$ films. In some cases the the step is even more pronounced [11, 98], in some it's less pronounced [95, 136], other do not reveal it at all [133, 137]. In amorphous RFe$_2$ films it is not observed.

Different explanations can be suggested for the origin if this signal: Firstly, a magnetic impurity with small coercive fields could be cause for a strong decrease at 0 T. Due to the fact that the intensity of the step is depending on the direction, amorphous ferromagnetic or crystalline paramagnetic samples like Dy or Tb impurities can be excluded. Another possible candidate like Fe inclusions, the employed Fe seed layer, or other reactions of the film with the buffer layer fails, because neither a thickness dependence of the effect nor X-ray reflections of crystalline iron needed in rather large proportions to explain such strong signals were detected. Other possible ferromagnetic impurities, like microcrystalline R$_x$Fe$_{1-x}$ accumulations, which would be hard to detect by X-ray or stoichiometry determinations by EDX, cannot be excluded but are rather unlikely to occur in a sufficient quantity without leaving a crystallographic trace.

A physical explanation for the occurrence of this step in the magnetization reversal of highly magnetostrictive RFe$_2$ films was given by Huth and Flynn [11]. They simulated the magnetization behavior of uncoupled ferromagnetic domains with the energy contributions of the magneto-crystalline anisotropy energy, the magnetoelastic energy, the Zeeman energy, and the demagnetization energy. For the given magnetic material constants of TbFe$_2$ the step in the magnetization reversal can only be explained if an anisotropic in-plane stress of the films is present. To some degree this contradicts the assumption of the calculations of chapter 4 and the literature [44, 130], where an isotropic stress in the film plane of (110)-oriented RFe$_2$ films due to different thermal expansion coefficients of film and substrate is assumed. However, due to the large uncertainty of the lattice parameter determination from the four-circle X-ray diffraction performed in this thesis, an in-plane stress anisotropy cannot be excluded. Further work has to be

Orientation	M**(1 T) [kA/m]**	H_C **[T]**	H_S **[T]**
(110), H $\parallel$ $c_{Al_2O_3}$	605	0.3	0.5
(110), H $\perp$ $c_{Al_2O_3}$	735	0.21	0.3
(110), H out-of-plane	555	–	≈2.5
(111), H $\parallel$ $c_{Al_2O_3}$	740	0.1	0.5
(111), H $\perp$ $c_{Al_2O_3}$	850	0.1	0.5
(111), H out-of-plane	540	–	≈4
on Mo$(211)_{non-fac}$, H $\parallel$ $c_{Al_2O_3}$	820	0.1	0.5
on Mo$(211)_{non-fac}$, H $\perp$ $c_{Al_2O_3}$	850	0.1	0.5
on Mo$(211)_{non-fac}$, H out-of-plane	700	–	≈4
on Mo$(211)_{fac}$, H $\parallel$ $c_{Al_2O_3}$	770	0.1	0.5
on Mo$(211)_{fac}$, H $\perp$ $c_{Al_2O_3}$	820	0.1	0.5
on Mo$(211)_{fac}$, H out-of-plane	530	–	≈4
$(211)_{non-fac}$, H $\parallel$ $c_{Al_2O_3}$	750	0.12	0.6
$(211)_{non-fac}$, H $\perp$ $c_{Al_2O_3}$	750	0.14	0.6
$(211)_{non-fac}$, H out-of-plane	650	0.16	≈2
$(211)_{fac}$, H $\parallel$ $c_{Al_2O_3}$	760	0.13	0.7
$(211)_{fac}$, H $\perp$ $c_{Al_2O_3}$	760	0.13	0.7
$(211)_{fac}$, H out-of-plane	685	0.05	≈2

Table 4.1: Characteristic magnetization values of $DyFe_2$ films.

done to solve this problem.

The results of the magnetization measurements and the magnetoelastic results are compiled in Tables 4.1, 4.2, 4.3, and 4.4.

All systems presented here show magnetization and magnetoelastic values comparable to those of single crystalline bulk samples. Some magnetization values observed were larger than those of crystalline bulks. This deviation can be due to the uncertainty in the determination of the film dimensions: The length and width of the cut samples was determined by a calliper with an error of 0.2 mm. A deviation of the film thickness, on the other hand, which was only determined by the deposition time, would furthermore lead to altered magnetoelastic values. A further possible reason could be a de-calibration of the VSM. After a long term usage deviations of 10% are reported, which have to be minimized by new calibration procedures.

The smallest values in the magnetoelastic response were obtained for the

Orientation	M**(1 T) [kA/m]**	H_C **[T]**	H_S **[T]**
(110), H $\parallel$ $c_{Al_2O_3}$	725	0.6	1.0
(110), H $\perp$ $c_{Al_2O_3}$	805	0.6	1.0
(110), H out-of-plane	240	–	≈6
$(211)_{non-fac}$, H $\parallel$ $c_{Al_2O_3}$	820	0.4	1.0
$(211)_{non-fac}$, H $\perp$ $c_{Al_2O_3}$	660	0.4	1.0
$(211)_{non-fac}$, H out-of-plane	220	–	≈6
$(211)_{fac}$, H $\parallel$ $c_{Al_2O_3}$	790	0.4	0.9
$(211)_{fac}$, H $\perp$ $c_{Al_2O_3}$	740	0.3	0.9
$(211)_{fac}$, H out-of-plane	560	–	≈6

Table 4.2: Characteristic magnetization values of TbFe$_2$ films.

Orientation	M**(1 T) [kA/m]**	H_C **[T]**	H_S **[T]**
(110), H $\parallel$ $c_{Al_2O_3}$	700	0.3	0.45
(110), H $\perp$ $c_{Al_2O_3}$	800	0.3	0.4
(110), H out-of-plane	355	–	≈4
on Mo$(211)_{fac}$, H $\parallel$ $c_{Al_2O_3}$	685	0.13	0.5
on Mo$(211)_{fac}$, H $\perp$ $c_{Al_2O_3}$	685	0.13	0.5
on Mo$(211)_{fac}$, H out-of-plane	420	0.27	≈4

Table 4.3: Characteristic magnetization values of Tb$_{0.3}$Dy$_{0.7}$Fe$_2$ films.

Orientation	$\Delta b^{\epsilon,2}$ **[MPa]**	$\Delta\lambda^{\epsilon,2}\cdot \mathbf{10^{-6}}$	H_C **[T]**
DyFe$_2$ (110)	-36.5	573	0.26
DyFe$_2$ (111)	-36.5	573	0.13
DyFe$_2$ on Mo$(211)_{non-fac}$	-33.5	525	0.13
DyFe$_2$ on Mo$(211)_{fac}$	-34	534	0.11
DyFe$_2$ $(211)_{non-fac}$	-37	580	0.16
DyFe$_2$ $(211)_{fac}$	-36.5	573	0.16
TbFe$_2$ (110)	-108	1695	0.62
TbFe$_2$ $(211)_{non-fac}$	-107	1680	0.48
TbFe$_2$ $(211)_{fac}$	-107	1680	0.5
Tb$_{0.3}$Dy$_{0.7}$Fe$_2$ (110)	-60	942	0.26
Tb$_{0.3}$Dy$_{0.3}$Fe$_2$ $(211)_{non-fac}$	-58	910	0.18

Table 4.4: Magnetoelastic data of the discussed RFe$_2$ films.

pseudo-ternary compound $Tb_{0.3}Dy_{0.7}Fe_2$. Due to difficulties in determining the stoichiometry of the films the Tb/Dy ratio is only nominally given by the evaporation rates of the effusion cells. A surplus of Dy could lead to finite, small coercive fields and to reduced magnetoelastic values.

The demands for application are a large magnetoelastic response at low magnetic fields, ideally smaller than 100 mT. None of the here discussed samples exhibited such small coercive fields. For $DyFe_2$ films the lowest coercive fields of 0.13 T were obtained for (111)-oriented epitaxial samples and for polycrystalline samples prepared on Mo (211) on sapphire m-plane. Epitaxial $DyFe_2$ (211) films, on the other hand, have slightly larger coercive fields of 0.16 T but also larger changes in the magnetoelastic coefficients. A reduction in the coercive field with respect to the (110) orientation is also observed for (211)-oriented $TbFe_2$ films. Furthermore, no significant difference of faceted (211)-oriented RFe_2 films as compared to non-faceted (211) films was observed. This again underlines the high crystalline quality of the faceted films. Additionally, the consistency of faceted and non-faceted films gives a good possibility to check differences in the properties of magnetostrictive surface acoustic wave (SAW) delay lines from the modulation of the surface. The new epitaxial (211) orientation of RFe_2 on Nb (211) on faceted or non-faceted sapphire is therefore a real enrichment for the research on RFe_2 films.

However, all of the observed films show a slow increase of the magnetoelastic response with increasing field and are still not saturated at 1.1 T. Amorphous TbFe films, on the other hand, reveal a strongly reduced magnetostriction of $400 \cdot 10^{-6}$ but also a reduced coercivity [85, 82, 83, 78] and especially amorphous TbFe/Fe multilayer show a reduced magnetostriction of $300 \cdot 10^{-6}$ at already 0.025 T [84]. Therefore, epitaxial RFe_2 films will only find applications where magnetic fields above 0.5 T can be supported. Then they will be superior due to the large magnetostrictive response that surpasses the values for amorphous layers by a factor of 4.

Chapter 5

Properties of Fe nanostructures

The mesoscopic hill-and-valley structure of faceted sapphire can be employed as template for the growth of crystalline metallic nanostructures. This was shown for the preparation of Nb nanowires, as discussed in chapter 2. A self-evident next step was to test the employed preparation technique for the preparation of ferromagnetic nanostructures. The fabrication of magnetic nanostructures is interesting for both, fundamental research and potential applications in magnetic recording technology. Fe was chosen from the three elemental room temperature ferromagnets. Firstly, it shows a four fold symmetry of the magnetic easy axes. With this property, an uniaxial shape anisotropy of the created structures could not be confused with the uniaxial anisotropy of for instance hexagonal Co. Secondly, compared to Ni, it possesses the larger Curie temperature and the larger magnetic moment, which may be important for the resolution in the magnetic measurements.

After successful preparation, the magnetic properties of the nano-patterned samples were measured in a vibrating sample magnetometer (VSM). Angular dependent magnetization measurements of some of these samples were furthermore performed by employing the magneto-optical Kerr effect (MOKE). An analysis of the obtained magnetic hysteresis curves was performed by micromagnetic modeling.

To study the magneto-resistance of a reduced number of Fe nanowires, samples were patterned in a two probe geometry and furthermore treated by focussed ion beam etching. Due to the nanoscopic scale of the wires, the occurrence of conductivity quantization was possible. Furthermore, as a result of the single domain state of the wires at saturation magnetization, an increased magneto-resistance could arise during magnetization reversal processes, when adjacent magnetic domains align in opposite directions.

In the first section of this chapter the technique of preparing Fe nanostructures is described. Afterwards, the magnetic properties of these features are presented. Additionally, the electrical properties of Fe nanowires will be shown. In the last part the magnetic measurements will be discussed and a model for the magnetization reversal process will be proposed.

5.1 Preparation of Fe nanostructures

The preparation of Fe nanostructures was performed by shallow incidence deposition on faceted sapphire m-plane, in analogy to the preparation of Nb nanostructures as was discussed in chapter 2. The first attempts of preparing Fe nanostructures were made by evaporating the iron out of an high temperature effusion cell. Later, Fe was evaporated out of the electron beam evaporator.

5.1.1 Preparation by effusion cell

Fe was evaporated out of a high temperature effusion cell at temperatures of 1500°C. Therefore, the Fe deposition rate, calibrated to normal incidence, amounted to 0.13 Å/s. To reduce de-wetting effects, the substrate temperature was kept at low temperatures of 100°C. Due to the rather narrow beam profile of an effusion cell, this low substrate temperatures were sufficient to prepare Fe nanostripes by employing the self-shadowing of the facets.

Figure 5.1 shows the development of the Fe coating on faceted sapphire in dependence of the deposition angle. In the top image a clean substrate is shown for clarification. In the middle image the deposition angle of Fe was about 9-11°. Here, the substrate is covered completely. This is in analogy to the observations on Nb deposited on faceted sapphire at low substrate temperatures. In the bottom image Fe was deposited under an incident angle of about 3-5°. Here, the substrate is only partly coated. The right facet sides reveal the flat surface of the substrate. Due to the low deposition temperature of 100°C, the building of stripes is mainly the result of the self-shadowing of the facets. Moreover, the low temperatures suggest a non epitaxial growth of Fe. Similar Fe nanostripes, prepared out of a high temperature effusion cell on substrates heated to 200°C, were also created and analyzed by A. Westphalen [138].

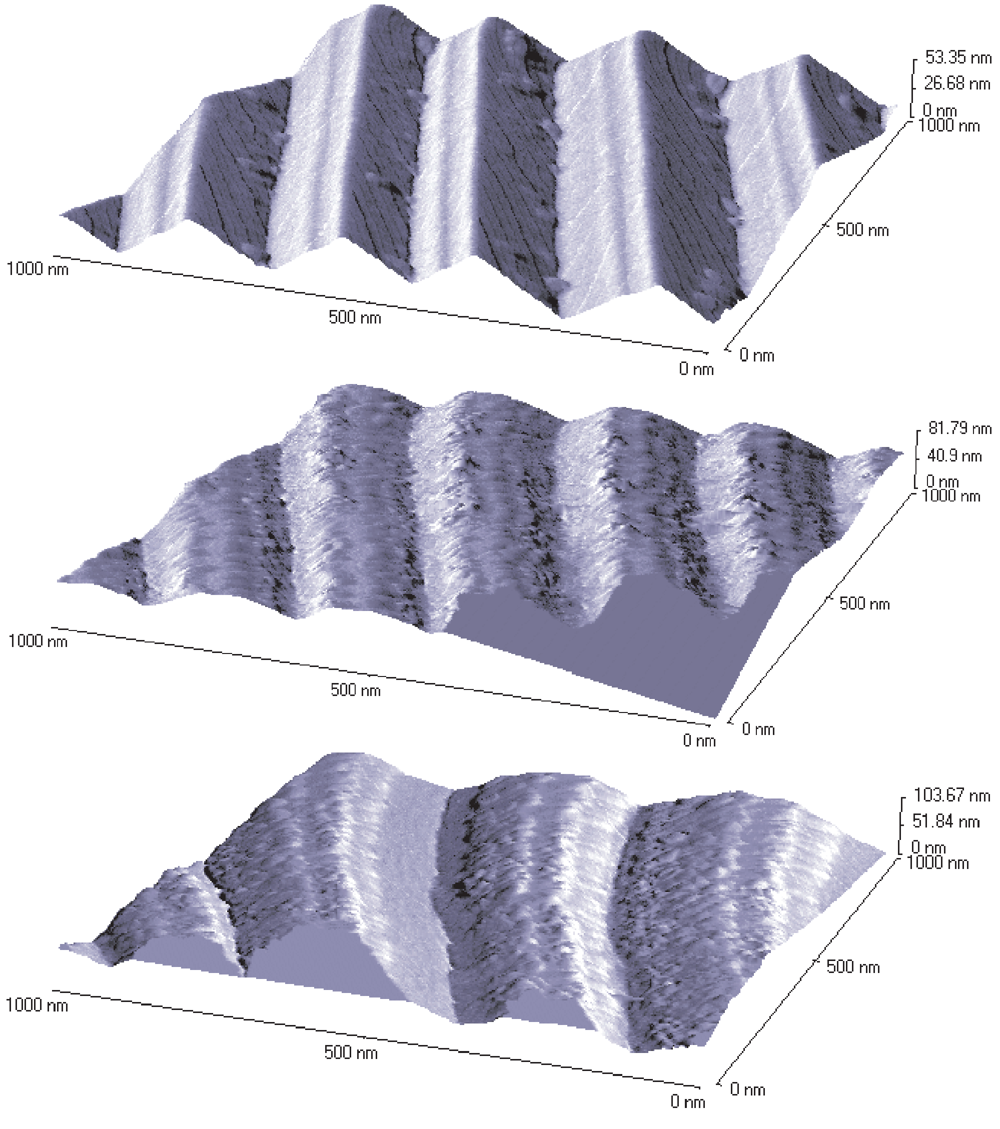

Figure 5.1: AFM image of Fe on faceted sapphire. The top image reveals a clean substrate; The middle image reveals a complete coating of the substrate with Fe that was deposited under an incident angle of 9-11°; In the bottom image the formation of Fe nanowires is observed. The Fe was deposited under incident an angle of 3-5°.

5.1.2 Preparation by electron beam evaporation

In a second attempt, Fe was deposited out of the electron beam evaporator. The Fe rate was controlled by the quadrupole mass spectrometer. Two different preparation series were performed to analyze the growth behavior of the Fe structures. In both series, the temperature of the faceted sapphire substrates was kept at 450°C. In the first series the incident angle of the iron beam was varied from 5° up to 15.5° and the deposition time was always set to 60 minutes. In the second series the deposition angle was kept at 5° but the deposition time was varied from 20 min to 120 min. In both preparation series, the system was subsequently covered with a 2 nm thick layer of Mo in normal incidence in order to protect the Fe from oxidation. Scanning electron microscopy (SEM) suggests the formation of morphologically and electrically isolated nano-patterned structures on the ridges of the facets. The length of these structures corresponds to the length of the individual facets. As already discussed in chapter 2, AFM did not give information about the thickness of the structures. Therefore, the thickness of the structures was estimated by evaluating the percentage of coverage of the substrate from the SEM images and comparing the height of the magnetic signal with those of flat Fe films of known thickness.

First preparation series: Angle dependent deposition

In the first preparation series the Fe rate was set to 0.13Å/s calibrated to normal incidence. The angle of deposition was varied from 5° to 15.5°.

Deposited at an angle of 5° Fe is forming sphere shaped dots strung together in a pearl-necklet-like structure. The SEM image in Figure 5.2 suggests the single drops to be physically isolated from each other. Their width varies from 25 nm to 70 nm. This drop size is mainly influenced by the width of the individual facets. For small facets and at the end positions where the individual facet vanishes to the benefit of new facets, the drop width is the smallest. Broad facets, on the other hand, show rather big drops and in some regions do two drops of medium size share the same point on the facet ridge. The distance in between the neighbored drops can be estimated to 8 nm. The average distance to the drops on the next facet can be estimated to 250 nm and is given the facet periodicity which is a result of the prior annealing temperature of the sapphire substrates. A comparison of the saturation moment of these films with the signal of continuous Fe films of known thickness gives the thickness of the Fe structures to approximately 19 nm.

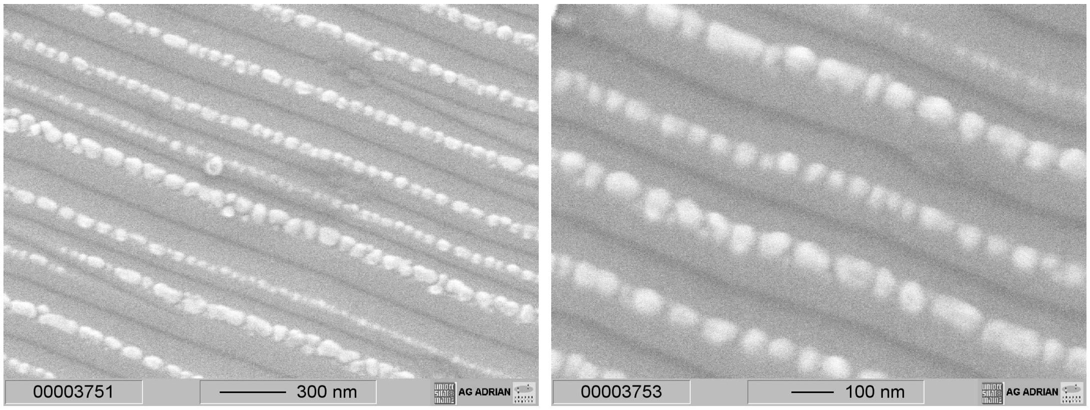

Figure 5.2: SEM image of Fe nanostructures. Deposition angle 5°.

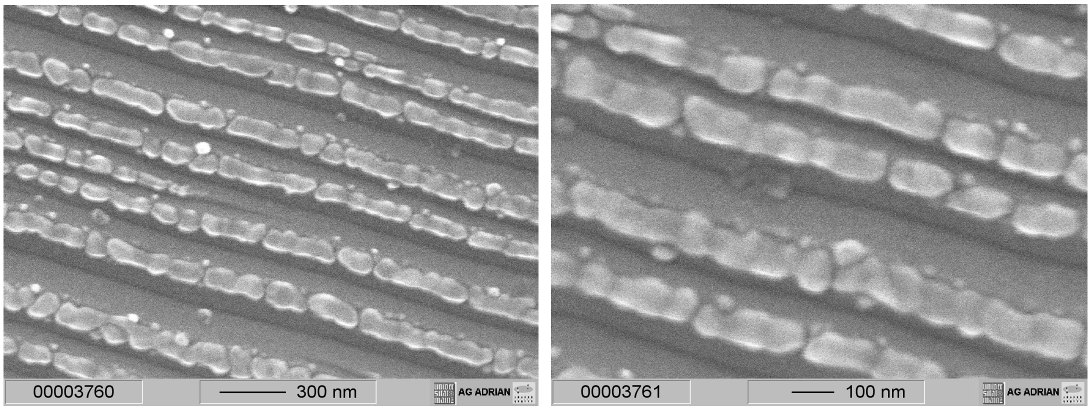

Figure 5.3: SEM image of Fe nanostructures. Deposition angle 8.5°.

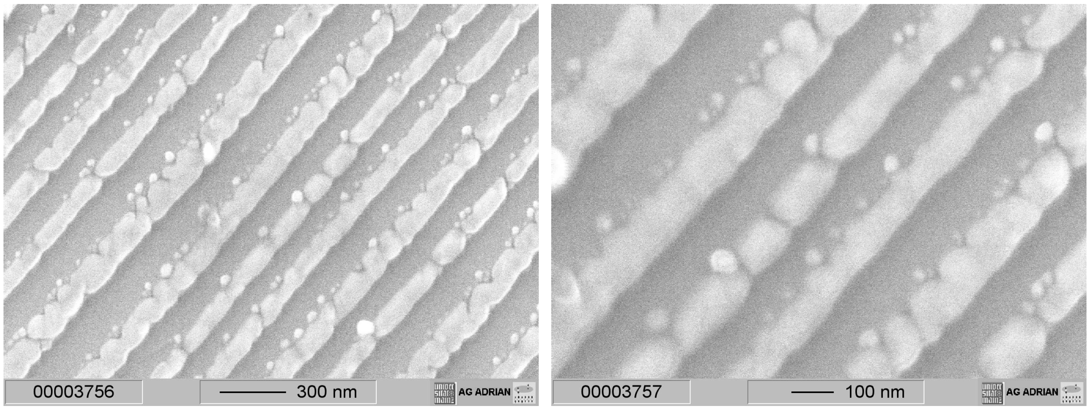

Figure 5.4: SEM image of Fe nanostructures. Deposition angle 15.5°.

For 8.5° deposition angle, Fe forms elongated structures. According to Figure 5.3 these oval shaped structures form due to coalescence of sphere shaped dots during the growth. The width of the structures amounts to 100 nm. The length of the structures varies from 100 nm to 500 nm. Their thickness amounts to approximately 25 nm.

For 15.5° deposition angle, Fe forms continuous nanowires, as shown in Figure 5.4. These wires still reveal the typical lacings from coalescence of the elongated structures. Their width amounts to 100 nm. The thickness is estimated to 41 nm.

The preparation of Fe nanostructures by means of incident angle deposition on faceted surfaces is also reported by Sugawara et al. [16]. Instead of faceted sapphire they employed the high temperature faceting of NaCl (110) into the (100) and (010) surface. Therefore, the facet angles were symmetrical and with 45° larger than the angles of faceted sapphire. Prior to the Fe deposition the surface was passivated by an amorphous SiO layer. Fe was deposited out of an electron beam evaporator at a rate of 0.15 Å/s under an angle of 65° with respect to the substrate normal. Sugawara et al. report a similar morphology of the Fe nanostructures like described above. For a deposition at elevated temperatures of 190°C they describe iron dots, which coalesce to tailed wires when the deposition time is increased.

Similar to the formation of Nb nanowires, the formation process of Fe nanostructures described above is thought to be driven by self-shadowing and de-wetting effects [29]. Firstly, due to a self-shadowing of the facets, the Fe deposition is mainly limited to the ridges of the facets. Secondly, the different surface energies of transition metals and the sapphire surfaces cause a de-wetting of the metal from the insulating facet surfaces at elevated temperatures. This leads to an accumulation of the metal on the facet ridges with an overgrowth over the edge of the facets and to the building of sphere-shaped nanostructures, comparable to the behavior of mercury on a glass plate.

Second preparation series: Time dependent deposition

In a second preparation series Fe was evaporated out of the electron beam evaporator at a higher rate of 0.21Å/s, calibrated to normal incidence. The substrate temperature was 450°C. Three sapphire substrates were mounted in parallel on the substrate holder: One faceted m-plane substrate annealed at 1650°C, one faceted m-plane substrate annealed at 1550°C and one non-faceted a-plane substrate. The deposition angle was always kept at 5°. The a-plane substrate was used for the estimation of the thickness of the nano-structure by comparison of the magnetic signals as described above. The nano-structures on the two m-plane substrates show a strong dependency on the size of the facets when the deposition time is varied from 20 minutes to 120 minutes.

After a deposition time of 20 min the substrates annealed at 1550°C show the more pronounced Fe structures due to the smaller facet angles. For the substrates annealed at 1650°C only thin stripes of Fe can be seen. On the substrates annealed at 1550°C the typical pearl-necklet like structure of sphere-shaped dots evolves, as shown in Figure 5.5. The diameter of the dots is about 35 nm. The thickness of the structures is estimated to be lower than 10 nm for the 1650°C substrate and to be 19 nm for the 1550°C substrate.

After a depositing time of 40 minutes, the 1650°C substrates reveal the formation of loosely packed small sphere-shaped dots. On the 1550°C substrates the sphere-shaped Fe dots are aligned in wire structures, as shown in Figure 5.6. Wether the dots are insulated against each other is not clearly apparent. The thickness of the structures is estimated to be 16 nm and 26 nm for the 1650°C and the 1550°C substrates, respectively.

For a deposition time of 90 minutes the 1650°C substrates also reveal Fe nanowire structures, shown in Figure 5.7. Compared to the Fe nanowires shown in Figure 5.4, where the wires are consisting of elongated structures coalesced from droplets, the wires consist of accumulations of small sphere-shaped drops of about 40 nm diameter. The thickness of the structures is estimated to be 25 nm. On the 1550°C substrates the dots seem to form continuous nanowires, as can be deduced from Figure 5.7. The thickness of the wires amounts to 35 nm.

After 120 minutes deposition time the thickness of the wire structures has increased, see Figure 5.8. The single nano-drops, which form the stripes, are not visible any more on both of the substrates. The thickness of the structures can be estimated to be 40 nm and 45 nm.

Similar observations of the Fe growth were also performed by Sugawara et al. [139]. In contradistinction to the above mentioned systems, they determined their structures to have thicknesses of 1 nm with dot sizes of 6.7 nm. Their characterization method was UHV scanning transmission electron microscopy (UHV-STEM). However, the dot diameters of the individual dots discussed here were larger than 35 nm. The thickness was solely determined by comparing the magnetization value with the signal of a continuous film of known thickness. Tak-

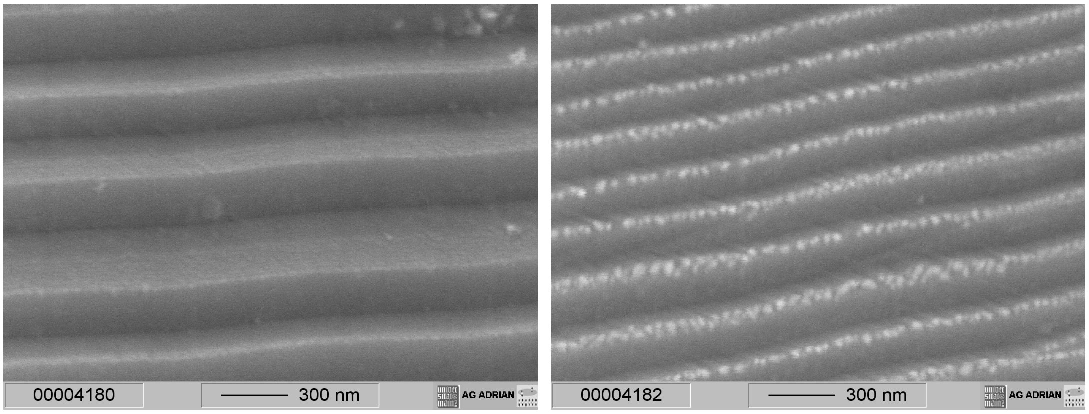

Figure 5.5: SEM image of Fe nanostructures. Second preparation series. Deposition time 20 minutes. Left: $T_{anneal}^{Al_2O_3}$=1650°C, Right: $T_{anneal}^{Al_2O_3}$=1550°C. Due to the smaller facet angles, the 1550°C substrate reveals the more pronounced structures.

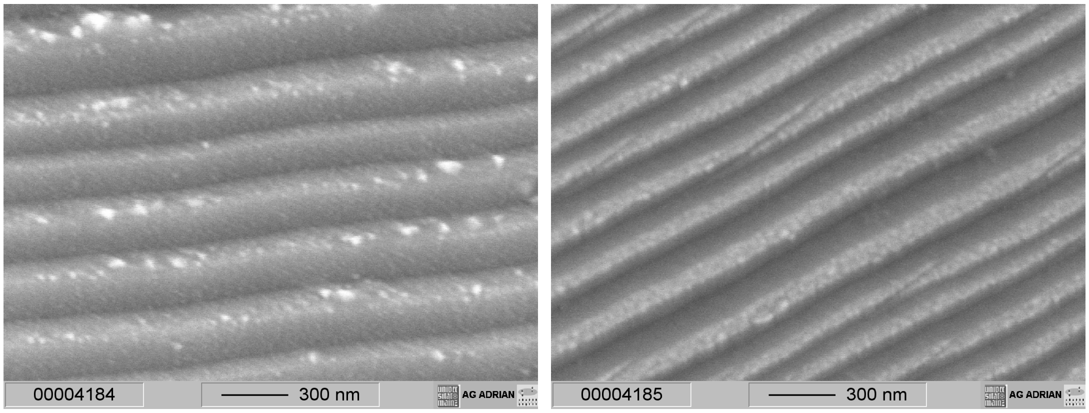

Figure 5.6: SEM image of Fe nanostructures. Second preparation series. Deposition time 40 minutes. Left: $\mathrm{T}_{anneal}^{Al_2O_3}$=1650°C, Right: $\mathrm{T}_{anneal}^{Al_2O_3}$=1550°C.

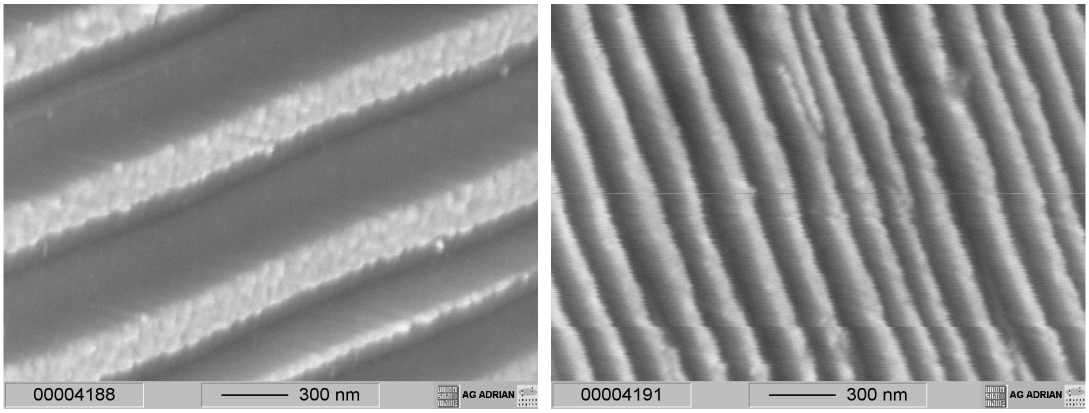

Figure 5.7: SEM image of Fe nanostructures. Second preparation series. Deposition time 90 minutes. Left: $T_{anneal}^{Al_2O_3}$=1650°C, Right: $T_{anneal}^{Al_2O_3}$=1550°C.

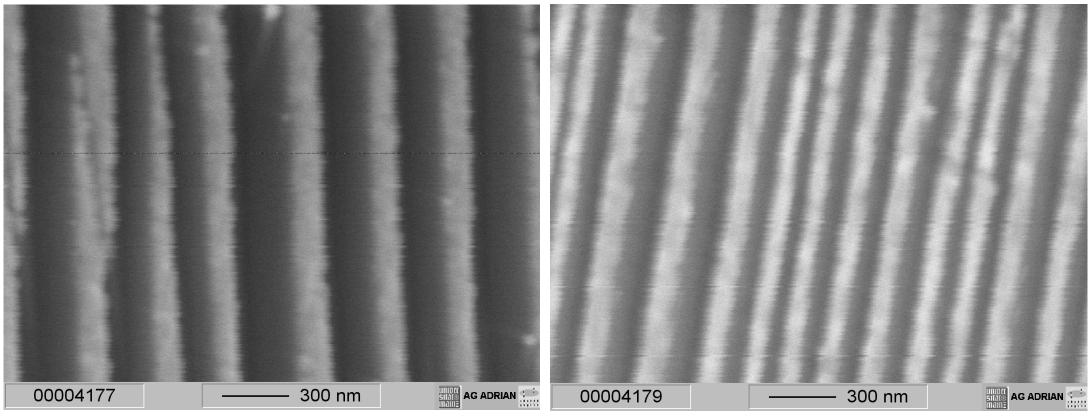

Figure 5.8: SEM image of Fe nanostructures. Second preparation series. Deposition time 120 minutes. Left: $T_{anneal}^{Al_2O_3}$=1650°C, Right: $T_{anneal}^{Al_2O_3}$=1550°C.

ing into account the nominal deposition rate of Fe and the de-wetting effect on the sapphire surface, which leads to a accumulation of adjacent Fe atoms in the droplets, structure thicknesses of the above mentioned values seem reasonable. The thickness of the sphere-shaped nanodots, however, is a very sensitive parameter for the discussion of the magnetization reversal processes, as will be discussed next.

5.2 Magnetic properties

The magnetic properties of the Fe nanostructures were measured in the vibrating sample magnetometer (VSM) and by the magneooptical Kerr effect (MOKE). Prior to the measurements, the samples were polished at the faces of the substrate edges to remove thereon deposited Fe. In the VSM, the hysteresis loops of the systems were taken at temperatures of 300 K. The magnetic field up to 0.4 T was aligned in the averaged sample plane. No angular dependent measurements could be performed due to the sample holder geometry in the VSM. However, the samples could be oriented with the facet ridges parallel and perpendicular to the field. To analyze the angular dependent behavior and for comparison magnetooptikal Kerr effect (MOKE) measurements were performed by M. Kallmayer of the samples of the first preparation series [140]. Again, the measurements were performed at room temperature with the magnetic field up to 0.16 T aligned in the sample plane. The light source was a diode laser with s-polarized light of 670 nm wavelength. The MOKE measurements were performed in longitudinal geometry, rendering the measurements solely sensitive to magnetic moments parallel to the incident plane of the light. The spot size of the laser focus on the sample was widened to 1 mm to yield an average over a large amount of stripes. The laser spot was set to the rotation axis of the sample in order to retain the detected area during a rotation of the sample. The loops were recorded in a full circle of 0° to 360° with regard to the field lines of the electromagnet, with an increment of 5°.

5.2.1 Magnetic properties of the first series

Both, the VSM and the MOKE measurement reveal a strong uniaxial magnetic anisotropy for all the films discussed here. The easy axis of magnetization was parallel, and the hard axis perpendicular to the facet ridges.

VSM measurements

The hysteresis loop of a film deposited at an angle of 5°, which has the morphology of strung sphere-shaped nanodots shown in Figure 5.2, is presented in Figure 5.9. Parallel to the facet ridges, as displayed in the upper graph, the hysteresis loop is of rounded rectangular shape. The saturation field is 0.2 T. The slope of the curve changes during the magnetization reversal process resulting in a wasp-like shape of the loop. With the facet ridges perpendicular to the magnetic field, shown in the lower graphs of Figure 5.9, the magnetization behavior is of hard-axis-type, as already mentioned above. Only a slight opening of the hysteresis loop can be observed, and the magnetization at 0.4 T is only 60% of the value parallel to the facet ridges.

Deposited at an incident angle of 8.5°, Fe reveals oval shaped structures, as presented in Figure 5.3. With the field parallel to the facet ridges, the hysteresis loop of these structures is not of rectangular shape, as shown in Figure 5.10. Compared to the sphere-shaped dots deposited at 5°, saturation sets in at 0.17 T. Furthermore, the change of the slope occurs at -0.03 T and is not as significant, i.e. it does not lead to a wasp shape. H_C again amounts to 0.05 T. In perpendicular orientation, shown in the lower graph of Figure 5.10, the s-shaped curve reveals a very slight opening of the hysteresis and at 0.4 T the magnetization is 85% of the value obtained in ridge-parallel orientation of the field.

Fe deposited under an angle of 15.5° reveals the constricted nanowires, as was shown in Figure 5.4. The hysteresis loop with the field aligned parallel to these wires is shown in Figure 5.11. Compared to the above discussed structures the wires cause a more rectangular hysteresis loop. The onset of the magnetization reversal occurs at 0.11 T, while the structures are already saturated at 0.14 T. The change in the slope of the magnetization reversal is reduced to a small dip which goes from 0 T to 0.035 T. The coercive field is 0.065 T.

Different anisotropy fields for the individual morphologies can be determined by analyzing the hard axis loops. For the nanostructures prepared at incident angles of 5° and 8.5° these values are below 0.2 T. For the nanowires prepared at an angle of 15.5° the anisotropy field is 0.8 T. Similar results are also obtained by the MOKE measurements reported next. Assuming a demagnetization factor of 1/2 for cylindric structures along the long axis, a Stoner-Wohlfarth like magnetization reversal process with the easy axis along the facet ridges would give an anisotropy field of 1 T for Fe. Therefore, the magnetization reversal process espe-

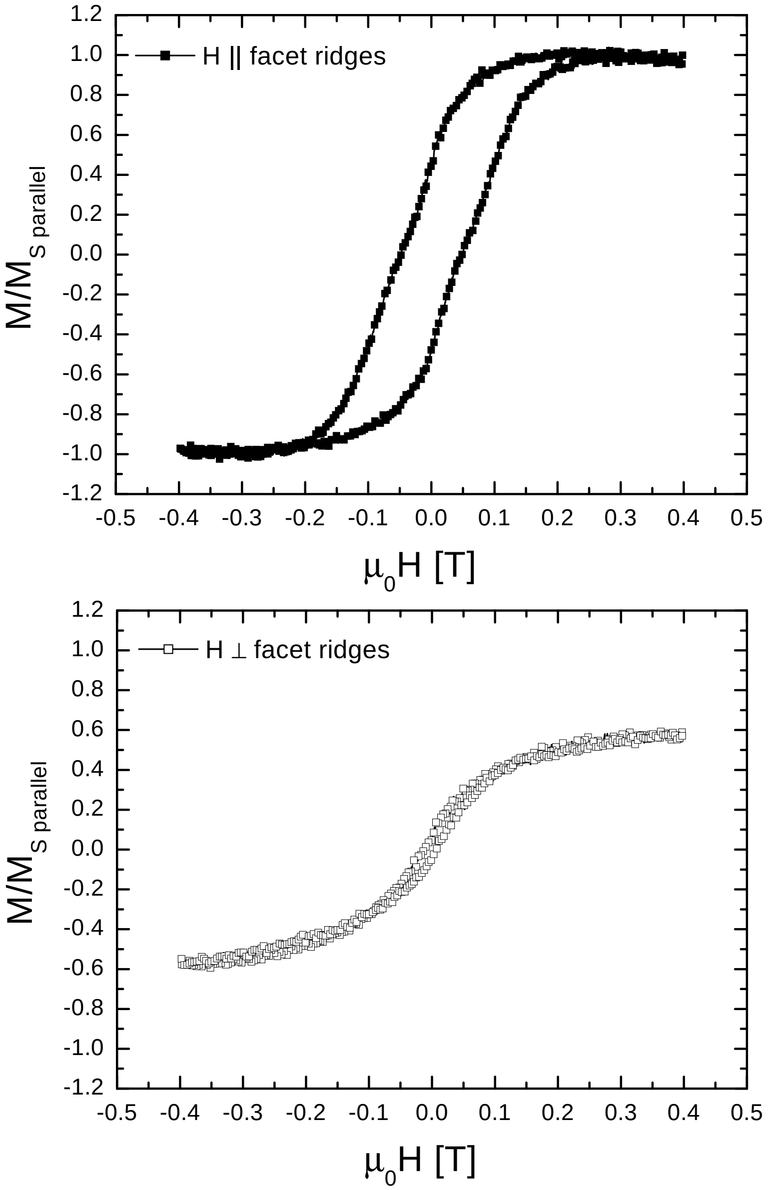

Figure 5.9: VSM measurements of Fe nanostructures at $T = 300$ K. First preparation series, deposition angle 5°. Top: Field parallel facets. Bottom: Field perpendicular facets.

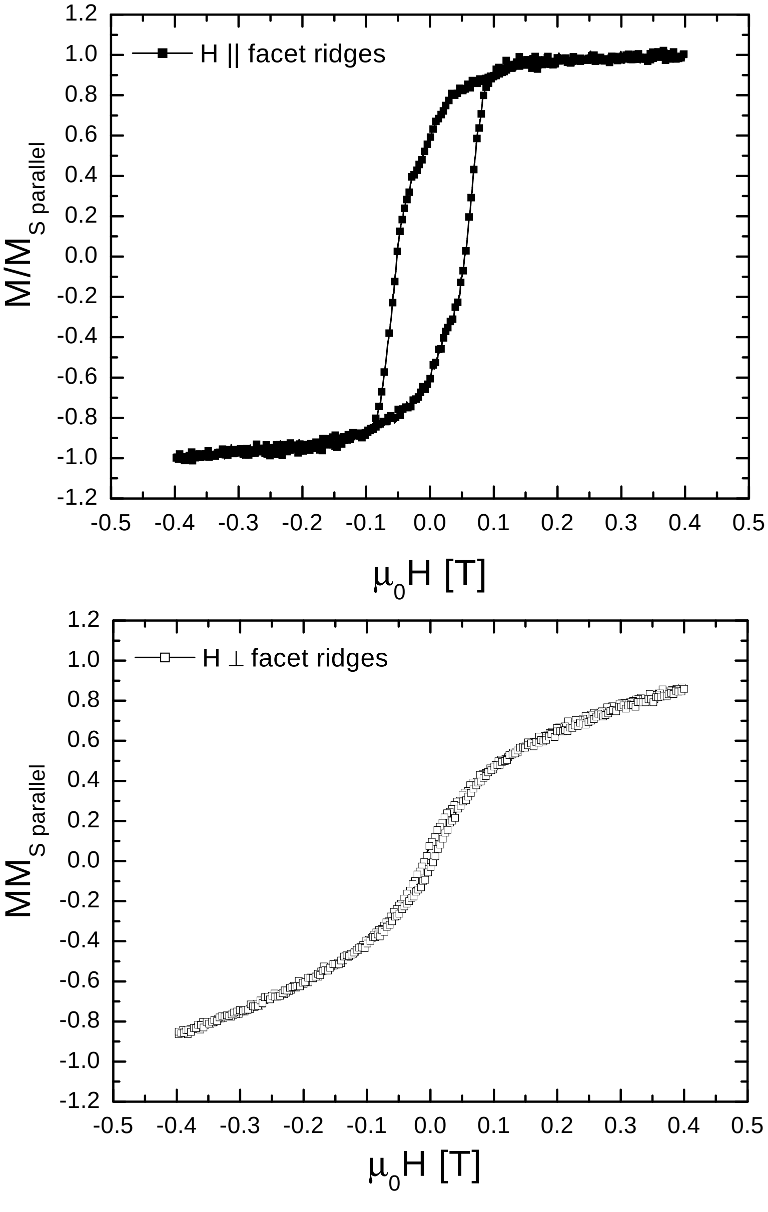

Figure 5.10: VSM measurements of Fe nanostructures at $T = 300$ K. First preparation series, deposition angle 8.5°. Top: Field parallel facets. Bottom: Field perpendicular facets.

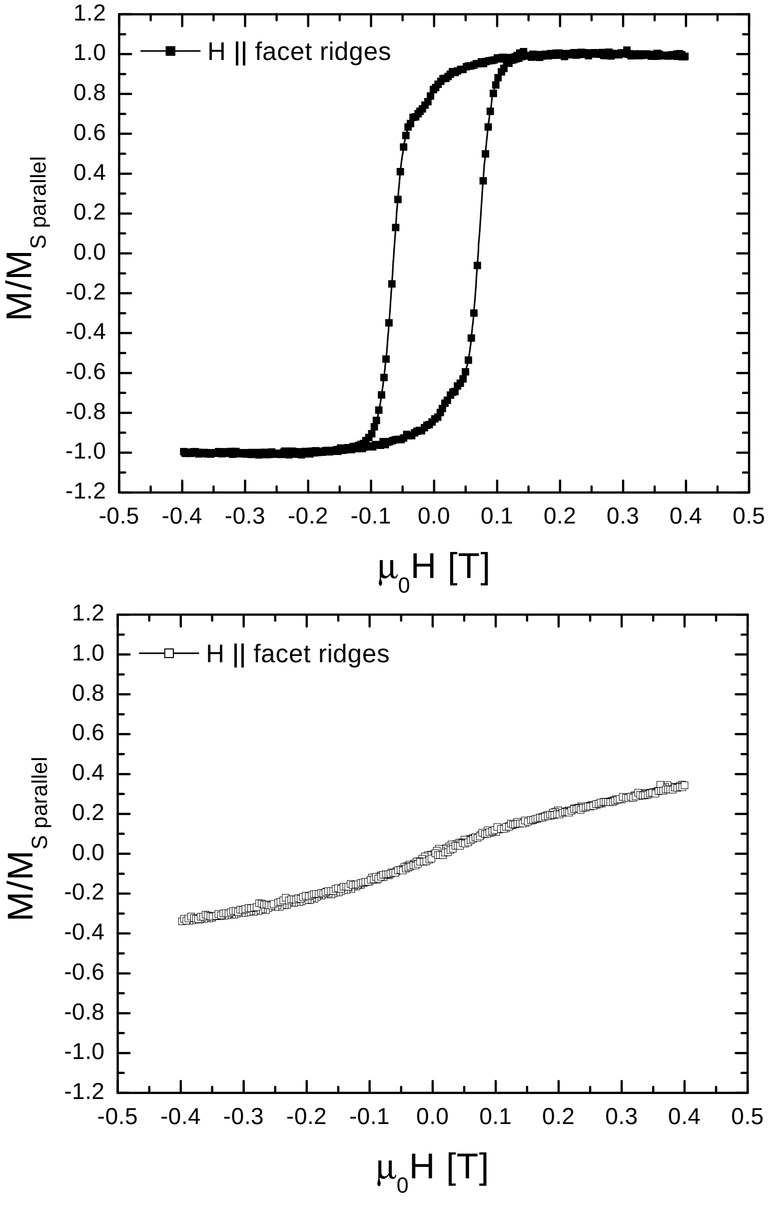

Figure 5.11: VSM measurements of Fe nanostructures at $T = 300$ K. First preparation series, deposition angle 15.5°. Top: Field parallel facets. Bottom: Field perpendicular facets.

cially of the sphere- and oval-shaped nanodots can not be described by coherent rotation of the magnetization, as will be discussed below.

To exclude the effect of (super-)paramagnetic inclusions in the nanostructures, the magnetization measurements were also performed at 5 K. They reveal the expected temperature dependent increase in the magnetization but no significant change of the qualitative loop shapes.

MOKE measurements

In accordance the VSM measurements, the MOKE measurements also reveal the uniaxial magnetic anisotropy in the film plane with the easy axis of magnetization aligned parallel to the facet ridges. Figure 5.12 shows angular-dependent measurements of a film deposited at 5° incident angle. With 0.065 T the coercive field parallel to the facet ridges is slightly enhanced when compared to the VSM measurements. Except for the stretched shape of the loops which originates from a non-compensated Farraday effect of the employed lenses, the form of the hysteresis curves is similar to the VSM measurements. One main agreement is the change of the slope observed at H_C. In contradiction to the VSM measurements the signal perpendicular to the facets is higher than in parallel direction.

Figure 5.13 shows the MOKE measurements of a 8.5° sample. Like in the VSM measurements a more squared shape of the hysteresis loop for fields parallel to the facet ridges is observed. Again, the coercive field of the parallel orientation amounts to 0.065 T like for the 5° sample and is therefore slightly enhanced when compared to the VSM measurement. Furthermore, the loop shape of the perpendicular direction is of straight hard-axis type and not s-shaped like in the VSM. The main difference is a lack of a slope change during magnetization reversal. A possible explanation might be that the system is not fully saturated at 0.16 T and that therefore only a minor loop is obtained.

MOKE measurements of a 15.5° sample, shown in Figure 5.14, reveal a square-shaped hysteresis loop with a coercive field of 0.075 T for fields aligned parallel to the facet ridges. Again, the shape of the loops is analogous to the VSM measurements, but a main deviation is the missing of the dip in the magnetization reversal.

In Figure 5.15 the angular dependence of the MOKE remanence signal is shown. All three films have the easy magnetization direction close to the facet ridges and the hard axis perpendicular. A $\cos^2$-fit is superior to describe the

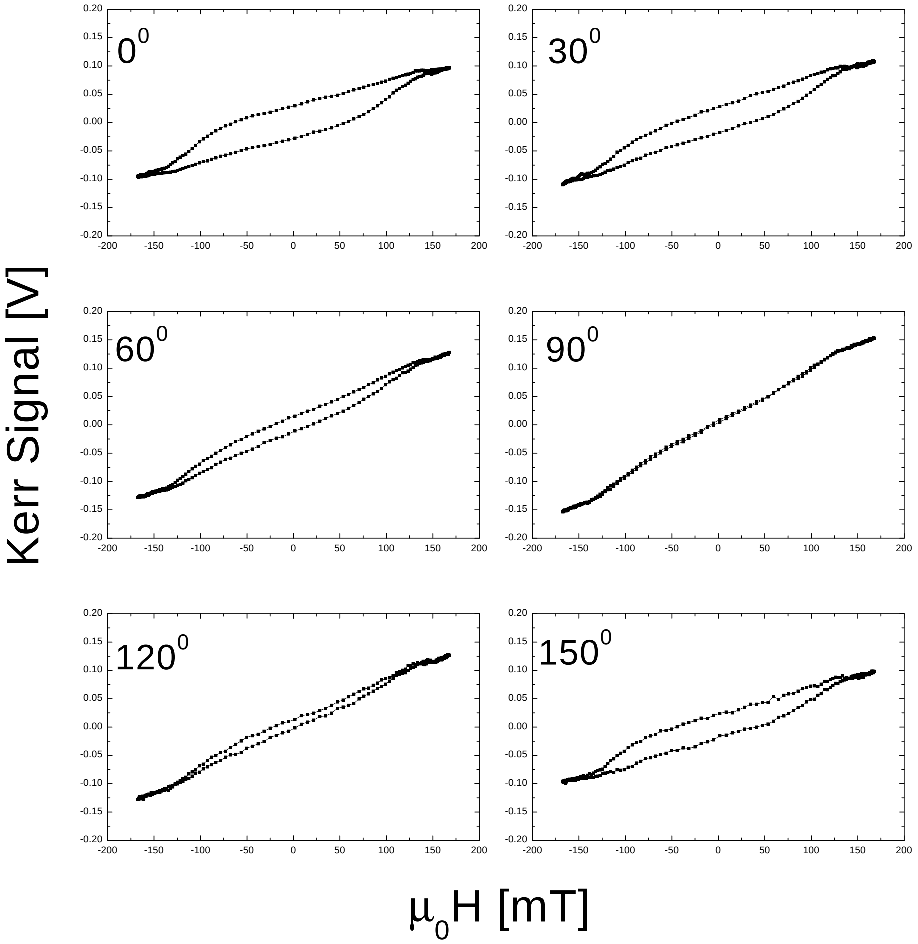

Figure 5.12: Kerr signal vs. field of Fe nanostructures at room temperature. For 0° the magnetic field is parallel to the facet ridges. First preparation series, deposition angle 5°.

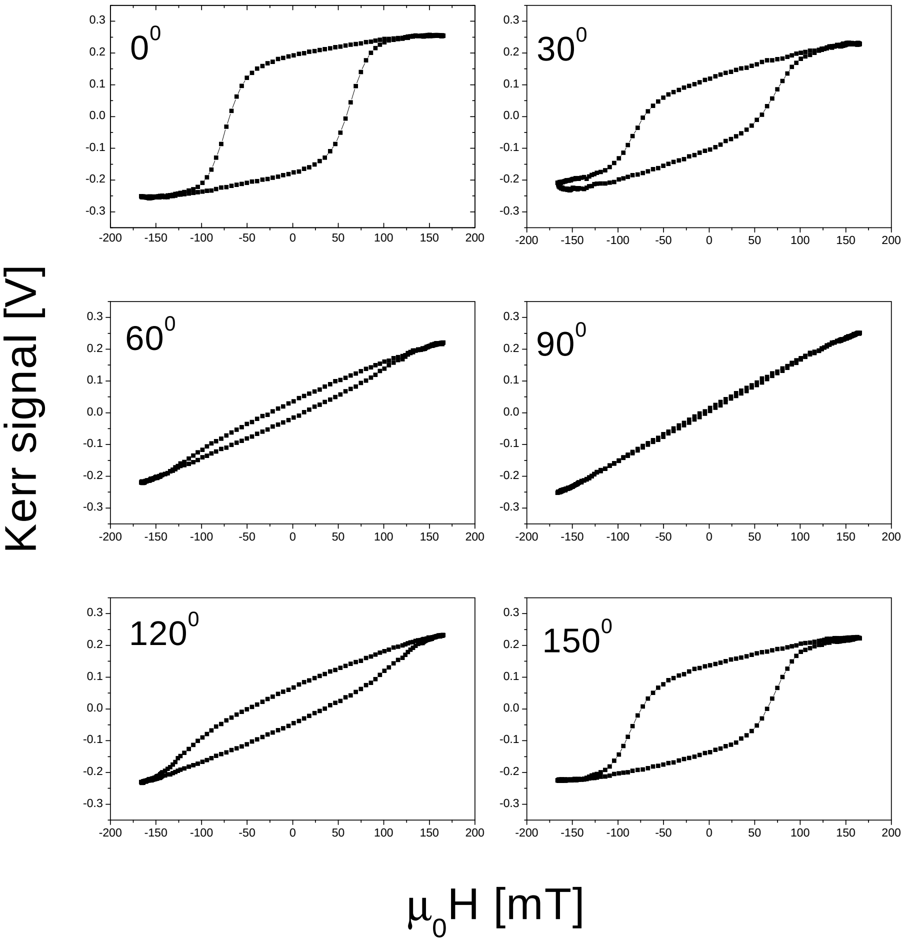

Figure 5.13: Kerr signal vs. field of Fe nanostructures at room temperature. For 0° the magnetic field is parallel to the facet ridges. First preparation series, deposition angle 8.5°.

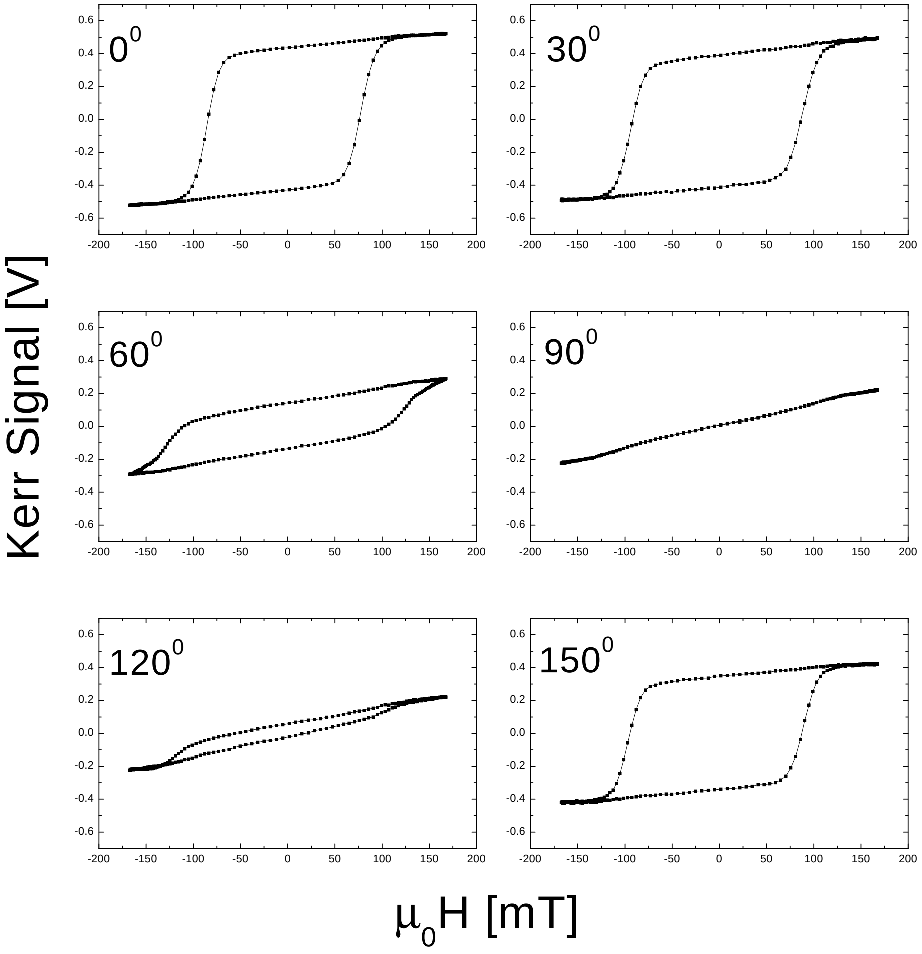

Figure 5.14: Kerr signal vs. field of Fe nanostructures at room temperature. For 0° the magnetic field is parallel to the facet ridges. First preparation series, deposition angle 15.5°.

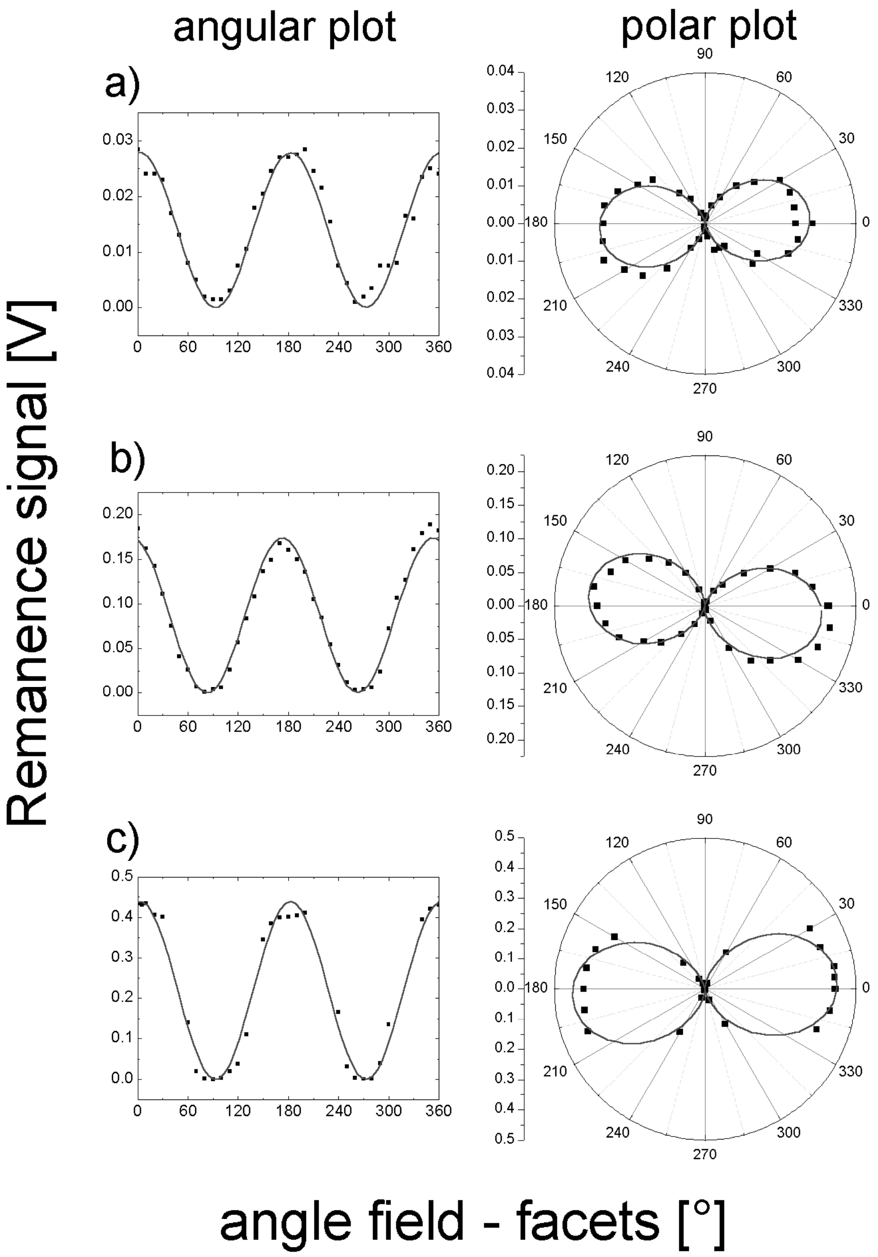

Figure 5.15: Remanence MOKE signal vs. angle between field and facet ridges of Fe nanostructures at room temperature. First preparation series, a) $\alpha_{Dep.} = 5°$, b) $\alpha_{Dep.} = 8.5°$, c) $\alpha_{Dep.} = 15.5°$. Continuous curve: $\cos^2$-fit.

trend of the angular dependence of the remanence signal. The $\cos^2$ fit curve is represented by the continuous line in the graphs. The maximum misalignment of the facets in the setup can be estimated to be approximately 5°. Therefore, the easy direction of magnetization of the samples prepared at an deposition angle of 5° and 15.5° is parallel to the facet ridges within the scope of accuracy. On the other hand, a small tilting of the easy axis with regard to the facet ridges of 6.5° for the sample prepared at 8.5° can be observed.

5.2.2 Magnetic properties of the second series

Like in the first preparation series, the nanostructures prepared in the time dependent series also show an uniaxial anisotropy with the easy axis aligned along the facet ridges. For abbreviation, only the measurements performed along the facet ridges are displayed.

In Figures 5.16 to 5.19 the VSM measurements of the structures prepared on substrates annealed at 1550°C are shown. The samples prepared for 20 minutes and 40 minutes reveal curved shapes with small coercive fields. For samples with enhanced deposition time the loops become more rectangular. This can be interpreted by a decrease of the saturation field with increasing structure thickness: From preparation times of 20 minutes to 120 minutes the structures saturate at 0.37 T, 0.34 T, 0.31 T, and 0.27 T, respectively. The coercive fields, on the other hand, increase with increasing structure thickness. For an increasing preparation time, H_C develops from 0.02 T, 0.03 T, and 0.06 T to 0.11 T. Furthermore, all loops reveal a change in the slope in magnetization reversal. This change occurs for all samples in the same field range. For the structures prepared from 20 minutes to 90 minutes this leads to a wasp like shape in the magnetization loop with the strangling close to H_C. The wasp shape is especially very pronounced at the structures prepared for 90 minutes, where the SEM images already reveal continuous wires. In the 120 min sample, the slope change occurs in the same field region, as already mentioned, but due to the high coercivity it only leads to a dip in the hysteresis loop. Therefore, the shape of the 120 min sample is similar to the Fe nanowires prepared at an incident angle of 15.5°, but the dip is more pronounced.

For structures prepared on substrates annealed at 1650°C the magnetization behavior is similar to the above described, as can be seen from Figures 5.20 to 5.23. With increasing deposition time the shape of the loops changes from curved

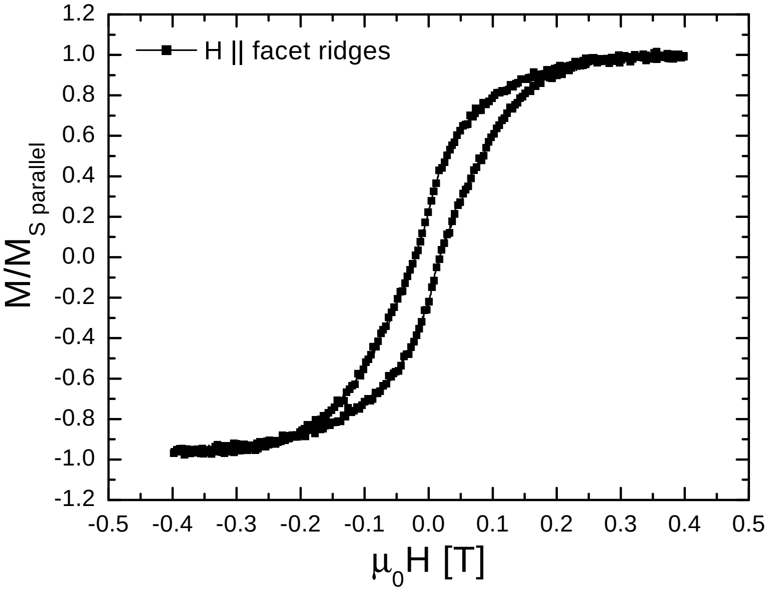

Figure 5.16: VSM measurements of Fe nanostructures at $T = 300$ K. $T_{anneal} = 1550°C$. Deposition time 20 min. Field parallel facets.

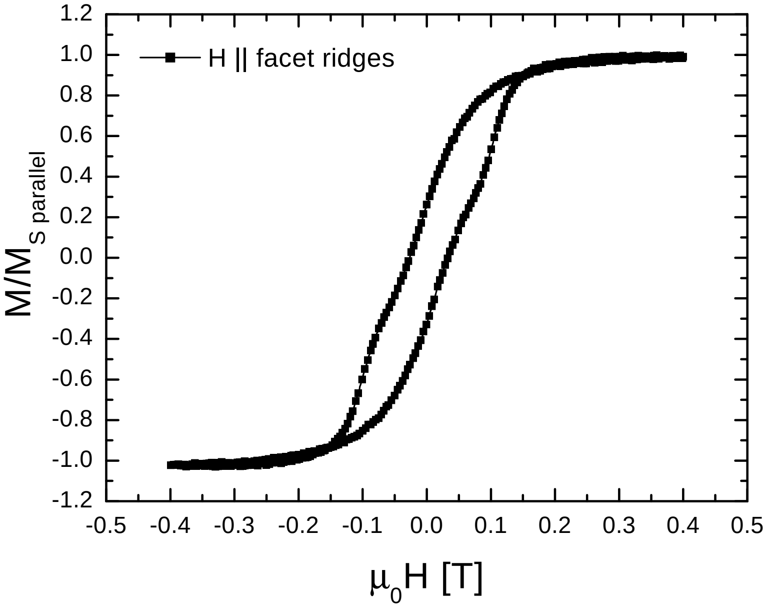

Figure 5.17: VSM measurements of Fe nanostructures at $T = 300$ K. $T_{anneal} = 1550°C$. Deposition time 40 min. Field parallel facets.

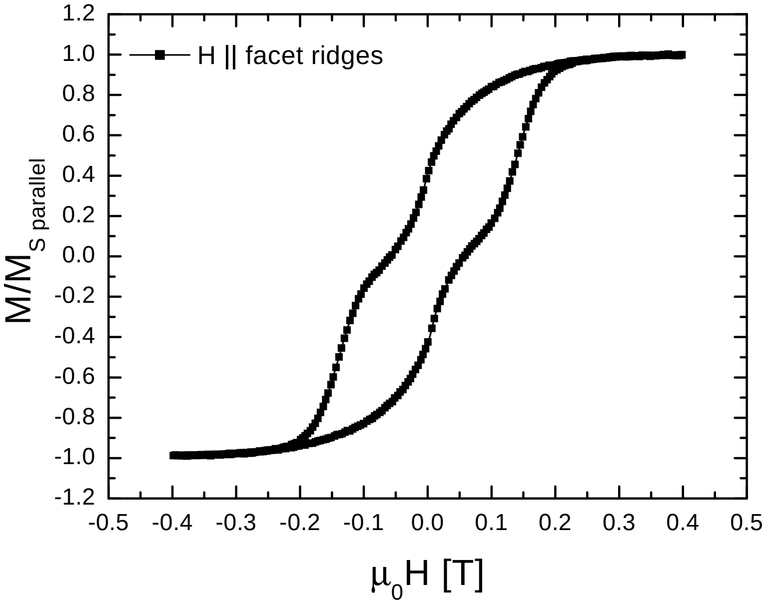

Figure 5.18: VSM measurements of Fe nanostructures at $T = 300$ K. $T_{anneal} = 1550°$C. Deposition time 90 min. Field parallel facets.

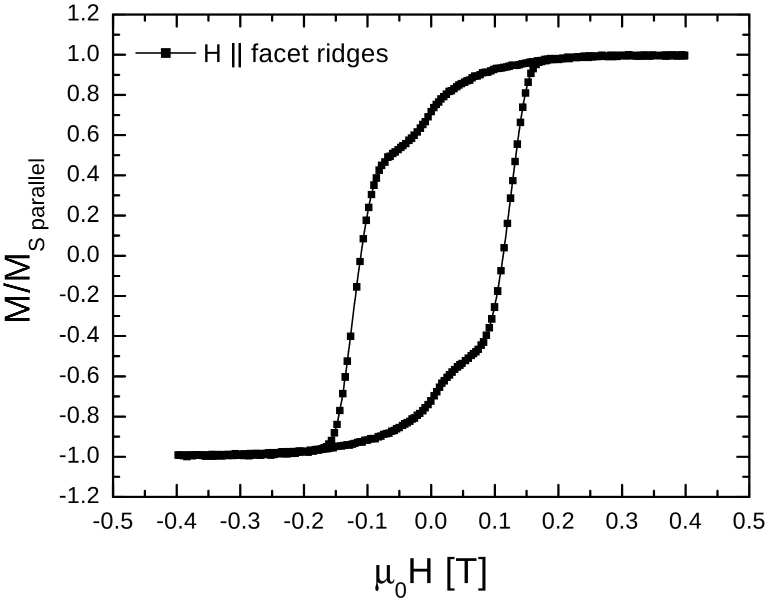

Figure 5.19: VSM measurements of Fe nanostructures at $T = 300$ K. $T_{anneal} = 1550°$C. Deposition time 120 min. Field parallel facets.

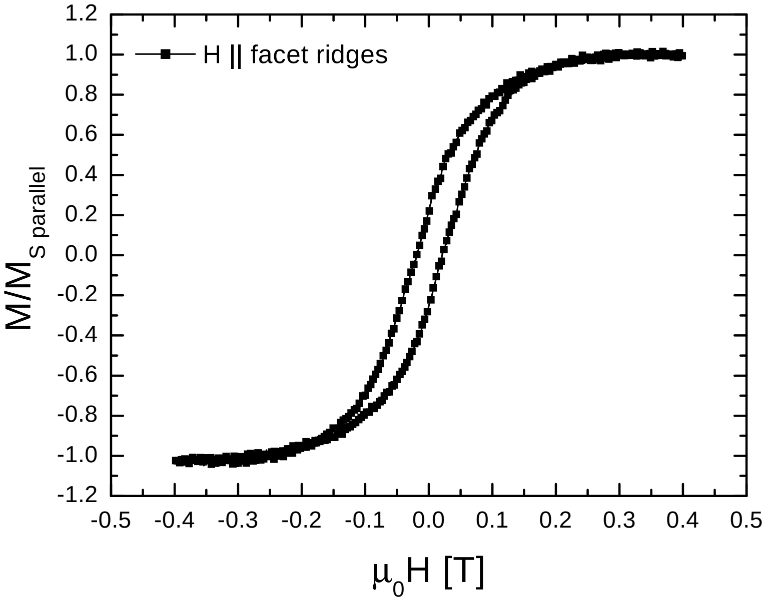

Figure 5.20: VSM measurements of Fe nanostructures at $T = 300$ K. $T_{anneal} = 1650°$C. Deposition time 20 min. Field parallel facets.

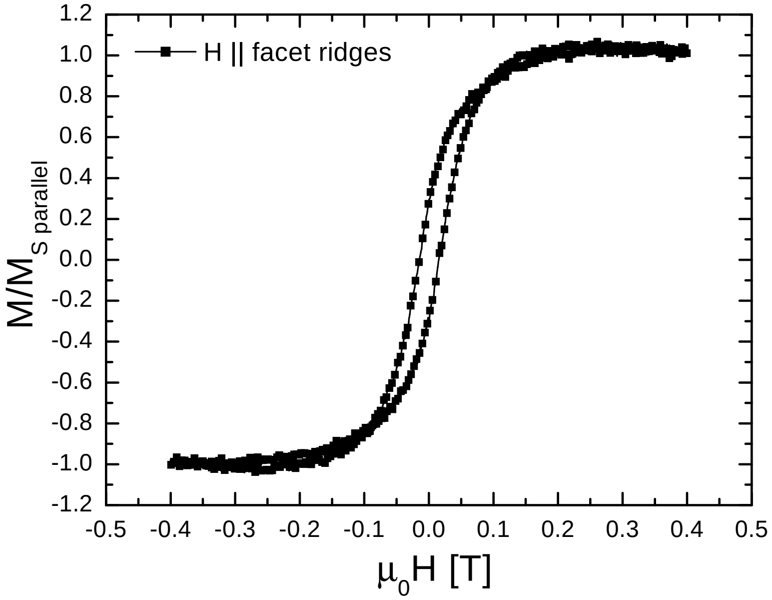

Figure 5.21: VSM measurements of Fe nanostructures at $T = 300$ K. $T_{anneal} = 1650°$C. Deposition time 40 min. Field parallel facets.

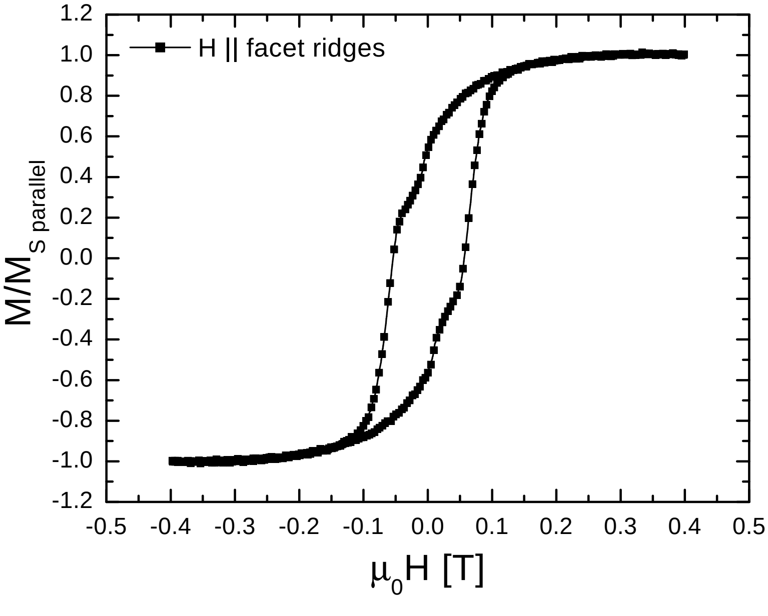

Figure 5.22: measurements of Fe nanostructures at $T = 300$ K. $T_{anneal} = 1650°\text{C}$. Deposition time 90 min. Field parallel facets.

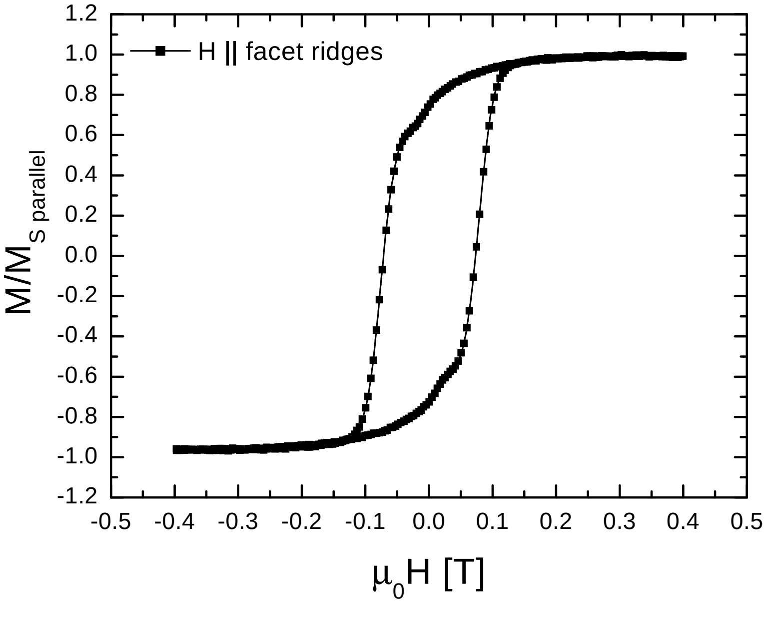

Figure 5.23: VSM measurements of Fe nanostructures at $T = 300$ K. $T_{anneal} = 1650°\text{C}$. Deposition time 120 min. Field parallel facets.

with small coercive fields to rectangular with larger coercive fields. H_C changes from 0.02 T, 0.01 T, 0.05 T to 0.08 T. Compared to the 1550°C samples no slope change for the 20 minutes and 40 minutes samples can be observed. The nanowires prepared for 120 minutes, on the other hand, reveal the same shape of the hysteresis loop like the wires presented in Figure 5.11.

5.3 Electrical properties

In addition to the magnetic properties, the electrical properties of single Fe nanowires were determined by M. Huth. The nano-wires were prepared by shallow incident deposition under an angle of 15.5° for 60 minutes. To reduce the nanowire array to a few parallel connected Fe nanowires, the film of Fe nanowires was patterned in a multi-step process. The wires were not covered by a metallic passivation layer. After preparation the film was coated with a photoresist. The photoresist was patterned such that two contact pad areas were exposed. The contact pads were separated from each other by a gap of 15 μm width, allowing electrical measurements parallel to the wires. Subsequently, the structured system was coated with platinum. Afterwards, the surplus platinum was removed in a lift off process with acetone. In the following step, the residual nanowires were removed by a second photolithograpy and ion-beam etching step, leaving the two electrical contact pads connected by about 150 Fe nanowires. A photography of the resulting structure appears in Figure 5.24.

In a second experiment Fe nanowires were also patterned in the above described way. In addition to this, the amount of nanowires in the gap was reduced by focussed ion-beam etching performed by N. Auth. Due to this procedure the amount of conducting Fe nano-wires could be reduced to about 12, see Figure 5.25.

The parallel electrical measurements of 150 and 12 Fe nanowires, respectively, were performed in a ^{4}He cryostate at 4 K with the magnetic field aligned parallel to the facets. The resistance of 150 nanowires amounts to 419 Ω, see Figure 5.26. The magneto-resistance changes by 0.01% during the magnetization reversal. For approximately 12 nano-wires, on the other hand, the electric resistance is strongly enhanced to 140 kΩ, see Figure 5.27. The change of the magneto-resistance can be estimated to be about 4%. During the measurement the resistance of the wires increased rapidly. It can be supposed that the current leads to an overheating and deterioration of single nanowires, eventually causing a reduction of the number of

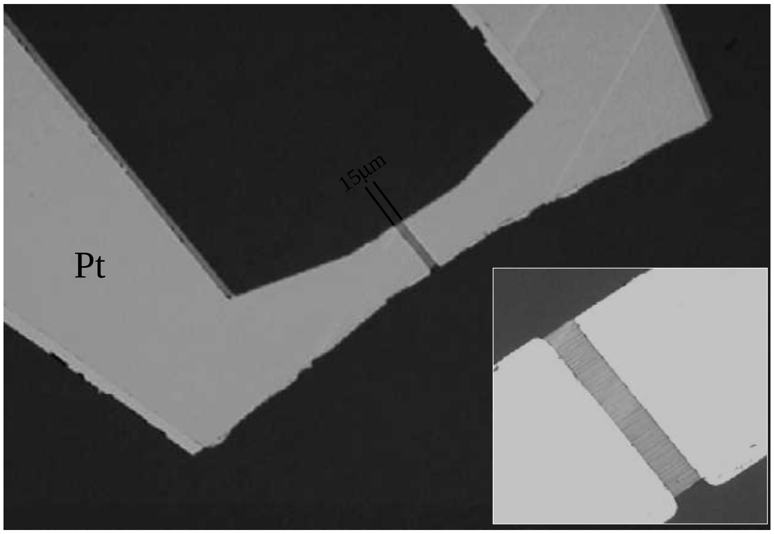

Figure 5.24: Photography of Pt contact pads connecting approximately 150 Fe nanowires. The patterning was performed by lift-off technique.

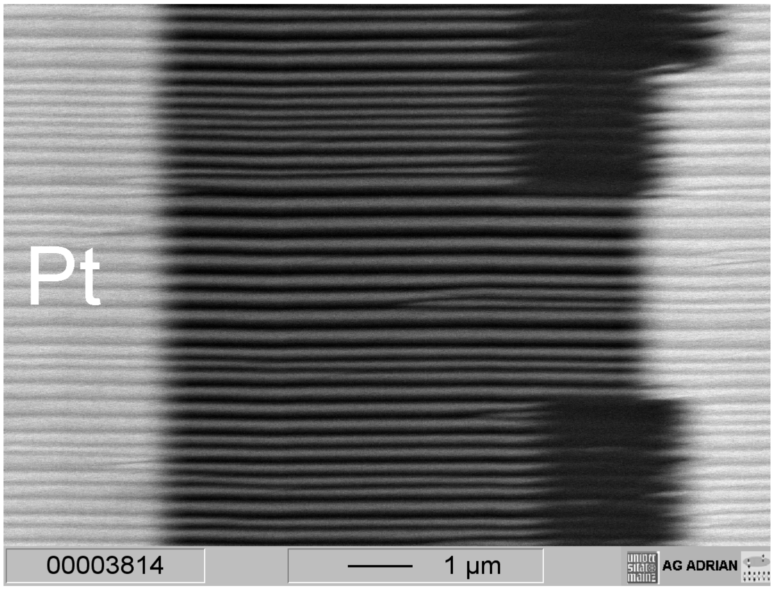

Figure 5.25: SEM image of Fe nanowires with Pt pads and paths etched by focussed ion beam.

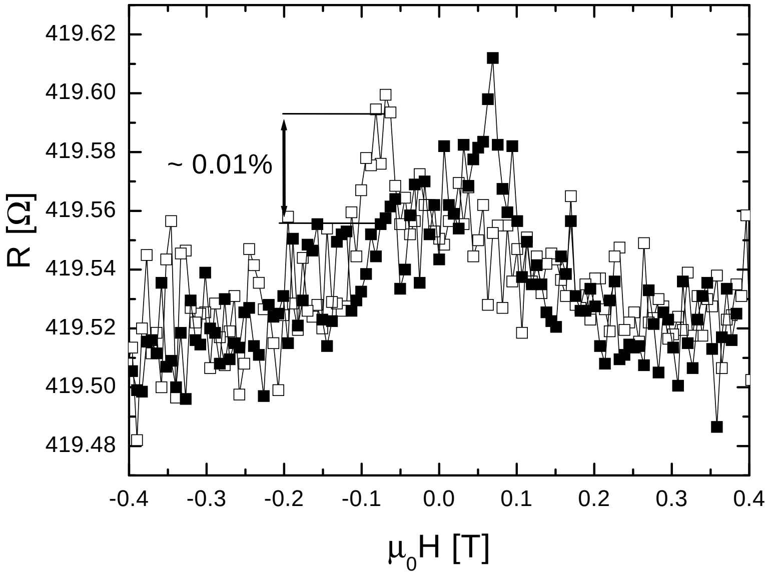

Figure 5.26: Electrical resistance vs. magnetic field of about 150 Fe nanowires. $T =$ 4K.

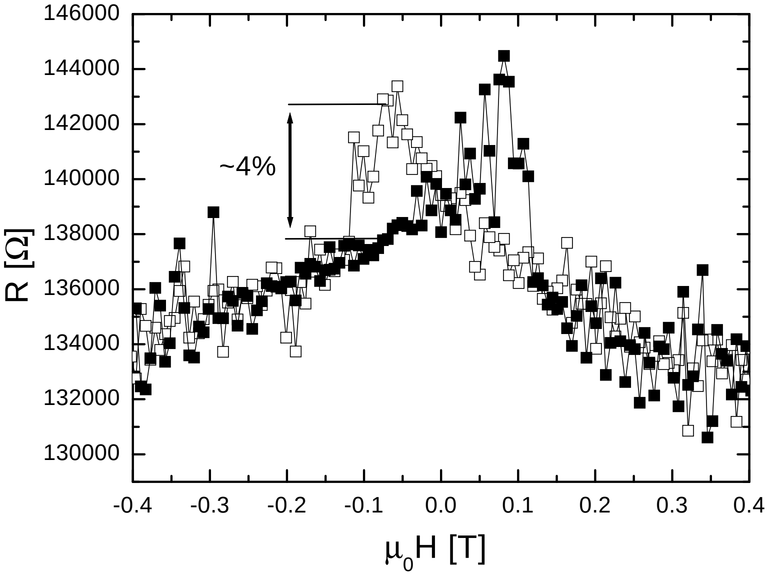

Figure 5.27: Electrical resistance vs. magnetic field of about 15 Fe nanowires. $T =$ 4K.

conducting wires. Due to the sensitivity of the setup and the deterioration of the wires, the statistics of the measurements was not sufficient to distinguish noise effects from real quantized conduction phenomena. With this first example of measuring a reduced number of metallic nanowires, further measurements with protected Fe wires and other materials or alloys are recommended.

5.4 Discussion: Magnetic properties

In the discussion of the magnetization reversal behavior of the Fe nanostructures, the shape of the objects has to be considered. Three different types of nanostructures have been introduced in the preparation part of this chapter: Firstly, Fe nanodots of sphere shape with diameters between 25 nm and 70 nm and average thicknesses of 10 nm to 25 nm. Their next neighbor distance is approximately 8 nm parallel and more than 200 nm perpendicular the facet ridges. Secondly, Fe nanodots of oval shape and a thickness of 25 nm have been prepared. Their short axis is 100 nm and their long axis reaches from 100 nm to 500 nm. Thirdly, 100 nm wide nano-wires of 30 nm to 45 nm thickness.

5.4.1 Sphere shaped Fe nanodots

Most micromagnetic calculations and experimental measurements on sphere shaped nanodots were performed at permalloy (Py) compounds [141, 142, 143, 144]. These investigations show that the magnetization reversal in submicron elements cannot be described by a down-scaling of the macroscopic world: Unlike a bulk sample in which the magnetization process is dominated by either wall motion or spin rotation or a combination of these two mechanisms, the magnetization process of a nanoparticle is dictated by the stability of the spin configuration.

In zero magnetic field ferromagnetic materials build domains to reduce the stray field energy. The domain pattern depends strongly on the shape and the size of the particle. The thickness δ of a domain wall is determined by the counterbalance between the exchange energy (which tends to increase it) and the anisotropy energy (which tends to disminish it). For Fe δ amounts to 40 nm. Nanostructures, especially the above described Fe sphere-shaped nanodots, can therefore not accommodate domain walls. Hence, the nanodots will build other spin structures to reduce magnetic stray field energy.

Experiments and calculations on permalloy show that if for a given radius R

the thickness t of a flat dot is smaller than a critical value t_c, the dot remains in an in-plane single-domain state at zero magnetic field, whereas for $t > t_c$ the dot is magnetically in a vortex state [141, 142]. In a single-domain state the magnetization of the particle acts like a magnetic dipole, leading to an corresponding stray field. In a magnetic vortex structure of a nanodot the magnetic moments order in the plane circular around the singular vortex center, where the magnetization points out of the plane. Therefore, the in-plane stray field is strongly reduced or even vanishing. The rotational direction of the vortex is called it's 'vorticity' while the central direction of magnetization is the so called "central polarization".

The critical thickness of the transition single-domain state - vortex state for non-interacting nano-dots in zero magnetic field was calculated by Höllinger et al. to [144]:

$$t_c(R) \approx 2R \left\{ \frac{1}{5.31} \{ \exp\left(\frac{8\pi}{2.41} \frac{l_m^2}{R^2} [2.67 + ln \frac{R}{5l_m} + 0.5] \right) - 1 \} \right\}^{1/0.88} \tag{5.1}$$

Here, $l_m = \sqrt{2\mu_0 A / M_S^2}$ denotes the exchange length, with the saturation magnetization M_S, and the stiffness constant A. For Fe the exchange length can be calculated to 3.7 nm [145], while for Py it is 5.7 nm [146]. A calculation for Fe nanodots according to Equation 5.1 is shown in Figure 5.28 and reveals that t_c of Fe is reduced when compared to Py for dot diameters smaller than 200 nm. But the thickness of the prepared dots with a radius as analyzed from SEM images is close to the calculated values for t_c and is in the region of the increasing slope of the curve: For dots with a diameter of 70 nm the critical size is 2.2 nm and therefore far beyond the estimated thickness. For dots with a diameter of 40 nm the critical thickness is strongly enhanced to 14 nm and for the smallest dots of 35 nm diameter t_c is 20 nm. Therefore, the magnetization of large dots in zero external field will definitely be in a vortex structure. For dots of smaller diameter a single-domain state of the magnetization cannot be excluded. Therefore, the magnetization reversal is possibly a mixture of single-domain magnetization and vortex states. However, for the here discussed samples the critical thickness of the dots might be altered due to the dipole coupling of the dots. Furthermore, the size of the particles is not monodisperse, leading to different shapes of the hysteresis loops even for the same magnetization reversal process. As can be seen from the slope of Figure 5.28 in the region of interest, the ratio of vortex to single-domain states will depend very strongly on the thickness of the dots.

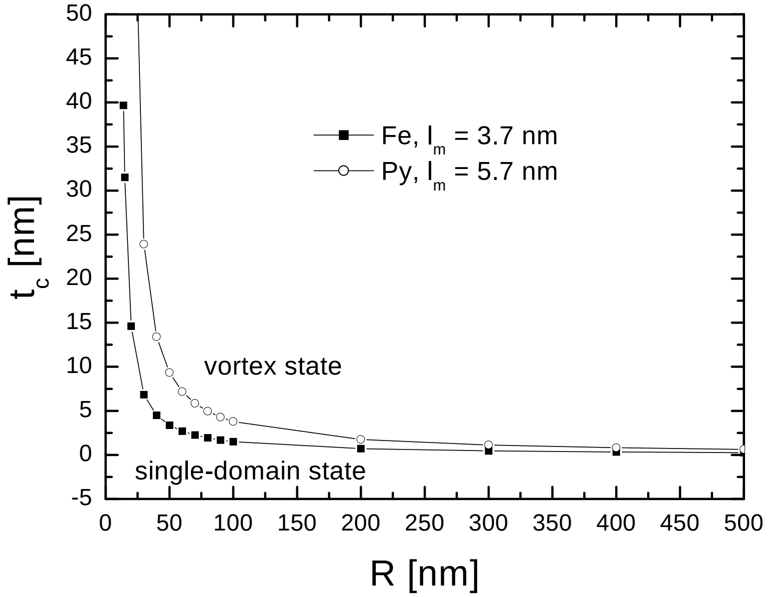

Figure 5.28: Critical thickness for the formation of single-domain and vortex state of uncoupled Fe and permalloy nanodots calculated by equation 5.1.

The two different magnetic states of the nanodots reveal a different magnetization reversal behavior. An example of a single-domain and a vortex state hysteresis loop, published by Cowburn et al. for Supermalloy ($Ni_{80}Fe_{14}Mo_5$), is shown in Figure 5.29. For a single-domain state the magnetization reversal is expected to occur by coherent rotation according to the Stoner-Wohlfarth model [147], see left graph of Figure 5.29. Here, a square-shaped hysteresis with coercive fields governed by the anisotropy of the system is predicted for magnetic fields directed along the easy axis. However, as will be shown in the micromagnetic modeling discussed below, the square shape of a loop can also be explained by an alternative reversal mechanism involving the formation of an instable vortex state. In the vortex state the influence of the magnetic field leads to a shifting of the center of the vortex perpendicular to the magnetic field direction, see right graph of Figure 5.29. Starting the magnetization reversal process at an uniformly magnetized state at high fields, the magnetization stays in the saturated state until the vortex nucleates at the edge of the dot. From there it shifts rapidly to the center of the structure driven by stray field energy reduction. At zero magnetic field a strongly reduced magnetization is observed. A further increase of the magnetization reversal field will shift the vortex out of the structure. During this process the stray field energy increases. As a result, the magnetic moment of the element increases gradually with increasing external magnetic field. At a certain magnetic field, the vortex becomes unstable and leaves the element. Above this field the particle will reveal a single-domain magnetization.

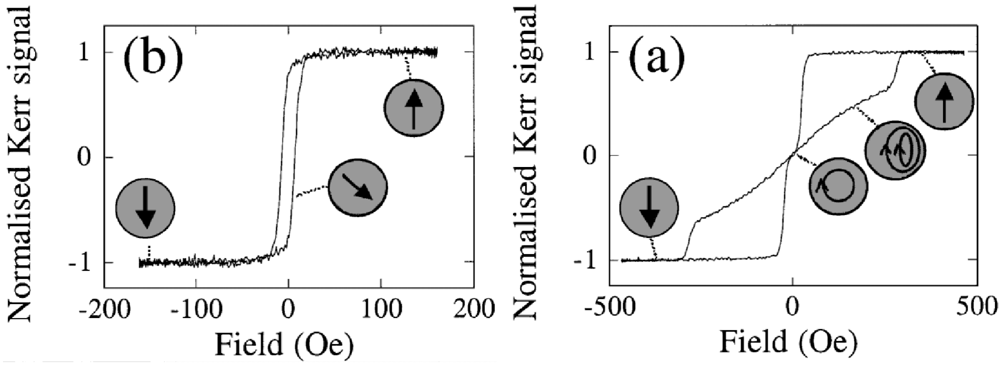

Figure 5.29: Magnetization behavior of single-domain (a) and vortex state (b) supermalloy ($Ni_{80}Fe_{14}Mo_5$) nanodots. Taken from [141].

As already mentioned, these considerations are mainly valid for non-interacting particles. Due to the small inter-particle distance of 8 nm on the individual facets of the structures prepared in this work a magnetic dipole interaction of the adjacent particles is expected. To minimize stray field energies both states, single-domain and vortex state, are expected to show an uniaxial anisotropy with the easy axis parallel to the next neighbors: For the single-domain state this is obvious, for the vortex state the magnetic moments will also prefer an alignment along the dot chain when the particle is in a single-domain state at large external magnetic fields.

For a quantitative determination of the magnetization reversals of the Fe nanostructures micromagnetic calculations were performed by F. Porrati [148]. Here, the the Landau-Lifshitz-Gilbert equation of motion was solved numerically using the program LLG *Micromagnetic Simulator*^{TM} v2.46 by M. Scheinfein. Special interest was put on the structures prepared under an incident angle of 5° in the first preparation series. The micromagnetic properties of the sphere-shaped Fe nanodrops were modelled by considering a series of chains of Fe dots. Each single chain was formed by an infinite number of dots of constant thickness t and diameter d[1]. A gaussian distribution of the dot diameter was assumed for

---

[1] Dots of thickness 16 nm$\leq t \leq$ 40 nm and diameter 30 nm$\leq d \leq$ 80 nm were considered. These values have been chosen after analysis of the SEM image.

the group of chains. The ratio r between thickness and diameter was chosen as constant for all the dots ($r = t/d \simeq 0.5$). The magnetostatic coupling of neighbor chains was neglected, while it was considered within each chain in neighbor dots. Single dots with periodical boundary conditions in the direction of the chain extension were considered to simulate the infinite number of dots in the chains.

The simulation volume was discretized in square prisms of size 2 nm in the xy directions and 4 nm in the z direction (parallel to the symmetry axis of the dot). The bulk constants of Fe were used in the calculations: exchange stiffness $A = 2.1$ μerg/cm, saturation magnetization $M_s = 1714$ emu/cm^3 and cubic anisotropy $k = 4.7 \times 10^5$ erg/cm^3. The cubic anisotropy is rotated by 30° with respect to the chain direction in the film plane, as deduced from the X-ray analysis discussed in chapter 2.

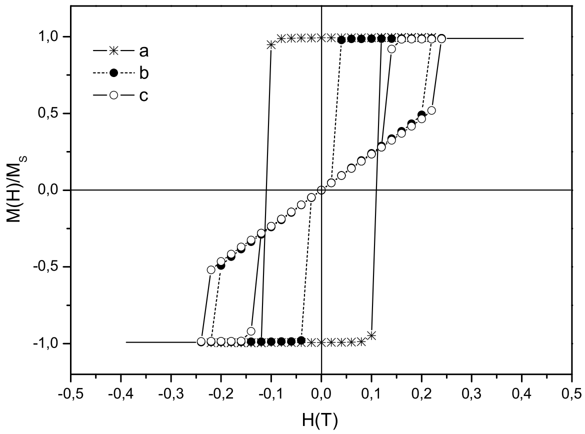

Figure 5.30: Magnetization reversal in single chains of dots. a: thickness $t = 20$ nm, diameter $d = 40$ nm. b: $t = 28$ nm, $b = 60$ nm. c: $t = 36$ nm, $d = 70$ nm. See text for details.

Figure 5.30 shows the three types of reversal obtained in the investigation. The simulations were performed by applying a magnetic field parallel to the chains. An inter-dot distance of 8 nm was assumed. Plot a represents the reversal for a chain of dots with thickness and diameter given respectively by $t = 20$ nm and $d = 40$ nm. The hysteresis loop is rectangular with a coercive field $H = -0.12$ T and remanence $M(H)/M_s = 1$. The shape of the loop might be erroneously attributed to a coherent rotational process. Actually the analysis of the micromagnetic configuration of the dot revealed that the reversal from $M(H)/M_s = 1$

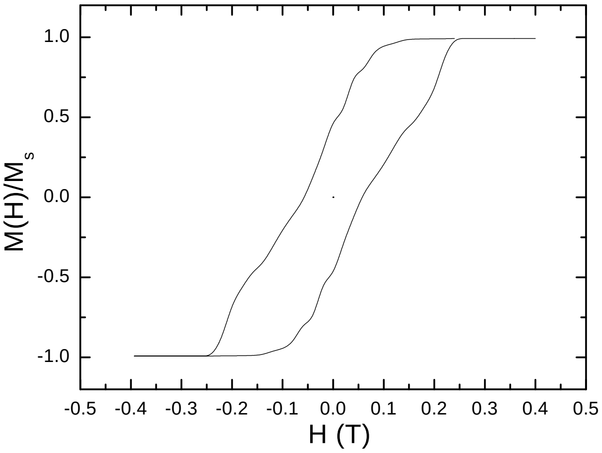

Figure 5.31: Hysteresis loop obtained with the contribution of chains of dots magnetostatically decoupled. In the sum the 'weight' of the chains is assumed to have a gaussian distribution. The small steps in the shape of the loop are due to the finite number of dot chains considered for the Gaussian distribution in the modeling.

to $M(H)/M_s = -1$ involves a vortex state, unstable for $H = -0.12$ T. Increasing the diameter of the dot, the vortex states becomes metastable. This case, shown in plot *b*, is valid for a chain of dots with $t = 28$ nm and $d = 60$ nm. The vortex nucleates at $H = 0.04$ T and annihilates at $H = -0.22$ T. In the previous two examples the reversal takes place almost uniformly in the z direction. For larger thickness the reversal is not uniform. Plot *c* refers to a chain of dots of thickness and diameter, respectively, equal to $t = 36$ nm and $d = 70$ nm. For $H > 0.16$ T the magnetization of the dots is uniform along the applied field. For $H = 0.16$ T the magnetic moments of the upper and the lower part of the dots rotate oppositely out of the field direction in order to minimize the magnetostatic energy. The rotation of the magnetic moments is asymmetric because the axis of the magnetic anisotropy is not parallel to the chain. For $H \leq 0.14$ T a magnetic vortex nucleates, propagates and annihilates, similarly to the case reported in plot *b*. Together with the three examples previously shown, similar hysteresis loops have been calculated for other chains with dots of different thickness and diameter. In Figure 5.31 the sum of all the hysteresis loops calculated is plotted. The comparison of the shape of the hysteresis loop, in particular the values of remanence, coercive field and saturation field, calculated are in good agreement with the experimental data reported in Figure 5.9.

5.4.2 Oval Fe nanodots

Similar to their sphere shaped counterparts ferromagnetic oval nanodots are expected to possess the above described magnetic structures. With a short axis of ≈100 nm, a long axis of up to 500 nm, and a thickness of 25 nm the magnetization of oval Fe nanostructures prepared at an incidence angle of 8.5°, shown in Figure 5.3, is definitively not in a single-domain state. Usov et al. have calculated the magnetization structure of soft ferromagnets of elliptical shape [149]. They state that the shape of the magnetization mode depends on the particle's aspect ratio. The occurrence of a single vortex in elliptic permalloy dots is therefore solely stable for a major to minor axis ratio $a/b \leq 3.5$ at a thickness of 30 nm. For higher aspect ratios the reduction of the particle's stray field energy is created by two or three vortices. Similar magnetic structures are therefore also expected in elliptic Fe nano-dots.

The quantitative analysis again was performed by F. Porrati by micromagnetic modeling [148]. In order to study the magnetization reversal of the nanostructures obtained in the experiment with an incident angle of deposition of 8°, a chain of interacting oval pillars was considered. In the modeling, each pillar is 32 nm thick and it is separated from the neighbor one by a distance of 8 nm. The planar section of the pillar was an oval with major axis a parallel to the chain extension and minor axis b perpendicular to it; their lengths were respectively $a = 300$ nm and $b = 170$ nm. In Figure 5.32 the result of the reversal process obtained by applying a magnetic field parallel to the chain extension is shown. The shape of the hysteresis loop indicates that the easy magnetization axis is along the major axis of the pillar, as observed experimentally. The reversal takes place by means of the formation of magnetic vortices, as shown in Figure 5.32. Similarly to the case reported above for sphere shaped dots (plot a, Figure 5.30), the state presenting magnetic vortices is not stable for $H = -0.08$ T. As a consequence, when reaching the nucleation field, the average magnetization reverses abruptly from $M(H)/M_s = 1$ to $M(H)/M_s = -1$. By comparing the modeling with the experiment, it may be noted that the remanence as well as the squareness of the loop are not identical. In order to obtain a closer correspondence with the experiment, a distribution of the nucleation field of the pillars might be considered.

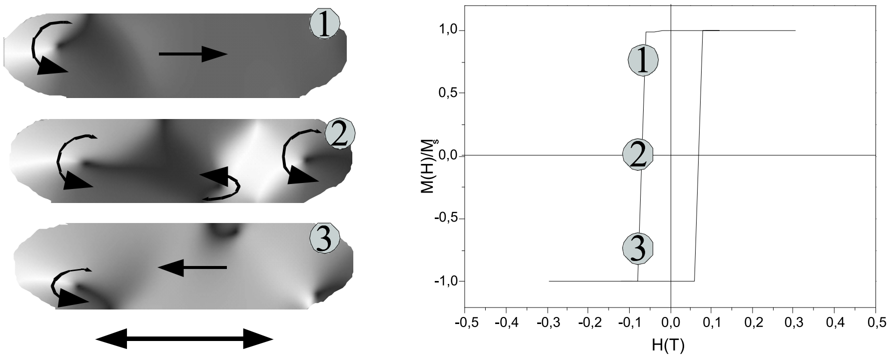

Figure 5.32: Magnetization reversal of a chain of magnetostatically interacting oval pillars.

5.4.3 Fe nanowires

Like for nanodots, the magnetic properties of nanowires are mostly reported for permalloy and cobalt compounds [150, 151]. Fe nano-wires are mostly prepared in porous alumina templates, leading to structures with diameters in the 10 nm range [152, 153].

Preliminary magnetic studies show that the magnetization reversal process in the here discussed nano-wires may be performed by the formation of vortex states. Possible nucleation centers are the ends of the wires and further discontinuities in the wire structure. In the sample prepared at an incident angle of 15.5° these discontinuities are the lacings of the wires. The wires obtained from the second preparation series, on the other hand, consist of an accumulation of nanodots. These dots could in this case be the origin of vortex formation.

A different explanation of the magnetization reversal process occurring in the nanowires could be the nucleation of several magnetic domains and a subsequent domain wall rotation. These processes were presumed by Schmitte et al. for 13 nm thick and 150 nm wide Fe nano-wires of 300 nm periodicity, scrutinized by vector-MOKE [154]. With this measurement technique an information of both, longitudinal and transversal magnetization of the wires is obtained. Parallel to the wires the nucleation of a number of domains instead of one single domain wall travelling along the nanowire is assumed. In perpendicular orientation the immediate nucleation of domains with different pinning potential is deduced. Between these extreme orientations, intermediate processes are assumed. The analysis of the magnetization vector during the magnetization reversal excludes coherent rotation to be a relevant process [154].

In a comparison of the measurement results of Schmitte et al. with the here discussed samples pro- and contra arguments for an adaptation of the deduced magnetization reversal process can be found. In analogy to the here discussed samples Schmitte et al. observe an uniaxial magnetic anisotropy with the easy axis parallel to the stripes. Furthermore, they observe a similar angular-dependence of the remanence signal. Despite these compliances, also some discrepancies occur. Firstly, the occurrence of an angular-dependent second coercivity reported by Schmitte et al. is not observed in the here discussed MOKE measurements. Secondly, Schmitte et al. observe a coercive field of $H_C = 25$ mT for both, non-patterned films and nanowires with the field directing parallel to the stripes. In the here discussed wire structures H_C is with approximately 70 mT strongly increased compared to 2 mT measured for a continuous Fe film. And thirdly, Schmitte et al. do not observe a step in the hysteresis loop at reversal fields of 0 T to 50 mT. These discrepancies may be solved by arguing that the quality of the here discussed samples is different from the polycrystalline wires of Schmitte et al. This could lead to an increased coercive field which may therefore mask hysteresis features in the non-saturated MOKE measurements performed on the here discussed samples. Furthermore, the step could be explained by an increased pinning in some regions of the wires. Then, the magnetization reversal processes could be explained analogously by the nucleation of domains. A final solution of the reversal process can only be gained by further measurements.

5.5 Conclusion

In analogy to the preparation of Nb nanowires, explained in chapter 2, it could be shown that by shallow incidence deposition on faceted sapphire m-plane substrates also semi-periodic ferromagnetic nanostructures can be created. From qualitative arguments and from micromagnetic modeling the occurrence of vortex states in the sphere and oval shaped nanodots can be deduced. The magnetization reversal process in the nano-wires is not clarified yet. First magnetic studies suggest the nucleation of vortex structures but also the nucleation and domain-wall movement of a number of domains is possible. For clarification further measurements have to be performed.

Several different experiments could be suggested to review the above discussed results. The magnetization reversal process of the nanowires could be scrutinized in a vector-MOKE measurement. With the same technique, the magnetic behavior of the nanodots could be determined: The coherent rotation of single-domain dots should give a different transversal signal as compared to vortex states. A direct observation of vortex states could be possible with magnetic force microscopy (MFM) [155, 156].

The single-vortex magnetization of periodically aligned nano-dots could be suitable for next generation magnetic recording media. Hereby not only the small size and high density of the particles is of favor compared to up to date systems, but also the enhanced information of the vortex state. This benefit is given due to the fact, that the magnetic vortex state of a dot has a fourfold topological degeneracy, since in principal one can measure (and flip) independently both the vorticity (r/l) of the state and the central polarization (+/–) of the vortex, i. e. for magnetic recording one has 2 bit per dot for a vortex state dot instead of only 1 bit for single-domain dots. However, several obstacles have to be overcome until a wide-spread use of this technique could become true. Firstly, a reproducible, fast and simplified technique to read and write the information of magnetic vortices has to be developed. This problem, of course, is not limited to the here described systems. Secondly, the size of the nanodots has to fit the single-vortex state. Therefore, only sphere shaped or small oval shaped dots of adequate thickness can be applied. In the here described technique of shallow incidence deposition, the size spread of the obtained dots must therefore be reduced. According to this, the periodicity of the dots on each facet ridge has to improve. Thirdly, to allow the reproducible positioning of a "read head" system, the periodicity of the facets has to be improved. This implies a reduced dispersion of the facet size. Additionally, the occurrence of facet boundaries should be prevented.

Taking the last three requirements, the main key to gain serious attraction for application is to study the controllability of the facetting process of sapphire m-plane.

Summary

The thin film properties of selected magnetic 3d- and 4f- systems on α-Al_2O_3 (sapphire) substrates were analyzed in this work. The preparation of the films was performed by molecular beam epitaxy (MBE) in a custom designed system. The interest was put as well on crystalline growth as on novel preparation techniques as on magnetic, magnetoelastic, and electric properties of the prepared samples. The substrates were employed in the $(11\bar{2}0)$ (a-plane) and the $(10\bar{1}0)$ (m-plane) orientation. The m-plane substrates were used in both, non-faceted and faceted morphology.

In a self-organization process sapphire m-plane substrates are known to reduce the surface energy by building a faceted zigzag like morphology at high temperature annealing. A preparation series of sapphire m-plane annealed for 24 h in air shows that the facet size increases with the annealing temperature. Starting from 1400°C the average width of the facets is 115 nm while the height amounts to 9 nm. The largest facets with still sharp facet ridges are obtained for 1650°C annealing temperature. Here, the average width and height amount to 250 nm and 50 nm, respectively. In addition to the size the angles of the facet planes with respect to the original surface increase with increasing temperature to maximum values of 17° for the $(10\bar{1}1)$ and to 22° for the $(10\bar{1}\bar{2})$ plane, respectively. The deviation of these experimental values from the theoretical values of 17.6° and 32.4° could be explained by cross section high resolution transmission electron microscopy (TEM) measurements. These show that the $(10\bar{1}1)$ plane is always formed in the faceting process, rendering the 130° facet angles independent of the annealing temperature. The second facet is expressed by a flat $(10\bar{1}\bar{2})$ surface close to the facet ridges and valleys. In between, the facet is curved, presumably due to diffusion limitation. The curves are formed by step bunches of $(10\bar{1}\bar{2})$ layers.

X-ray analysis and TEM measurements show a twin-free (211)-oriented epitaxial growth of the 3d bcc metals Nb and Mo on as well non-faceted as faceted sapphire m-plane substrates according to the established three dimensional relationship. In the film plane the bcc $[01\bar{1}]$ direction is parallel to the sapphire [010] direction while bcc $[\bar{1}11]$ is parallel to sapphire [001]. As concluded from the high epitaxial quality of the films and verified by the TEM measurements, the bcc metals overgrow the faceted structures homogenously. On top of the sapphire $(10\bar{1}1)$ and $(10\bar{1}\bar{2})$ plane the 3d metals grow (111)- and (001)-oriented with a tilt of 2° and -3°, respectively. The growth of Fe on sapphire m-plane, on the other hand, is much more complicated. At least four twins are observed, which furthermore differ for faceted and non-faceted substrates. The excellent growth properties of Nb and Mo on sapphire m-plane as compared to Fe can be explained by a reduced lattice mismatch of the two refractory metals with respect to the rhombohedral unit cell of the sapphire crystal.

The twin-free growth of Nb and Mo on sapphire can be furthermore exploited as template for the epitaxial growth of the highly magnetostrictive C15 Laves phases of the rare earth (R, here R = Tb, Dy, $Tb_{0.3}Dy_{0.7}$) iron compounds RFe_2. In addition to the established (110)-oriented growth on a (110)-oriented Nb buffer layer on sapphire a-plane and the (111)-oriented growth on Mo (110) on the same substrate orientation, a twin-free epitaxial (211)-oriented growth of the RFe_2 compounds on Nb (211) on faceted and non-faceted sapphire m-plane was found in this work. Due to the cube to cube growth on the Nb template the in-plane relationship of the RFe_2 compound with respect to the substrate is analogous to Nb and Mo. In analogy to the twin-free growth of the two bcc metals on faceted sapphire, RFe_2 crystals overgrow the faceted structure homogenously. On (211)-oriented Mo templates, on the other hand, the RFe_2 compounds grow in several crystal orientations.

Magnetic and magnetoelastic measurements on the epitaxial RFe_2 films were performed in a vibrating sample magnetometer (VSM), by magnetooptical Kerr effect (MOKE), and in a self designed magnetoelasticity measurement setup. Most investigated systems reveal a magnetization in the range of 800 kA/m and magnetoelastic values comparable to those of single crystalline bulks. For $DyFe_2$ films the lowest coercive fields of 0.13 T are obtained for (111)-oriented epitaxial samples and for polycrystalline samples prepared on Mo (211) on sapphire m-plane. Epitaxial (211)-oriented $DyFe_2$ films, on the other hand, reveal slightly higher coercive fields of 0.16 T. Compared to $DyFe_2$ films the coercive fields of

$Tb_{0.3}Dy_{0.7}Fe_2$ films are not reduced. Epitaxial $TbFe_2$ films, on the other hand, reveal the highest coercive fields of the three investigated systems. However, in analogy to $DyFe_2$ films, in (211)-oriented films the coercive field is reduced compared to those of (110) orientation.

Epitaxial films of $DyFe_2$ reach magnetoelastic value changes $\Delta b^{\epsilon,2}$ of -36 MPa at 1.1 T which can be attributed to a magnetostriction of approximately $570 \cdot 10^{-6}$. Polycrystalline $DyFe_2$ films on Mo (211) on non-faceted and faceted sapphire reach magnetoelastic parameters of -34 MPa ($\Delta\lambda^{\epsilon,2} \sim 530 \cdot 10^{-6}$). The magnetoelastic response of $Tb_{0.3}Dy_{0.7}Fe_2$ films is considerably smaller than according bulk materials. At 1.1 T $\Delta b^{\epsilon,2}$ reaches values of -60 MPa ($\Delta\lambda^{\epsilon,2} \sim 940 \cdot 10^{-6}$). Like in bulk samples, $TbFe_2$ films reveal the highest magnetoelastic response. With -108 MPa ($\Delta\lambda^{\epsilon,2} \sim 1695 \cdot 10^{-6}$) $\Delta b^{\epsilon,2}$ reaches 75% of the bulk values at 1.1 T.

Furthermore, no significant difference in the magnetic and magnetoelastic properties of faceted (211)-oriented RFe_2 films compared to non-faceted (211) films could be observed. This again underlines the high crystalline quality of the faceted films. The novel epitaxial (211) orientation of RFe_2 on Nb (211) on faceted or non-faceted sapphire is therefore a real enrichment for the research on RFe_2 films. Further measurements of magnetostriction induced surface acoustic wave (SAW) delay effects are in progress.

In addition to the preparation of undulated metallic films covering the complete faceted surface of sapphire m-plane the feasibility of preparing metallic nanostructures on the hill-and-valley morphology by shallow incidence deposition was tested. Exploiting the hitchless propagation of atomic beams in ultrahigh vacuum the self shadowing of the facets and de-wetting effects of the metal-insulator interface create feature sizes smaller 100 nm. Applying this technique, insulated Nb nanowires could be prepared, which were superconducting as shown by magnetization measurements.

Next to Nb, Fe nanostructures were prepared by shallow incidence deposition on faceted sapphire substrates. Scanning electron microscopy (SEM) measurements revealed the formation of insulated structures. Their morphology depends strongly on the preparation parameters. It reaches from pearl-necklet like strung sphere-shaped nanodots to oval-shaped nanodots to continuous nanowires. Magnetization measurements in the (VSM) and by longitudinal magnetooptical Kerr effect(MOKE) revealed an uniaxial anisotropy of the structures with the easy axis of magnetization parallel to the facet ridges. Estimations give the sphere-shaped nanodots to be at the boarder between single-domain and single-vortex magnetization. Accordingly, the magnetization reversal process of the sphere shaped nanodots is attributed to a mixture of Stoner-Wohlfarth like coherent rotation and vortex-nucleation. The oval-shaped nanodots are believed to create a multi-vortex state at low magnetic fields. Quantitatively, these estimations were proofed by micromagentic modeling of the hysteresis loops. For the nanowires the magnetization reversal can be interpreted by the formation of vortices and domain nucleation.

Bibliography

[1] D. W. Susnitzky and C. B. Carter, J. Am. Ceram. Soc. **75**, 2463 (1992)

[2] S. Ramamurthy, B. C. Herbert, and C. B. Carter, Philos. Mag. Lett. **72** , 269 (1995)

[3] J. R. Heffelfinger and C. B. Carter, Surf. Sci. **389**, 188 (1997)

[4] R. D. Greenough, I. M. Reed, and M. P. Schulze, in: *Advances in Actuator*, edited by A. P. Dorey and J. H. Moore (IoP Pub., 1995, Ch. 8)

[5] D. C. Jiles, in: *New Materials and their Applications*, edited by D. Holland (Institute of Physics, Bristol, 1990)

[6] H. Uchida, M. Wada, K. Koike, H. H. Uchida, V. Koeninger, Y. Matsumura, H. Kaneko, and T. Kurino, J. Alloys Compd. **211/212**, 576 (1994)

[7] V. Koeninger, Y. Matsumura, H. H. Uchida, and H. Uchida, J. Alloys Compd. **211/212**, 581 (1994)

[8] A. E. Clark, in: *Ferromagnetic Materials*, edited by E. P. Wohlfarth (North Holland, Amsterdam, 1980), Vol. 1

[9] A. E. Clark, in: *Handbook of the Physics and Chemistry of Rare Earth*, edited by K. A. Gschneider and L. Eyring (North Holland, Amsterdam, 1982), Vol. 2

[10] V. Oderno, C. Dufour, K. Dumesnil, Ph. Mangin, and G. Marchal, J. Cryst. Growth **165**, 175 (1996)

[11] M. Huth and C. P. Flynn, Phys. Rev. B **58**, 11526 (1998)

[12] M. Huth and C. P. Flynn, J. Mag. Mag. Mater. **204**, 204 (1999)

[13] J. Mayer, C. P. Flynn, and M. Rühle, Ultramicroscopy **33**, 51 (1990)

[14] C. P. Flynn and M. B. Salamon, in: *Handbook of the Physics and Chemistry of Rare Earths*, edited by K. A. Gschneider Jr. and L. Eyring, (North Holland, Amsterdam, 1996), Vol. 22

[15] A. R. Wildes, J. Mayer, and K. Theis-Bröhl, Thin Solid Films **401**, 7 (2001)

[16] A. Sugawara, G. G. Hembree, and M. R. Scheinfein, J. Appl. Phys. **82**, 5662 (1997)

[17] A. Sugawara, T. Coyle, G. G. Hembree, and M. R. Scheinfein, Appl. Phys. Lett. **70**, 1043 (1997)

[18] W. E. Lee and K. P. D. Lagerlöf, J. Electron Micros. Techniques **2**, 247 (1985)

[19] M. Yoshimoto, T. Maeda, T. Ohnishi, H. Koinuma, O. Ishiyama, M. Shinohara, M. Kubo, R. Miura and A. Miyamoto, Appl. Phys. Lett. **67**, 2615 (1995)

[20] B. Wölfing, K. Theis-Bröhl, C. Sutter, and H.Zabel, J.Phys.: Condens. Matter **11**, 2669 (1999)

[21] H. Meffert, J. Oster, P. Haibach, M. Huth, and H. Adrian, Physica B **259-261**, 298 (1999)

[22] M. Huth, H. Meffert, J. Oster, and H. Adrian, J. Cryst. Growth **231**, 203 (2001)

[23] O. Fruchart, S. Jaren, and J. Rothman, Appl. Surf. Sci. **135**, 218 (1998)

[24] M. Durbin, J. E. Cunningham, and C. P. Flynn, J. Phys. F **12**, L75 (1982)

[25] I. Schuller, Phys. Rev. Lett. **44**, 1597 (1980)

[26] J. J. Rhyne, R. W. Erwin, in: *Handbook of Magnetic Materials*, edited by K. H. Buschow (North Holland, Amsterdam,1995), Vol. 8

[27] Z. S. Shan and D. J. Sellmyer, in: *Handbook of the Physics and Chemistry of Rare Earths*, edited by K. A. Gschneider Jr. and L. Eyring, (North Holland, Amsterdam, 1996), Vol. 22

[28] J. R. Heffelfinger, M. W. Bench, and C. B. Carter, Surf. Sci. **343**, L1161 (1995)

[29] M. Huth, K. A. Ritley, J. Oster, H. Dosch, and H. Adrian, Adv. Func. Mater. **12**, 333 (2002)

[30] C. Hering, Phys. Rev. **82**, 87 (1951)

[31] P. Hartman, J. Cryst. Growth **49**, 166 (1980)

[32] C. Rottman and M. Wortis, Phys. Rep. **103**, 59 (1984)

[33] V. A. Shchukin and D. Bimberg, Rev. Mod. Phys. **71**, 1125 (1999)

[34] A. F. Andreev, JETP Lett. **32**, 640 (1980)

[35] A. F. Andreev, Sov. Phys.-JETP **53**, 1063 (1981)

[36] V. I. Marchenko, JETP Lett. **33**, 381 (1981)

[37] V. A. Shchukin, A. I. Borokov, N. N. Ledentsov, and P. S. Kop'ev, Phys. Rev. B **51**, 17767 (1995)

[38] E. du Trémolet de Lacheisserie, in: *Magnetostriction, Theory and Applications* (CRC, Boca Raton FL, 1993)

[39] D. Sander, Rep. Prog. Phys. **62**, 809 (1999)

[40] E. Kneller, in: *Ferromagnetismus* (Springer, Berlin, 1962)

[41] R. Koch, M. Weber, K. Thürmer, and K. H. Rieder, J. Magn. Magn. Mater. **159**, L1116 (1996)

[42] D. Sander, A. Enders, and J. Kirschner, J. Magn. Magn. Mater. **198-199**, 519 (1999)

[43] V. Oderno, C. Dufour, K. Dumesnil, Ph. Bauer, Ph. Mangin, and G. Marchal, Phys. Rev. B **54**, R17375 (1996)

[44] A. Mougin, C. Dufour, K. Dumesnil, N. Maloufi, Ph. Mangin, and G. Patrat, Phys. Rev. B **59**, 5950 (1999)

[45] A. Mougin, C. Dufour, K. Dumesnil, and Ph. Mangin, Phys. Rev. B **62**, 9517 (2000)

[46] E. du Trémolet de Lacheisserie, Phys. Rev. B **51**, 15925 (1995)

[47] E. Klokholm, IEEE Trans. Magn. **12**, 819 (1976)

[48] E. du Trémolet de Lacheisserie and J. C. Peuzin, J. Magn. Magn. Mater **136**, 189 (1994)

[49] E. van de Riet, J. Appl. Phys. **76**, 584 (1994)

[50] M. Weber, R. Koch, and K. H. Rieder, Phys. Rev. Lett. **73**, 1166 (1994)

[51] E. Klokholm and C. V. Jahnes, J. Magn. Magn. Mater. **152**, 226 (1996)

[52] P. M. Marcus, J. Magn. Magn. Mater. **168**, 18 (1997)

[53] J. Rhyne and S. Legvold, Phys. Rev. **138**, A507 (1965)

[54] A. E. Clark, B. DeSavage, and R. Bozorth, Phys. Rev. **138**, A216 (1965)

[55] F. Laves and H. Witte, Metallwitschaft **15**, 840 (1936)

[56] F. Laves, *Crystal Structure and Atomic Size* in: *Theory of Alloy Phases*, ASM, Cleveland (Ohio), p. 124 (1956)

[57] A. E. Clark and H. Belson, Phys. Rev. B **5**, 3642 (1972)

[58] P. Liu, F. R. de Boer, P. F. de Châtel, R. Coehoorn, and K. H. J. Bushow, J. Magn. Magn. Mater. **132**, 159 (1994)

[59] G. Hilscher, H. Rais, and H. R. Kirchmayr, Phys. Stat. Sol. **59**, K5 (1973)

[60] U. Atzmony, M. P. Dariel, E. R. Bauminger, D. Lebenbaum, I. Nowik, and S. Ofer, Phys. Rev. B **7**, 4220 (1973)

[61] R. Abbundi and A. E. Clark, IEEE Trans. Mag. **MAG-13**, 1519 (1977)

[62] J. Cullen and A. E. Clark, Phys. Rev. B **15**, 4510 (1977)

[63] K. H. J. Buschow and R. P. van Stapele, J. Appl. Phys. **41**, 4066 (1970)

[64] K. H. J. Buschow, Rep. Progr. Phys. **40**, 1179 (1977)

[65] L. Sandlund, M. Fahlander, T. Cedell, A. E. Clark, J. B. Restorff, and M. Wun-Fogle, J. Appl. Phys. **75**, 5656 (1994)

[66] D. C. Jiles, J. Phys. D: Appl. Phys. **27**, 1 (1994)

[67] D. C. Jiles and J. B. Thoelke, Phys. Stat. Sol. A **147**, 535 (1995)

[68] R. C. Fenn, J. R. Downer, D. A. Bushko, V. Gondhalekar, and N. D. Ham, Smart Mater. Struct. **5**, 49 (1996)

[69] E. du Trémolet de Lacheisserie, Silic. Ind. **9-10**, 176 (1993)

[70] M. Vazquez and H. Hernando, J. Phys. D **29**, 939 (1996)

[71] Y. Lu and A. Nathan, Appl. Phys. Lett. **70**, 526 (1997)

[72] E. du Trémolet de Lacheisserie, K. Mackay, J. Betz, and J. C. Peuzin, J. Alloys Comp. **275-277**, 685 (1998)

[73] S. H. Lim, T. H. Noh, I. K. Kang, S. R. Kim, and S. R. Lee, J. Appl. Phys. **76**, 7021 (1994)

[74] T. Tanaka, H. Arimura, S. Kikuchi, S. Sugimoto, M. Okada, M. Homma, and K. I. Arai, J. Jpn. Ins. Metals **59**, 447 (1995)

[75] Y. Hayashi, T. Honda, K. I. Arai, K. Ishiyama, and M. Yamaguchi, IEEE Trans. Magn. **29**, 3129 (1993)

[76] T. Honda, K. I. Arai, and M. Yamaguchi, J. Appl. Phys. **76**, 6994 (1994)

[77] P. J. Grundy, D. G. Lord, and P. I. Williams, J. Appl. Phys. **76**, 7003 (1994)

[78] F. Schatz, M. Hirscher, M. Schnell, G. Flik, and H. Kronmüller, J. Appl. Phys. **76**, 5380 (1994)

[79] P. I. Williams and P. J. Grundy, J. Phys. D: Appl. Phys. **27**, 897 (1994)

[80] A. Hernado, C. Prados, and C. Prieto, J. Mag. Mag. Mater. **157/158**, 501 (1996)

[81] T. Miyazaki, T. Saito, and Y. Fujino, J. Magn. Magn. Mater. **171**, 320 (1997)

[82] E. Quandt, B. Gerlach, and K. Seemann, J. Appl. Phys. **76**, 7000 (1994)

[83] E. Quandt, J. Appl. Phys. **75**, 5652 (1994)

[84] E. Quandt, J. Alloys Comp. **258**, 126 (1997)

[85] F. Schatz, M. Hirscher, G. Flik, and H. Kronmüller, Phys. Stat. Sol. A **137**, 197 (1993)

[86] P. I. Williams, D. G. Lord, and P. J. Grundy, J. Appl. Phys. **75**, 5257 (1994)

[87] A. Speliotis, O. Kalogirou, and D. Niarchos, J. Appl. Phys. **81**, 5696 (1997)

[88] A. Speliotis, O. Kalogirou, N. Vouroutzis, and D. Niarchos, J. Mag. Mag. Mater. **187**, 17 (1998)

[89] P. Farber and H. Kronmüller, J. Mag. Mag. Mater. **214**, 159 (2000)

[90] S. F. Fischer, M. Kelsch, and H. Kronmüller, J. Mag. Mag. Mater. **195**, 545 (1999)

[91] D. W. Forester, C. Vittoria, J. Schelleng, and P. Lubitz, J. Appl. Phys. **49**, 1966 (1978)

[92] Y. S. Choi, S. R. Lee, S. H. Han, H. J. Lim, and S. H. Lim, J. Alloys Comp. **258**, 155 (1997)

[93] M. Wada, H. Uchida, and H. Kaneko, J. Alloys Comp. **258**, 169 (1997)

[94] A. G. Jenner, L. A. Stone, and H. V. Snelling, J. Alloys Comp. **258**, 138 (1997)

[95] S. Jaren, E. du Trémolet de Lacheisserie, D. Givord, and C. Meyer, J. Mag. Mag. Mater. **165**, 172 (1997)

[96] N. Négre, M. Goiran, S. Jaren, C. Meyer, R. Barbaste, A. R. Fert, and S. Askénazy, J. Magn. Magn. Mater. **198-199**, 315 (1999)

[97] M. Ciria, J. I. Arnaudas, C. Dufour, V. Oderno, K. Dumesnil, and A. del Moral, J. Appl. Phys. **81**, 5699 (1997)

[98] M. Huth and C. P. Flynn, J. Appl. Phys. **83**, 7261 (1998)

[99] A. Mougin, C. Dufour, K. Dumesnil, N. Maloufi, and Ph. Mangin, Appl. Phys. Lett. **76**, 1449 (2000)

[100] K. Ried, M. Schnell, F. Schatz, M. Hirscher, B. Ludescher, W. Sigle, and H. Kronmüller, Phys. Stat. Sol. A **167**, 195 (1998)

[101] N. H. Duc, K. Mackay, J. Betz, and D. Givord, J. Appl. Phys. **79**, 973 (1996)

[102] R. Koch, H. Leonhard, G. Thurner, and R. Abermann, Rev. Sci. Instrum. **61**, 3859 (1990)

[103] D. Winau, R. Koch, A. Führmann, and K. H. Rieder, J. Appl. Phys. **70**, 3081 (1991)

[104] A.C. Tam and H. Schroeder, J. Appl. Phys. **64**, 5422 (1988)

[105] A. J. Schell-Sorokin and R. M. Tromp, Phys. Rev. Lett. **64**, 1039 (1990)

[106] D. Sander, A. Enders, and J. Kirschner, Rev. Sci. Instrum. **66**, 4734 (1995)

[107] P. Farber, M. Hörmann, M. Bischoff, and H. Kronmüller, J. Appl. Phys. **85**, 7828 (1999)

[108] A. Sugawara and K. Mae, J. Cryst. Growth **237-239**, 201 (2002)

[109] R. Du and C. P. Flynn, J. Phys.: Condens. Mater **2**, 1335 (1990)

[110] R. Dekkers, C. F. Woensdregt, and P. Wollants, J. Non-Cryst. Solids **282**, 49 (2001)

[111] J. Mayer, G. Gutekunst, G. Möbius, J. Dura, C. P. Flynn, and M. Rühle, Acta Metall. Mater. **40**, S217 (1992)

[112] M. Tinkham, in: *Introduction to Superconductivity*, (McGraw-Hill, USA, 1996)

[113] D. D. Morrison and R. M. Rose, Phys. Rev. Lett. **25**. 356 (1970)

[114] O. Daldini, P. Martinoli, J. L. Olsen, and G. Berner, Phys. Rev. Lett. **32**, 218 (1974)

[115] P. Martinoli, Phys. Rev. B **17**, 1175 (1978)

[116] O. K. Soroka and M. Huth, Low Temp. Phys. **28**, 842 (2002)

[117] O. K. Soroka, M. Huth, V. A. Shklovskij, J. Oster, and H. Adrian, Physica C **388**, 73 (2003)

[118] C. Teichert, J. Barthel, H. P. Oepen, and J. Kirschner, Appl. Phys. Lett. **74**, 588 (1999)

[119] L. Z. Mezey and J. Giber, Appl. Phys. A **35**, 87 (1984)

[120] L. Z. Mezey and J. Giber, Surf. Sci. **234**, 210 (1990)

[121] E. Fort, C. Ricolleau, and J. Sau-Pueyo, Nano Lett. **3**, 65 (2003)

[122] M. Hansen and K. Anderko, in: *Constitutions of Binary Alloys*, (McGraw-Hill, New York, 1958)

[123] M. B. Salamon, S. Sinha, J. J. Rhyne, J. E. Cunningham, R. Erwin, J. Borchers, and C. P. Flynn, Phys. Rev. Lett. **56**, 259 (1986)

[124] J. Kwo, M. Hong, and S. Nakahara, Appl. Phys. Lett. **49**, 319 (1986)

[125] C. F. Majkrzak, J. Kwo, M. Hong, Y. Dafet, D. Gibbs, C. L. Chien, and J. Bohr, Adv. Phys. **40**, 99 (1991)

[126] B. Krause and K. Theis-Bröhl, J. Phys.: Condens. Matter **12**, 4675 (2000)

[127] R. C. C. Ward, E. J. Grier, A. K. S. Petford-Long, J. Mater. Sci. - Mater. Electron. **14**, 533 (2003)

[128] W. Święch, M. Munsdschau, and C. P. Flynn, Surf. Sci. **437**, 61 (1999)

[129] K. H. J. Bushow, Rep. Prog. Phys. **40**, 1179 (1977)

[130] V. Oderno, C. Dufour, K. Dumesnil, Ph. Bauer, Ph. Mangin, G. Marchal, L. Hennet, and G. Patrat, Europhys. Lett. **36**, 713 (1996)

[131] G. F. Clark, B. K. Tanner, and H. T. Savage, Phil. Mag. B **46**, 331 (1982)

[132] C. de la Fuente, J. I. Arnaudas, M. Ciria, A. del Moral, C. Dufour, A. Mougin, and K. Dumesnil, Phys. Rev. B **63**, 054417 (2001)

[133] J. I. Arnaudas, C. de la Fuente, M. Ciria, L. Benito, C. Dufour, K. Dumesnil, and A. del Moral, J. Magn. Magn. Mater. **240**, 389 (2002)

[134] D. G. Lord, V. Elliott, A. E. Clark, H. T. Savage, J. P. Teter, and O. D. McMasters, IEEE Trans. Magn. **24**, 1716 (1988)

[135] E. E. Fullerton, C. H. Sowers, J. P. Pearson, S. D. Bader, X. Z. Wu, and D. Lederman, Appl. Phys. Lett. **69**, 2438 (1996)

[136] J. M. L. Beaujour, G. J. Bowden, A. A. Zhukov, B. D. Rainford, P. A. J. de Groot, R. C. C. Ward, and M. R. Wells, J. Appl. Phys. **93**, 8639 (2003)

[137] M. Goiran, N. Négre, S. Jaren, C. Meyer, R. Barbaste, A. R. Fert, J. C. Ousset, and S. Askénazy, Physica B **246-247**, 542 (1998).

[138] A. Westphalen, Diploma thesis, supervised by K. Theis-Bröhl and H. Zabel, Ruhr-Universität Bochum, 2002

[139] A. Sugawara and M. R. Scheinfein, Phys. Rev. B **56**, R8499 (1997)

[140] M. Kallmayer, Diploma thesis, supervised by H. J. Elmers, Johannes Gutenberg-Universität Mainz, 2003

[141] R. P. Cowburn, D. K. Koltsov, A. O. Adeyeye, M. E. Welland, D. M. Tricker, Phys. Rev. Lett. **83**, 1042 (1999)

[142] R. P. Cowburn and M. E. Welland, Science **287**, 1466 (2000)

[143] J. Raabe, R. Pulwey, R. Sattler, T. Schweinböck, J. Zweck, and D. Weiss, J. Appl. Phys. **88**, 4437 (2000)

[144] R. Höllinger, A. Killinger, and U. Krey, J. Magn. Magn. Mater. **261**, 178 (2003)

[145] A. Yamasaki, W. Wulfhekel, R. Hertel, S. Suga, and J. Kirschner, Phys. Rev. Lett. **91**, 127201 (2003)

[146] J. K. Ha, R. Hertel, and J. Kirschner, Phys. Rev. B **67**, 064418 (2003)

[147] E. S. Stoner and E. P. Wohlfarth, Philos. Trans. R. Soc. London, Ser. A **240**, 599 (1948)

[148] J. Oster, F. Porrati, M. Kallmayer, L. Wiehl, H. J. Elmers, H. Adrian, and M. Huth, *accepted at J. Magn. Magn. Mater.*

[149] N. A. Usov, C. R. Chang, and Z. H. Wei, J. Appl. Phys. **89**, 7591 (2001)

[150] R. Skomski, H. Zeng, and D. J. Sellmyer, J. Magn. Magn. Mater. **249**, 175 (2002)

[151] K. Theis-Bröhl, T. Schmitte, V. Leiner, H. Zabel, K. Rott, H. Brückl, and J. McCord, Phys. Rev. B **67**, 184415 (2003)

[152] S. Yang, H. Zhu, D. Yu, Z. Jin, S. Tang, and Y. Du, J. Magn. Magn. Mater. **222**, 97 (2000)

[153] T. G. Sorop, C. Untiedt, F. Luis, L. J. de Jongh, M. Kröll, and M. Raşa, J. Appl. Phys. **93**, 7044 (2003)

[154] T. Schmitte, K. Theis-Bröhl, V. Leiner, H. Zabel, S. Kirsch, and A. Carl, J. Phys.: Condens. Matter **14**, 7525 (2002)

[155] Y. Martin and H. K. Wickramasinghe, Appl. Phys. Lett. **50**, 1455 (1987)

[156] J. J. Sáenz, N. García, P. Grütter, E. Meyer, H. Heinzelmann, R. Wiesendanger, L. Rosenthaler, H. R. Hibder, and H. J. Güntherodt, J. Appl. Phys. **62**, 4293 (1987)

List of Publications

Magnetic properties of Fe nanowires on faceted α-$\mathbf{Al_2O_3}$ m-plane
J. Oster, F. Porrati, M. Kallmayer, L. Wiehl, H. J. Elmers, H. Adrian, and M. Huth
J. Appl. Phys. **97**, 1 (2005)

Magnetic and magnetoelastic properties of epitaxial (211)-oriented $\mathbf{RFe_2}$ (R = Dy, Tb) thin films
J. Oster, L. Wiehl, H. Adrian, and M. Huth
Accepted at J. Magn. Magn. Mater. In Press.

Growth of Fe nanostructures
J. Oster, M. Huth, L. Wiehl, and H. Adrian
J. Magn. Magn. Mater. **272 - 276**, 1588 (2004)

Guided vortex motion in Nb films on faceted substrate surfaces
O. K. Soroka, M. Huth, V. A. Shklovskij, J. Oster, and H. Adrian
Physica C **388 -389**, 773 (2003)

Highly ordered Fe and Nb stripe arrays on faceted α-$\mathbf{Al_2O{-}3}$ $(10\bar{1}0)$
M. Huth, K. A. Ritley, J. Oster, H. Dosch, and H. Adrian
Adv. Funct. Mater. **12**, 333 (2002)

Re-entrance phase formation of CeSb thin films
M. Huth, H. Meffert, J. Oster, and H. Adrian
J. Cryst. Growth **231**, 203 (2001)

Magnetotransport properties of epitaxial (100)- and (111)-oriented CeSb thin films

H. Meffert, M. Huth, J. Oster, P. Haibach, and H. Adrian
Physica B **281-282**, 447 (2000)

Thermally induced emission of light from a metallic diffraction grating, mediated by surface plasmons
M. Kreiter, J. Oster, R. Sambles, S. Herminghaus, S. Mittler-Neher, and W. Knoll
Optics Communicatins **168**, 117 (1999)

Thin film preparation of the low carrier density Kondo system CeSb
H. Meffert, J. Oster, P. Haibach, M. Huth, and H. Adrian
Physica B **259-261**, 298 (1999)